Active Photonic Crystal Devices Based on InP/InGaAsP/InP Slab Waveguides: Theoretical Considerations and Fabrication

A dissertation submitted to

ETH ZURICH

for the degree of
Doctor of Sciences ETH Zurich

presented by

PETER KASPAR

Dipl. Phys. ETH
born July 14th, 1980
citizen of Switzerland

accepted on the recommendation of

Prof. Dr. Heinz Jäckel, examiner
Prof. Dr. Gian-Luca Bona, co-examiner
Dr. Anne Talneau, co-examiner

2012

Abstract

Line defect waveguides in photonic crystals (PhC) have a number of properties that make them interesting for photonic integrated circuits (PIC): Through modifications of the crystal geometry, the waveguide dispersion can be designed to exhibit a frequency range with slow light propagation. By slowing down the light, nonlinear effects can be enhanced, and the interaction length in an amplifier can be reduced. The building blocks of a PIC can potentially be reduced in size, and new building blocks can be conceived. The main challenge is to find a way of fabricating electrically pumped active components without dramatic propagation losses. Vertically pumped waveguides need cladding layers to separate the absorbing metal contact from the optical mode. Typically, such devices are formed by epitaxial growth of a guiding layer and a top cladding on a semiconductor substrate such as indium phosphide (InP). These so-called substrate-type PhC waveguides are known to be very lossy. But where exactly do the losses come from? What can we do to reduce them? Is it still possible to achieve gain in a single-moded PhC waveguide through electrical pumping? These are the essential questions discussed in the present dissertation.

The first part of the dissertation deals with theoretical considerations about PhC waveguides. The principal achievement is the introduction of the so-called *background line* as a replacement for the *light line*. It is a widespread misconception that the light line is the separatrix in a dispersion diagram of any PhC waveguide that divides it into a region of guided modes and a region of lossy modes. We show that, for substrate-type waveguides with a strong lateral mode confinement, the light line concept is not quite correct. The background line concept can be viewed as a refinement of the light line concept, and it becomes relevant for narrow PhC waveguides. It enlarges the design flexibility for low-loss PhC waveguides.

In the second part of the dissertation, advances in the fabrication of PhC waveguides are presented. A crucial step in the fabrication process is to provide a good hardmask for the dry-etching process of the InP-based semiconductor material. Silicon nitride (SiN_x) was chosen as the hardmask material. Conventionally, nanostructures in SiN_x with ver-

tical sidewalls are obtained by careful additions of oxygen to a CHF_3 dry-etching plasma. The oxygen helps to remove fluorocarbon depositions that form during the etching process. The chemical balance in the plasma is critical, and varying conditions of the reactor chamber walls can have a severe impact on the etching quality and reproducibility. Therefore, an alternative process was developed, which performs etching and fluorocarbon removal in two separate steps that are repeated in cycles. This approach conceptually resembles the so-called Bosch process (used for silicon etching). However, while our process introduces a separate step for the removal of a passivation layer, the Bosch process uses an intermediate step to deposit such a layer.

After the successful implementation of a robust process for SiN_x etching, a new technique is demonstrated to overcome the limitations in etching depth in SiN_x (presented by the selectivity of the hardmask fabrication process between electron beam resist and SiN_x). After etching circular structures halfway through a thick SiN_x layer, a thin film of titanium is evaporated on top it. During titanium deposition, the sample is mounted at an angle with respect to the evaporation direction, such that the bottom of the hole stays clean. Then, another etching step can be performed. This technique is termed "self-aligned mask renewal".

Using the improved SiN_x hardmask, single-line defect (W1) PhC waveguides were fabricated, and their propagation losses were measured in a port-to-port setup. The lowest ever reported propagation losses were measured (540 dB/cm at a wavelength of $\lambda = 1550$ nm, and 335 dB/cm around $\lambda = 1490$ nm). In the partner project of R. Kappeler, propagations losses in PhC waveguides were investigated numerically. These simulations serve as a benchmark for the experimental loss results. The excellent agreement between theoretical loss figures obtained with perfectly cylindrical holes and measured values suggests that fabrication imperfections are not the limiting factor in terms of propagation loss. It can be concluded that the dominant loss mechanism is the fact that the waveguides are operated above the background line. Therefore, future waveguide designs will have to enable operation below the background line.

The third part of the dissertation is dedicated to the experimental demonstration of electrically driven active PhC waveguides. The fabri-

cation of electrical contacts to waveguides of sub-μm width is demonstrated. Continuous wave lasing at room temperature of PhC lasers as narrow as $1.5\,\mu$m was achieved. To assess the separate influences of propagation loss and carrier leakage on the lasing threshold, the PhC lasers were compared to lasers formed of deeply etched trench waveguides. It is concluded that lateral escape of carriers is a significant issue for narrow PhC waveguides. With state-of-the-art waveguide designs, gain in a W1 PhC waveguide seems to be out of reach. On the other hand, an exciting new waveguide design is proposed, that has the potential to overcome the problem of high propagation losses and that would allow for vertical current injection.

Zusammenfassung

Optische Wellenleiter in photonischen Kristallen (PhC) haben einige Eigenschaften, die sie für integrierte optische Schaltkreise (PIC) interessant machen: Durch geeignete Modifikationen der Kristall-Geometrie kann die Wellenleiter-Dispersion so beeinflusst werden, dass ein Frequenzintervall entsteht, in welchem die Fortpflanzung des Lichts massiv verlangsamt ist. Dadurch wird die Energie eines Lichtpulses auf ein kleines Volumen gebündelt, nichtlineare Effekte werden verstärkt, und die Interaktionslänge in einem optischen Verstärker kann verkürzt werden. Dies eröffnet die Möglichkeit Bauelemente eines PIC zu verkleinern und neuartige Bauelemente zu planen und zu konstruieren. Die grosse Herausforderung liegt darin, aktive Elemente elektrisch zu kontaktieren, ohne dabei grosse Propagationsverluste zu erzeugen. Vertikal gepumpte Wellenleiter benötigen Mantelschichten um den absorbierenden Metallkontakt räumlich von der optischen Mode zu trennen. Typischerweise werden solche Elemente aus epitaktisch gewachsenen Schichtstrukturen hergestellt, die auf einem Substrat wie Indiumphosphid (InP) aufgebaut werden. Diese sogenannten Substrat-Typ PhC-Wellenleiter sind bekannt für ihre grossen optischen Verluste. Aber wie genau entstehen diese Verluste? Was können wir tun um sie zu vermindern? Ist es dennoch möglich Verstärkung zu erreichen durch elektrisches Pumpen eines einmodigen PhC-Wellenleiters? Dies sind die wesentlichen Fragen, welche der vorliegenden Dissertation zugrunde liegen.

Der erste Teil dieser Dissertation widmet sich theoretischen Aspekten von PhC-Wellenleitern. Die Haupterrungenschaft ist die Einführung der sogenannten *Background-Linie*, welche die gebräuchliche *Lichtlinie* ersetzt. Es wird gemeinhin angenommen, dass die Lichtlinie im Dispersionsdiagramm eines beliebigen PhC-Wellenleiter eine Separatrix darstellt, welche zwischen geführten und verlustbehafteten Moden unterscheidet. Wir zeigen, dass dies für Substrat-Typ Wellenleiter mit starkem lateralen Moden-Einschluss nicht ganz richtig ist. Das Konzept der Background-Linie kann als Verfeinerung der Lichtlinie betrachtet werden und hat grosse Relevanz für schmale dielektrische Wellenleiter (z.B. PhC-Wellenleiter). Es vergrössert die Flexibilität im Design verlustarmer PhC-Wellenleiter.

Im zweiten Teil der Dissertation werden Fortschritte in der Herstellung von PhC-Wellenleitern vorgestellt. Ein zentraler Punkt im Fabrikationsprozess ist die Verfügbarkeit einer qualitativ hochstehenden Hartmaske für die Trockenätzung der InP-basierten Halbleitermaterialien. Als Material für die Hartmaske wurde Siliziumnitrid (SiN_x) verwendet. Herkömmliche Prozesse für die Ätzung von Nanostrukturen in SiN_x mit vertikalen Seitenwänden verwenden ein CHF_3-Plasma mit wohldosierten Zugaben von Sauerstoff. Der Sauerstoff hilft die Fluorkohlenstoff-Ablagerungen zu entfernen, die sich während dem Ätzprozess bilden. Die genaue chemische Zusammensetzung des Plasmas ist entscheidend für die Qualität des Ätzresultats. Veränderliche Bedingungen in der Reaktor-Kammer können das Gleichgewicht stören und verheerende Folgen haben für die Reproduzierbarkeit des Prozesses. Daher wurde im Rahmen dieser Arbeit ein alternativer Prozess entwickelt, welcher die Ätzung und die Entfernung der Fluorkohlenstoff-Ablagerungen in zwei separaten Schritten durchführt, welche zyklisch wiederholt werden. Dieser Ansatz hat eine konzeptionelle Ähnlichkeit mit dem sogenannten Bosch-Prozess (für Silizium), funktioniert aber eigentlich nach dem umgekehrten Prinzip. Während für unser Prozess ein Schritt für die Entfernung der Passivierungsschicht eingeführt wird, verwendet der Bosch-Prozess einen Zwischenschritt um eine solche Schicht aufzubauen.

Nach der erfolgreichen Demonstration eines robusten Prozesses für die Ätzung von SiN_x wird eine neue Technik vorgestellt, welche es ermöglicht die Limitierungen in der Ätztiefe in SiN_x zu überwinden (welche durch die Selektivität des Hartmaske-Prozesses zwischen dem Elektronenstrahl-Lack und SiN_x). Nachdem man kreisförmige Strukturen halb durch eine dicke SiN_x geätzt hat, wird ein dünner Titan-Film aufgedampft. Dies geschieht unter einem Neigungswinkel gegenüber der Depositionsrichtung, sodass die untere Ätzfläche im Loch nicht bedeckt wird. Dann wird ein weiterer Ätzschritt durchgeführt. Diese Methode wird hier als "self-aligned mask renewal" bezeichnet.

Mit der verbesserten SiN_x Hartmaske wurden PhC-Wellenleiter mit einer einzigen fehlenden Lochreihe (W1) hergestellt. Durch Transmissionsmessungen wurden für diese Art Wellenleiter die tiefsten je gezeigten Verluste gemessen (540 dB/cm bei einer Wellenlänge von $\lambda = 1550\,\text{nm}$, und 335 dB/cm bei $\lambda = 1490\,\text{nm}$). Im Partner-Projekt

von R. Kappeler wurden die Propagationsverluste mittels numerischer Methoden untersucht. Diese Simulation dienen als Benchmark für die experimentellen Verluste. Die hervorragende Übereinstimmung zwischen theoretischen Resultaten mit idealisierten Lochformen und den experimentellen Werten lässt darauf schliessen, dass Ungenauigkeiten in der Herstellung nicht der limitierende Faktor sind in Bezug auf Propagationsverluste. Es kann gefolgert werden, dass der dominante Verlust-Mechanismus die Tatsache ist, dass die Wellenleiter oberhalb der Background-Linie betrieben werden. Dies bedeutet, dass zukünftige Wellenleiter-Designs das Betreiben unterhalb der Background-Linie ermöglichen müssen.

Der dritte Teil dieser Dissertation ist der experimentellen Demonstration von elektrisch gepumpten PhC-Wellenleitern gewidmet. Ein Herstellungsprozess für elektrische Kontakte auf Wellenleitern von sub-μm Breite wurde entwickelt. Mit dieser Technologie konnten PhC-Laser realisiert werden, welche den Dauerstrichbetrieb bei Raumtemperatur für bis zu $1.5\,\mu$m schmale Wellenleiter erlauben. Um den separaten Einfluss von Propagationsverlusten und von Trägerverlusten abzuschätzen, wurden die PhC-Laser mit Lasern verglichen, deren Wellenführung durch tiefgeätzte Gräben gegeben ist. Es wird gefolgert, dass der seitliche Abfluss von Trägern für schmale PhC-Wellenleiter ein wichtiger Effekt darstellt. Mit dieser Art von Substrat-Typ PhC-Wellenleitern wird Verstärkung in einem W1-Wellenleiter kaum möglich sein. Stattdessen wird ein interessantes neues Design vorgeschlagen, welches das Potential besitzt das Problem der grossen Propagationsverluste zu überwinden und dennoch vertikales Pumpen erlaubt.

Table of Contents

1

Introduction

The work presented in this thesis is inspired by the vision of photonic integrated circuits (PIC), which have to compete with electronic circuits not only in terms of speed but also in terms of footprint, cost, power consumption, and integrability with other circuits and systems. The main prerequisite for powerful PICs is the availability of all required functionalities in a single integration platform. The individual elements of a circuit have to be mutually compatible with regard to the materials used and the technology and equipment required for their fabrication. Moreover, interconnects between elements should be small, efficient and cheap. One approach for the construction of such an integration platform is to use photonic crystal (PhC) waveguides as a basic building block.

In Sec. 1.1 of this chapter, the state of the art of PICs is briefly reviewed and the potential role of PhCs is addressed. In Sec. 1.2, the state of the art of PhC devices is reviewed. The main challenges and unsolved problems that the PhC technology is confronted with in the context of PICs are identified. It is the objective of this work to clarify some theoretical issues associated with PhCs and to advance the fabrication technology to a point where its merits and drawbacks can be

traded off and its promise as an enabling technology for an integration platform for PICs can be evaluated. The specific contributions made by this thesis are summarized in Sec. 1.3.

1.1. Photonic integrated circuits

1.1.1. A historical overview

The idea of PICs came up in the late 1960s [1]. Rapid advances in semiconductor-based optics were triggered by the invention of the laser diode [2] and the ensuing progress in epitaxial fabrication technology [3]. A variety of devices were already available and well understood at that time, such as waveguides, bends, directional couplers, channel dropping filters, etc. [4, 5]. In 1970, the first continuous wave (cw) laser diode in GaAs was demonstrated [6], which was a big step towards electro-optically modulated signal transmission. Even earlier than that, in 1966, Kao and Hockman first proposed the use of optical fiber as a data transmission medium [7], although the optical fibers used at that time suffered from unacceptable losses. In the late 1970s, low-loss optical fibers[1] and connectors were developed as well as reliable cw laser diodes. However, at that time the prospect of the huge available bandwidth offered by optical communications could not trigger a major boost in research efforts, simply because no urgent need for such a bandwidth was asserted. In 1979, Tamir put it like this: "Seeing that optical communications is the most immediate and profitable application of integrated optics, the lack of urgency to develop this area affects its funding, which is generally on the low side" [8]. In the 1980s, optical fibers largely replaced metallic wires in telecommunications [9, Chap. 1]. This development was boosted by the demonstration of high-gain erbium doped fiber amplifiers (EDFA) [10]. In the meantime, microfabrication techniques such as photolithography have matured to a point where submicron linewidths could be achieved. In 1988, the arrayed waveguide grating (AWG) was proposed by Smit. Allowing for optical wavelength (de)multiplexing operations, it became one of the crucial elements in wavelength division multiplexing (WDM) systems. Nevertheless, it took another decade for the first large-scale PICs to appear. One of the most complex PICs reported in the 20th century was a monolithically integrated four wavelength 2x2 optical cross-connect (OXC). It integrates two AWGs with 16 Mach-Zehnder

---

[1]Nowadays, a loss of 0.2 dB/km is a routine specification for silica fiber.

interferometer (MZI) switches [11]. Around the same time, advances in nanotechnology enabled the demonstration of the first PhC devices integrated on a chip, operating at optical wavelengths. This triggered hopes that slow light propagation might be used to engineer improved or even new integrated devices, such as optical switches exploiting enhanced nonlinear effects or optical buffers [12].

In the past decade, the complexity of PICs started to increase rapidly. The first successful commercialization of a large-scale PIC chip was achieved by Infinera in 2004. It was a 10-channel transmitter with a 10 Gb/s operation of each channel. This circuit was followed by transmitter chips of increasing complexity [13–15]. Another example of large-scale integration is demonstrated in 2009 by a group at the University of California in Santa Barbara (UCSB). Their 8x8 monolithic tunable optical router (MOTOR) is capable of 40 Gb/s operation per port [16]. The main limitation towards a competitive all-optical alternative to electronic routers is set by optical buffering. Potential solutions based on PhC membranes have been demonstrated by the NTT Basic Research Laboratories [17]. The biggest challenge associated with an integration scheme based on membrane PhCs is current injection into nano-scale active regions.

1.1.2. Building blocks

What are the building blocks required for all-optical networks? The answer to this question depends on what we mean by "building block". There are different levels of sophistication that can be considered. For instance, on the level of *network elements*, the answer could be:
- Receiver
- Router
- Regenerator
- Transmitter

These elements are composed of a variety of *functional units*, such as
- Multiplexers
- Demultiplexers
- Transmitter sources (laser)
- Semiconductor optical amplifiers (SOA)
- Modulators
- Photodiodes
- Optical cross-connects (OXC)

- Wavelength converters
- Spot size converters
- Optical clocks
- Optical buffers

Even these functional units can be rather complex devices. However, the EuroPIC project[2] is working on a generic integration technology for which only three [18] (or four[3]) *basic building blocks* (BBB) are identified:

- Waveguide
- Phase modulator
- Amplitude modulator
- (Polarization converter)

According to the EuroPIC terminology, all functional units can be constructed from variations of these BBBs. For instance, an AWG is essentially a waveguide device, a laser is little more than an amplitude modulator, etc. This makes the task of designing complex PICs appear remarkably simple. However, it has to be pointed out that more than one type of waveguide will be required [19]. Deep ridges are beneficial for narrow bends [20], whereas electrical pumping is more efficient in shallow ridge waveguides due to reduced carrier recombination at etched sidewalls. Moreover, different types of amplifiers are needed for preamplifiers (high saturation power) than for switches (low saturation power) [16].

1.1.3. Integration platform

To define a generic integration platform, a number of decisions have to be made. What material systems shall be used for active and passive waveguide sections? How should active and passive elements be integrated? How shall different devices be interconnected?

The most common material systems used commercially and in research are silicon or InP for passive elements and InP for active devices. Both substrates are transparent in the telecom wavelength range around $\lambda = 1.55\,\mu\text{m}$. In addition, InP allows for the lattice-matched

---

[2]The EuroPIC project is coordinated by COBRA and brings together partners from industry and academia. The aim is to reduce the investment costs for SMEs to get access to applications in micro-systems and PICs

[3]http://europic.jeppix.eu/

epitaxial growth of active quaternary $In_xGa_{1-y}As_yP_{1-y}$ layers. In contrast to silicon, InP exhibits a direct bandgap which enables efficient radiative recombinations of electrons and holes. Silicon, on the other hand, is often favored for passive devices due to the widely available microfabrication and CMOS technology.

Concerning active/passive integration, the distinction between monolithic and hybrid integration is made. For monolithic integration, the following approaches are commonly used [21]:

- Growth-etch-regrowth: After growth of the active layers, they are removed by etching in those areas which are to host the passive elements. Then regrowth of the passive waveguide layers and the cladding is performed. This approach is used by Infinera (a manufacturer of long-haul optical transmission equipment) and by EuroPIC [18]. It results in butt-joint transitions and provides the highest flexibility in the choice of the properties of the two waveguide sections, since they are almost independent of each other [22].
- Quantum well intermixing (QWI): After growth of the active QW layers, the bandgap of these layers is shifted in certain areas of the chip to turn them into passive material. This technique is successfully employed by the UCSB group [23]. It offers a reduced fabrication complexity compared to the the growth-etch-regrowth method.
- Multiguide vertical integration (MGVI): All epitaxial layers are grown in one run on top of each other. Light is coupled vertically back and forth between active and passive layers using mode adaptors. No regrowth process is required, which eliminates yield and cost constrains associated with regrowth [24]. This approach is followed by OneChip Photonics.

Monolithic integration allows for relatively simple fabrication processes, but it is restricting in terms of material properties. Advantageous properties of two or more different materials can be exploited by hybrid integration. The different materials can be grown or bonded on top of each other. A renowned example is Intel's hybrid silicon laser [25]. InP-based material for light generation and amplification is bonded to a silicon waveguide that forms the laser cavity. Also other companies such as Luxtera or CIP Technologies use bonding to add III/V active elements to PICs based on silicon. Alternative hybrid integration technologies include polymer waveguide devices integrated with active

components [26] or epitaxial growth of III/V materials on mismatched substrates [27].

Finally, a lateral waveguide geometry has to be chosen. Conventional examples are deeply etched ridges, surface ridges (shallow etch), as well as buried channels or ribs. Typically, the waveguide loss increases with stronger mode confinement, if similar sidewall roughness is assumed. This is related to the fact that waveguides with a large refractive index contrast need to be narrower for single-mode operation [22, 28]. If not all required elements for a given PIC can be implemented with a single waveguide geometry, then the transition between different waveguides has to be made by mode transformers or spot size converters. Ideally, such transitions should be avoided to reduce the complexity of the fabrication process. A PhC-based approach has the potential to solve this issue by a direct implementation of all functionalities in PhC waveguides. Furthermore, PhC waveguides are considered promising in terms of small circuit footprint. Sharp bends with low optical losses have been demonstrated theoretically [29] and experimentally [30, 31]. The prospect of using slow-light waveguides to reduce the interaction length in devices with active functionalities has added further impetus to the idea of using PhCs for PICs. In general terms, the high flexibility in tailoring the dispersion properties of PhC waveguides has stimulated the hopes that any conceivable functionality could be implemented and added to the "toolbox" of PhC-based building blocks.

1.2. Photonic crystals

1.2.1. A historical overview

Periodic media for electromagnetic waves have been studied since many decades. The unique reflectivity properties of naturally occurring crystals were observed more than 100 years ago [32]. Floquet's theorem was brought in conjunction with periodically structured electromagnetic waveguides in a standard textbook as early as 1954 [33]. The phenomenon of pass bands and stop bands was well-known in radio and microwave technology long before the term *photonic crystal* appeared in the literature. Artificially manufactured periodic sub-micron structures for applications at optical frequencies date back as far as the late 1960s and early 1970s when the first distributed feedback lasers (DFB)

were demonstrated experimentally [34, 35]. The first mention of three-dimensional photonic bandgap materials was made in 1979 by Ohtaka *et al.*, who developed a mathematical formalism to study the photonic energy bands of a model system composed of identical dielectric spheres arranged in a three-dimensional lattice [36]. This work was inspired by an earlier experiment which made use of Bragg diffraction theory to determine the lattice period of ordered colloidal suspensions [37].

The pioneering work typically associated with the term *photonic crystals* was done in 1987 by Yablonovitch [38] and John [39]. The principal motivation of their independent work was, on one hand, the potential of PhCs to inhibit spontaneous emission (and thereby improving the performance of semiconductor lasers) and, on the other hand, the prospect to strongly localize photons. After these milestone papers, periodic optical media started to receive a rapidly increasing amount of attention. At first, a major focus was on 3D PhCs, because of their complete bandgaps. However, 3D PhCs are not easy to fabricate, especially not for optical wavelengths. Due to this difficulty of experimental verification of the theory and due to the limited potential for commercial applications, 3D PhCs soon had to give way to simplified geometries. For PICs, the planar PhCs (also referred to as slab PhCs, *quasi-2D*, or simply 2D PhCs) are the most straightforward option. They started to receive a lot of attention after the first experimental demonstration at optical wavelengths [40]. On the other hand, a 2D periodicity was also used for PhC fibers (or *holey fibers*) [41], and the concept was successfully commercialized.

1.2.2. Active photonic crystal devices for photonic integrated circuits

One of the major challenges associated with PhCs and PICs is the implementation of electrically driven active PhC devices in a chip. In 1996, a first laser device was demonstrated which made use of a PhC mirror on one side of the cavity, while the other end of the cavity was a cleaved facet [42]. The reflectivity of the PhC mirror was estimated to $\sim 50\%$. Later on, similar devices were demonstrated with improved fabrication technology [43], and the wavelength-dependence of the mirror reflectivity was analyzed numerically [44]. The first laser fully based on a 2D PhC was demonstrated in 1999 [45]. It was an optically pumped point-defect device in InGaAsP, emitting at a wavelength of $1.55\,\mu$m.

The laser was operated in pulsed mode (10 ns pulses, 4% duty cycle) at a substrate temperature of 143 K, but a room temperature variant followed soon thereafter [46]. One of the unique properties of PhC point defects is their influence on spontaneous emission characteristics of an active host material. This effect is known as the Purcell effect. It can be exploited for sources with low pumping threshold, low noise, and high-speed response [47]. For networking applications, the high-speed response is particularly interesting. Modulation speeds in excess of 100 GHz have been demonstrated [48]. However, all of the cited microcavity lasers are optically pumped and surface-emitting, which makes on-chip interconnection with other functional units rather difficult.

An electrically-driven microcavity laser was demonstrated in 2004 [49]. A ring-shaped n-contact enclosed a PhC pad with a point defect in its center. Current was pumped laterally through the PhC and through a narrow post beneath the point defect. The device was operated at room temperature in pulsed mode (6 ns pulses, 2.4% duty cycle), and it was also surface-emitting. Only recently, the experimental demonstration of an electrically pumped in-plane laser was reported [50]. The carriers were injected through a lateral p-i-n junction, and the device was operated at 150 K in cw mode.

In contrast to point-defect devices, line-defect lasers are in-plane emitters by nature of their geometry. The introduction of a line-defect into a 2D periodic structure reduces the symmetry to a 1D periodicity. Therefore, lasers built from such waveguides can be thought of as DFB lasers. A DFB laser operates near the bandedge, because there the density of states (DoS) is increased and, therefore, the gain is enhanced. In 2003, an optically pumped laser was demonstrated, whose cavity was formed by a single line defect PhC waveguide (W1) [51]. The device consisting of a membrane of nine stacked InGaAsP quantum wells (QW) was operated in pulsed mode (100 ns pulses, 1% duty cycle) at room temperature and emitted at a wavelength of 1515 nm. Later on, the same group investigated the influence of waveguide width on the lasing wavelength [52]. A strong dependence was observed, which is related to the fact that the line defect modes of a single-moded PhC waveguide shifts considerably in the dispersion diagram when the width of the waveguide is modified. This effect can be viewed as a "tunability" of the lasing wavelength by variation of the waveguide width, while keep-

ing the period of the PhC constant. This qualifies the line-defect PhC lasers as a special class of DFB laser. They are sometimes referred to as 2D DFB lasers [53]. The second dimension of the periodicity introduces an additional degree of design freedom.

Electrically pumped lasing in a single line-defect has not yet been achieved.[4] However, several devices with wider line-defect waveguides have been demonstrated [54–56]. The narrowest examples are around $2\,\mu$m in width (W5 along ΓK or W4/3 along ΓM [55]). To obtain a single-mode emission, the PhC waveguides are sometimes modified by adding one [56] or several [55] constrictions. The coupled cavities created in this way induce a mode selection. Such lasers could be easily integrated with other PhC-based devices. However, it has to be noted that the performance of the cited devices is not superior to that of conventional designs, such as 1D DFB lasers.

1.2.3. Substrate-type versus membrane-type photonic crystal waveguides

From now on, we will distinguish between *substrate-type* and *membrane-type* 2D PhC waveguides, as shown in Fig. 1.1. The two types of structures differ in the refractive index contrast that is responsible for light confinement in the 2D plane. The substrate-type PhCs have a small index contrast, i.e., the refractive index of the guiding layer is close to that of the substrate/cladding. A typical example is a PhC etched into an epitaxially grown layer stack of III/V semiconductor materials. The membrane-type PhCs have a large index contrast. The guiding layer is either suspended in air or supported by a low-index material. Typical examples are free-standing membranes of silicon or III/V semiconductor materials or silicon-on-insulator (SOI) structures.

There are two important differences between substrate-type and membrane-type PhCs (we will restrict the discussion to hole-type PhCs operated at a wavelength around 1550 nm):

Waveguide losses: While in W1 membrane-type PhC waveguides, propagation losses as low as 2 dB/cm were measured at a wavelength of 1550 nm [57], the losses in substrate-type structures are higher by

---

[4]One might consider the laser reported in Ref. [50] as a short line-defect device, but we prefer to think of it as a point defect device.
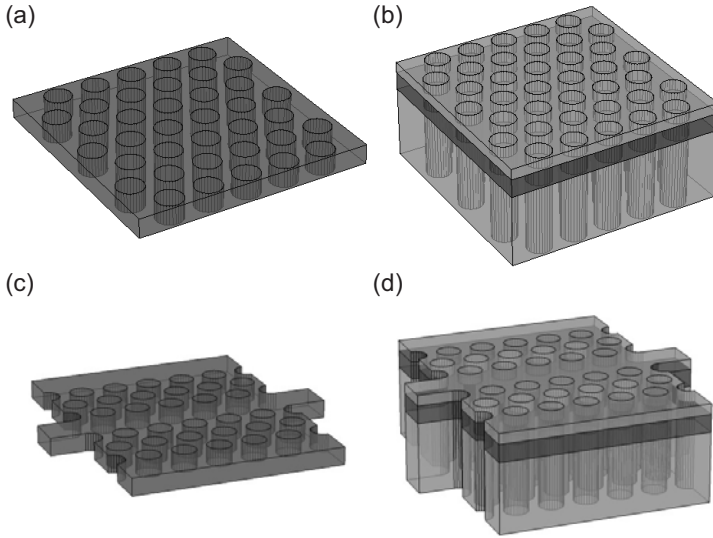
Figure 1.1. Planar PhC waveguides; (a) membrane-type; (b) substrate-type. Line-defect waveguides are obtained by omitting one or several rows of holes; (c) membrane-type; (d) substrate-type.

orders of magnitude. In the same wavelength range, state-of-the-art losses are around 800 dB/cm [58]. There are two kinds of explanations for this. Firstly, the fabrication of substrate-type PhCs is more challenging, because high aspect ratio holes have to be etched to a high degree of accuracy. In InP-based materials, deep ($> 3\,\mu$m) and perfectly cylindrical holes are difficult to achieve. Typical experimental hole shapes are conical. This fabrication imperfection introduces propagation losses. The second explanation for high losses in substrate-type PhC waveguides is based on the fact that they are often operated in a frequency region where no guided modes exist in a strict sense. This statement will be addressed in detail in Sec. 2.3. In the effort of designing a low-loss substrate-type waveguide, it is crucial to understand the quantitative importance of each of the two factors: What is the lowest loss figure that we can expect if we bring the fabrication to perfection? This question was unanswered at the time when this thesis was initiated. In the meantime, more insight based on numerical simulation is provided in the dissertation of Roman Kappeler [59].

Current injection: Electrical pumping of active PhC waveguides is more straightforward for substrate-type structures than for membranes. Vertical current injection is enabled by the cladding layers, which can be used to spatially separate the optical mode from the strongly absorbing contacts. Membrane-type PhC waveguides can only be pumped laterally through the PhC (because there is no electrically conductive, non-absorbing, low-index material by which the membrane could be supported). However, the conductivity of the perforated layers is low [50, 60, 61], and the fabrication of a lateral p-i-n junction involves several process steps (for instance using ion implantation [50]). A vertical p-i-n junction can be formed during growth of the slab waveguide structure and requires no additional fabrication steps. This seems like a clear advantage that would favor the substrate-type PhCs for applications in PICs. But if the unique properties of PhCs are to be exploited, then a narrow, single-moded waveguide has to be used. The typical width of a W1 waveguide being clearly below $1\,\mu\text{m}$, the current injection becomes a non-trivial issue. For one thing, a high demands are put on the fabrication; for another thing the carriers have to be guided through a narrow channel with little lateral confinement and a high carrier recombination rate has to be expected at etched sidewalls of the PhC holes. To avoid the delicate issue of current injection into PhC waveguides, one interesting approach was proposed, in which in-plane optical pumping is used [62, 63]. This could be a promising route for an integration platform which combines substrate-type and membrane-type PhC structures.

1.3. Objectives and contributions of this work

In Sec. 1.1.3, we summarized some of the decisions that have to be made for the definition of a generic integration platform for PICs. We pointed out that using PhC waveguides as a BBB is a promising approach, because PhCs have the potential to facilitate the implementation of functionalities that are otherwise hard to obtain. The list of BBBs as defined by the EuroPIC project (cf. Sec. 1.1.2) makes it clear, that an electrically pumped waveguide is the key component. It is essential for SOA-based devices as well as for phase modulators. Table. 1.1 summarizes the benefits that an electrically pumped active PhC waveguide can offer in view of PICs. The list distinguishes between properties/effects associated with slow light and those related to dispersion tailoring. For each property/effect, examples of active applications are given in the

Table 1.1. Potential benefits of active PhC devices in PICs. We distinguish between the properties/effects associated with slow light (SL) and those related to dispersion tailoring.

	Physical property/effect	Application
Slow light	Enhanced gain	- SOA for preamplification amplification
		- Low-threshold laser
	Enhanced nonlinearities	- SOA for 2R regeneration
		- Phase modulators
		- Switches
	Small size	- Any waveguide application
Dispersion tailoring	Broad region of SL	- Any application relying on SL
	Wavelength tuning of SL mode	- DFB laser
	Mirror with predefined reflectivity	- high-efficiency laser
	Coupling between PhC and ridge waveguide	- mode converter

third row of the table.

In Sec. 1.2.3 the distinction between substrate-type and membrane-type PhCs was introduced, and the advantages and drawbacks of both types were briefly discussed. For the present work, the substrate-type approach was considered to be the more attractive choice, mainly because the issue of electrical pumping of active membrane-type devices is a major challenge. It goes without saying that the substrate-type approach also poses its major challenge, namely the fact that W1 waveguides suffer from high propagation losses. If this issue cannot be resolved, the use of substrate-type PhCs becomes unattractive. Many of the benefits that PhCs can offer rely on slow-light propagation, which can only be effectively exploited in single-moded waveguides, i.e., in W1 waveguides (or slightly wider variants). All experimental demonstrations of slow light in PhCs, that have come to our attention, were performed in membranes [64–67]. It is, therefore, the main endeavor of this work, and that of the partner project by Roman Kappeler, to

assess whether a low-loss substrate-type PhC waveguide can be engineered in an InP-based material system. In this context, the following questions have to be addressed:

- Is it possible from a theoretical point of view to design a low-loss W1 PhC waveguide that allows for vertical current injection?
- How much room for improvement is there in terms of etching of deep holes in InP-based structures?
- How do we implement electrical pumping of active PhC waveguides, without disturbing the PhC dispersion properties?

This thesis has made contributions to all of these questions. The main focus is on the fabrication of PhCs and of electrical contacts, but some important theoretical contributions are also made. The following list summarizes the achievements:

Chapter 2: Theoretical considerations
- Light velocities: Slow light being one of the major assets of PhCs, we believe that it is worth reviewing the concepts of phase, group and energy velocity. The textbook definition of group velocity is $v_{gr} = d\omega/dk$, where ω is the angular frequency and k is the Bloch index of a monochromatic mode. This definition was introduced by analogy to the case of a plane wave in a homogeneous medium (with k the wave number). To our knowledge, it was never checked if the definition actually reflects the propagation behavior of a group of Bloch modes. We do this in Sec. 2.2. Furthermore, the concepts of phase and energy velocity are also reviewed.
- The light line: Since optical propagation losses in substrate-type PhC waveguides present the severest obstacle on the way to efficient active devices, a thorough understanding of the loss mechanisms would be desired. It is often pointed out that substrate-type PhC waveguides exhibit the fundamental flaw of being operated exclusively *above the light line* (or *inside the light cone*) of the substrate/cladding [68–71]. It is argued that an operation above the light line inevitably results in *coupling to substrate modes* and hence to optical losses. Section 2.3 clarifies this issue by pointing out that for structures resembling *buried rectangular waveguides* it is not the light line of the substrate which defines a boundary in the dispersion diagram between guided and radiative modes [72].

Chapter 3: Fabrication-related issues

- Deeply etched holes - mask fabrication: The weak refractive index contrast of the layer structure for vertical mode confinement and the requirement of a thick top cladding imply that the PhC holes have to penetrate deeply into the substrate. Ideally, the hole shape (circular in our case) should be perfectly preserved along the hole axis (leading to a cylindrical profile in our case). In dry-etching, the quality and the maximum depth of the holes are ultimately limited by the quality of the mask. For the present work, a large effort was put into providing a reproducible high-quality silicon nitride (SiN_x) mask [73]. This result is presented in Sec. 3.1.

- Deeply etched holes - increasing the mask thickness: For a given masking material (SiN_x in our case) and a given etching chemistry, the maximum etching depth is limited by the thickness of the mask. Therefore, a new fabrication technique is introduced which allows to increase the masks thickness by a factor of ~ 2. The same technique has a lot of potential to be applied for a wide variety of purposes in micro and nanofabrication [74]. These results are detailed in Sec. 3.2.

- Deeply etched holes - InP etching: For a given mask, a better hole shape and/or a larger hole depth can only be achieved by changing the etching chemistry. Our standard process [75, 76] results in conical holes with bottom parts that deviate from a straight vertical axis in a seemingly random fashion. We believe that these imperfections are at least partially responsible for the large optical propagation losses in our waveguides (which are state-of-the-art). A process using a different chemistry was implemented at TU Eindhoven on the same type of equipment that we have in our lab [77], and the results looked promising for improved hole shape characteristics. In Sec. 3.3, we report on the implementation of a similar process on our own equipment. A thorough investigation of the limitations of this process chemistry is also presented [78].

- Propagation loss measurements: The new mask fabrication process is applied to fabricate substrate-type W1 PhC waveguides. The optical performance is measured and compared to numerical simulations in Sec. 3.4. The comparison shows that, in terms of propagation losses, the fabrication quality is no longer the limiting factor [79].

Chapter 4: Issues related to current injection

- Air-bridge contacts: In order to exploit the unique effects of PhCs, such as slow light or high-Q cavities, it is vital that PhC properties are not affected by the metal contact or by an electrically isolating layer which is sometimes used to planarize the PhC device surface. In Sec. 4.1.2 it is shown that a planarization layer can, indeed, affect the band diagram of a PhC. Furthermore, a fabrication technique for air-bridge contacts is presented [80].

- Gain in PhC waveguides: The active devices mainly studied in this thesis are separate confinement heterostructure (SCH) laser diodes. The gain medium is composed of InGaAs/InGaAsP quantum wells, lattice-matched to InP. Lasing can easily be achieved for broad PhC waveguides (continuous wave and at room temperature) as shown in Sec. 4.3.1. However, broad waveguides are multi-moded and only of limited interest for PICs. On the other hand, single-moded W1 PhC waveguides are extremely lossy and lasing is not easily achieved. In Sec. 4.2, the epitaxial structure used in the experiments is analyzed with regard to the maximum achievable gain and the optimum number of QWs to be used. The question is discussed if attaining sufficient gain is possible theoretically to compensate the losses that are typically observed in substrate-type W1 waveguides. This includes modelling of the active material as well as a comparison to experimental data from fabricated devices.

- PhC waveguide vs. deep trench waveguide lasers: Vertically injected lasers are demonstrated experimentally for both PhC waveguides and deeply etched trench waveguides. Lasing in PhC waveguides as narrow as W4 is reported in cw mode at room temperature. The lasing threshold current density is strongly dependent on waveguide width. In the case of the trench waveguides, this behavior can be attributed to increasing waveguide losses and, to some extent, to an increased influence of surface recombination of carriers at the etched sidewalls. In the case of PhC waveguides, there are additional carrier losses due to current spreading and lateral diffusion through the PhC structure. Separating all these effects is a challenging task. Sec. 4.3 discusses these phenomena from an experimental and empirical point of view.

- Active/passive integration: For PICs, active and passive components must be integrated on the same chip. For ease of standardization, this is ideally done monolithically. Sec. 4.4.2 presents

trench waveguide lasers which are monolithically integrated with passive PhC waveguides. Both coupling into substrate-type and coupling into membrane-type PhC waveguides are demonstrated experimentally. This constitutes a proof of concept for the monolithic integration of active and passive components operating at $\lambda = 1.55\,\mu\mathrm{m}$ in an InP-based material system.

An overview of the publications resulting from this dissertation is provided on pp. 191. Several collaborations with various institutions were pursued. The most successful ones are listed here in chronological order:

- COBRA, Technische Universiteit Eindhoven, Netherlands: PhC patterns were etched into InP through a hardmask of SiO_2 that was fabricated using an intermediate chromium mask. This work was published in Ref. [77]. Our own process makes use of an intermediate titanium mask. Both strategies lead to results of comparable quality. Chromium turned out to cause more micromasking during InP etching than titanium. We therefore continued using titanium.
- Electrochemistry Laboratory, Paul Scherrer Institut (PSI), Switzerland: The formation of fluorocarbon layers during SiN_x etching in CHF_3 plasmas was investigated using x-ray photoelectron spectroscopy (XPS). These results are presented in Sec. 3.1 and were published in Ref. [73].
- Laboratory of Food Process Engineering, ETH Zurich, Switzerland: SiN_x membranes for membrane emulsification were fabricated using the fabrication technology developed for PhC hardmasks. Preliminary results are shown in Sec. 3.2.4 and in Ref. [74].
- SINTEF ICT, Microsystems and Nanotechnology, Oslo, Norway: PhC membranes were fabricated in a layer stack of $SiN_x/SiO_2/SiN_x$. The lithography and etching of PhC structures was performed at ETH Zurich. The membranes were tested in an optical setup for the detection of single nano-particles. They should eventually be used for biosensor applications. This work was submitted for publication and is currently waiting for peer-review [81].

2

Theory

The chapter starts out with a review of the fundamentals of PhC theory. It is shown how the Bloch theorem for optical modes in periodically modulated media follows from Maxwell's equations and from symmetry considerations (Sec. 2.1). Section 2.2 critically reviews the physical concepts of phase velocity, group velocity, and energy velocity of Bloch modes. In Sec. 2.3, the role of the *light line* in a waveguide dispersion diagram is commented. It is pointed out that, for certain waveguide geometries resembling buried rectangular waveguides (BRWG), the light line is not a suitable tool to discriminate between guided and lossy modes of propagation. As an alternative concept, the *background line* is introduced and shown to bear more practical relevance than the light line in the specific cases of the BRWG and substrate-type PhC waveguides. This provides new design flexibilities for theoretically loss-free PhC waveguides.

2.1. Basic theory of photonic crystals

In this section, some concepts of photonic crystal (PhC) theory shall be reviewed. The focus shall be on ideas which will be needed in the

following sections. For more comprehensive treatments, the reader can revert to several standard textbooks [82–86].

We consider systems composed of non-absorbing dielectric materials. The permittivity $\varepsilon(\mathbf{r})$ shall be a scalar function of the position $\mathbf{r}$ in space. Assuming charge neutrality and the absence of currents, Maxwell's equations can be used to derive the following wave equation for the $\mathbf{H}$-field [83],

$$\nabla \times \left(\frac{1}{\varepsilon(\mathbf{r})} \nabla \times \mathbf{H}(\mathbf{r}, t) \right) + \frac{1}{c^2} \frac{\partial^2}{\partial t^2} \mathbf{H}(\mathbf{r}, t) = 0. \tag{2.1}$$

If $\varepsilon(\mathbf{r})$ is independent of time, we can separate Eq. (2.1) into two eigenvalue problems,

$$\frac{1}{c^2} \frac{\partial^2}{\partial t^2} \mathbf{H}(\mathbf{r}, t) = - \left(\frac{\omega}{c} \right)^2 \mathbf{H}(\mathbf{r}, t), \tag{2.2}$$

related to the time evolution of $\mathbf{H}(\mathbf{r}, t)$, and

$$\nabla \times \left(\frac{1}{\varepsilon(\mathbf{r})} \nabla \times \mathbf{H}(\mathbf{r}, t) \right) = \left(\frac{\omega}{c} \right)^2 \mathbf{H}(\mathbf{r}, t), \tag{2.3}$$

governing the field distribution in space. The solutions of Eq. (2.2) are harmonic in time. Therefore, we can use the variable separation $\mathbf{H}(\mathbf{r}, t) = \mathbf{H}(\mathbf{r}) e^{-i\omega t}$, with the angular frequency ω. The spatial problem can be stated as

$$\boldsymbol{\Theta} \mathbf{H}(\mathbf{r}) = \left(\frac{\omega}{c} \right)^2 \mathbf{H}(\mathbf{r}), \tag{2.4}$$

with the operator $\boldsymbol{\Theta} = \nabla \times (\frac{1}{\varepsilon(\mathbf{r})} \nabla \times)$ of the eigenvalue problem. It can easily be verified [82] that $\boldsymbol{\Theta}$ is a Hermitian operator with respect to the inner product $(\cdot, \cdot)$ defined by

$$(\mathbf{H_1}, \mathbf{H_2}) = \int \mathbf{H_1}^* \cdot \mathbf{H_2} \, d\mathbf{r}, \tag{2.5}$$

where the asterisk denotes the complex conjugate. The Hermiticity of $\boldsymbol{\Theta}$ allows us to make implications about the symmetry properties of the system. If $\boldsymbol{\Theta}$ commutes with a given symmetry operator, we know that we can find a common basis of eigenmodes for the two operators. In other words, the eigenmodes of $\boldsymbol{\Theta}$ can be classified according to their

symmetry properties. For instance, if $\boldsymbol{\Theta}$ commutes with the operator of a given mirror symmetry, then the eigenmodes of $\boldsymbol{\Theta}$ can be divided into modes of even and odd parity with respect to the mirror plane. This principle is widely used in quantum mechanics and can be found in all standard text books on the subject (e.g., Ref. [87, Sec. 5.2]). For spatially periodic systems, the translational symmetries are of particular interest. Let $\mathbf{T_R}$ denote the translation operator for a translation by a vector $\mathbf{R}$, i.e., $\mathbf{T_R}\,\mathbf{H}(\mathbf{r}) = \mathbf{H}(\mathbf{r} + \mathbf{R})$. The eigenfunctions of this operator are harmonics in space, $\mathrm{e}^{\mathrm{i}\mathbf{k}\cdot\mathbf{r}}$, and the corresponding eigenvalues are $\mathrm{e}^{\mathrm{i}\mathbf{k}\cdot\mathbf{R}}$. Many harmonics with different $\mathbf{k}$ can have the same eigenvalue. If $\boldsymbol{\Theta}$ commutes with $\mathbf{T_R}$, then we can find a common basis of eigenmodes, i.e., each eigenmode of $\boldsymbol{\Theta}$ can be represented as a superposition of spatial harmonics which share a given eigenvalue of $\mathbf{T_R}$. Furthermore, we can use the eigenvalues of both operators, $\boldsymbol{\Theta}$ and $\mathbf{T_R}$, to classify the eigenmodes of $\boldsymbol{\Theta}$. Each eigenvalue of $\mathbf{T_R}$ can be referred to by a $\mathbf{k}$ vector that produces it. The fact that this $\mathbf{k}$ vector is not unique, naturally leads to the concept of Brillouin zones. By restricting the $\mathbf{k}$ vectors to the irreducible Brillouin zone, we can assign well-defined values of ω and $\mathbf{k}$ to each mode $\mathbf{H}_{\omega,\mathbf{k}}(\mathbf{r})$. When writing out the sum of spatial harmonics for an eigenmode of $\boldsymbol{\Theta}$, the so-called Bloch theorem is found: In a non-absorbing dielectric system with a periodic spatial modulation ($\varepsilon(\mathbf{r})$ periodic), all eigenmodes of Eq. (2.4) can be written in the form

$$\mathbf{H}_{\omega,\mathbf{k}}(\mathbf{r}) = \mathbf{u}_{\omega,\mathbf{k}}(\mathbf{r})\,\mathrm{e}^{\mathrm{i}\mathbf{k}\cdot\mathbf{r}}, \tag{2.6}$$

where $\mathbf{u}_{\omega,\mathbf{k}}(\mathbf{r})$ is a complex vectorial function with the periodicity of the dielectric function $\varepsilon(\mathbf{r})$. Since all modes $\mathbf{H}_{\omega,\mathbf{k}}(\mathbf{r})$ are composed of a discrete set of harmonics, there will be a discrete set of solutions for each value of ω. In other terms, we can introduce an alternative mode classification by enumerating the solutions with $\boldsymbol{\Theta}$-eigenvalue ω by a consecutive number $n \in \mathbb{N}$. The pair $(\omega, \mathbf{k})$ is replaced by (ω, n) and the mappings $\mathbf{k}_n(\omega)$. Equation 2.6 rewrites as

$$\mathbf{H}_{\omega,n}(\mathbf{r}) = \mathbf{u}_{\omega,n}(\mathbf{r})\,\mathrm{e}^{\mathrm{i}\mathbf{k}_n(\omega)\cdot\mathbf{r}}. \tag{2.7}$$

Now let's consider the case of a continuous translational symmetry. A specific example is a homogeneous material, for which $\boldsymbol{\Theta}$ commutes with $\mathbf{T_R}$ for all $\mathbf{R} \in \mathbb{R}^3$. Furthermore, all translation operators commute with each other. Therefore, there is a basis of eigenmodes common to $\boldsymbol{\Theta}$ and all translation operators. This can only be the basis of spatial harmonics, which implies that the solutions of Eq. (2.4) are plane

waves. Although this might not seem surprising, it is important to note that the plane wave modes of a homogeneous space are a consequence of the continuous translational symmetry, whereas the Bloch modes of a periodic system follow from the discrete translational symmetry. Furthermore, it is important to bear in mind that the **k** vector of a plane wave is not the same thing as the *Bloch index* **k**. While the former can be considered a physical quantity related to phase fronts or to the wavelength of a plane wave, the latter contains only part of the phase information of the Bloch mode. In order to make this more clearly visible, we consider the case of a system with a 1D periodicity, for which Eq. (2.7) can be written as (the index n is omitted for brevity):

$$\mathbf{H}_\omega = \mathbf{h}_\omega(y, z) \, u_\omega(x) \, e^{i[k(\omega)x - \omega t]}, \tag{2.8}$$

where $\mathbf{h}_\omega(y, z)$ represents the field distribution in the transverse plane. To visualize the phase information, we switch to a polar representation of the periodic function $u_\omega(x)$,

$$\mathbf{H}_\omega = \mathbf{h}_\omega(y, z) \, |u_\omega(x)| \, e^{i[k(\omega)x + \varphi(\omega, x) - \omega t]}, \tag{2.9}$$

where $\varphi(\omega, x)$ is a real-valued phase function that satisfies the relations $u_\omega(x) = |u_\omega(x)| \, e^{i\varphi(\omega, x)}$ and $\varphi(\omega, x + \Gamma) - \varphi(\omega, x) = 2\pi m$, $m \in \mathbb{N}$, for all x. The total phase $\Phi_\omega(x, t)$ of the Bloch mode is

$$\Phi_\omega(x, t) = k(\omega)x + \varphi(\omega, x) - \omega t, \tag{2.10}$$

and it becomes apparent that the Bloch index $k(\omega)$ is not sufficient to describe its spatial evolution. This should be kept in mind, whenever physical quantities (such as the group velocity) are derived from $k(\omega)$. Since not the full physical information is available in $k(\omega)$, the definitions should be handled with some care. It might be instructive to consider the analogy to Bloch modes in solid state physics. The momentum of a given Bloch mode $|\psi\rangle$ is not simply given by $\hbar$ multiplied by the Bloch index of the mode (as is the case for the plane-wave momentum), but by $\langle\psi|\hat{\mathbf{p}}|\psi\rangle$, which contains a weighted sum over all plane-wave components [88, p. 139].

Equation (2.9) is not a conventional way of representing a Bloch mode. In the following, this representation will serve as a key element in a critical review of the concepts of phase and group velocity of Bloch modes.

2.2. Velocity of Light

Most of the content of this section will be submitted for publication [89].

Since one of the main assets of photonic crystals is their capability to control the propagation velocity of light, some words should be said about the various definitions of wave velocity. The terms phase velocity, group velocity and energy velocity are widely used for systems that support harmonic wave propagation, such as dielectric waveguides. Surprisingly, the standard textbooks on photonic crystals do not discuss the applicability of these concepts to spatially periodic systems in much detail. Since the pioneering works of Yariv *et al.* [90] and Yeh *et al.* [91], it has been taken for granted that the group velocity in periodic systems can be expressed as $v_{\mathrm{gr}} = \mathrm{d}\omega/\mathrm{d}k$, where k is the Bloch index. The definition was introduced by analogy to the case of homogeneous systems, without making reference to the different nature of wave number and Bloch index. This seems astonishing, since it was pointed out in the same articles [90, 91] that the definition of phase velocity has to be reconsidered for precisely that reason. In fact, there appears to be a general consensus in the photonic crystal community that phase velocity has no definite meaning in the context of Bloch modes [82, 83], while the definition of group velocity is not put into question. In general, we have to expect that all physical quantities associated with a Bloch mode are periodic in space and *not* constants. Expecting a spatially invariant group velocity would mean that we expect the system to behave like an effective material. But for an effective material, we wouldn't make a Bloch mode ansatz. Instead, we would make a plane-wave ansatz using an effective permittivity. If we intend to use the definition $v_{\mathrm{gr}} = (\mathrm{d}k/\mathrm{d}\omega)^{-1}$ for the group velocity of a Bloch mode, we have to explain why it is invariant in space.

In the following subsections, definitions of phase and group velocity shall be given in such a way that they can be applied to systems with continuous as well as discrete translational symmetries. To do so, we have to specify what we mean by the terms *phase* and *group*. The discussion shall be restricted to waveguide systems with a 1D periodicity along the propagation direction and mode solutions of the form of Eq. (2.8). Both homogeneous ($u_\omega(x) \equiv 1$) and spatially periodic ($u(x+\Gamma) = u(x)$, if Γ is the lattice constant) systems are accounted for. The phase of a Bloch mode is defined in Eq. (2.10), which allows

us to identify phase fronts defined through $\Phi_\omega(x,t) = \Phi_0$, where Φ_0 is a constant. From these phase fronts, a definition of the phase velocity can be derived (cf. Sec. 2.2.1). A *group* will be referred to as a weighted superposition of Bloch modes using a complex spectral function $G(\omega)$. The resulting field function is

$$\mathbf{H}(x,t) = \int G(\omega)\,\mathbf{H}_\omega(x,t)\,\mathrm{d}\omega = \int G(\omega)\,\mathbf{h}_\omega\,u_\omega(x)\,\mathrm{e}^{\mathrm{i}\Phi_\omega(x,t)}\,\mathrm{d}\omega \quad (2.11)$$

At a fixed location x_0 in space, the temporal evolution of $\mathbf{H}(x_0,t)$ is obtained by a Fourier transform of the spectral function $G(\omega)$. If, at a different location $x_0 + \Delta x$, the same temporal evolution is recorded with a constant time shift Δt, then we can define an average group velocity by $v_{\mathrm{gr}} = \Delta x/\Delta t$. This analysis will be carried out in detail in Sec. 2.2.2. Finally, in Sec. 2.2.3, a few words will be said about the concept of energy velocity.

2.2.1. Phase Velocity

The phase of a plane wave field is $\Phi_\omega(x,t) = kx - \omega t$, where $k = k(\omega)$ is the wave number and ω is the angular frequency. The phase velocity is the rate at which the phase fronts (lines of constant phase) propagate in space. That is, $v_{\mathrm{ph}} = \omega/k$ for a plane wave. In a more general case, where we have a field of the form

$$\mathbf{H}_\omega = \mathbf{h}_\omega(y,z)\,|u_\omega(x)|\,\mathrm{e}^{\mathrm{i}\Phi_\omega(x,t)}, \quad (2.12)$$

with an arbitrary phase $\Phi_\omega(x,t)$, we can use the local wave number $k(\omega,x,t) = \partial_x\Phi_\omega(x,t)$ and the angular frequency $\omega = \partial_t\Phi_\omega(x,t)$ to define the local phase velocity [92]. In a 1D-periodic system, we get

$$v_{\mathrm{ph}}(x) = -\frac{\partial_t\Phi_\omega}{\partial_x\Phi_\omega} = \frac{\omega}{k(\omega) + \partial_x\varphi(\omega,x)}. \quad (2.13)$$

In contrast to the case of a homogeneous system, the phase velocity becomes a periodic function of space. This is in accordance with the Bloch ansatz, which is useful whenever a system *cannot* be adequately described as an effective homogeneous system.

2.2.2. Group Velocity

The group velocity is the velocity of a group or a "packet" of eingenmodes of a given system. In a homogeneous system, the packet is

made up of plane waves; in a spatially periodic system, it is made up of Bloch modes. The simplest example [93] of a packet, or rather of a succession of packets, is the beating of two harmonic waves, $A\cos(k_1 x - \omega_1 t)$ and $A\cos(k_2 x - \omega_2 t)$, with $k_1 = k + \Delta k$, $k_2 = k - \Delta k$, $\omega_1 = \omega + \Delta\omega$, $\omega_2 = \omega - \Delta\omega$ and amplitude A. The sum of the two waves is $2A\cos(kx - \omega t)\cos(\Delta k x - \Delta\omega t)$, and we can easily distinguish between the velocity of the phase fronts $v_{\mathrm{ph}} = \omega/k$ and the envelope $v_{\mathrm{gr}} = \Delta\omega/\Delta k \to \mathrm{d}\omega/\mathrm{d}k$ for $\Delta k \to 0$. Another typical example of a packet, which is often used to motivate the definition of group velocity, is the Gaussian pulse, formed by a continuous spectrum of harmonic waves. Again, an analytical treatment reveals that the envelope propagates at the group velocity $v_{\mathrm{gr}} = \mathrm{d}\omega/\mathrm{d}k$; and it retains a Gaussian shape if third and higher order dispersion terms can be neglected [94, Chap. 7]. Generally speaking, the concept of group velocity is only applicable to narrow-band signals.

A more generic definition of the group velocity can be constructed by looking at how the individual components in a group add up. If a group, as defined in Eq. (2.11), is to propagate without distortion, then the phase relation between the components has to remain constant. W.l.o.g., we consider a pulse with an initial temporal evolution

$$\mathbf{H}(0, t) = \int G(\omega)\, \mathbf{h}_\omega\, u_\omega(0)\, \mathrm{e}^{-\mathrm{i}\omega t}\, \mathrm{d}\omega, \tag{2.14}$$

i.e., with $\varphi(\omega, 0) = 0$. After some propagation, we get

$$\mathbf{H}(\bar{x}, t + \bar{t}) = \int G(\omega)\, \mathbf{h}_\omega\, u_\omega(\bar{x})\, \mathrm{e}^{\mathrm{i}[k(\omega)\bar{x} - \omega(t + \bar{t})]}\, \mathrm{d}\omega. \tag{2.15}$$

In case of an undistorted propagation of the group, the same temporal evolution as in Eq. (2.14) is expected at the location $\bar{x}$ with a time shift $\bar{t}$,

$$\mathbf{H}(\bar{x}, t + \bar{t}) = \mathbf{H}(0, t)\, \mathrm{e}^{\mathrm{i}\varphi_0}, \tag{2.16}$$

for all t and some constant phase shift φ_0. If $\bar{x}$ is an integer multiple of Γ, then inserting Eqs. (2.14) and (2.15) in Eq. (2.16) yields the requirement

$$k(\omega)\bar{x} - \omega\bar{t} = \varphi_0 \tag{2.17}$$

for all ω. If we define $\phi(\omega, \bar{x}, \bar{t}) = k(\omega)\bar{x} - \omega\bar{t}$, then Eq. (2.17) can be rewritten as

$$\frac{\mathrm{d}^n \phi}{\mathrm{d}\omega^n} = 0 \text{ for all } n \geq 1. \tag{2.18}$$

Equation (2.18) with $n = 1$ defines the trajectory $\bar{x}(\bar{t})$ of the group, whereas the equations with $n > 1$ can only be fulfilled if the material properties of the system allow it. If the material requirements are not fulfilled exactly, we can nevertheless proceed to use $\mathrm{d}\phi/\mathrm{d}\omega = 0$ to define an *approximate* trajectory of the pulse and the corresponding group velocity, keeping in mind that the group will be distorted. This definition of the group velocity will be reasonable over a limited range of $\bar{x}$. The size of this range depends on the materials and the initial pulse shape. The condition $\mathrm{d}\phi/\mathrm{d}\omega = 0$ is equivalent to

$$\frac{\mathrm{d}k}{\mathrm{d}\omega}(\omega)\,\bar{x} - \bar{t} = 0. \tag{2.19}$$

For an undistorted group, Eq. (2.19) is valid for all $\bar{x} = m\Gamma$, $m \in \mathbb{N}$. Therefore, we can define the average group velocity

$$\langle v_{\mathrm{gr}} \rangle = \frac{\bar{x}}{\bar{t}} = \left(\frac{\mathrm{d}k}{\mathrm{d}\omega}(\omega) \right)^{-1}. \tag{2.20}$$

This confirms that the commonly used definition is reasonable, since in most experiments it is the average group velocity over macroscopic distances that is of interest. Nevertheless, we want to get some further insight about what happens *between* the periods. We consider the "artificial" example of a system in which $|u_\omega(x)|$ is a constant with respect to x, i.e., $u_\omega(x) = u_\omega\, \mathrm{e}^{\mathrm{i}\varphi(\omega,x)}$. Assuming this form of $u_\omega(x)$ is instructive, because it allows us to use the method of stationary phase [95] to define the trajectory of the group in a similar way as above. Eqs. (2.14) and (2.15) rewrite as

$$\mathbf{H}(0,t) = \int G(\omega)\, \mathbf{h}_\omega\, u_\omega\, \mathrm{e}^{\mathrm{i}\Phi_\omega(0,t)}\, \mathrm{d}\omega \tag{2.21}$$

and

$$\mathbf{H}(\bar{x}, t+\bar{t}) = \int G(\omega)\, \mathbf{h}_\omega\, u_\omega\, \mathrm{e}^{\mathrm{i}\Phi_\omega(\bar{x}, t+\bar{t})}\, \mathrm{d}\omega, \tag{2.22}$$

where $\Phi_\omega(x,t) = k(\omega)x + \varphi(\omega,x) - \omega t$. With $\phi(\omega, \bar{x}, \bar{t}) = \Phi_\omega(\bar{x}, t+\bar{t}) - \Phi_\omega(0,t)$ and $\varphi(\omega, 0) = 0$, the stationary phase requirement, $\mathrm{d}\phi/\mathrm{d}\omega = 0$, translates into

$$\frac{\mathrm{d}k}{\mathrm{d}\omega}(\omega)\,\bar{x} + \frac{\mathrm{d}\varphi}{\mathrm{d}\omega}(\omega,\bar{x}) - \bar{t} = 0. \tag{2.23}$$

By taking a time-derivative, the group velocity $v_{\mathrm{gr}} = \mathrm{d}\bar{x}/\mathrm{d}\bar{t}$ can be extracted,

$$\frac{\mathrm{d}}{\mathrm{d}\bar{x}}\left(\frac{\mathrm{d}k}{\mathrm{d}\omega}(\omega)\,\bar{x} + \frac{\mathrm{d}\varphi}{\mathrm{d}\omega}(\omega,\bar{x}) \right) \cdot v_{\mathrm{gr}} = 1. \tag{2.24}$$

The group velocity, as defined in Eq. (2.24), depends on the location in space. We can compute the average group velocity along the trajectory,

$$
\begin{aligned}
\langle v_{\mathrm{gr}}(\omega) \rangle^{-1} &= \frac{1}{\Gamma} \int_x^{x+\Gamma} v_{\mathrm{gr}}(\omega, \bar{x})^{-1} \mathrm{d}\bar{x} \\
&= \frac{1}{\Gamma} \int_x^{x+\Gamma} \frac{\mathrm{d}}{\mathrm{d}\bar{x}} \left(\frac{\mathrm{d}k}{\mathrm{d}\omega}(\omega)\,\bar{x} + \frac{\mathrm{d}\varphi}{\mathrm{d}\omega}(\omega, \bar{x}) \right) \mathrm{d}\bar{x} \\
&= \frac{\mathrm{d}k}{\mathrm{d}\omega}(\omega) + \frac{1}{\Gamma}\frac{\mathrm{d}}{\mathrm{d}\omega}\left(\varphi(\omega, x+\Gamma) - \varphi(\omega, x) \right) \\
&= \frac{\mathrm{d}k}{\mathrm{d}\omega}(\omega).
\end{aligned}
\tag{2.25}
$$

Using the spatial average, we reproduce a result which is formally identical to that of systems with a continuous translational symmetry. However, our example shows that, if the phase of $u_\omega(x)$ is dependent on x, then the group velocity fluctuates between the periods. From a conceptual point of view, this is an important insight. Note that it is important that the spatial average be taken over v_{gr}^{-1} and *not* over v_{gr}. Physically meaningful values are obtained by either averaging v_{gr} over time or v_{gr}^{-1} over space. This can be seen by considering a 1D trajectory $r(t)$ of a particle. The average velocity $\langle v \rangle$ of the particle traveling a distance Δr during the time interval Δt is given by $\langle v \rangle = \frac{\Delta r}{\Delta t} = \frac{1}{\Delta t}\int 1\,\mathrm{d}r = \frac{1}{\Delta t}\int \frac{\mathrm{d}r}{\mathrm{d}t}\,\mathrm{d}t = \frac{1}{\Delta t}\int v\,\mathrm{d}t$. The integration of v has to be performed over time. If, instead, we compute the average over distance, we get $\frac{1}{\Delta r}\int v\,\mathrm{d}r = \frac{1}{\Delta r}\int \frac{\mathrm{d}r}{\mathrm{d}t}\,\mathrm{d}r = \frac{1}{\Delta r}\int \frac{\mathrm{d}r}{\mathrm{d}t}\frac{\mathrm{d}r}{\mathrm{d}t}\,\mathrm{d}t = \frac{\Delta t}{\Delta r}\left(\frac{1}{\Delta t}\int v^2\,\mathrm{d}r \right) = \frac{\langle v^2 \rangle}{\langle v \rangle} \geq \langle v \rangle$. Hence, the average of v over distance results in an overestimated velocity. On the other hand, if we average v^{-1} over distance we get $\frac{1}{\Delta r}\int v^{-1}\,\mathrm{d}r = \frac{1}{\Delta r}\int \frac{\mathrm{d}t}{\mathrm{d}r}\,\mathrm{d}r = \frac{1}{\Delta r}\int 1\,\mathrm{d}t = \frac{\Delta t}{\Delta r} = \langle v \rangle^{-1}$, which is the physically meaningful result.

In conclusion, we have seen that $\mathrm{d}\omega/\mathrm{d}k$ is a meaningful quantity that represents the average group velocity $\langle v_{\mathrm{gr}}(\omega) \rangle$ of a Bloch mode in a periodic medium. This is not a trivial result, because a one-to-one analogy between the wave vector of plane waves and the Bloch index of a Bloch mode cannot *a priori* be taken for granted. It is an important insight for all applications where the macroscopic properties are of interest, such as slow light propagation in photonic crystal waveguides of macroscopic length. On the other hand, it is shown for a specific type of Bloch modes that the propagation of a group *cannot* in general

be adequately described by spatially constant phase and group velocities. This finding rules out a widespread misconception. It will mainly have an impact in situations where local/microscopic properties are of interest, rather than global/macroscopic ones. For instance, whenever interference effects of two Bloch modes are of importance, the microscopic phase properties will matter. In particular, we believe that for the experimental measurement of the group velocity using interference fringe patterns, microscopic effects should be taken into account.

It was mentioned above that the group velocity can only be defined in a strict sense if an undistorted pulse propagation is possible. This is the case for materials or material systems with a linear dispersion relation. In the presence of second order dispersion, it is still possible to make an unambiguous definition of the group velocity if it is restricted to the propagation of a Gaussian pulse; a Gaussian shape is conserved along the propagation axis, although the pulse is broadened and its maximum intensity is attenuated. For more complicated dispersion relations, the envelope of a group can undergo a complicated evolution, and the appropriate definition depends on the physical insight that one intends to gain from a given experiment. The problem was actively discussed a few decades ago, and a total of eight different propagation velocities were defined [96, 97]. If undistorted pulse propagation is desired, the design flexibility of PhCs offers the unique possibility to tailor the dispersion relation and to make it linear over a significant range of frequency. A systematic approach to designing "flat band" PhC waveguides has been demonstrated, which maximized the group index - bandwidth product [98].

2.2.3. Energy Velocity

On some occasions [99, Chap. 6], the physical relevance of the definition of group velocity in periodic media, $v_{gr} = d\omega/dk$, was motivated by the fact that for the energy velocity, defined via Poynting vector S and energy density $\mathcal{U}$, the same result was found: $v_{en} = d\omega/dk$.

The standard definition [93, 94, 100] of the energy velocity is $v_{en} = \langle S \rangle_T / \langle \mathcal{U} \rangle_T$, where $\langle \cdot \rangle_T$ denotes a temporal average over one period. In non-absorbing media with a *continuous* translational symmetry along a propagation axis, it can be shown [95, 101, 102] that this definition leads to $v_{en} = d\omega/dk$. Concerning media with a periodic modulation

along the propagation axis, the only discussion of the definition of energy velocity that has come to our attention is the one by Yariv and Yeh [90, 91]. In their work, the definition $v_{en} = \langle S \rangle_T / \langle \mathcal{U} \rangle_T$ was used, and it was pointed out that both quantities, $\langle S \rangle_T$ and $\langle \mathcal{U} \rangle_T$, are periodic functions of space. In order to obtain a position-independent quantity, a spatial average was performed: $v_{en} = \langle \langle S \rangle_T \rangle_\Gamma / \langle \langle \mathcal{U} \rangle_T \rangle_\Gamma$, where $\langle \cdot \rangle_\Gamma$ is an average over one spatial period Γ of the medium. There was no justification given for this step other than "it is desirable". We note that, while an integration over a unit cell of the energy density seems natural (it represents the total energy contained in a unit cell), an integration over a unit cell of the energy flux density has no immediate physical significance. Nevertheless, the "expected" result $v_{en} = d\omega/dk$ was obtained, where k is the Bloch index of the modes in the periodic system. However, without a thorough motivation of all operations required for the definition of v_{en}, there is little physical insight in this finding.

We will now make an attempt at putting the definition of the energy velocity on more solid ground. Instead of using the textbook definition, we will derive our own version and see how it compares to the one typically cited in the literature. The objective is to produce a definition for the energy velocity v_{en} without having to perform averages of quantities, that are not physically motivated.[1]

Consider a wave propagating along the x-coordinate of a non-absorbing system. The system shall be either homogeneous or periodic along x. Further consider a box of length L along the x-axis and with a cross-section A as shown in Fig. 2.1. We assume a 2D mode confinement in the y-z plane and that A is large compared to the transverse mode size, such that energy fluxes through surfaces perpendicular to A can be neglected. If the energy contained in the volume $V = L \cdot A$ flows out through the area A within time τ, then we can define the energy velocity as $v_{en} = L/\tau$. This definition is on solid ground if τ can be unambiguously determined, i.e., if the energy in V is constant in time. We will see that for harmonic waves this can be guaranteed by choosing the length of the box to be an integer multiple of the wavelength. For Bloch modes, this is not possible, and the issue has to be solved by

---

[1]If we are not guided by a clear physical argument, then we cannot decide *how* the averaging should be carried out. We could perform the average of the absolute values, of the squares, or in many other ways. All of these methods will return different results. But which one is correct?

choosing large values of L. Since an integration over the volume V is involved, v_{en} cannot be understood as a local quantity. We will think of it as an average energy velocity and denote it $\langle v_{en} \rangle$.
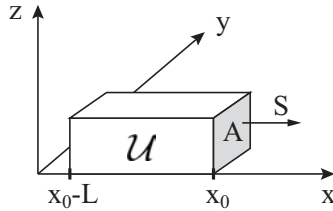
Figure 2.1. Box of length L and cross-section area A. An electromagnetic wave propagates along x. The energy density in the box is $\mathcal{U}$ and the energy flux density through the area A is S.

Let the energy density be denoted by $\mathcal{U}(x, y, z, t)$ and the energy flux density by $S(x, y, z, t)$. The total energy flowing through the area A during a time interval τ is $E(\tau) = \int_A \int_0^\tau S \, dt \, dy dz$, and the total energy contained in the box is $E_{box} = \int_V \mathcal{U} \, dx dy dz$, where $V = L \cdot A$. In the case of a harmonic time-dependence of the fields with period T, we can write $\int_0^\tau S \, dt = \tau \langle S \rangle_T$ for large τ. Moreover, if $\mathcal{U}$ is the product of periodic functions along x, we have $\int_V \mathcal{U} \, dx dy dz = L \cdot \int_A \langle \mathcal{U} \rangle_L \, dy dz$ for large L. The energy velocity can now be defined as $\langle v_{en} \rangle = L/\tau$, for the time τ satisfying $E(\tau) = E_{box}$, which is equivalent to $\tau \int_A \langle S \rangle_T \, dy dz = L \int_A \langle \mathcal{U} \rangle_L \, dy dz$. This justifies the definition

$$\langle v_{en} \rangle = \frac{\int_A \langle S \rangle_T \, dy dz}{\int_A \langle \mathcal{U} \rangle_L \, dy dz}. \tag{2.26}$$

The time τ can only be unambiguously determined if E_{box} (and therefore $\langle \mathcal{U} \rangle_L$) is constant in time. This is the case, e.g., for a plane-wave field with $\mathcal{U} \sim \cos^2(kx - \omega t)$, if we choose the size of the box such that L is an integer multiple of $2\pi/k$.

The standard textbook definition [93, 94, 100] of energy velocity in homogeneous media is $\langle v_{en} \rangle = \langle S \rangle_T / \langle \mathcal{U} \rangle_T$. Integrals over the surface A might be added if the mode is confined. The difference to our definition is the time-average of $\mathcal{U}$ instead of a space-average. For harmonic waves with $\mathcal{U} \sim \cos^2(kx - \omega t)$, the two definitions are equivalent since

both averages return the same result. To our understanding, the time-average of $\mathcal{U}$ in the textbook definition can only be justified through this equivalence.

For a Bloch mode, it can be shown (the proof is given in Appendix A.1) that $\lim_{L\to\infty}\langle\mathcal{U}\rangle_L = \langle\langle\mathcal{U}\rangle_T\rangle_\Gamma$. This allows us to rewrite Eq. (2.26) as

$$\langle v_{\text{en}}\rangle = \frac{\int_A \langle S\rangle_T \,\mathrm{d}y\mathrm{d}z}{\int_A \langle\langle\mathcal{U}\rangle_T\rangle_\Gamma \,\mathrm{d}y\mathrm{d}z}. \tag{2.27}$$

The denominator in Eq. (2.27) is constant along the x-coordinate, but what about the numerator? The time-averaged energy flux $\langle S\rangle_T$ certainly has to be considered dependent on x. On the other hand, the integral over A has to be independent of x, because otherwise the energy conservation would be violated (we could easily conceive a box similar to the one in Fig. 2.1 with a constant energy outflow through the surface A at x_0 that exceeds the energy inflow through an equivalent surface at $x_0 - L$). Therefore, adding a spatial average $\langle\cdot\rangle_\Gamma$ around $\langle S\rangle_T$ in the numerator of Eq. (2.27) makes no difference, and we arrive at an expression similar to the standard definition given by Yariv and Yeh.

We cannot directly prove the spatial invariance of the numerator in Eq. (2.27) (we have to rely on energy conservation), but we can show a numerical example to underpin it. Figure 2.2 shows the example of a 2D photonic crystal waveguide. The simulation was performed with COMSOL Multiphysics, a commercially available finite element solver, using the supercell shown in the inset of Fig. 2.2 (a) and periodic boundary conditions. The permittivities of the substrate and the holes are 11.4 and 1, respectively. The r/Γ ratio is 0.3 (r: hole radius; Γ: lattice constant). In the dispersion diagram, the studied mode is located at $(u,k) = (0.2321, 0.6122)$, where $u = \omega\Gamma/(2\pi c)$ is the reduced frequency and k is the Bloch index in units of $2\pi/\Gamma$. Mode confinement takes place only along the y-direction, but not along z. Nevertheless, our claim of an invariant $\langle S\rangle_T$ holds within the numerical accuracy of the simulation, as shown by the integrated time-averaged power flux values plotted in Fig. 2.2 (a). The integration was performed along cuts parallel to the y-axis. Figure 2.2 (b) shows two examples of how the x-component of the energy flux depends on the y-coordinate. They correspond to the solid and dashed vertical lines indicated in the inset of Fig. 2.2 (a). The inset of Fig. 2.2 (b) visualizes the time-averaged vector field of the en-

ergy flux.

To conclude this section, we emphasize again that the standard definitions of both group and energy velocity have to be understood as averaged quantities. As pointed out above, it is essential that the averaging procedure is motivated by physical arguments. In this sense, the findings of this section retrospectively form an indispensable basis for further considerations such as the proof of the equivalence $v_{\mathrm{gr}} = v_{\mathrm{en}}$ in lossless systems [90, 91] or the decomposition of v_{en} into weighted contributions from each Fourier component of a Bloch mode [103]. In fact, the equivalence result, $v_{\mathrm{gr}} = v_{\mathrm{en}}$, only now unfolds its full physical meaning.
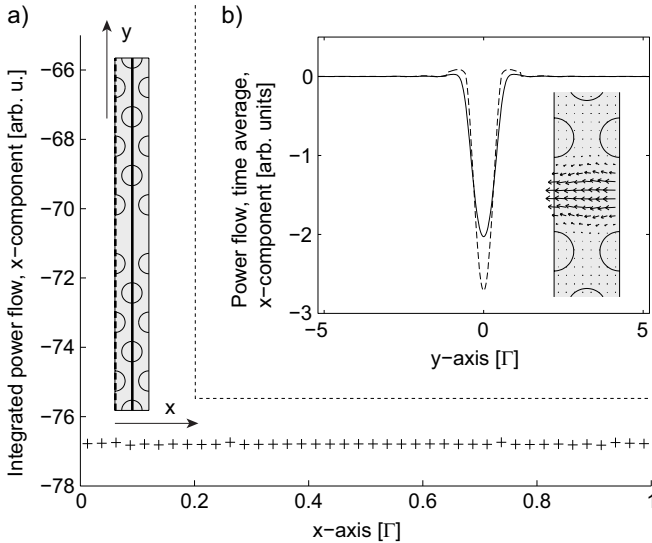
Figure 2.2. (a) Time-averaged power flux of a PhC waveguide mode, integrated along cuts parallel to the y-axis; the inset shows the supercell of the COMSOL Multiphysics simulation. (b) The x-component of the time-averaged power flux as a function of the y-coordinate; the solid and dashed curves correspond to the cuts indicated in the inset of (a). The inset of (b) shows the time-averaged vector field of the energy flux.
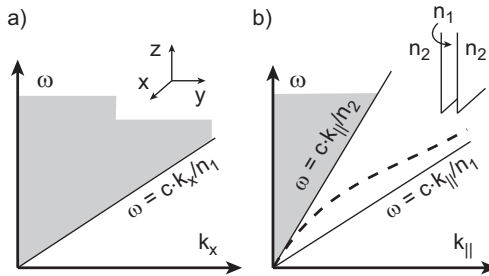
2.3. The light line

Most of the content of this section is published in [72]

One of the main challenges faced by PhC-based waveguide applications is the optical propagation loss, which is particularly pronounced in slow-light operation [104, 105], and in the case of structures with a weak refractive index contrast between the planar waveguide layers. Several arguments have been put forward to explain the difference in loss between substrate-type (low index contrast) and membrane-type (high index contrast) structures. One of them is based on the so-called *light line* concept: membrane-type PhC waveguides can be easily designed to have line defect modes below the light line of the cladding (e.g. air), whereas in the first Brillouin zone of substrate-type structures the entire bandgap is typically situated above the light line of the substrate. This observation is used to imply that there are no "truly" guided line defect modes of the substrate-type PhC waveguide, whereas the membrane-type structure naturally exhibits guided modes (theoretically loss-free) [106]. However, there is a flaw in this line of arguments, which can be boiled down to the fact that the geometry for lateral confinement is not taken into account when the light line concept is applied in a too simplistic manner. It is the purpose of this section to substantiate this statement and to replace the light line argument by a more accurate model to predict the separatrix between high-loss and low-loss modes in a dispersion diagram. We believe that, in the past, over-stressing the light line concept has caused many workers in the field to reject substrate-type PhC waveguides in general for being a fundamentally ill-suited workhorse. We intend to demonstrate that this might have been unjustified.

We will briefly introduce the concept of the light line in Sec. 2.3.1. Then, a buried rectangular waveguide (BRWG) is investigated, which resembles a deeply etched planar PhC waveguide in terms of geometry of the cross-section. No periodic dielectric modulation is considered in this section (Sec. 2.3.2). The dispersion diagram of the BRWG is analyzed in detail with respect to the separatrix that marks the boundary between guided and non-guided modes. In Sec. 2.3.3, the insights gained from the BRWG are applied to PhC waveguide structures. It is shown that there is some more design freedom for substrate-type PhC waveguides than expected up to date.

2.3.1. The dispersion diagram and the light line

A dispersion diagram is the graphical representation of the dispersion relation between angular frequency ω and wave vector $\mathbf{k}$. Typically, one specific propagation direction is fixed (according to the studied geometry), and the angular frequency ω is plotted against the corresponding component of $\mathbf{k}$. Fig. 2.3(a) shows the dispersion diagram of optical modes in a homogeneous and isotropic medium of refractive index n_1. The angular frequency is plotted against k_x, the wave vector component along the x-direction. The blank area represents a region, where no propagating modes can exist in the medium. The solid line $\omega(k_x) = c \cdot k_x/n_1$, where c is the vacuum velocity of light, represents all modes (plane waves) propagating along the x-axis. It is often referred to as the light line of the medium of refractive index n_1. In the shaded area above the light line, there is a continuum of modes whose propagation directions have non-vanishing components along the y- or z-direction.

Figure 2.3. Dispersion diagrams of (a) a homogeneous medium, (b) a symmetric planar dielectric waveguide with refractive indices $n_1 > n_2$. The light lines are indicated by solid lines and labeled with their respective dispersion relations. In the homogeneous medium (a), all modes above the light line (shaded) are oscillatory, whereas in the blank area below the light line the solutions to Maxwell's equations are exponentially decaying. In the planar waveguide (b), the dashed line schematically represents the fundamental guided mode with $k_z = 0$. No oscillatory modes can exist in the blank area below the core light line, whereas there is a continuum of such modes (shaded) above the cladding light line.

In Fig. 2.3(b) we consider a planar dielectric waveguide with refractive indices $n_1 > n_2$, a system whose boundary value problem can be

treated analytically. The angular frequency ω is plotted against the in-plane component, $k_\parallel$, of the wave vector. The dashed line schematically represents the fundamental guided[2] mode. Above the cladding light line, there exists a continuum of oscillatory radiation modes. In summary, we can view the light line as a separatrix with the following properties:

1) Below the light line $\omega(k_\parallel) = c \cdot k_\parallel / n_2$, all existing modes are guided by the waveguide core.

2) Above the light line $\omega(k_\parallel) = c \cdot k_\parallel / n_2$, there are no guided modes.

This separatrix interpretation is what we refer to as the light line concept. It follows directly from an analytical mode analysis of the planar dielectric waveguide. In the case of an asymmetric planar dielectric waveguide (top and bottom cladding of different refractive indices), the cutoff boundary is given by the light line of the higher-index cladding material. In the following, we will investigate if the light line concept is applicable also to waveguides with a 2D mode confinement. The applicability is often taken for granted in the context of PhCs [44, 70, 71, 107, 108] and in integrated optics [109]. Nevertheless, we shall see that the concept is not correct in full generality.

In terms of effective refractive index of a guided mode in a system with 2D confinement, the light line concept translates into

$$\max_{\mathbf{r}\in\mathbb{R}^2} n(\mathbf{r}) > n_{\text{eff}} > \max_{\mathbf{r}\in\partial\mathbb{R}^2} n(\mathbf{r}), \tag{2.28}$$

where $\partial\mathbb{R}^2$ is the "boundary at infinity" of the cross-section $\mathbb{R}^2$ of the waveguide. In analogy to the case of a planar waveguide, the condition is based on the definition of guided modes, i.e., on the prerequisite that *at infinite distances from the core* all fields of a guided mode decay to zero and no oscillatory fields are supported. However, whether or not this prerequisite leads to Eq. (2.28) depends on the geometry of the system. To make this clear, we will now discuss an example system for which guided modes exist that violate the condition in Eq. (2.28).

2.3.2. The buried rectangular waveguide

We consider the structure shown in Fig. 2.4 (a) and refer to it as the buried rectangular waveguide. All materials are non-absorbing and their

---

[2]We use the term "guided" to describe a propagating mode, which is oscillatory along the propagation direction but decays to zero in one (1D confinement) or two (2D confinement) transverse directions.

(a)

(b)
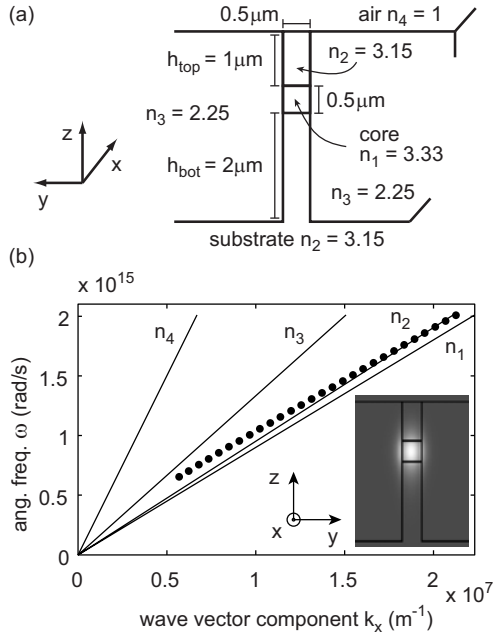
Figure 2.4. (a) Schematic structure of a buried rectangular waveguide; (b) Dispersion diagram $\omega(k_x)$. The solid lines are the dispersion lines of the materials present in the structure, labeled with their respective refractive indices. The waveguide modes (bullets) are computed by Lumerical in a range between 0.9 and 3.0 μm (= cutoff). The inset shows the field intensity $|\mathbf{E}|^2$ distribution of a mode with an effective refractive index of $n_{\text{eff}} = 3.0$; the field intensity is scaled from black (low) to white (high).

refractive indices are indicated in the figure. The simulated dispersion diagram of the waveguide is shown in Fig. 2.4 (b), along with the dispersion lines of homogeneous materials for each of the refractive indices present in the structure. We show the fundamental modes of odd parity[3] with respect to the x-z mirror plane ($E_x = H_y = E_z = 0$ in the symme-

---

[3]Let σ_y denote a reflection in the x-z plane, i.e., $\sigma_y\hat{\mathbf{x}} = \hat{\mathbf{x}}$, $\sigma_y\hat{\mathbf{y}} = -\hat{\mathbf{y}}$, $\sigma_y\hat{\mathbf{z}} = \hat{\mathbf{z}}$ for the unit vectors $\hat{\mathbf{x}}$, $\hat{\mathbf{y}}$, and $\hat{\mathbf{z}}$, respectively. $\mathbf{E}$ transforms like a vector, whereas $\mathbf{H}$ transforms like a pseudovector under an orientation-reversing map. A mode of even parity is characterized by $\mathbf{E}(\sigma_y\mathbf{r}) = \sigma_y\mathbf{E}(\mathbf{r})$ and $\mathbf{H}(\sigma_y\mathbf{r}) = -\sigma_y\mathbf{H}(\mathbf{r})$, a mode of odd parity by $\mathbf{E}(\sigma_y\mathbf{r}) = -\sigma_y\mathbf{E}(\mathbf{r})$ and $\mathbf{H}(\sigma_y\mathbf{r}) = \sigma_y\mathbf{H}(\mathbf{r})$. Note that different conventions of parity might be used in other contexts.

try plane), computed by Lumerical (bullets), a commercially available 2D finite difference frequency domain (FDFD) eigenmode solver [110]. The simulation domain is terminated by a perfectly matched layer (PML). For large propagation constants ($k_x \to \infty$), the waveguide mode crosses the dispersion line of the substrate (n_2) and converges (not shown here) to the dispersion line of the core (n_1). For small propagation constants, a cutoff is found near an effective refractive index of 2.6. This observation is in clear disagreement with the condition in Eq. (2.28), which for our BRWG writes as $n_1 = 3.33 > n_{\text{eff}} > n_2 = 3.15$.

To analyze the discrepancy between our simulation and Eq. (2.28), it has to be verified whether the modes under question can qualify as guided modes. In the strict sense, the fields of a guided mode decay to zero at infinite distances from the waveguide core. Numerically, this criterion is hard to assess in a rigorous manner. The classification is generally done based on the amount of energy in the PML surrounding the computational domain, using some arbitrary threshold. Fig. 2.5 shows the propagation loss introduced to the BRWG of Fig. 2.4 by the PML. Four different sizes of h_{bot} are considered, while h_{top} is kept constant at $1\,\mu$m. The four curves correspond to h_{bot} values of $2\,\mu$m, $4\,\mu$m, $6\,\mu$m, and $8\,\mu$m. The size of the simulation domain and the mesh resolution
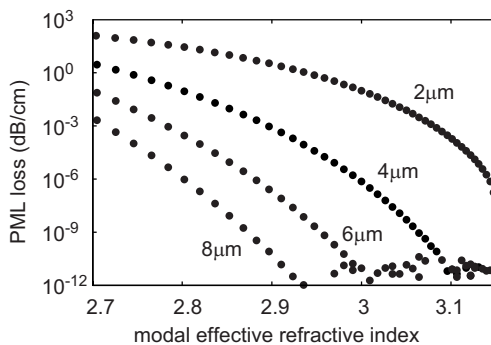
Figure 2.5. Simulated optical loss in the PML around the structure of Fig. 2.4 (a) as a function of modal effective refractive index. The four curves correspond to different values of h_{bot}: $2\,\mu$m, $4\,\mu$m, $6\,\mu$m, $8\,\mu$m. Around a loss of 10^{-10} dB/cm, the limit of numerical accuracy of the simulation is reached. In this range, some points with a negative result occur; they are omitted from the plot.

are the same for all curves. The PML loss near cutoff is substantial for $h_{\mathrm{bot}} = 2\,\mu\mathrm{m}$, but is drastically reduced for the larger values of h_{bot}. The limit of numerical accuracy is reached around $10^{-10}\,\mathrm{dB/cm}$. It is interesting to note that if the position of the PML is moved further away from the waveguide core, the change in PML loss is negligible. This indicates that the main contribution to the PML loss is given by an oscillatory field rather than a decaying one. In this respect, we cannot classify the modes as guided modes. Nevertheless, the results of Fig. 2.5 suggest that arbitrarily low PML losses can be obtained by increasing h_{bot} to infinity. We conclude that, for a BRWG with $h_{\mathrm{bot}} \to \infty$, guided modes exist with effective refractive indices outside the range given in Eq. (2.28).

In order to understand why the condition of Eq. (2.28) is violated for the guided modes of the BRWG with $h_{\mathrm{bot}} \to \infty$, we have to go back to the prerequisites from which the condition is supposed to follow. As indicated above, Eq. (2.28) is based on the requirement that the dielectric "background" at infinity must not support any oscillating solutions of Maxwell's equations. For simplicity, we will let $h_{\mathrm{top}} \to \infty$, as well. The background at infinity of this system is composed of the materials of refractive indices n_2 (thin slab) and n_3 (two half-spaces), i.e., it is essentially a slab waveguide structure.[4] The oscillating modes of a slab waveguide are either guided modes or radiation modes of the slab, and they can be computed analytically [112]. There is no oscillating mode of the slab with refractive index $n_{\mathrm{eff}} = n_2$. Therefore, the dispersion line of the substrate (n_2) cannot be relevant in the determination of the BRWG cutoff. Instead, the relevant separatrix in the dispersion diagram, which separates guided from non-guided modes, is the dispersion curve of the fundamental mode of the background system (the $n_3/n_2/n_3$ slab waveguide). We will refer to this separatrix as the "background line". Propagating modes of the full BRWG system, which are located below the background line are guided modes and theoretically loss-free.

As a further validation of our background line concept, Fig. 2.6

---

[4]It might be interesting to note that the condition of Eq. (2.28) for guided modes can be proven by a rigorous mathematical analysis, as long as there is a radius R around the core, for which $n(\mathbf{r}) = n_\infty$ for all $\mathbf{r} \in \mathbb{R}^2$ with $|\mathbf{r}| > R$ [111]. In other words, Eq. (2.28) holds for all guided modes, if outside of a circle of radius R the background is made up of a homogeneous medium of refractive index n_∞. This condition is not fulfilled by the structure of Fig. 2.4 if we let $h_{\mathrm{bot}} \to \infty$.

shows the cutoff of the BRWG of Fig. 2.4 together with the background line. Depending on the parity (w.r.t. the x-z symmetry plane) in the core of the BRWG fundamental mode (bullets), the TE or TM modes of the background slab waveguide have to be considered (solid lines). The simulation of the BRWG is again performed with the Lumerical mode solver, and the results of odd parity correspond to those of Fig. 2.4 (b). The background lines are calculated from analytical equations [112]. Cutoff for both parities occurs as predicted. This confirms that the background line bears more practical relevance than the condition of Eq. (2.28) (dotted vertical line in Fig. 2.6) if h_{bot} is large.
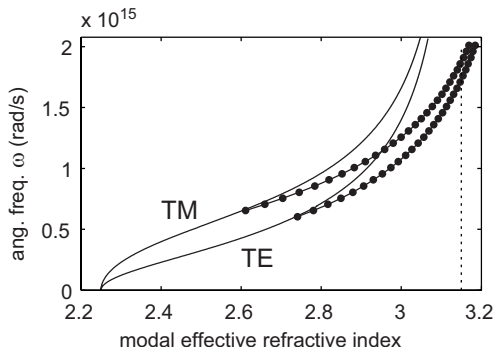
Figure 2.6.   Illustration of mode cutoff for the BRWG depicted in Fig. 2.4 (a). The bullets are the numerical mode solver results for the two parities. The solid lines represent the TE and TM fundamental mode of the background slab waveguide, as indicated in the graph. The dashed vertical line indicates the dispersion line of the substrate material.

Here, the background line was motivated from first principles. However, there are a few cases in the literature, where the concept was implicitly used. In the context of holey fibers, the band diagram of a 2D PhC structure is projected onto the out-of-plane axis [113] and the gaps appearing in this way are exploited for low-loss light propagation [41]. Furthermore, the *effective index method*, which is a popular analytical approximation to find the modes of integrated optical waveguides (such as ridge waveguides), makes use of the background modes as one of the steps in the simplification procedure for an analytical mode analysis. It is important to note that, while the effective index method makes considerable errors in determining the dispersion near cutoff of certain

waveguides, the cutoff is always predicted on the correct separatrix in the dispersion diagram (but not at the correct location on the separatrix).

The background line cannot predict the cutoff frequency of a given waveguide structure; it only represents the separatrix in the dispersion diagram on which the cutoff is to be expected. Therefore, it seems legitimate to ask of what practical use it might be. The answer is simple: it is useful, whenever we compute the dispersion diagram of a waveguide numerically with a method that doesn't easily allow us to distinguish between guided and non-guided modes. A prominent example is a dispersion diagram of a photonic crystal waveguide computed with the plane wave expansion method.

It is a widespread misconception that the condition of Eq. (2.28) follows directly from the law of total internal reflection when considering the interface of a waveguide core with the surrounding material of highest refractive index. In our case of the BRWG, this would mean that at the lower interface between the core and the substrate material total internal reflection dictates the cutoff behavior of the structure. However, this reasoning contains two mistakes at a time. Firstly, the condition of total internal reflection cannot be represented simply as a line in a dispersion diagram. This works in a 1D system, where mode confinement occurs only in one direction, but not for systems with 2D mode confinement. Secondly, it is wrong to assume that the loss of total internal reflection is responsible for mode cutoff in waveguides with a 2D mode confinement. This is treated in detail by Marcuse [112] for the case of weakly guiding optical fibers with a circular cross-section.

2.3.3. Substrate-type photonic crystal waveguides

In the photonic crystal community, the light line or light cone concept is often used to interpret numerically computed band diagrams of 2D-periodic systems, which are not uniform in the third dimension. Two examples of such a system are depicted schematically in Fig. 1.1 (a) and (b). They are 2D-periodic arrays of holes etched into a slab waveguide. To analyze the system of Fig. 1.1 (a), the band diagram is computed for 3D unit cells, and then it is overlaid with the light cone of the surrounding homogeneous material in order to retain only the guided modes of the waveguiding structure [114]. This is a reasonable approach

for many waveguide structures, but the applicability of the concept depends on the geometry of the background "at infinity". As we saw in the preceding section, our background line constitutes a more general formulation of the same concept.

First, we will briefly address the membrane-type PhC structures, surrounded by a homogeneous low-index material. It can be a PhC slab waveguide as in Fig. 1.1 (a), a line defect waveguide as in Fig. 1.1 (c), or a PhC microcavity device. For the simple PhC slab, the background at infinity is composed of the homogeneous material on top and below, since there is no lateral confinement. If defect modes are considered, then the lateral field decay is guaranteed by the PhC, as long as the device is operated within the photonic bandgap. In this sense, the background line corresponds to the light line for the membrane-type structures, which confirms the common practice of using this line as a separatrix between guided (or localized in the case of a point defect) and non-guided modes.

Now we turn to the case of a substrate-type PhC waveguide with large h_{top} and h_{bot} (as defined in Fig. 2.4 (a)), the background is formed (if h_{top}, $h_{bot} \to \infty$) by an infinitely extended 2D line defect PhC waveguide. The set of background modes is a lot more complicated than it was for the BRWG system studied above. To numerically determine the background line, the modes of the line defect waveguide have to be simulated for all propagation directions. All oscillating modes of the background system have to be included into a band diagram which is projected onto the core axis of the full system. In Fig. 2.7 we consider a single line defect (W1) PhC waveguide based on an InP/InGaAsP/InP layer structure, which resembles the BRWG of Fig. 2.4 (a) in terms of geometry of the cross-section. The lateral mode confinement is no longer given by a homogeneous material but by a PhC structure of triangular geometry and an r/Γ ratio of 0.34 (r: hole radius; Γ: lattice constant). The simulations are performed by the plane wave expansion method (MPB package [115]), using a supercell as indicated in the inset of Fig. 2.7. The shaded area in Fig. 2.7 comprises all oscillating modes of the background (regardless of parity). The lower bound of the shaded area marks the background line (dashed line). It qualitatively resembles the fundamental mode of a dielectric slab waveguide and clearly lies above the light line of the substrate (solid line). All propagating modes of the full waveguide system (including the core), which are located be-

low the background line, are guided modes. Contrary to common belief, this also applies to those modes, which are situated between the light line of the substrate and the background line. For the task of designing a waveguide with guided modes, the position of the background line has to be taken into account *instead* of the substrate light line.
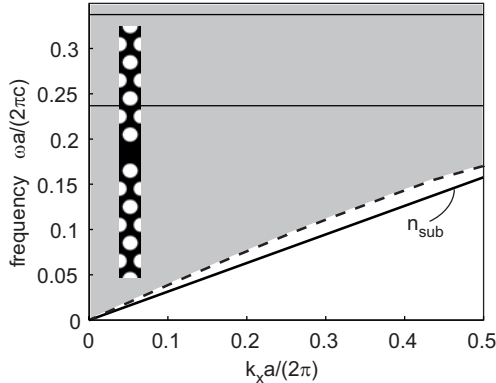
Figure 2.7. Simulation of the background line (dashed) of a W1 PhC waveguide. The shaded area indicates the radiation modes of the system (oscillating background modes). The light line of the substrate (n_{sub}) is also indicated (solid). The horizontal lines represent the upper and lower boundaries of the TE bandgap for light propagation in the *x-y* plane. The supercell used for the computations is shown as an inset.

We are looking for guided modes which lie below the background line and inside the photonic bandgap. As a coarse reference, the TE bandgap of the underlying PhC is indicated in Fig. 2.7 by two horizontal lines. Although the background line is still far below any potential bandgap mode in the present example, two kinds of strategies can be pursued to design a waveguide that exhibits guided modes within the bandgap. Firstly, the background line can be pushed upward in the dispersion diagram. This can be realized by decreasing the waveguide width. Secondly, the bandgap can be pushed downward by using a core material of higher refractive index (if available) or by modifying the PhC geometry. In Sec. 4.4.1, one specific design approach is briefly addressed. Performing a full structure optimization is very complex; the problem is addressed in [116]. At this stage, it is worth emphasizing that the last word has not been said about losses in substrate-type

PhC waveguides. Two open questions remain:

1. Is it possible to design a theoretically loss-free substrate-type
    PhC waveguide based on realistic materials? The above consid-
    erations show that it is not hopeless, but Fig. 2.7 also shows that
    for our particular material system it will be very challenging.
2. How much loss do we have for a given mode above the back-
    ground line? The background line marks the separatrix for
    guided modes. However, in a typical PhC waveguide, such as the
    one of Fig. 2.7, the main component of the Bloch mode is located
    in the second Brillouin zone [103] and below the background line.
    Only the Fourier component of the first Brillouin zone lies above
    the background line, and only that component will contribute to
    the waveguide loss [117]. The quantitative connection between
    the strength of this component and the theoretical propagation
    loss has not been established to our knowledge.

As long as these questions remain open, the final answer cannot
be given as to whether or not substrate-type PhC waveguides are vi-
able candidates for a platform of photonic integrated circuits. So far,
we cannot demonstrate the "perfect" design for a substrate-type PhC
waveguide. But in Sec. 4.4.1 we give an outlook of what could be further
investigated within the framework of InP and related materials.

3

Photonic Crystal Fabrication

The fabrication of active PhC devices presents a number of challenges that have to be overcome. For the substrate-type waveguide approach (as in Fig. 1.1 (c)), one of the main difficulties is the accurate etching of deep holes. Our solution to this problem is covered in detail in this chapter. The fabrication of deeply etched planar PhC waveguides in an InP-based material system requires the following steps (the choice of materials and equipment is specific to our process):

- Epitaxy of the the planar waveguide structure (InP/InGaAsP/InP) using metal-organic vapor phase epitaxy (MOVPE)
- Deposition of a SiN_x layer (400 nm, hardmask for InP dry-etching) by plasma enhanced chemical vapor deposition (PECVD)
- Deposition of a titanium layer (35 - 40 nm, intermediate metal mask for hardmask fabrication) by electron beam physical vapor deposition (EBPVD)
- Electron beam lithography (EBL) on PMMA (200 - 220 nm)

- Development of the exposed resist
- Reactive ion etching (RIE) of the mask (Ti and SiN_x)
- Inductively coupled plasma RIE (ICP-RIE) into the semiconductor structure
- Removal of mask (SiN_x) residuals (using hydrofluoric acid (HF))

The etching of deep cylindrical holes in InP using ICP-RIE requires a high-quality mask. Ideally, the mask of any dry-etching process would be very thin and completely stable in the etching plasma. The resists used for EBL are too soft for a Cl_2-based etching chemistry typically used for InP etching. A harder mask is required, and the most popular candidates are SiO_2 or SiN_x hardmasks. The large amount of knowledge about dry-etching of these materials (from silicon fabrication technology) makes them readily applicable for the implementation of new processes. However, the selectivity of SiO_2 and SiN_x to InP in Cl_2-based ICP-RIE processes is still limited (~ 10, depending on the exact composition of the plasma). For a final etching depth of $> 3\,\mu m$, a hardmask thickness of more than $300\,nm$ is indispensable for this etching technology. To avoid faceting [118], a margin of $\sim 100\,nm$ should be added. This results in a hardmask thickness of $\sim 400\,nm$ in which the PhC holes of diameters of the order of ~ 200 - $300\,nm$ have to be defined. In other words, an aspect ratio of up to 2 in SiO_2 or SiN_x has to be achieved. Taking into account the limited etching resistance of EBL resists in the fluorine-based RIE plasmas typically used for SiO_2 and SiN_x etching, the accurate fabrication of a PhC hardmask is a very challenging task in itself. Our own approach (inspired by Ref. [119]) makes use of an intermediate metal mask (titanium). That mask can be made very thin (35 - $40\,nm$) and provides an excellent stability in a CHF_3 plasma. The titanium is opened in an SF_6/N_2 plasma which offers a selectivity of 1:4 towards PMMA. Therefore, a PMMA thickness of $200\,nm$ is sufficient to open the titanium layer. This means that the aspect ratio in the exposed and developed PMMA is less than 1, which is a good value to avoid detrimental deformation effects during dry-etching. Large aspect ratios in the resist can also become problematic for the reliability of the development process.

The remaining challenges are to design etching processes, first for the hardmask and then for the semiconductor, which exhibit straight vertical sidewalls. The most successful approaches to hole shape control are those employing a *passivation layer* to protect the etched side-

walls from lateral etching. A typical example is the so-called *Bosch process* [120], which alternates etching steps with deposition steps of a thin protecting film. For the fabrication of our hardmask, we developed a new process which is based on a slightly different concept. The passivation layer is formed *during* the etching step, while a separate O_2 plasma step is introduced to control the degree of lateral etch inhibition. As in the Bosch process, these two steps are alternated in cycles. Fig. 3.1 schematically depicts the three different approaches. In Sec. 3.1, our new approach is presented in detail. It results in a very robust process for nanostructures with excellent vertical profiles [73]. The same process can be applied for a the "self-aligned mask renewal" method [74] to obtain an increase in aspect ratio by a factor of > 2 without the necessity of an additional lithography step (Sec. 3.2). Finally, the pattern of the hardmask must be transferred into the semiconductor structure as accurately as possible. The main challenge is the same: anisotropic etching for vertical and smooth sidewalls. But since the materials to be etched are different, the solution cannot be the same. In previous work, ICP-RIE etching processes based on Cl_2/N_2 [75] and Cl_2/O_2 [121] chemistries were presented. They claim to also make use of a passivation layer, but they are not cyclic processes. The Cl_2/N_2-based process presented in Ref. [75] is implemented in our lab and is used as a standard process for most of our devices. However, a Cl_2/O_2-based process used at TU Eindhoven seems slightly more promising in terms of hole shape and depth. Therefore, the potential of using a similar process is investigated in Sec. 3.3.

3.1. Hardmask fabrication - Cyclic etching of SiN_x

Most of the content of this section is published in [73].

3.1.1. Introduction

Figure 3.1 depicts three different etching concepts that can be applied to obtain vertical etching profiles in a dry-etching process. In a given process step, the symbols E, D, and R denote the occurrence of etching, deposition of a passivation layer, and removal of the passivation layer, respectively. The concept labeled EDR is widely used for the plasma-assisted dry-etching of SiO_2 and SiN_x in fluorocarbon-based chemistries (CHF_3, CF_4, C_4F_8, etc.). The slope of the sidewalls is typically controlled by adding gases such as O_2 to the plasma chemistry. However,

the results depend critically on the gas fluxes of the species impinging on the sample surface, and the condition of the reactor chamber walls is crucial [122–124]. In research facilities where etching chambers are often used for multiple processes, it is desirable to implement robust protocols and avoid having to maintain the delicate balance between the fluxes of etching and film forming species. Therefore, we developed an RIE process for which only one gas (CHF_3) is fed to the reactor at a time. Instead of continuously adding O_2 to the etching chemistry, we interleave the CHF_3 etching with oxygen plasma treatments. We show experimentally that by accurate timing of the two steps, high-quality hardmasks with vertical and smooth sidewalls can be fabricated [73].

The mechanism behind the proposed process corresponds to the concept labeled ED/R in Fig. 3.1. It relies on the fact that during
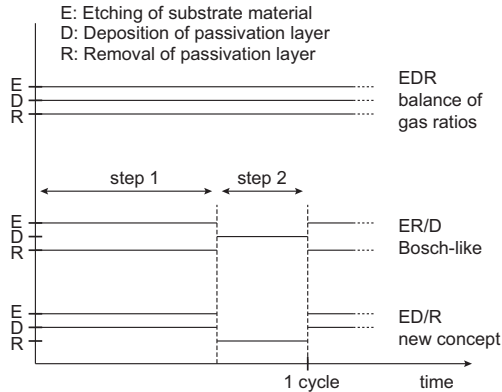
Figure 3.1. Dry-etching process concepts for vertical sidewall profiles. The graph shows the temporal evolution of the three approaches. For the first concept (EDR), a passivation layer is formed during etching of the substrate and simultaneously controlled in thickness by additions of auxiliary species (e.g., oxygen) to the etching plasma. The Bosch-like approach (ER/D) uses a separate step to build up a passivation layer, which, during etching of the substrate, is gradually removed. Profile control is achieved by cyclic repetition of these two steps. The new concept (ED/R) uses an etching plasma that, during the actual etching, forms a passivation layer. A separate step is introduced to control this layer by removing it partially or entirely. Profile control is also achieved by cyclic repetition of the two steps.

etching of SiN$_x$ in a pure CHF$_3$ plasma, a fluorocarbon layer gradually forms on the surfaces. The etching takes place by the transport of chemical species through this layer [125–127]. If thick enough, this layer can eventually inhibit etching in both the vertical and lateral directions [125, 128]. During etching, the vertical and lateral etching rates evolve in time as the thickness of the fluorocarbon layer increases. A separate oxygen plasma step can be used to interrupt the etching process and partially or completely remove the passivating fluorocarbon film. This opens up the possibility of controlling the etching characteristics by alternating CHF$_3$ etching steps with O$_2$ plasma treatments in cycles and by adjusting their respective durations.

3.1.2. Experimental verification of process mechanism

The proposed patterning concept uses O$_2$ plasma steps to interrupt fluorocarbon film formation during SiN$_x$ etching in a CHF$_3$ plasma. First, we experimentally demonstrate the impact of these intermediate O$_2$ plasma steps on the sidewall angle. Figure 3.2 shows three SiN$_x$-coated substrates that were all etched in a CHF$_3$ plasma for 25 min at a chamber pressure of 21 mTorr and a rf power of 50 W. They differ only in the number of interruptions by O$_2$ plasma steps. When continuous CHF$_3$ etching is used, a positive taper with 84° sidewall angles is obtained (Fig. 3.2 (a)). One intermediate step of O$_2$ plasma treatment (60 s, 200 mTorr, 30 W rf power) after half of the etching time already leads to a markedly steeper slope of 87° (Fig. 3.2 (b)). Ten cycles of alternating CHF$_3$ (150 s) and O$_2$ (60 s) plasma steps result in an almost vertical profile with an 89° tilt and little sidewall bowing (Fig. 3.2 (c)). These results confirm that the thickness and/or the constitution of the fluorocarbon layer are/is significantly altered by the oxygen plasma.

In order to verify the deposition/removal mechanism of the fluorocarbon film, we performed x-ray photoelectron spectroscopy (XPS) [129] analysis on a set of four samples that had been subjected to different etching procedures. The first sample was a reference sample of a bare, unprocessed SiN$_x$ layer. The second sample was patterned with PMMA (large circular opening of 0.7 mm diameter) and etched continuously for 10 min in CHF$_3$ (21 mTorr, 50 W rf power). The remaining samples were patterned and etched in three cycles of alternating CHF$_3$ (100 s, 21 mTorr, 50 W rf power) and O$_2$ (15 s, 200 mTorr, 40 W rf power) plasmas for the third sample, the cycles started with
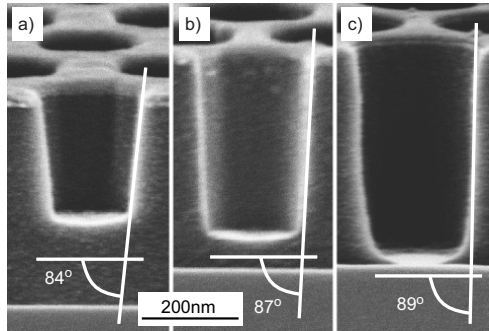
Figure 3.2. Circular openings etched into SiN_x for 25 min in a CHF_3 plasma at 21 mTorr and 50 W of rf power. (a) Without oxygen plasma, $84°$ tilt, (b) one intermediate step of 60 s of O_2 plasma at 200 mTorr and 30 W of rf power, $87°$ tilt, (c) ten cycles of alternating CHF_3 etching and O_2 plasmas, $89°$ tilt.

O_2 and ended with CHF_3, whereas for the fourth sample, the sequence was reversed. XPS measurements are performed on the etched bottom surfaces (*not* on sidewalls). In Table 3.1, the relative contributions of Si, C, N, O, and F species are listed. The reference sample shows contaminations of carbon (16 at. %), oxygen (6 at. %), and fluorine (1 at. %). Oxygen and carbon contents may be attributed to an oxidation of Si and organic species, formed upon the exposure to air during transfer to the XP-spectrometer. The small amount of fluorine on the unprocessed SiN_x may originate from PECVD chamber walls, which are routinely subjected to fluorine-containing cleaning plasmas. The Si/N ratios of all samples are comparable. Therefore, an etching rate enhancement due to a deficiency of nitrogen and formation of NO during O_2 plasmas can be excluded. The formation of a fluorocarbon film is evident from the significantly increased amounts of carbon (> 30 at. %) and fluorine (> 20 at. %) on the surfaces of the samples for which processing was terminated after CHF_3 etching ("continuous" and "stop after CHF_3"). The last row of Table 3.1 lists the summed-up contents of silicon and nitrogen, giving a qualitative indication of the fluorocarbon film thicknesses. On the sample for which processing was terminated after O_2 treatment ("stop after O_2"), the fluorocarbon film appears to have been removed almost completely. The fluorine content is decreased to ~ 3 at. %, and the amount of carbon is comparable to that of the unetched reference sample. Furthermore, the oxygen content in
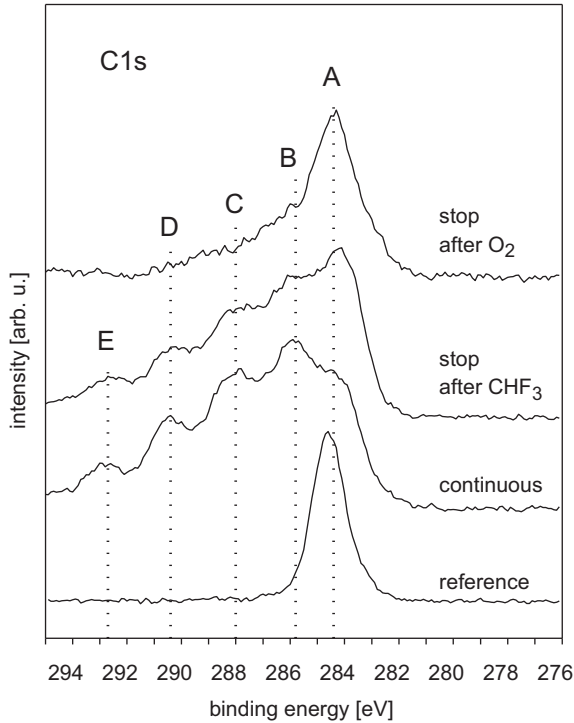
Table 3.1. Relative contributions from Si, C, N, O, and F to the XPS spectra of four samples [unprocessed SiN_x reference sample; continuously etched sample (10 min); sample etched in three cycles of CHF_3 (100 s) and O_2 (15 s), terminated after CHF_3; sample etched in three cycles of CHF_3 (100 s) and O_2 (15 s), terminated after O_2]. The sum of Si and N gives a qualitative indication of the fluorocarbon film thickness. All samples were transferred to the XPS chamber through atmosphere.

	SiN_x reference	CHF_3 continuous	Cycles, stop after CHF_3	Cycles, stop after O_2
Si	42.1	15.4	20.8	37.0
C	15.8	33.1	30.5	14.4
N	35.2	12.2	16.2	26.4
O	6.0	7.0	9.2	18.9
F	0.9	32.4	23.3	3.3
Si + N	77.3	27.6	37.0	55.9

the O_2-treated film is strongly increased. As a side remark, we mention that the presence of O_2 might increase the etching rate by inhibiting fluorocarbon buildup through mechanisms similar to those that enhance reactions between a SiO_2 substrate and fluorinated polymers [127, 130]. Moreover, O_2 addition to a CHF_3 plasma has been observed on several instances to increase the etching rate of SiN_x [131, 132].

The C 1s spectra of all samples are depicted in Fig. 3.3. They were normalized to the C 1s line appearing at a binding energy of 284.4 eV, which is the typical binding energy for carbons and hydrocarbons (peak A in Fig. 3.3). On the reference sample, only this carbon peak A is detected, whereas after etching in CHF_3, at least four additional higher binding energy peaks (peaks BE in Fig. 3.3) are found. According to the literature [133, 134], these additional peaks can be ascribed to fluorinated polymers. Poly(vinyl fluoride) has two different binding energies associated with CH bonds, which correspond to peaks B and C. In poly(vinylidene fluoride), the binding energies associated with CH and CF bonds can be assigned to the peaks B and D, respectively. Finally, peak E can be attributed to the CF_2 groups in a perfluorinated polymer.

After an O_2 plasma treatment, the fluorocarbon peaks are not individually resolved anymore and are significantly weaker in intensity.

Figure 3.3. XP-spectra of the C 1s core level region of all four measured samples [unprocessed SiN$_x$ reference sample; continuously etched sample (10 min); sample etched in three cycles of CHF$_3$ (100 s) and O$_2$ (15 s), terminated after CHF$_3$; sample etched in three cycles of CHF$_3$ (100 s) and O$_2$ (15 s), terminated after O2]. A single peak is observed for the unetched sample (reference), whereas clear signals of fluorinated polymers are observed after etching in CHF$_3$. After 10 min of etching (continuous) the corresponding peaks are more pronounced than after a 100 s long CHF$_3$ etching step (stop after CHF$_3$). After an O$_2$ plasma treatment the fluorocarbon peaks are not individually resolved anymore and are significantly weaker in intensity (stop after O$_2$). The peaks are identified as follows (Refs. [133, 134]): (A) carbon, hydrocarbon, (B) poly(vinyl fluoride), poly(vinyliden fluoride), (C) poly(vinyl fluoride), (D) poly(vinyliden fluoride), and (E) fluorinated ethylene propylene.

However, compared to the reference sample, a peak broadening toward higher binding energies is apparent, which can be explained by the formation of CO groups on the surface, evidenced by large amounts of oxygen (18.9 at. %, see Table 3.1). The CF bonds in the fluorocarbon film seem to be effectively cracked, and the fluorine atoms form volatile compounds.

In conclusion, the XPS measurements prove that the O$_2$ plasma steps almost entirely remove the fluorocarbon film. However, since the XPS measurements were performed on large areas, this conclusion applies exclusively to the deposits on the bottom surfaces and not to the passivation layers on the sidewalls of nanostructures. To obtain an almost vertical profile, as in Fig. 3.2 (c), we expect that the sidewalls have to be passivated during the entire process. While the fluorocarbon deposits on horizontal SiN$_x$ surfaces are temporarily removed by O$_2$ plasma steps, the layers on sidewalls are probably only reduced in thickness. To our understanding, the key to profile control is to keep the sidewall passivation layer as thin as possible, but thick enough to guarantee effective lateral etch-inhibition. In a plasma, the bottom of the features can be etched by energetic ions that impinge on these surfaces, whereas the sidewalls are effectively protected from ions that are directed perpendicular to the substrate. However, for the lack of appropriate experimental methods, we cannot directly analyze the fluorocarbon deposits on the sidewalls of etched nanostructures. Therefore, we chose an empirical experimental approach to optimize the process parameters. These results will be presented in Sec. 3.1.3. Figure 3.4 schematically shows the temporal evolution that we expect for fluorocarbon film thicknesses on the bottom and the sidewalls during our process. The trends are qualitative and the axes are in arbitrary units. The dynamics for the bottom surfaces are investigated in more detail in Sec. 3.1.4, whereas the curves for the sidewall depositions are inferred by an analogy and from the above reasoning about sidewall passivation for vertical profiles. The main difference between the two curves is that the fluorocarbon film thickness periodically reaches a value of zero (allowing for efficient vertical etching), while the thickness on the sidewalls oscillates between finite values (which inhibits lateral etching).
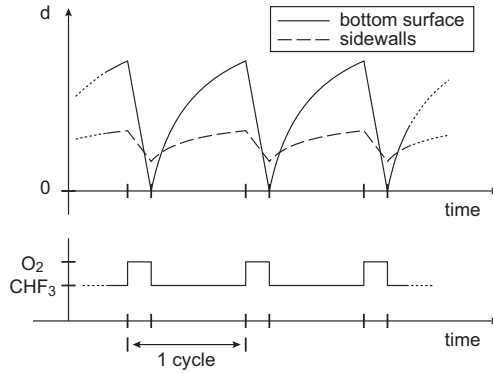
Figure 3.4. Schematic mechanism of the proposed cyclic process. The bottom graph depicts the alternating steps of CHF_3 and O_2 plasmas. The top graph shows the temporal evolution of the thicknesses d of fluorocarbon layers deposited on bottom surfaces (solid line) and sidewalls (dashed line) qualitatively and in arbitrary units. The sidewalls are covered with a thin passivation layer at all times. The film thickness fluctuates periodically between finite values such that lateral etching is inhibited. The fluorocarbon depositions on the bottom surfaces are completely removed during O_2 plasma treatments, which allows for efficient vertical etching.

3.1.3. Process optimization

So far, we have shown that cyclic interruptions of the etching process improve the vertical profile of our nanostructures, and we verified the proposed deposition/removal mechanism of the fluorocarbon film. Process optimization still remains. Sidewall anisotropy and smoothness were optimized experimentally by varying the process parameters and using an orthogonal design technique, as described in Refs. [75, 135]. More details about the method and its terminology are given in Appendix A.2. The method is particularly well-suited whenever a set of process parameters have independent influence on the outcome. Therefore, it is vital to choose input parameters that fulfill this requirement. For the experiments presented here, the input parameters are as follows: pressure, duration of CHF_3 etching steps, CHF_3 plasma rf power, duration of O_2 etching steps, and O_2 plasma rf power. The pressure for the O_2 plasma is kept constant at $200\,mTorr$. For each parameter, four levels (summarized in Table 3.2) are defined based on the results from preliminary experiments. An $L_{16}\,4^5$ orthogonal array is set up to de-

Table 3.2. Input parameters of the DOE and corresponding level settings. Printed in boldface are the values resulting from the optimization experiment.

Input parameter	Level 1	Level 2	Level 3	Level 4
Pressure (mTorr)	15	18	**21**	24
CHF_3 duration (s)	75	**90**	150	300
CHF_3 power (W)	40	**50**	60	70
O_2 duration (s)	**15**	30	45	60
O_2 power (W)	20	30	**40**	50

termine the randomized optimization experiments. Finally, the quality of each run of the array is judged based on the two output parameters: sidewall anisotropy and sidewall smoothness. The latter classification is based on the visual inspection of the scanning electron microscopy (SEM) images[1] and, therefore, is not entirely independent of the experimenter. An averaging procedure is applied in order to determine the influence of each input parameter on the output parameters. Table 3.3 gives an overview of the findings of our 16 DOE runs. The etching rate is included in the third row of the table; however, it is not used for the evaluation of the optimal set of input parameters.

Considering the input parameters of the CHF_3 etching duration in Table 3.3, it becomes evident that a tradeoff has to be made between the two output parameters. Smoothness and verticality are not maximized for the same parameter settings. Therefore, an intermediate level setting is chosen for the etching step duration. The optimum values for the other three input parameter settings can be pinpointed in a more straightforward fashion. The resulting values are printed in bold face in Table 3.2. Cross-sectional SEM images of a photonic crystal hardmask, fabricated with optimized parameters, are depicted in Fig. 3.5. A comparison to Fig. 3.2 shows that there is, indeed, an improvement in sidewall profile after parameter optimization.

The optimized process became the standard process for the device fabrication in our laboratory. For more than a year, its performance was regularly monitored. Although the condition of the plasma reactor was subject to fluctuations, the sidewall characteristics of the etched nanostructures remained very stable. For instance, for a CHF_3 plasma

---

[1]The images were taken in a Zeiss ULTRA 55 system.

Table 3.3. Response of output parameters on input parameter level settings. The arrows indicate the direction of change of the output parameter when the value of the input parameter is increased. For sidewall verticality and smoothness, an improvement is symbolized by the arrow pointing upward. The symbols "↑↓" and "↓↑" mean that a maximum or a minimum is reached, respectively, whereas "→" means that no significant or unclear impact is observed. The etching rate is shown as an output parameter merely for information, it is not included in the evaluation of the DOE optimum.

Input parameters	Sidewall verticality	Sidewall smoothness	Etching rate
Pressure (mTorr)	↑↓	↑	↓
CHF$_3$ duration (s)	↓	↑	↓
CHF$_3$ power (W)	↑↓	↓	↑↓
O$_2$ duration (s)	↓↑	→	→
O$_2$ power (W)	↑↓	↓	→

(21 mTorr, 50 W rf power), the self-bias varied in a range between -253 and -266 V. Similarly, for an O$_2$ plasma (200 mTorr, 40 W rf power), the self-bias varied in a range between -92 and -112 V. These are long-term variations. For individual runs, the self-bias shows only small fluctuations of less than 1 %. The etched profile has never deteriorated when inspected by SEM. Prior to this research, a process based on the mixtures of gases (CHF$_3$/O$_2$) had been successfully implemented in the same environment, but it could not be maintained over a similarly long period of time even by making gradual adjustments.

3.1.4. Etching rate dynamics

In general, the implementation of a process that makes use of the proposed etching concept requires the formation of a passivation layer and etching to occur on a timescale that is comparable to the duration of the etching step in a cycle. Therefore, it is interesting to investigate the dynamics of our etching step in more detail. Ideally, we should analyze the evolution of etching rates and fluorocarbon depositions in both the lateral and the vertical direction. However, experimental data on etched sidewalls of nanostructures are not easily obtainable. Therefore, we made the simplification of restricting our investigation to the vertical etching direction of large-area features.
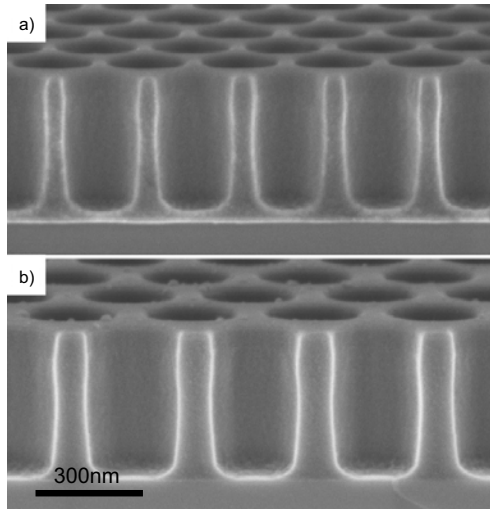
Figure 3.5. Cross-sectional SEM image of holes etched using the optimized process parameters: $100\,s$ steps of CHF_3 etching at $50\,W$ rf power and $21\,mTorr$; $15\,s$ steps of O_2 at $40\,W$ rf power and $200\,mTorr$. The test structures are holes arranged in a triangular lattice with (a) $260\,nm$ and (b) $340\,nm$ pitch.

We measured the time-dependence of the vertical etching rate of SiN_x in a continuous CHF_3 plasma. We observed that the vertical etching rate is large at the beginning of etching (r_0), when the SiN_x surface is clean. However, the etching rate decreases as a function of time as the passivating film thickness, d, increases. After several minutes of continuous etching, the etching rate approaches a constant value r_s, which can be related to a steady-state passivation layer thickness d_s. We claim that for a given set of etching conditions, a maximum freedom of control is provided when the difference between the etching rates r_0 and r_s is large. This statement is supported by the reasoning that the proposed etching concept relies on the possibility to control the "average" passivation layer thicknesses. The experimentally accessible quantity that can be related to the fluorocarbon film thickness is the etching rate. The larger the span between r_0 and r_s, the more freely the etching rate can be controlled. Therefore, we introduce the ratio r_0/r_s as a figure of merit to quantify the amount of control offered by the given etching conditions. In order to determine this figure experimentally, the rates

r_0 and r_s need to be measured. Since an etching plasma typically takes a few seconds to stabilize after ignition, the value of r_0 is only accessible by extrapolation. We will, therefore, present a mathematical model for the nonlinear behavior of the etching rate that allows us to extrapolate and obtain a good estimate for r_0 and thus for r_0/r_s. Furthermore, this model will allow us to define a time constant T for the dynamic formation of the passivation layer, which we can compare to the duration of an etching step in our cyclic process. A comparison between the two time constants can provide a useful reference for future implementations of processes that are based on the same working principle.
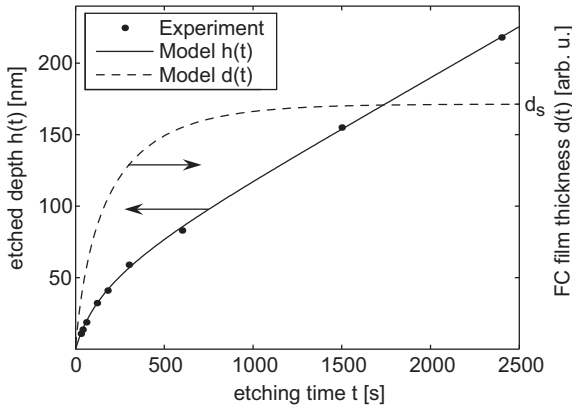
Figure 3.6. Etched depth in SiN_x vs time in a CHF_3 plasma at $21\,mTorr$ and $50\,W$ rf power. The solid line represents the model in Eq. (3.4), fitted to the experimental data (bullets, left ordinate). The computed fluorocarbon film thickness is represented in arbitrary units (dashed line, right ordinate), ds denoting the steady-state thickness.

Figure 3.6 shows our experimental data for etched depth (bullets, left ordinate) versus etching duration for large-area structures; i.e., only small fractions of the chip are masked by photoresist. The curve fitted to the experimental data is based on the mathematical description of the dynamics of the etching rate, which is developed below. From that same model, the evolution of the fluorocarbon film thickness can be derived up to a constant multiplication factor. The corresponding curve is plotted using the right ordinate of Fig. 3.6 in arbitrary units. The experimental data for etched depth per cycle were obtained by etching

several cycles and dividing the etched depth by the respective number of cycles. For instance, the value corresponding to 40 s of etching was obtained by repeating a 40 s etching step (21 mTorr, 50 W rf power) 15 times with intermediate oxygen plasma steps (15 s, 200 mTorr, 40 W rf power). This resulted in a total depth of 204 ± 3 nm. Division by the number of cycles yielded 13.6 ± 0.2 nm etched in 40 s.

Our mathematical model is based on the work of Schaepkens *et al.* [127] and relies on an empirical exponential relation between the etching rate and the thickness of the fluorocarbon film,

$$r(d) = r_0 \, e^{-d/\lambda}, \tag{3.1}$$

where r denotes the etching rate, d is the film thickness, r_0 is the etching rate on a clean SiN_x surface (i.e., $r_0 = r(d=0)$), and λ is a characteristic length parameter. This exponential behavior has been confirmed experimentally [127].

Following the reasoning of Schaepkens *et al.*, the temporal evolution of the fluorocarbon film thickness can be described by the equation

$$\frac{d}{dt} d = D - E_\infty \left(1 - e^{-d/\lambda}\right) - C_0 \, e^{-d/\lambda}. \tag{3.2}$$

This equation accounts for polymer deposition, polymer etching directly by the plasma, and polymer removal during SiN_x etching due to chemical reactions with the fluorocarbon film, all taking place simultaneously. The first term on the right hand side is the constant polymer deposition rate D during etching. The second term is the fluorocarbon etching rate, which depends on the polymer film thickness in a similar manner as the SiN_x etching rate. E_∞ is the rate at which a semi-infinite fluorocarbon layer is etched. The third term describes the fluorocarbon consumption rate during the etching of SiN_x and is assumed to be proportional to the SiN_x etching rate r. For $d \rightarrow 0$, the consumption rate approaches C_0. In a situation where the film thickness reaches a steady-state, we have $C_0 < D < E_\infty$. If $C_0 > D$, then the deposition rate would be negative at $d=0$, and if $D > E_\infty$, then the deposition rate would still be positive for $d \rightarrow \infty$. By introducing the substitutions $\delta = D - C_0 > 0$ and $\sigma = E_\infty - C_0 > 0$, Eq. (3.2) can be restated as

$$\frac{d}{dt} d = \delta - \sigma \left(1 - e^{-d/\lambda}\right). \tag{3.3}$$

In order to fit the mathematical model to our measurements, the
solution of Eq. (3.3) has to be inserted into Eq. (3.1), and then the
etched depth $h(t)$ can be found by integration (cf. Appendix A.3 for
the details)

$$h(t) = \int_0^t r(\tilde{t})\,\mathrm{d}\tilde{t} = r_s \cdot t + r_0 \frac{\lambda}{\sigma} \ln \left(\frac{r_0}{r_s} - \left(\frac{r_0}{r_s} - 1 \right) \mathrm{e}^{-\frac{r_s}{r_0} \cdot \frac{\sigma}{\lambda} \cdot t} \right), \quad (3.4)$$

where the boundary conditions $d(0) = 0$ and $r(t \to \infty) = r_s$ were ap-
plied. The steady-state etching rate r_s can be immediately identified
as the slope of the linear region (large values of time t) in Fig. 3.6.
From a numerical fit of Eq. (3.4) to the experimental data of $h(t)$, the
parameters r_0, r_s, and λ/σ can be retrieved. The time constant λ/σ
has no immediate physical significance. Instead, we define T such that
$d(T) = (1 - \mathrm{e}^{-1}) \cdot d(t \to \infty)$. Table 3.4 summarizes the results returned
by numerical fitting. In order to estimate the impact of measurement
errors on the accuracy of the fitted parameters, the fitting process was
repeated for data to which some random noise was added; e.g., column
3 of Table 3.4 shows the standard deviation (in percent) of 1000 data
sets with a maximum $\pm 1\%$ noise. The experimental error of our data
is estimated to be around 1-2%. For comparison, the etching rate of
SiO_2 in the same plasma is indicated. It is stable in time, suggesting
that either a steady-state fluorocarbon film thickness is reached within
a few seconds or that $C_0 > D$ holds for SiO_2 and no fluorocarbon layer
is formed at all.

For the ratio between etching rates, Table 3.4 lists a value of
$r_0/r_s = 6.1$ with an estimated error of less than 3%. The characteristic
time constant T is around $200\,\mathrm{s}$. This is in the same order of magnitude
as the etching step duration in our optimized process, which is $100\,\mathrm{s}$
(Sec. 3.1.3). Thus, we established a connection between the experimen-
tally accessible time constant T and the etching step duration that can
only be obtained indirectly through an optimization process. Also, we
point out that these two time constants are significantly longer than
the time needed for a plasma to stabilize after its ignition, which is
around $5\,\mathrm{s}$ for our CHF_3 plasma. If they would be comparable to the
plasma stabilization time, it would be difficult to reliably implement a
cyclic process. We believe that these values retrieved from the experi-
mental data will provide a useful reference, when similar processes will
be set up on different etching equipment, perhaps even when materials
other than SiN_x are etched. However, we emphasize again that direct

Table 3.4. Fitting parameters from the formula in Eq. (3.4) (with the time constant T instead of λ/σ) and the experimental data shown in Fig. 3.6. The etching rate for SiO_2 is shown for comparison. It is constant in time under the same etching conditions used for SiN_x.

Fitting parameter	Value returned by numerical fitting	Std. dev. for $\pm 1\%$ noise (%)	Std. dev. for $\pm 2\%$ noise (%)
r_0	26.2 nm/min	2.0	4.0
r_s	4.28 nm/min	1.4	2.9
r_0/r_s	6.12	1.3	2.5
T	198 s	5.9	12.1
etching rate for SiO_2	$9.8 \pm$ nm/min		

experimental data on fluorocarbon film formation on etched sidewalls are currently missing. For a full understanding of the process, this gap would have to be bridged by appropriate experimental techniques.

3.1.5. Potential application of process concept to SiO_2

After presenting a successful process of type ED/R (cf. Fig. 3.1) for SiN_x etching in a CHF_3 plasma, the question arises if the same concept can be applied to obtain vertical profile nanostructures in other materials. The great advantage of an ED/R solution as opposed to EDR is that the necessity for a careful balance of gas ratios is avoided. Instead of balancing gas ratios, the timing of the cycles has to be adjusted to yield the desired sidewall profile. Setting up a process of type ED/R can become an interesting option if the chemistry in an EDR process turns out to be too complex to maintain a repeatable balance between the feed gases during the etching step. This might be the case in a multipurpose environment, where many processes are run on various materials in the same reactor. Notably, an O_2 content in a fluorocarbon-based etching plasma introduces a large amount of possible chemical reactions within the discharge and on surfaces of the reactor chamber. If the chamber walls cannot be well conditioned, then the chemical balance will be shifted, and the effective O_2 content available for etching can become difficult to control. Such effects are expected to be of less importance when keeping the chemistry simple as in the proposed approach.

We would like to focus the discussion on SiO_2 and to fluorocarbon-based plasma chemistries (CHF_3, CF_4, C_4F_8, etc.). The literature provides a lot of useful information on this topic since plasma-assisted dry-etching of Si, SiO_2, and SiN_x has been studied for many years [120, 124–128, 130–132, 136–146]. In fluorocarbon-based plasmas, the formation of thin films on etched surfaces was reported at an early stage [130, 144]. The thickness d of these films depends on the material [127], $d_{Si} > d_{SiN_x} > d_{SiO_2}$, as well as on temperature [139] and self-bias [136, 145, 146] in the plasma reactor. But, most importantly, it depends on the F/C ratio in the discharge; the film thickness can be increased for a low F/C ratio [130, 137]. Also, fluorocarbon deposition can be influenced by the addition of gases such as hydrogen or oxygen to the plasma chemistry. By forming HF bonds, hydrogen decreases the effective F/C ratio [126, 142], whereas oxygen has an opposite effect due to the formation of CO [126, 147].

When a process of type ED/R should be implemented for SiO_2, we must take into account that the buildup of fluorocarbon films is strongly dependent on the substrate material as well as the F/C ratio of the plasma chemistry. SiO_2 requires a lower F/C ratio than SiN_x to enable film formation. The effective ratio of CHF_3 is somewhere between 2 and 3, depending on the fraction of F-radicals lost to HF formation. Under the processing conditions of the present experiments, this is too high for an effective fluorocarbon buildup on SiO_2 during etching. The chemistry has to be adjusted to provide a lower F/C ratio. Very successful high-aspect-ratio etching of SiO_2 was recently demonstrated [143] using C_4F_6 as a feed gas, complemented by additions of CH_2F_2 and O_2, in a Bosch-like cyclic process, which alternates between etching and deposition steps. The F/C ratio of C_4F_6 is 1.5, and it is presumably further reduced by CH_2F_2 whose F/C ratio is situated somewhere between 0 and 2. The addition of O_2 is necessary to increase the effective F/C ratio during the etching step, whereas no O_2 is used for the deposition step. All in all, this represents a process of type ER/D, although there might be some fluorocarbon deposition during the etching step as well. Setting up a process of type ED/R seems very promising with similar feed gases. The etching step could be based on C_4F_6, and the fluorocarbon film formation can be adjusted by adding some CH_2F_2 (to decrease F/C) or CHF_3 (to increase F/C). The fluorocarbon removal step would be a simple O_2 plasma.

3.2. Hardmask fabrication - Deep etching of SiN_x

The content of this section is published in [74].

The SiN_x hardmask fabrication process described in Sec. 3.1 gives excellent results for a mask thickness of about 400 - 500 nm. For the etching of the InP (or InP/InGaAsP/InP) substrate, it would be desirable to provide significantly thicker SiN_x hardmasks, so that longer etching times can be used. It might be possible to slightly increase the hardmask thickness by using thicker layers of titanium and PMMA for its fabrication, but at some point the resolution requirements can no longer be met by the lithography. Therefore, we propose an alternative solution, which allows to "renew" the titanium layer after RIE etching, such that another RIE etching step can be applied. No additional alignment step is required. Since the titanium layer acts as a mask for the fabrication of the SiN_x hardmask, we refer to the technique as self-aligned mask renewal (SAMR). The method is not restricted to our specific purpose, nor is it restricted to our material choices of the mask (titanium) and the substrate (SiN_x). We believe that it shows some potential for other applications in various engineering fields. In Sec. 3.2.4 we will briefly elaborate on the use of the SAMR method for the fabrication of perforated membranes for emulsification experiments in food engineering or pharmaceutics.

3.2.1. The method

The starting point for the mask-renewal technique is a sample patterned with circular holes which are etched anisotropically into a layer of any given material. The etching depth is insufficient for the considered application, but the remaining mask on the sample is too thin to allow for further etching without loss of profile quality or complete failure of the mask. The goal is to renew the mask and to perform an additional etching step in order to attain the required aspect ratio. Figure 3.7 shows how the method works. The new mask is deposited using a line-of-sight deposition process as, e.g., EBPVD. By mounting the sample at an angle, α, with respect to the deposition direction, no masking material is deposited on the bottom surface of the etched structure. The angle is chosen according to the aspect ratio of the initial etching step. To obtain a uniform layer on the etched sidewalls, the sample is rotated about an axis perpendicular to the sample surface. The rotation speed must be large enough to ensure several complete revolutions within the
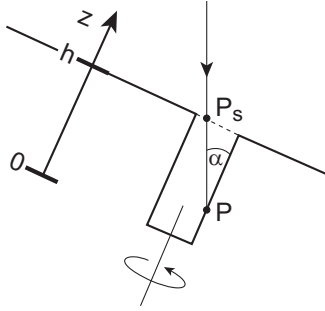
Figure 3.7. Self-aligned mask renewal method. A line-of-sight (vertical arrow) deposition process is used to deposit the new mask. The sample is tilted by an angle, α, to avoid covering the bottom surface of the etched hole with masking material. To guarantee a homogeneous layer, the sample is rotated about an axis perpendicular to the sample surface. The drawing illustrates the construction of the point P_s starting from a point P on the sidewall surface, for the derivation of Eq. (3.5).

total deposition time.

The thickness of the layer deposited on the sidewalls of the etched structures, d_{side}, can be related to that on the top surface, d_{top}, by

$$
d_{\text{side}}(z) = \begin{cases} d_{\text{top}} \cdot \tan(\alpha) \cdot \frac{1}{\pi} \arccos(\frac{h-z}{2R}\tan(\alpha)) \\ \qquad\qquad\qquad , z > h - \frac{2R}{\tan(\alpha)} \\ 0 \qquad\qquad\qquad , z < h - \frac{2R}{\tan(\alpha)} \end{cases} \qquad (3.5)
$$

where h is the depth of the hole, R is the radius and z is the coordinate along the axis of the hole, measured from the bottom surface. The derivation of Eq. (3.5) is detailed in Appendix A.4 and can be outlined as follows: For a point, P, on the etched sidewall, parameterize a line through P using a vector pointing in the deposition direction. Determine the intersection point P_s of that line with the plane defining the sample surface. If P_s lies inside the circumference of the hole, then the deposition rate on the sidewall (at time t_0) is given by $r(P, t_0) = r_{\text{hor}} \cdot \sin(\alpha)$, where r_{hor} is the rate on the top surface of a horizontally mounted sample (i.e., the rate for the case of $\alpha = 0$). If P_s lies outside the circumference of the hole, then the point on the sidewall is shadowed and we get $r(P, t_0) = 0$. When the sample is ro-

tating about the axis of the hole, the point P moves on a trajectory $P(t)$ on which it is sometimes shadowed and sometimes not. As long as $d_{side} \ll R$, the trajectory is approximately circular. The deposition rate integral along this circular trajectory results in Eq. (3.5). Near the top surface, a maximum thickness of $d_{side}(z \to h) = \frac{1}{2} \cdot \tan(\alpha) \cdot d_{top}$ is expected. Figure 3.8 shows an SEM image of a processed sample with a titanium layer deposited at an angle of $\alpha = 50°$ on a hole in SiN_x. In the right-hand panel, the same image is overlaid with the theoretical curve according to Eq. (3.5). A good agreement between experiment and prediction is observed.
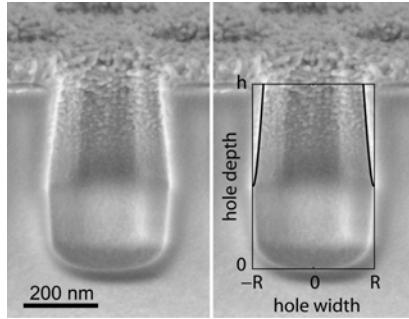
Figure 3.8. Deposited sidewall layer. Left: an SEM micrograph of a SiN_x sample with a titanium layer of $d_{top} = 50\,nm$ evaporated at an angle of $\alpha = 50°$; right: the same micrograph overlaid with the theoretical curve according to (Eq. (3.5)).

Ideally, the new masking layer exhibits a maximum etching selectivity toward the substrate and is deposited at a small angle to obtain a thin sidewall layer. The best uniformity on the sidewalls is guaranteed by a large number of revolutions of the sample about the axis of the hole; in this respect, fast rotation and a small deposition rate would be favorable. However, the surface microstructure resulting from an EBPVD process is dependent on the evaporation parameters [148]. In our particular case, small deposition rates (e.g., 0.2 nm/s) of titanium lead to the formation of large grains, whereas much smaller grains can be obtained at larger deposition rates (e.g., 0.5 nm/s, cf. Fig. 3.8). In order to minimize the roughness on the surface edges of the holes, the grain size should be kept as small as possible. Hence, for a given rotation speed, the deposition rate has to be chosen to obtain a good

trade-off between uniformity of the sidewall thickness and smoothness of the microstructure of the new masking layer.

3.2.2. Circular holes in SiN$_x$

We now proceed to etch circular holes of 280 nm diameter and vertical sidewalls into a SiN$_x$ layer of 1 μm thickness, using the new method. A SiN$_x$ layer of 1 μm thickness is deposited (PECVD), followed by 35 nm of titanium (EBPVD) and 200 nm of PMMA (spin-coating). PhC patterns are defined by EBL, and a first RIE etching step is performed, transferring the pattern into SiN$_x$ to a depth of 400 - 500 nm (cf. Fig. 3.9 (a)). At this point, the mask needs to be renewed. This is done by depositing a titanium layer of $d_{\text{top}} = 40$ nm at an angle of $\alpha = 25°$. The optimal deposition angle was determined experimentally from a series of samples produced with varying angles.[2] A second etching step is performed; however, it is still not sufficient to reach the substrate below the SiN$_x$ layer (cf. Fig. 3.9(b)). Therefore, the mask is renewed a second time by depositing a titanium layer of $d_{\text{top}} = 40$ nm at an angle of $\alpha = 18.4°$, and a third etching step is carried out. Figure 3.9(c) shows the final result with vertical and smooth sidewalls. The titanium depositions on the sidewalls are still visible. The final aspect ratio of the holes is almost 3.6, twice as much as achievable with the original single-step etching process. To our knowledge this is the highest value reported in SiN$_x$ for an RIE process.

The obvious advantage of the mask renewal method is that any masking material can be used. Since the new mask does not have to be opened in an etching step, it can be very resistant to any possible etching technique. This flexibility in material choice makes masking materials accessible, which could otherwise only be used in a lift-off process. So far, titanium remains the only masking material tested (due to compatibility concerns with other processes run on the same equipment), but we believe that there is great potential in the large variety of potential candidates to replace it.

Along with the new opportunities of the method, there are also disadvantages. The most obvious drawback is that the etched structures

---

[2]A deviation in α of $\pm\,3°$ results in similar hole shapes. A more precise tolerance statement can only be made if the hole shape requirements are clearly defined. They depend on the specific application. In our EBPVD system, the angle can be set to an accuracy of $\pm\,0.5°$, which is well within the estimated tolerance of our process.
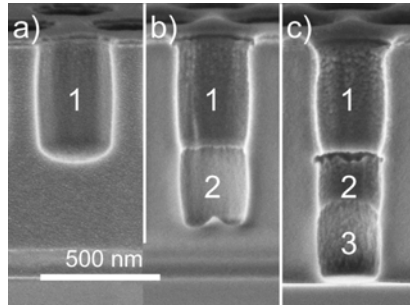
Figure 3.9. Three steps of SiN_x etching. Two mask renewal steps were carried out, both with titanium and $d_{top} = 40\,nm$. The first renewal was performed at an angle of $\alpha = 25°$, the second at $\alpha = 18.4°$, taking into account the higher aspect ratio available in (b) as compared to that in (a). The parts of the holes etched during the first, second, and third etching step are labelled with the numbers 1, 2, and 3, respectively.

are limited to patterns of circular holes, if the sidewall depositions are to be uniform in thickness. In addition, the optimal angle at which the new masking layer is deposited depends critically on the initial aspect ratio of the holes. Therefore, the range of radii usable in a single lithography step is limited. Figure 3.10 shows the results of four different hole sizes patterned on the same chip. While the hole in Fig. 3.10(c) exhibits a good sidewall verticality, the other ones are clearly inferior in quality. The initial aspect ratio (i.e., after the first etching step) varies in a range of 1.17 to 1.56 for the holes of Fig. 3.10(a) to (d). Given the drastic effect of initial aspect ratio, it has to be emphasized that the results of Fig. 3.10 are from a three-step etching process (two mask renewals). The effect is significantly less severe for a two-step process.

3.2.3. Hardmask for dry-etching of photonic crystal patterns into III/V semiconductor materials

We now use the deeply etched SiN_x layer as a hardmask for the fabrication of PhC patterns in InP. The etching of InP is performed by ICP-RIE using a Cl_2/N_2-based chemistry. The process is described in detail in Ref. [75] and is implemented as a standard process on our equipment. All essential parameters are listed in Appendix B.1. In spite of a high selectivity between SiN_x and InP (> 10, in our process), it is nevertheless the mask thickness which sets the main limit to the max-
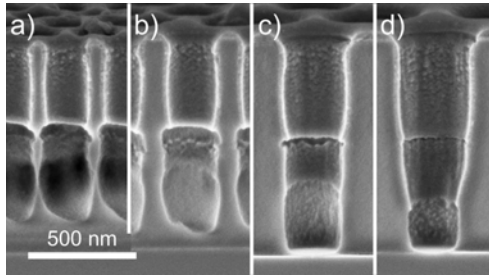
Figure 3.10. SEM micrographs of a three-step etching process for varying initial aspect ratios ranging between (a) 1.17 and (d) 1.56. The scale is the same for all images. The sidewall verticality depends critically on the initial aspect ratio.

imum hole depth that can be reached. Our standard SiN_x hardmask is 400 nm thick, 500 nm would be possible with some adjustments to the fabrication process of Sec. 3.1. Using the SAMR method, we can increase this thickness by a factor of 2. With a hardmask of 1μm, we obtain excellent hole depths of up to 5.7μm. For a hole diameter on the order of 280 nm, we demonstrate the highest reported aspect ratio, $AR = 20$, etched into InP by ICP-RIE. Even though higher aspect ratios have been reported for holes of 130 nm diameter [77], those results are strongly dependent on hole size, and the aspect ratio tends to decrease rapidly for larger diameters. Typical diameters for InP-based photonic crystal devices operated at a wavelength of 1550 nm (telecom) are in a range of roughly 180 - 430 nm. With respect to the results obtained with a SiN_x hardmask thickness of 400 nm, the present results constitute a hole depth increase by a factor of 1.5. Taking into account the PMMA layer thickness of only 200 nm for the lithography step, we demonstrate an overall selectivity of 28.5 between PMMA and InP. Figures 3.11(c) and (d) show magnified views of photonic crystal holes etched for 180 s and 220 s, respectively. The etched sidewalls are very smooth after 180 s, but they start deteriorating below the mask for longer etching times. The etching time is more than doubled with respect to a process with a 400 nm hardmask, but due to the aspect ratio dependent etching rate [149], the depth does not scale linearly with etching time (dashed line in Fig. 3.11(a)). Therefore, we believe that for a further improvement of hole depth in InP, increasing the mask thickness beyond 1μm is not the most efficient approach. Instead, choosing a
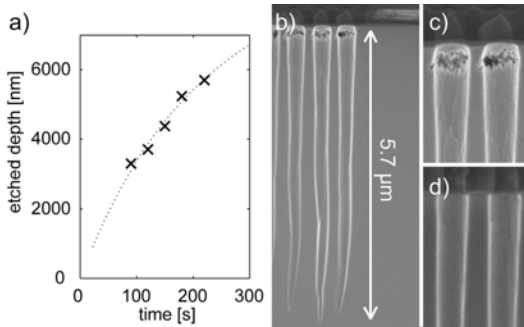
Figure 3.11. ICP-RIE etching of InP using a SiN_x hardmask of $1\,\mu$m thickness; a) the etching depth is plotted versus etching time; the dashed line is a theoretical fit assuming a linear dependence of the etching rate on the aspect ratio [150]; b-d) SEM micrographs of the holes obtained with etching times of (b,c) 220 s and (d) 180 s.

different masking material would be more promising. Here, the method of self-aligned mask renewal can greatly widen the range of potential materials.

3.2.4. Perforated membranes for droplet formation

As a second application, the SAMR method was used to micro-engineer SiN_x membranes used in membrane emulsification. This was done in a collaboration with Sebastian Holzapfel (Laboratory of Food Process Engineering, ETH Zurich). Since it is an on-going project, we can only show preliminary results. Membrane emulsification is an extremely gentle method to produce emulsions with narrow droplet size distributions. The process can be used to create tailor made emulsions for food-, pharmacy- and chemistry applications. Moreover, foams can be produced with low energy input [151, 152]. One fluid is pushed through a perforated membrane into a second immiscible fluid. Droplets form at the membrane pores and are detached by viscous drag induced by forced convection of the second fluid. Droplet size is mainly controlled by the pore size, the viscous drag, the interfacial tension, and the flow rate through the pores. A pore separation distance ≥ 10 times the pore diameter is important to avoid steric hindrance and coalescence of droplets during formation [153, 154]. Micro engineered membranes are advantageous over most other membrane types such as sintered membranes,

where pore size and distribution is less well-defined, the supporting structure creates an additional pressure drop, and membrane fouling is promoted. The low surface roughness usually achievable with standard MEMS techniques is of great benefit to study droplet formation and detachment under nearly ideal conditions. SiN_x membranes on silicon supports match the desired properties in terms of mechanical and chemical stability for the emulsification process and can be generated with standard MEMS processes (deposition and etching). Membranes have to resist the pressure drop during emulsification. Especially for small pore diameters, the pressure resistance becomes crucial, since $\Delta P \sim 1/d^4$ [155], where ΔP is the pressure drop for a given flow rate through the pores and d is the pore diameter. Mechanical stability of the membrane can be altered by changing the free-standing membrane area and its thickness [156]. A thick membrane with small diameter pores means that a high aspect ratio is required. For membrane emulsification, an aspect ratio in excess of 3 is highly desirable.

Using the process described in Sec. 3.1, $2\,\mu$m thick SiN_x membranes were fabricated with pore diameters of $\sim 1\,\mu$m. The process can be easily scaled up from small chips (7×7 mm) to a full 4" wafer. Free-standing membranes were released by KOH etching of the silicon substrate from the backside. A cross flow emulsification setup is currently being built for droplet formation. Similar experiments have been conducted before [156]. The fabrication process presented in section 3.2.2 is promising in three respects: Firstly, the patterning is done by EBL, which significantly lowers the minimum pore size compared to structures created by photolithography. Secondly, very high aspect ratios can be obtained, which enables the use of strong/thick membranes for sub-micron sized pores. Finally, the pore shape can, to some extent, be controlled. For instance, an isotropic dry-etching step can be used after the renewal of the mask to create a funnel. This would be interesting for the design of membranes with high pressure resistance and low minimum transmembrane pressure.

Preliminary etching tests for high aspect ratio membranes were performed on 7×7 mm chips. Figure 3.12 shows SEM images of three holes of different diameter (730 nm, 640 nm, 570 nm, from left to right), which were defined by EBL (in PMMA) and etched into a 2.5 μm thick layer of SiN_x using one intermediate mask renewal step (deposition of Ti at $\alpha = 18°$, 0.5 nm/s, $d_{\text{top}} = 210$ nm). For the smallest hole size, this cor-

responds to an aspect ratio larger than 4.3. The sidewalls of the holes are untapered, but they exhibit some roughness, which tends to get enhanced for increasing hole diameters. Further improvements of the process will be targeted by the following measures:

1) To increase the membrane stability, SiN_x films produced by low pressure chemical vapor deposition (LPCVD) will be used instead of PECVD grown material [156–159].
2) The dry-etching process, which was originally optimized for the smaller holes presented in section 3.2.2, will be adjusted to improve the sidewall quality of the holes.
3) Different etching chemistries will be tested after mask renewal to obtain funnel-shaped pores.
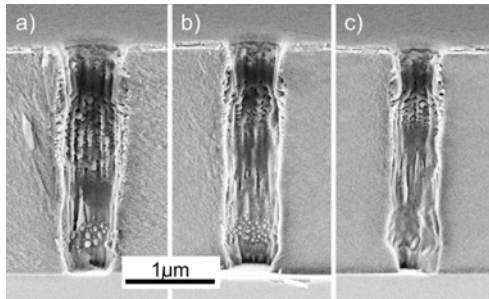
Figure 3.12. High aspect ratio holes in a $2.5\,\mu$m thick layer of SiN_x . The hole diameters are (a) $730\,$nm, (b) $640\,$nm, and (c) $570\,$nm. The etching was performed in two steps with one mask renewal in between.

3.3. Indium phosphide etching

Most of the content of this section is published in [78].

For dry-etching of InP, standard feed gases for plasma discharges are chlorine-based [160] (Cl_2, BCl_3, $SiCl_4$) or methane (CH_4). Iodine- and bromine-based chemistries have also been reported [161–163], whereas fluorine-based chemistries are not suitable due to the limited volatility of group III fluorides [164], which would appear as products on the surfaces of the samples. Chlorides of indium (mainly $InCl_3$) become sufficiently volatile at moderate temperatures of 170 - 200°C. Active

heating of the sample is generally necessary. The process development for all mentioned chemistries is largely empirical. The volatility of reaction products is one of the few quantitative measures routinely used to explain differences between etching chemistries.

Our discussion shall be restricted to ICP-RIE etching with chemistries based on the feed gas Cl_2. Iodine and bromine, though they might be interesting candidates to be further investigated, they were not available in our lab. Methane, on the other hand, proves not to be an ideal choice for high aspect ratios in InP because of heavy polymer depositions which form during etching [76, 160] and because InGaAsP is typically etched at markedly lower rates, which makes it difficult to uniformly etch through an InP/InGaAsP/InP planar waveguide structure. To achieve straight vertical sidewall profiles, additives of N_2 or O_2 are widely used. It is argued that they promote the passivation of the sidewalls [121, 165, 166]. In the case of a Cl_2/N_2 mixture, the mechanism is likely to be governed by the nitridation of InP as the dominant surface reaction [167]. The separate influence of various input parameters of the Cl_2/N_2 process was analyzed in detail in Ref. [75]. The results presented in Ref. [75] suggest, e.g., that there is a fundamental correlation between deep holes and rough sidewall surfaces. However, the data were not consistent enough to enable a clear identification of inherent trade-offs between all relevant output parameters, such as hole depth, hole shape, and sidewall roughness. A similar trade-off between hole verticality and sidewall roughness is observed in a $BCl_3/Cl_2/N_2$ plasma [168]. In Sec. 3.3.2, we present a study for a Cl_2/O_2 chemistry is similar in terms of methodology to the one in Ref. [75], but due to a careful selection of input and output parameters, the trade-offs between the output parameters can now be clearly identified. This allows for important conclusions about the limitations that are to be expected for this specific etching approach.

3.3.1. Comparison between Cl_2/N_2 and Cl_2/O_2-based ICP-RIE plasma chemistries

In Fig. 3.13, we juxtapose the results of two established processes for the etching of deep PhC holes into InP or planar waveguide structures of InP/InGaAsP/InP. One of them uses a Cl_2/N_2 gas mixture with an additional He component for dilution of the plasma [75]. It is the standard process in our lab (FIRST), and a typical result is shown in

Fig. 3.13 (a). The other process is based on a Cl_2/O_2 mixture and is implemented on equivalent equipment in the COBRA lab of TU Eindhoven [77]. A typical result is shown in Fig. 3.13 (b). Both labs use an ICP180 system of Oxford Instruments. The attributes of the two processes are summarized in Table 3.5.
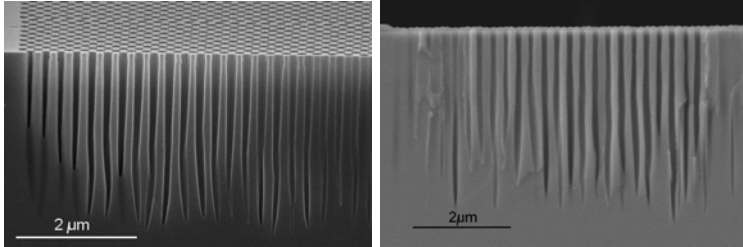
Figure 3.13. Deeply etched PhC holes in InP. Left: Cl_2/N_2 process using a SiN_x hardmask, performed in FIRST at ETH Zurich (permission of Dr. Patric Strasser). Right: Cl_2/O_2 process using a SiO_2 hardmask, performed at COBRA of TU Eindhoven (permission of Dr. Fouad Karouta).

Table 3.5. Summarized attributes of the two processes shown in Fig. 3.13.

Chemistry	Cl_2/N_2	Cl_2/O_2
Masking material	SiN_x	SiO_2
Intermediate masking material	titanium	chromium
Mask thickness	400 nm	500 nm
Feed gas flux ratio	Cl_2:Ar:N_2:He $= 13$:5:5:15	Cl_2:$O_2 = 14$:2
Stage temperature	200°C	200°C
Selectivity to mask	~ 10	~ 12
Max. aspect ratio	16 - 20	> 20
Hole shape	conical	conical, slightly more cylindrical than the Cl_2/N_2 process

The quality of the results from both processes is comparable. On one hand, the Cl_2/O_2 process seems somewhat more promising due to a slightly superior mask selectivity which enables higher aspect ratios.

In addition, the N_2 content in the Cl_2/N_2-based plasma is critical and process drifts over long periods (months/years) have been observed. On the other hand, the vertical profile of the SiO_2 mask is always slightly tapered (in contrast to the SiN_x mask presented in Sec. 3.1) and the intermediate chromium mask is more difficult to handle than a titanium mask (redepositions and micromasking during ICP-RIE). Therefore, the use of our SiN_x mask together with a Cl_2/O_2-based process is the obvious next step. However, although the equipment of the two labs is equivalent, the process could not be transferred one-to-one. Figure 3.14 shows the result obtained at FIRST with the process parameters of COBRA. While the sidewalls are quite vertical, the selectivity of InP towards the mask is poor and some lateral etching is observed (hole widening). The etching conditions in the two machines are clearly different. Therefore, an thorough optimization was necessary. This is presented in Sec. 3.3.2.
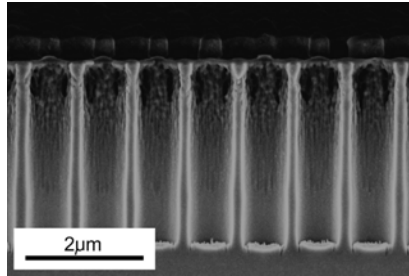
Figure 3.14. Etching result after a direct transfer of the Cl_2/O_2-based process from an ICP-RIE machine of the same model in the COBRA laboratory. There is significant lateral etching under the SiN_x hardmask. The same process performed in the two machines clearly leads to different results. To obtain similar etching profiles as those shown in Fig. 3.13, a substantial adjustment needs to be made to the process parameters.

3.3.2. Experimental study of the limitations of a Cl_2/O_2-based etching process

To implement a Cl_2/O_2-based in our own lab, a similar optimization procedure was used as the one presented in Ref. [75] for the Cl_2/N_2 process: An orthogonal array for the four input parameters listed in Table 3.6 is set up to define a small but well-randomized set of experimental runs. The same technique was used in Sec. 3.1.3 for the

optimization of the mask fabrication process, and the details of it are explained in Appendix A.2. A SiN_x mask of 800 nm thickness was used. It was fabricated using one SAMR step according to Sec. 3.2. The levels of the input parameters in Table 3.6 are again chosen based on observations in preliminary experiments. Notably, the addition of argon to the plasma (in analogy to the Cl_2/N_2 process) has shown some promise in these experiment and was, therefore, included in the investigation. An important difference compared to Ref. [75] is that the RIE power is not used as an input parameter, but is replaced by the dc self-bias of the plasma reactor. The reason for this is that, in order for the orthogonal array to yield statistically relevant results, the input parameters must be mutually independent. We therefore selected the input parameters which can be most closely related to the physical quantities governing the etching characteristics. The ICP power is related to the density of reactive species in the inductively coupled plasma, whereas the self-bias is related to the kinetic energy of the ions impinging on the sample. For a fixed RIE power, the self-bias depends on the ICP power. An increase in ICP power leads to a decrease in self-bias, because a larger amount of positively charged ions is available to neutralize the negative charge that is responsible for the self-bias. In the experiment, the ICP power was fixed, and then the RIE power was adjusted to attain the targeted self-bias. The chamber pressure was not considered as an input parameter, because it is expected to affect the density of reactive species and, therefore, cannot be used as an independent input parameter along with the ICP power. The pressure value of 2 mTorr is chosen in accordance with optimized values reported for similar processes [75, 121]. The temperature was fixed at $200°C$.

Table 3.6. Input parameters of the process optimization and corresponding level settings. The stage temperature and the pressure were kept constant at values of $200°C$ and $2\,mTorr$, respectively.

Input parameter	Level 1	Level 2	Level 3	Level 4
ICP power (W)	600	900	1200	1500
Self-bias (V)	280	320	360	400
O_2 flux (sccm)	0	1	2	3
Ar flux (sccm)	2	4	6	8
He flux (sccm)	5	15		

The quality of each run is judged with respect to the aspect ratio, the conicity of the holes, the verticality, and the sidewall smoothness. The aspect ratio used for comparison is an extrapolated aspect ratio that could be expected for an etching time, which leaves a remainder of $200\,\mathrm{nm}$ of the SiN_x mask (assuming a constant etching rate). For the conicity, the standard deviation of the hole width along the depth of the hole is measured and divided by the depth of the hole. The verticality of the hole axis is quantified by measuring the standard deviation of the sidewall angle along the depth of the hole. To avoid a cumbersome terminology, we will speak of "hole verticality", although it is the *deviation* from it that is actually measured. Finally, the sidewall smoothness is rated based on a visual inspection of the SEM images and, therefore, is not entirely independent of the experimenter.

The findings of the experiment are summarized in Table 3.7, where for each input parameter the influence on all output parameters is indicated by arrows. They indicate the direction of change of the output parameter when the value of the input parameter is increased. For instance, hole conicity and verticality both decrease with an increasing O_2 flux. The second row of the table ("desired trend") shows the direction of the trend of each output parameter that we judge as beneficial for our optical devices. A single arrow is given if the impact is clear but with outliers in the experimental data. A double arrow is given for an unambiguous impact of moderate magnitude, whereas a triple arrow indicates a strong effect. Entries are left blank if an insignificant or ambiguous impact is observed.

The results shown in Table 3.7 are remarkably consistent in the sense that an improvement of the aspect ratio coincides with an improvement of the conicity and with a degradation of both the hole verticality and the sidewall smoothness. This observation is *independent* of the input parameter.[3] This means that not all output parameters can be optimized at the same time using the given input parameters; a trade-off between the output parameters has to be made such that all of them are in a "tolerable" range. The precise definition of "tolerable" can be very difficult to specify. For instance, for the optimization of PhC devices, the impact of each output parameter on the optical properties of the

---

[3]This consistency could not be achieved when using the RIE power as an input parameter instead of the self-bias (results not shown here), which underlines the importance of a large degree of mutual independence of the input parameters.

Table 3.7. Response of output parameters on input parameter level settings. The arrows indicate the direction of change of the output parameter when the value of the input parameter is increased. The row "desired trend" indicates the direction of change which represents an improvement of the respective output parameter.

Input parameters	Aspect ratio	Conicity	Hole verticality	Sidewall smoothness
desired trend	↑	↓	↑	↑
ICP power (W)	↓↓↓		↑↑↑	↑
Self-bias (V)	↓	↑↑	↑	↑↑
O$_2$ flux (sccm)	↑	↓	↓	↓↓
Ar flux (sccm)			↑	
He flux (sccm)	↓	↑	↑	↑

device under test would have to be known in detail. This knowledge is, however, limited [169] and very difficult to obtain experimentally. Alternatively, the optical properties themselves could be used as output parameters in a similar experiment. This would mean that a full device (or a complete integrated circuit) would have to be fabricated and characterized for each set of input parameters.

Figure 3.15 shows two examples of etching results from the set of runs of the orthogonal array. On the left, the holes have a high aspect ratio (note the large amount of remaining mask), but the lower ends deviate considerably from the vertical axis. In addition, there is some roughness of the sidewalls starting to develop at the upper parts of the holes. The right-hand micrograph of Fig. 3.15 shows low-aspect ratio holes with little deviation from the vertical axis and very smooth sidewalls.

If we compare our results of Cl$_2$/O$_2$-based etching to those of our standard Cl$_2$/N$_2$-based process, we observe that similar quality holes can be achieved with both chemistries. Replacing N$_2$ with O$_2$ leads to no significant improvement; and the clear identification of the quality trade-offs shows that no quantum leap can be expected as long as we are restricted to variations of the parameters that we used for the experiments. In order to fully exploit the potential of substrate-type PhCs, we believe that other etching chemistries (e.g., based on iodine
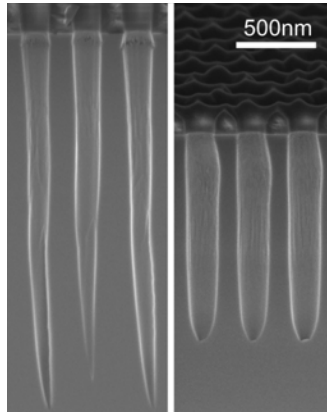
Figure 3.15. Two etching runs with different ICP power (same length scale). Low power (600 W) to the left and high power (1500 W) to the right. The SiN_x mask of both samples is still intact. The two pictures show clearly how a high aspect ratio goes along with a degraded verticality of the hole and an increased sidewall roughness (near the top surface).

or bromine) should also be investigated in more depth. Possibly, similar trade-offs will be found, but even then the correlations might be of different strength. We believe that our work provides useful guidelines for the assessment of other etching technologies.

3.4. Propagation loss in waveguides

Most of the content of this section is submitted for publication [79].

In Sec. 3.2 we have introduced the SAMR method to fabricate thick SiN_x hardmasks and, based on the results of Sec. 3.3, we can claim with some confidence that the quality of our deeply etched holes in InP is close to the optimum that can be achieved with the available equipment. It remains to test the optical performance of devices fabricated with the thick hardmask (which allows for longer InP etching times). For us, the relevant figure of merit is the propagation loss in single-line defect waveguides formed in triangular-lattice PhCs. In the following, the fabrication and optical characterization of waveguides suitable for loss measurements will be presented. First, the measurement method and the chip design are explained (Sec. 3.4.1), then the fabrication is

addressed in detail (Sec. 3.4.2) and finally the experimental results are discussed (Sec. 3.4.3).

3.4.1. Loss measurement method and chip design

There are mainly two standard methods which are widely used for the measurement of losses in passive integrated waveguides. The Fabry-Pérot method uses the interference fringes of monochromatic cw light that passes multiple times between two mirrors (typically cleaved facets) of a cavity. The fringe spacing contains information about the cavity length and the effective refractive index of the propagating mode, whereas the fringe contrast (difference between maxima and minima) is related to the damping of the mode due to waveguide losses as well as mirror losses. Details of the Fabry-Pérot method are given in Appendix A.5. The second method is generally referred to as the *cutback* method. It makes use of several waveguides of different lengths. Light is coupled in at the input and collected at the output of each waveguide. The longer the waveguide, the smaller is the mode intensity at the output. By fitting an exponential curve to the experimental output intensity, the loss coefficient can be extracted. In Appendix A.6 the method and some associated practical considerations are discussed. The preference for one or the other measurement method depends on the reflection coefficients at in- and outputs of the waveguides under test. For very low mirror reflectivities, the Fabry-Pérot method is not suitable, because the fringe contrast is weak and dominated by the mirror loss. In this case, the cutback method would be favorable. For high reflectivities, the fringe method works well, whereas the cutback method can become inaccurate due to the superposition of light components that made different numbers of round-trips in the cavity. In our specific case, the intensity reflectivity of cleaved facets is of the order of 30 %. This value is neither very high nor very low, such that both methods can be employed. We decided to use the cutback method for a very practical reason. Forming a Fabry-Pérot cavity between cleaved facets would mean that we would have to use very long PhC waveguides. Cleaving a bar of less than 1 mm from the 350 μm thick substrates that we typically use is not easy to do reliably. If we assume literature values for substrate-type W1 PhC waveguides, which are roughly 800 dB/cm, a 1 mm long waveguide would cause 80 dB propagation loss. The input intensity in our setup is of the order of 0 dBm and the noise floor is around -70 dBm. Hence, a 1 mm long waveguide would not be measur-

able.

To employ short waveguides ($< 400\,\mu$m) for the cutback method on a bar of 2 mm (a convenient value for us), the use of access waveguides is unavoidable. We used waveguides formed by deeply etched trenches. They are $5\,\mu$m wide and have $100\,\mu$m long taper sections at the in- and output of the PhC waveguide. This configuration was optimized in previous work [76, Chap. 5]. The reflection coefficients are small at the interfaces to the PhC waveguides [170], such that round-trips within the internal PhC waveguide cavity can be neglected. We used five PhC waveguides with 30×2^n periods of $\Gamma = 380\,$nm, $n \in [1, 5]$. The longest waveguide is hence $365\,\mu$m long, the shortest $22.8\,\mu$m.

3.4.2. Fabrication

The main challenge in the fabrication of a chip for cutback measurements lies in the SAMR method that we want to use for a thick hard-mask. The mask renewal works only for *circular* features, and once the process is calibrated for a given hole diameter, the hole size is fixed. This means that the access waveguides for a PhC waveguide cannot be fabricated in the same lithography step. As a consequence, the alignment between the two types of waveguides becomes a difficult issue. It has to be accurate to less than 100 nm. This requires the use of markers at in- and outputs of every PhC waveguide. These markers have to be composed of circles, because that's the only available feature in the first lithography step. The process flow can be summarized as follows:

- Epitaxy of the the planar waveguide structure (InP/InGaAsP/InP) and deposition of SiN_x (800 nm), Ti (~ 40 nm) and PMMA (200 - 220 nm).
- EBL lithography; only circles of fixed diameter (210 nm).
- Two-step SAMR process (cf. Sec. 3.2). For 800 nm of SiN_x, two steps are sufficient.
- ICP-RIE of deep holes. Here, we used our standard Cl_2/N_2-based etching process. The etching time was set to 160 s. For 400 nm of SiN_x, the etching time is limited to ~ 90 s.
- Removal of SiN_x residues in hydrofluoric acid and deposition of a new stack of masking layers (SiN_x, Ti, PMMA). For the access waveguides, 400 nm of SiN_x are sufficient. To make sure that the holes are well protected, 400 nm of SiN_x were deposited and

etched back in an anisotropic RIE process before the final SiN_x layer was deposited. This planarization step will be described in more detail in Sec. 4.1.

- Second EBL lithography step. Markers which were written in the first EBL step have to be recognized and used to align the access waveguides accurately to the PhC waveguide in- and outputs.
- Standard hardmask RIE step.
- ICP-RIE of access trench waveguides and removal of hardmask residues in HF.
- Cleaving of the chip to a bar of 2 mm width.

The most critical step is the alignment of the access waveguides to the PhC waveguides. Figure 3.16 shows an example of global and local markers. The global markers (large cross) are used to set the coordinate system of the stage on which the samples are mounted in the EBL chamber. Local markers (small cross) are used to adjust the coordinate system of the column. This procedure is usually referred to as a write field alignment (WFA). For an optimal alignment result, it is best if the WFA is done near the most critical locations in the design. Inaccuracies can occur due to stage drift during writing of the time-intensive PhC waveguides. For short waveguides, only one WFA is done. For long PhC waveguides input and output ports are aligned separately.
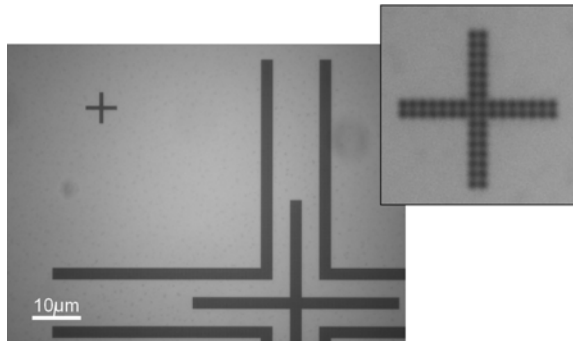
Figure 3.16. Optical microscopy image of a global marker (large cross) and local marker (small cross). Both types of markers are composed of circular holes which are compatible with the SAMR process. The inset shows a magnified view of the local marker, whose lines are formed by two rows of holes.
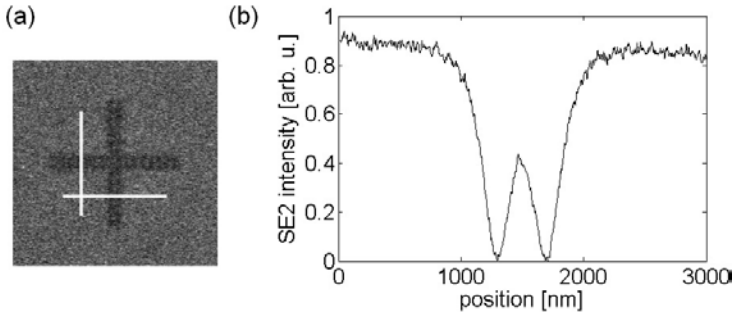
Figure 3.17. Line scan for automatic WFAs. (a) Line scans are indicated by white bars on an SEM image of a local marker; (b) Intensity profile of a line scan recorded by an SE2 detector.

The alignment is carried out automatically using two line scans on a total of three cross-shaped markers per alignment. The line scans are indicated by two white bars in Fig. 3.17 (a). For each scan, an intensity profile is recorded. An example in shown in Fig. 3.17 (b). The circular holes that form the marker appear darker than the surroundings in the SEM detector. The markers are formed by two rows of holes, which results in a small intensity peak in the center of the marker scan. The position of the markers is determined by detecting the left- and rightmost flanks of the dips at a given intensity threshold. This routine proved to be very reliable. Figure 3.18 shows an SEM image of a short PhC waveguide (not used for the optical characterization) including the
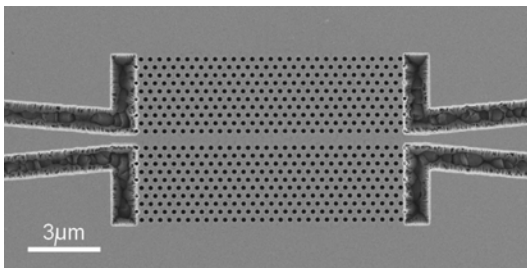
Figure 3.18. SEM micrograph of a PhC waveguide of 30 periods with well-aligned access waveguides.

access waveguides aligned to it. The alignment accuracy is very high.

3.4.3. Experimental propagation loss results

The characterization of the PhC waveguides is performed by a port-to-port measurement as described in detail in [76, pp. 118]. Monochromatic cw light from a tunable laser source (1470 - 1630 nm) is coupled into the access waveguides via a polarization-maintaining lensed fiber. TE polarized light is used for the measurements.[4] After propagation through the chip, the light couples out through the facet and is collimated by a microscope objective. The output power is measured by an InGaAs detector. The cutback method is applied as outlined above. The measured loss figure is plotted versus wavelength in Fig. 3.19 (thick solid line). To appraise the fabrication quality of the PhC waveguides, we benchmark them with numerical simulations using perfectly cylindrical hole shapes. The numerical method is explained and validated in Ref. [170]. It applies the finite difference time domain method (FDTD) using the freely available MEEP program developed at the Massachusetts Institute of Technology [171]. Since the fabricated holes are slightly conical, there is some uncertainty in choosing the appropriate hole radius in the simulations for comparison of the loss data. From SEM micrographs, the radius of the fabricated holes is determined to be $r = 100$ nm at the chip surface. The corresponding 3D FDTD data are plotted as a dashed line in Fig. 3.19. To account for the conicity, the simulations were repeated for two slightly smaller hole radii, $r = 95$ nm (dotted) and $r = 90$ nm (solid). The best agreement is found for $r = 95$ nm. Apart from a wavelength shift of about 20 nm, it matches the experimental curve remarkably well. Most important for the present discussion is the observation that the minimum loss figure is around 335 ± 5 dB/cm in the simulation as well as in the experiment. We conclude that the fabrication quality is not the limiting factor in terms of propagation loss. As long as we use waveguide designs which are operated above the background line, we cannot expect a significant improvement if we further improve the fabrication process of the PhCs. This knowledge is vital in the decision-making process of future research efforts.

---

[4]TE means that there is no **E**-field along the symmetry axis. In the context of 2D PhCs, the symmetry axis is generally defined by the PhC, *not* by the waveguide axis. Thus, the **E**-field of the light coupled into the waveguides is oriented parallel to the chip surface.
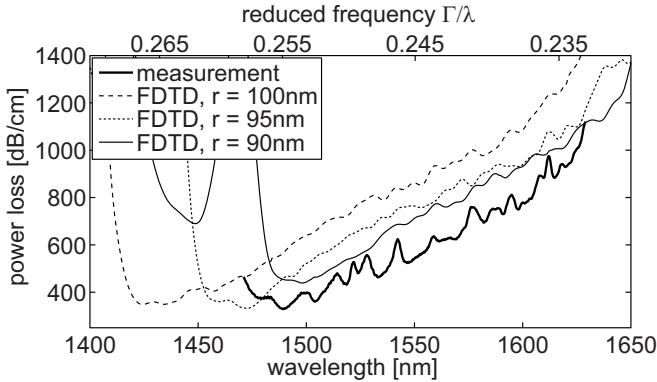
Figure 3.19. Propagation loss of a W1 substrate-type PhC waveguide with lattice constant $\Gamma = 380\,\text{nm}$. Experimental data (thick solid line) are compared to 3D FDTD results (thin lines). For the simulations, a cylindrical hole shape is assumed. Since fabricated holes are slightly conical, the simulations were performed for three different hole radii, $r = 90\,\text{nm}$ (solid), $r = 95\,\text{nm}$ (dotted), $r = 100\,\text{nm}$ (dashed). The best agreement is found for $r = 95\,\text{nm}$.

To our knowledge, the experimental loss figures presented in Fig. 3.19 are record values for substrate-type W1 PhC waveguides. While the minimum value at $\lambda = 1490\,\text{nm}$ is around $335\,\text{dB/cm}$, the losses at $\lambda = 1550\,\text{nm}$ are still at a rather low level of about $540\,\text{dB/cm}$. From Fig. 3(d) in Ref. [58] we read loss values of about $600\,\text{dB/cm}$ at $\lambda = 1490\,\text{nm}$ and $800\,\text{dB/cm}$ near $\lambda = 1550\,\text{nm}$. These are the lowest literature values for comparable waveguides that we are aware of.

To conclude the discussion of this experiment, we want to make an attempt at explaining the increasing trend of the propagation loss as a function of the wavelength (as observed in Fig. 3.19). The following gedankenexperiment is on the level of a plausibility argument, but we believe that it conveys a good notion of the physical mechanism. First, let's consider a waveguide of a width w much larger than the wavelength of the excitation, $w \gg \lambda$. The corresponding mode will have most of its energy in the waveguide core, i.e., there is only a small energy overlap with the PhC. Due to this small overlap, the 1D periodic modulation along the propagation direction can be regarded as "weak". In the Bloch representation of the mode, this means that there will be a strongly dominating Fourier component in one Brillouin zone and significantly

weaker components in the neighboring Brillouin zones. Typically, for our InP-based devices, the dominating component is located in the 2nd Brillouin zone [59, Ch. 9]. Only the weak component in the 1st Brillouin zone lies above the background line and hence contributes to the propagation loss. The stronger this "lossy" component is, the larger are the propagation losses of the mode. Now, if we reduce the waveguide width, the energy overlap with the PhC increases, i.e., the periodic modulation becomes stronger and with it the "lossy" Fourier component above the background line. To sum it up, the propagation losses depend on the ratio w/λ, which is related to the lateral energy confinement of the mode in the core. If we restrict the discussion to W1 waveguides, for which w is directly related to the lattice constant Γ, we can then state that the propagation losses are governed by the ratio Γ/λ, which is often referred to as the reduced frequency u. If u is increased, the energy confinement in the core goes up and the losses go down, which is what we observe in Fig. 3.19.

3.5. Outlook

We have seen in Sec. 3.4 that our PhC fabrication process is capable of producing W1 PhC waveguides with losses that are comparable to simulation results with perfectly cylindrical hole shapes. As long as we use the same substrate-type waveguide design, there is no necessity to further improve the etching process. However, once we can design better waveguides with low inherent propagation losses, the fabrication quality might become an issue again. As pointed out in Sec. 3.3, the control over the shape of deeply etched holes in InP is limited by a trade-off between aspect ratio and hole verticality. We believe that a significant improvement in etching quality can only be achieved if new process chemistries are explored or if different dry-etching equipment is used. This would require large investments and a fair amount of optimization work. An alternative approach of improving the quality of the holes is to apply a post-treatment process. Shahid *et al.* have demonstrated a thermally driven reflow process carried out under PH_3 atmosphere at $630°C$, which results in nearly vertical sidewall profiles [172]. We have tested the process on our equipment (MOVPE reactor) using our PhC holes. Figure 3.20 shows a result that looks very promising. The verticality of the holes is very high, and the conicity is almost entirely removed.
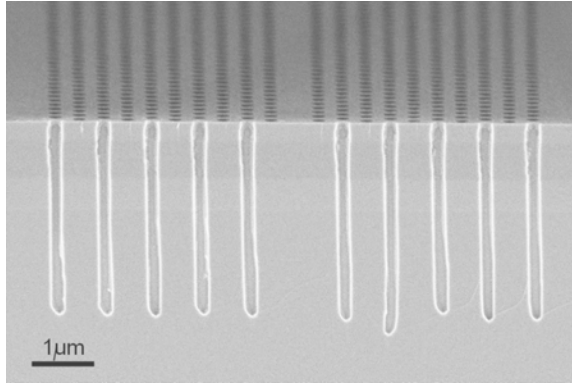
Figure 3.20. Cross-sectional SEM micrograph of PhC holes which were post-treated using a thermally driven reflow process. The shape of the holes is very cylindrical and their verticality is very high.

So far, we have not measured the optical performance of post-treated waveguides. The potential benefit that we expect for our standard waveguide design is rather small, as pointed out in Sec. 3.4. The losses that we achieve without post-treatment are already very close to simulated loss figures with ideal hole shapes. Nevertheless, we believe that the post-treatment process is a promising method for future designs of substrate-type waveguides that can be operated below the background line.

Alternative solutions to further reduce the propagation losses will have to involve modifications of the waveguide design. This can mean that

- the PhC pattern is altered to suppress the Fourier component above the background line, or that
- the cladding layers are manipulated in such a way that the background line itself is modified.

According to Kuang *et al.*, the first approach can be followed by shifting the PhC on one side of the waveguide by half a period along the waveguide axis [117]. The new symmetry is predicted to reduce the propagation losses drastically. So far, this was only confirmed numerically [169]. The second approach can be realized experimentally by enlarging the PhC holes in the cladding layers using a selective wet etching process.

For the dissertation of R. Kappeler [59], we have performed some etching tests in HCl:H_2O = 2:3 with additions of citric acid (encouraged by Ref. [173], which reports smooth etching surfaces after additions of organic acids). The hole enlargement seems to be well controllable and reproducible, but the etching is non-isotropic, and the resulting background line is hard to simulate. Preliminary results suggest that the propagation loss can be significantly reduced with respect to the results presented in Fig. 3.19. Instead of merely enlarging the holes in the claddings, the wet etching can be performed to such a degree that the holes connect and the PhC disappears entirely in the claddings. A membrane-type PhC waveguide is obtained, whose capability for low-loss propagation is well-known. In Sec. 4.4.1 we will present a waveguide, which is underetched such that the PhC pattern disappears in the claddings but narrow posts of InP remain above and below the waveguide core. This design is promising not only for low-loss propagation, but also for current injection vertically through the device. So far, the etching process is not controlled very well, and no experimental loss measurements are available. However, using 3D FDTD simulations, propagation losses below $20\,\mathrm{dB/cm}$ are predicted in a bandwidth of $\Delta\lambda = 23.3\,\mathrm{nm}$ around a center frequency of $\lambda = 1550\,\mathrm{nm}$ [116].

4

Current Injection for Active Photonic Crystal Devices

In Chap. 3 the fabrication of substrate-type PhCs was discussed. The second challenge in view of electrically pumped PhC waveguide devices is the fabrication of metal contacts on the PhC waveguide. The perforated surface of the substrate has to be planarized to set the preconditions for a lithography step with sub-100 nm resolution. In addition, high demands are imposed on the alignment accuracy. A single-moded W1 waveguide (as in Fig. 1.1 (c)) has a width of about 400 to 500 nm. A contact strip of 300 nm width has to be aligned to the waveguide with

an accuracy in the order of 100 nm. Furthermore, the planarization of the holes can affect the PhC properties. Therefore, the material used for planarization is, in the ideal case, removed after contact fabrication. In other words, a metal air-bridge has to be formed to connect the nanostructured contact to a macroscopic pad which can be accessed by external electrical circuitry for current injection. A solution to this task is presented in Sec. 4.1.2.

For the implementation of active devices, an active material must be chosen. In this work, a multiple quantum well (MQW) structure is used. This choice is briefly motivated in Sec. 4.2.1. Three quantum wells (QW) are embedded into a planar waveguide structure which forms a p-i-n diode. PhC waveguides are etched into this structure and furnished with electrical contacts for vertical current injection. In Sec. 4.2.3 the gain of this structure is modeled from first principles. Then, in Sec. 4.2.5, the active material is characterized experimentally with respect to gain and loss.

Finally, PhC lasers of various waveguide widths are presented (Sec. 4.3). The narrowest PhC device for which lasing was achieved in continuous wave (cw) mode was a W4 waveguide. Similar devices reported in the literature are slightly wider and often pumped in pulsed mode (cf. Sec. 1.2.2). In this respect, our devices can match the state-of-the-art. Nevertheless, the ultimate goal of achieving gain in a W1 waveguide is not quite within reach. Between W4 and W1 waveguides, the losses increase dramatically and carrier leakage becomes a severe problem. Therefore, the final question to be answered in this chapter is: Will we ever be able to achieve gain in a W1 waveguide?

4.1. Contact fabrication for active photonic crystal devices

Parts of this section were presented at the *22nd International Conference on Indium Phosphide and Related Materials IPRM* and published in the conference proceedings [80].

After the fabrication of PhC waveguides, the formation of metal contacts requires additional lithography steps. One lithography step is needed to define the narrow contact strips on the waveguide, another one to pattern the contact pads which are accessible for the connection

to external circuitry. The main challenges in defining a narrow contact strip on a planar PhC waveguide are:

- Surface planarization: The surface of a planar PhC device is perforated with sub-μm diameter holes. Spin-casting of resist on such a surface results in uneven layer thicknesses. Close to the PhC holes, the resist layer is considerably thinner than far away. If a layer of 200 nm is spun on the sample, then the resist thickness on a narrow PhC waveguide is nearly zero.
- Alignment: A W1 PhC waveguide for an optical wavelength of $\lambda = 1550$ nm is 400 - 500 nm wide, a W3 is around $1\,\mu$m wide. Considering the difficult surface topology, these constraints are demanding. The use of photolithography is hardly practicable.

These problems can be solved in different ways. We distinguish two types of contacts that have been fabricated for the purposes of this thesis:

- **C1**: Contact strips opened in a planarization layer. Large contact pads are defined on the planarization layer for a connection to external circuitry (cf. Fig. 4.1 (a)).
- **C2**: Air-bridge contacts. Microscopic contact strips on the waveguides are connected to macroscopic contact pads through a metal air-bridge (cf. Fig. 4.1 (b)).
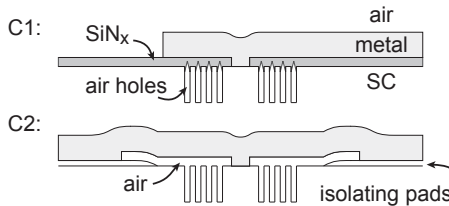
Figure 4.1. Different types of contacts for narrow PhC waveguides. C1: Contact pads defined on a planarization layer; C2: Air-bridge contact (cf. Sec. 4.1.2).

Fabrication details for contacts of type C1 are given in Sec. 4.1.1. These are the "standard" contacts used for the active devices presented in Sec. 4.3. The air-bridge contacts (type C2) can be used to avoid

adverse effects of a planarization layer on the unique properties of the PhC. The fabrication of such contacts is presented in Sec. 4.1.2.

4.1.1. Contacts with planarization layer

Figure 4.2 shows the process flow for contacts of type C1. The first step is the planarization of the PhC holes (Fig. 4.2 (b)). It can be achieved by iterative deposition and dry-etching of SiN_x. If the deposition step is more isotropic than the etching step, planarization is possible. Therefore, a highly directional etching process has to be chosen. To etch SiN_x, using CHF_3 as a feedgas generally provides good anisotropy. For an increased etching rate, careful additions of O_2 can be considered, which inhibits the formation of a fluorocarbon film on the SiN_x surface [132]. However, lateral etching will rapidly set in for too large O_2 contents.
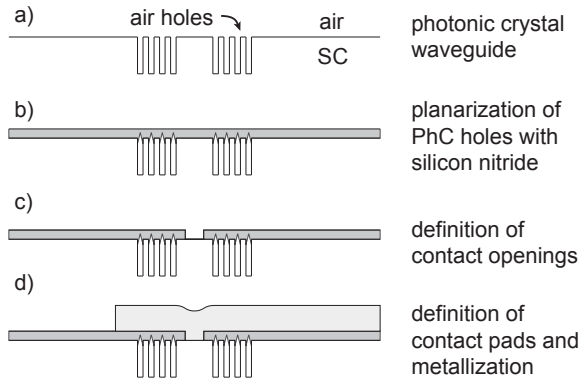
Figure 4.2. Fabrication sequence of contacts of type C1. (a) Bare sample after PhC fabrication; (b) planarization of the surface with SiN_x; (c) definition of an opening in the isolating layer for the contact strip; (d) to form the contact pads, a lift-off process is necessary if more than one device is fabricated on the same chip. The detailed process parameters can be found in Appendix B.2.

Figure 4.3 illustrates the planarization of a 900 nm wide trench in InP by three cycles of etching and deposition of 300 nm of SiN_x. Three cycles are needed to fully close the gap. For PhC holes of less than 300 nm diameter, only one etching step is required, as can be deduced from Fig. 4.4, which shows the planarization of a 300 nm wide

trench. Commercial tools from Oxford Instruments are used for deposition of SiN$_x$ layers (Plasmalab System80Plus PECVD) as well as for dry-etching (Plasmalab System80Plus RIE). The feedgas ratio for the etching step is CHF$_3$:O$_2$ = 11:1. The plasma is operated at a pressure of 45 mTorr and a self-bias voltage of 380 V (cf. Appendix B.2).
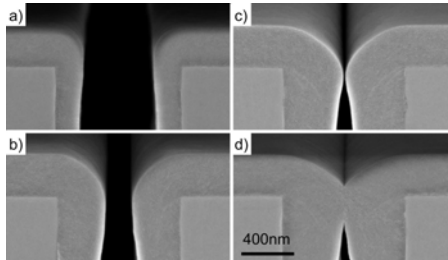
Figure 4.3. Planarization of a 900 nm wide trench etched in InP. 300 nm of SiN$_x$ are deposited and dry-etched in alternating steps. (a) single deposition step; (b) one etching cycle; (c) two etching cycles; (d) three etching cycles.
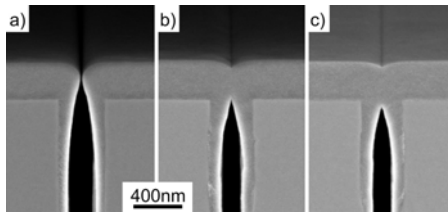
Figure 4.4. Planarization of a 300 nm wide trench in InP using the same procedure as in Fig. 4.3. For a sacrificial layer thickness of 100 nm, one cycle of etching is sufficient. This corresponds to panel (b).

The second step is to define narrow contact openings. Using a dry-etching process similar to the one for the planarization step, this can easily be achieved by means of an electron beam lithography (EBL) mask. Here, the most critical issue is the precise alignment with the PhC waveguide, which, depending on the application, can exceed the millimeter length range. This alignment is achieved by EBL (Raith150) using deeply etched alignment markers which are fabricated simultaneously with the PhC patterns. A marker recognition routine of the EBL software allows to adjust the write field parameters of the pattern

generator to a sub-50nm accuracy. For a similar alignment routine on the same equipment, a systematic evaluation of the alignment accuracy was performed by Andreas Alt (Laboratory for Millimeter-Wave Electronics, ETH Zurich). An average offset of $18.0\,\mathrm{nm}$ from the target position was found with a standard deviation of $12.5\,\mathrm{nm}$. Figure 4.5 shows an SEM top view of a metallized W1 PhC waveguide. The left half of the image depicts the metallized part, whereas the right half shows the contact opening etched into a $200\,\mathrm{nm}$ thick SiN_x layer.
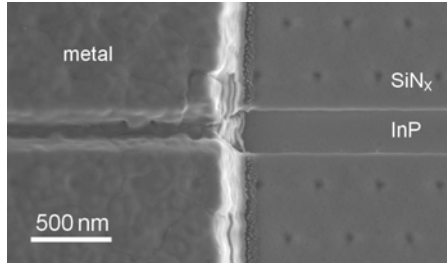
Figure 4.5. SEM top view of a W1 PhC waveguide. On the left side, the waveguide is metallized. The right side shows the contact opening in SiN_x without metal.

The metalization used throughout this thesis is a Pt/Ti/Pt/Au layer stack. It is deposited on a highly p-doped ($2{\cdot}10^{19}\,\mathrm{cm}^{-3}$) $In_{0.53}Ga_{0.47}As$ contact layer by EBPVD. $In_{0.53}Ga_{0.47}As$ has the smallest bandgap among the InP lattice-matched materials and is, therefore, best-suited to form low-resistivity ohmic contacts. The most widely used metalization used is Ti/Pt/Au with Ti for adhesion on the semiconductor surface, and the intermediate Pt layer to prevent diffusion of Au. The Pt interlayer between the Ti/Pt/Au and the p-InGaAs was added to lower the effective barrier height [174]. Contact resistances between $1{\cdot}10^{-7}$ and $1{\cdot}10^{-6}\,\Omega{\cdot}\mathrm{cm}^2$ were measured for these p-contacts using the transmission line model (TLM) with a linear structure [175, 176]. Contacts of various widths between $50\,\mathrm{nm}$ and $1\,\mu\mathrm{m}$ were used to confirm a good performance on the nano-scale. For the narrowest contacts ($50\,\mathrm{nm}$), a value of $2{\cdot}10^{-7}\,\Omega{\cdot}\mathrm{cm}^2$ was measured.

4.1.2. Air-bridge contacts

For PICs, the use of PhCs is interesting because of their unique properties like slow light or the possibility to create and actively control high-Q cavities. For such experiments it is vital that PhC properties be not affected by the metal contact or by an electrically isolating layer which is sometimes used to planarize the PhC device surface. Such layers can shrink and shift the bandgap [177, 178]. Figure 4.6 shows 3D mode simulation results illustrating how the bandgap of a triangular lattice PhC in InP changes when the holes are filled with SiN_x. Making predictions about the case of partially filled holes would be rather difficult. Hence, for sophisticated PhC functionalities, the accurate device modelling becomes very challenging. Therefore, we developed an air-bridge contacting technique which can access PhC structures like waveguides or waveguide cavities down to a feature size of $< 200\,nm$.
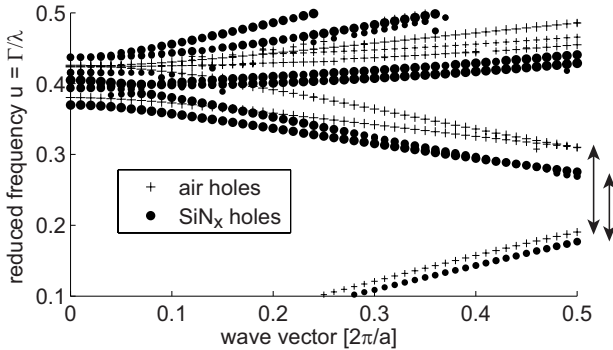
Figure 4.6. 3D simulation (plane wave expansion method) of TE modes of a triangular lattice PhC in InP. The size of the markers scales with the energy density in the core layer of the corresponding modes. Completely filling the air holes with SiN_x shrinks the bandgap and shifts it slightly (indicated by arrows). The effect of partial filling as in Fig. 4.4 would be challenging to predict accurately

The fabrication of electrical air-bridge contacts on narrow PhC waveguides is faced with a number of challenges. In Fig. 4.7, the proposed process flow is depicted schematically. The first challenge is to find a suitable material to planarize the PhC holes (step (c) in Fig. 4.7). At the same time, that material has to provide the possibility to reliably

define narrow and clean contact openings (step (d)). In addition, it has to serve as a sacrificial layer for the formation of the air-bridge (step (f)). It turns out that SiN_x, which we have used as an isolating layer for contacts of type C1 fulfills these requirements. The planarization issue and the definition of narrow openings for contacts have already been discussed, and the removal of the sacrificial SiN_x (to form the air-bridge) can be performed by wet-etching in hydrofluoric acid (HF). HF removes the SiN_x layer, including sidewall depositions in the PhC holes, very effectively. The removal of SiN_x from sidewalls is crucial to avoid partial filling of holes.
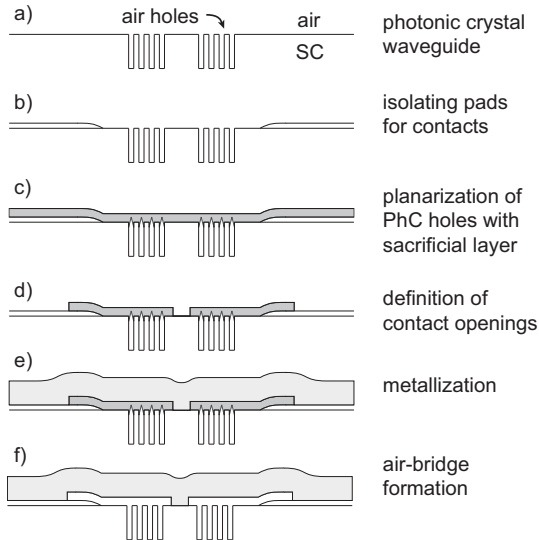
Figure 4.7. Schematic cross-sectional representation of process flow for air-bridge contact fabrication. In our specific case, the semiconductor (SC) is an InP-based PIN junction

The second challenge is to form electrically isolating contact pads. Given the choice of SiN_x for the sacrificial layer and all involved fabrication steps, high demands are set on the isolating material for the contact pads. It must be resistant to high temperatures (SiN_x deposition, contact annealing), insoluble in acetone (metal lift-off), resistant to HF etching (air-bridge formation), and there has to be a way to structure thin layers ($\sim 200\,nm$) on InP surfaces without interfering

with PhC holes (e.g., permanent filling of holes). Promising material candidates to electrically isolate the contact pads are the CycloteneTM resins from the Dow Chemical Company. In particular, the photosensitive 4000-series (Photo BCB) is attractive for its potential as a negative resist for both photolithography and EBL [179]. The material was positively tested with regard to all process requirements [80]. Details about the handling of Photo BCB can be found in Appendix B.2.

Figure 4.8 shows an SEM micrograph of a metal air-bridge contact to a W3 waveguide (triangular PhC lattice with three omitted rows of holes), fabricated according to the process flow depicted in Fig. 4.7. It is a Pt/Ti/Pt/Au ohmic contact for an InP-based PIN diode structure, suspended in air and laterally supported by Photo BCB isolating pads. The design is symmetric for mechanical stability reasons. The bridge is formed using a SiN_x sacrificial layer. After metalization and contact annealing, the SiN_x layer was removed by HF wet etching for 20 minutes. Using the same procedure, we have fabricated Fabry-Pérot lasers of $10\,\mu$m width using PhC and trench waveguides. Their performance is similar to that of laser devices with contacts in a SiN_x isolation layer (type C1 contacts). These latter devices will be discussed in Sec. 4.3. The further use of air-bridge contacts was then suspended due to the fact that the quality of our substrate-type PhCs is not yet sufficient to render hole filling a relevant issue. As long as PhC properties such as slow light cannot be exploited, the partial filling of holes with SiN_x is not a top priority problem.
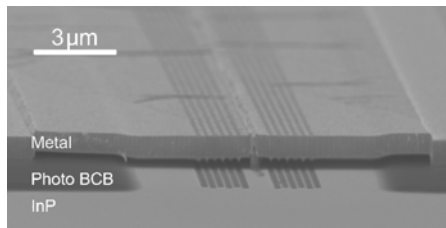
Figure 4.8. SEM image of a metal air-bridge contact ($\sim 200\,$nm width) to a W3 PhC waveguide in InP. It is suspended in air and supported by Photo BCB isolating pads. The pattern on the gold layer is a replication of shallow dimples present on the sacrificial layer after planarization of the PhC holes.

4.2. Gain

For the implementation of an SOA or a laser in a given material system, modal gain is the key property. The gain has to compensate propagation losses and, in the case of a laser, the mirror losses. In this section, we will first motivate our choice of using QWs as a gain material in a high-loss environment. Then we discuss the optimum number of QWs to be used for a given waveguide loss (Sec. 4.2.2). We use a standard empirical model that relates current density to gain. The crucial coefficient of this model will be determined theoretically (Secs. 4.2.3 and 4.2.4) and experimentally (Sec. 4.2.5). A good agreement is found between theory and experiment. The experimental value will be used to compute the optimum number of QWs for our specific material. This leads to the discussion about whether or not it is possible to achieve light amplification in a W1 PhC waveguide through vertical current injection. The question will be tackled from an experimental point of view in Sec.4.3.

4.2.1. The active material: bulk vs. quantum well

In 1963, the use of double heterostructures (DH) for semiconductor lasers was suggested to form potential barriers for the carriers in the active region, such that they "cannot readily flow off" [180]. These diffusion barriers allow for efficient carrier injection and facilitate lasing. The role of heterostructures as optical waveguide structures was only recognized at a later stage. The waveguiding mechanism of the homostructure lasers reported at that time was not understood in detail [181]. The subsequent investigation of thin heterostructure layers led to the observation of quantized energy levels [182] and to the realization of quantum well lasers [183, 184]. Although not immediately confirmed experimentally, the prospect of lower pumping thresholds (due to the step-like density of states in QWs) initiated strong research efforts in the direction of QW lasers. It turned out that "in almost every respect, the QW laser is somewhat better than conventional lasers with bulk active layers" [185]. We list the most notable ones:

- Tunability of wavelength: By changing the width of the QW, the quantized energy levels can be shifted and, thereby, the wavelength of the emitted radiation can be tuned.

- Lower threshold currents: A high gain requires population inversion of levels with a high density of states. The step-like energy density of states of a QW allows to immediately fill energy levels of high density of states. In contrast, the density of states of a bulk material has a square-root dependence on energy and, therefore, many lower lying energy levels have to be filled before population inversion can occur at energies with a high density of states. In a QW, more gain per injected carrier can be obtained, which reduces the pumping threshold.
- Higher efficiency and output power: Through free-carrier absorption and intervalence band absorption (IVBA), the injected carriers generate absorption losses in the waveguide. Hence the QW laser, which requires fewer injected carriers, is more efficient than a conventional laser and can produce more output power.
- Improved temperature stability: The higher the dimensionality of a quantum confinement, the less sensitive on temperature is the pumping threshold [186, 187].

Structures for quantum confinement of higher dimensionality potentially exhibit even more favorable properties than the QWs (1D-confinement). Quantum wires (2D-confinement) and especially quantum dots (3D-confinement) are hot topics of research and can theoretically outperform bulk and QW devices in many respects. However, the technology for the fabrication of devices based on quantum dots has not sufficiently matured to make them the standard choice of active materials. A similar technology boost was necessary to establish QWs as the preferred choice. In contrast to bulk gain materials, QWs pose the technological need for slow-growth epitaxy (MBE, MOVPE). Nowadays these technologies are widely available.

The heterostructure used for the experimental work on active devices throughout this thesis is shown in Fig. 4.9. It is a separate confinement heterostructure (SCH), meaning that the optical confinement in the vertical direction is guaranteed by a refractive index contrast between the InP and InGaAsP layers. The QWs are embedded within this guiding layer. They are positioned in the center of the confinement layer to maximize the confinement factor Γ (overlap between the optical mode and the QW). The three 7.5 nm wide InGaAs QWs are designed for an emission wavelength of $\lambda = 1550$ nm. They are separated by InGaAsP barriers of 12 nm to avoid coupling. The QWs were designed by

Lohe *et al.*, and more details can be found in Ref. [188].

InGaAs:Zn $2 \cdot 10^{19}$, 170nm

InP:Zn $1 \cdot 10^{18}$, ~1000nm

InGaAs QWs (nid), 7.5nm
InGaAsP Q1.2 (nid), 522nm

InP:Si $2 \cdot 10^{18}$, 400nm

InP:Si $3 \cdot 10^{18}$, 335μm

substrate
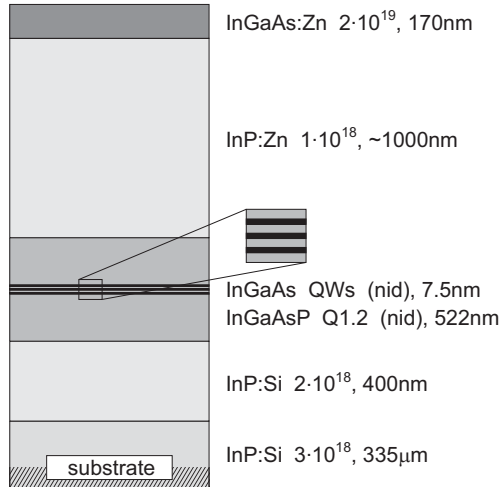
Figure 4.9. Epitaxially grown heterostructure for active devices. The layer thicknesses as well as the doping types and concentrations are indicated (nonintentionally doped layers are marked "nid"). Three QWs of 7.5 nm width, separated by 12 nm wide barriers, are centered on the InGaAsP guiding layer of the SCH. The notation Q1.2 refers to a quaternary material with an energy gap that corresponds to an emission wavelength of 1.2 μm. All layers are grown lattice-matched to InP in an MOVPE reactor.

4.2.2. How many quantum wells?

When using QWs as an active material, an important decision to be made is the one about the number of QWs that shall be used. The more QWs are used, the more gain can potentially be achieved. On the other hand, the current density needed to pump the material to transparency also scales with the number of QWs. To analyze this trade-off, we use the often-cited logarithmic relation between modal intensity gain g and current density J,

$$g = g_0 \cdot \ln \left(\frac{J}{J_0} \right), \tag{4.1}$$

where g_0 is the modal gain coefficient of a single QW and J_0 is the material transparency current density. The behavior described by Eq. (4.1)

is empirical and was experimentally confirmed in many publications, e.g. [189, 190]. Some further justification for the use of the logarithmic relation will be given in Sec. 4.2.4. In the presence of a number N of QWs, we assume that the injected carriers are evenly distributed among the QWs. In each of the QWs we have a fraction $1/N$ of the total current density. Further, we assume that the optical mode overlap with all QWs is the same (and equal to the case of a single QW). The gain of N QWs can then be written as

$$g(N) = N g_0 \cdot \ln\left(\frac{J}{N J_0}\right). \tag{4.2}$$

Transparency of the waveguide is reached if $g = \alpha$, where α denotes the waveguide loss (e.g., due to scattering at fabrication imperfections or free carrier absorption in doped cladding layers). The waveguide transparency current density is thus given by

$$J_{\text{tr}}(N) = N J_0 \cdot e^{\alpha/(N g_0)}. \tag{4.3}$$

A formally identical equation can be written for the threshold current density J_{th} in a laser, if α includes the mirror losses. In most laser applications, a low J_{th} is a desirable property. We, therefore, optimize the number of QWs such that J_{th} (or J_{tr}) is minimized. From Eq. (4.3) it follows that the minimum is found at[1]

$$N = \frac{\alpha}{g_0}. \tag{4.4}$$

In some cases, the number N of QWs might be a given, and the question would be "how much waveguide loss can we tolerate?". The answer to that question can be given in a similar way, using Eq. (4.3). If α goes beyond $N g_0$, then the exponential term starts growing very fast. Therefore, the number $N g_0$ defines the order of magnitude that should not be exceeded by the waveguide loss.

We see from this discussion that the knowledge of the value g_0 is crucial if statements about the gain of a waveguide are to be made. In Sec. 4.2.5 the value will be determined experimentally, which will allow us to discuss the feasibility of active devices based on a W1 PhC

---

[1]A similar procedure to find the optimum number of QWs is developed in Ref. [191], however, without using the explicit gain relation given in Eq. (4.1) (which was not well-established at that time).

waveguide. But first, we have a closer look at the theory. In Sec. 4.2.3, we introduce a physical gain model and compare it to the empirical one. This not only gives us a means to justify the use of the empirical model, it also enables us to make a theoretical prediction of g_0.

4.2.3. Theoretical gain calculation for InGaAs quantum wells in InGaAsP

The fact that substrate-type PhC waveguides exhibit severe geometry-related losses raises the question of how much gain a given active structure can generate at maximum. So far, we have used the empirical relation $g = g_0 \cdot \ln(J/J_0)$. This relation suggests that there is no upper limit, if we just pump hard enough. From a physical point of view, however, we would expect that the gain saturates at high population inversions of the QW states. Even if we ignore thermal effects for the moment (they will be addressed later), we have to expect that the empirical model has its limitations. We will, therefore, use a physical model of QW gain and compare it to the empirical one. The physical model is reported in the literature [192], and its derivation is outlined in Appendix A.7. We will apply it to our case of InGaAs quantum wells embedded in an InGaAsP SCH and determine the theoretical maximum value of $g(J)$. Then, we will identify the range of J in which the empirical model can be regarded as a reasonable approximation of the physical model.

Throughout this chapter, *linear intensity gain* will be considered, defined through $\frac{\mathrm{d}I}{\mathrm{d}x} = gI$, where I is a field intensity of the optical mode and x is the propagation distance. The term "linear" refers to the fact that the gain figure g is independent of the field amplitude. The intensity gain differs from the amplitude gain by a factor of 2, since $\frac{\mathrm{d}A}{\mathrm{d}x} \sim \frac{\mathrm{d}}{\mathrm{d}x}(I^{\frac{1}{2}}) = \frac{1}{2}I^{-\frac{1}{2}}\frac{\mathrm{d}I}{\mathrm{d}x} = \frac{1}{2}gI^{\frac{1}{2}} \sim \frac{1}{2}gA$. The formulation in terms of amplitude is sometimes useful, because the gain/loss coefficient can be directly linked to the imaginary part of the complex propagation constant of an optical mode, $k = \beta + \mathrm{i}\alpha$, if α is the amplitude loss.

The band structure of the studied QWs is shown in Fig. 4.10. The conduction band (ΔE_c) and valence band (ΔE_v) discontinuities were found experimentally to be related as $\Delta E_v = 1.5\Delta E_c$ in InGaAsP/InP heterostructures [192, p. 429]. The numerical values of these and all other relevant parameters are listed in Table 4.1. The quantized ground states of the conduction (ε_e) and valence (ε_h) band were computed us-

ing the approximation of Makino [193], where $\varepsilon_{e,h} \ll \Delta E_{c,v}$ is assumed.
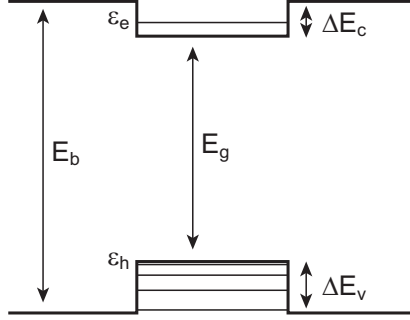
Figure 4.10. Band diagram of the InGaAsP/InGaAs QW of Fig. 4.9. Both materials are lattice-matched to InP. The As content of the $In_xGa_{1-x}As_yP_{1-y}$ barrier is $y = 0.47$.

Following the treatment of Agrawal and Dutta [192, Ch. 9], the modal gain of a single quantum well at the band edge (without broadening of the transition from a quantized energy level in the conduction band to that in the valence band) can be written as

$$g(\hbar\omega = E_0) = \Gamma \cdot \frac{1}{3} \frac{\pi}{a} \frac{\alpha_f}{\sqrt{\epsilon}} \frac{M}{1+M} \frac{E_g(E_g + \Delta_0)}{E_g + \frac{2}{3}\Delta_0} \frac{1}{E_0}$$
$$\times \left[1 - \exp\left(-\frac{n_{QW}^{2D}}{N_c^{2D}} \right) - \exp\left(-\frac{1}{M} \frac{p_{QW}^{2D}}{N_c^{2D}} \right) \right], \quad (4.5)$$

with the symbols as defined in Table 4.1. The derivation of Eq. (4.5) is outlined in Appendix A.7, and the relevant assumptions are explained. An important assumption is that only one subband of the valence band is occupied. From Eq. (4.5), an upper limit of the gain can be estimated by filling the electronic QW level up to the band edge of the barrier. This yields a maximum carrier density of

$$n_{QW}^{2D} = \int_{\varepsilon_e}^{\Delta E_c} \rho(E)\, dE = \frac{m_e}{\pi\hbar^2}(\Delta E_c - \varepsilon_e) = 1.51 \cdot 10^{12}\,\mathrm{cm}^{-2}. \quad (4.6)$$

In the integral, $\rho(E)$ is the 2D energy density of states of a QW. For our structure, the resulting maximum gain value is $11.49\,\mathrm{cm}^{-1}$ for

Table 4.1. Definitions and numerical values of the symbols used in Fig. 4.10 and Eq. (4.5).

Symbol	Physical quantity	Numerical value
$\hbar\omega$	photon energy	$0.8\,\mathrm{eV}$
a	QW width	$7.5\,\mathrm{nm}$
α_f	fine-structure constant	$1/137$
ϵ	effective permittivity[a]	11.2^e
m_0	electron mass	$9.109{\cdot}10^{-31}\,\mathrm{kg}$
M	$M = m_{hh}/m_e$	8.936
m_e	electron effective mass[b]	$0.047\,m_0{}^e$
m_{hh}	heavy hole effective mass[b]	$0.420\,m_0{}^e$
E_g	bandgap energy of the QW material	$0.747\,\mathrm{eV}^e$
E_b	bandgap energy of the barrier	$1.032\,\mathrm{eV}^e$
Δ_0	energy of the spin-orbit splitting[b]	$0.35\,\mathrm{eV}^e$
E_0	$E_g + \varepsilon_e + \varepsilon_h$	$0.795\,\mathrm{eV}$
ΔE_c	conduction band offset	$0.114\,\mathrm{eV}$
ΔE_v	valence band offset	$0.171\,\mathrm{eV}$
ε_e	quantized energy level of an electron in the conduction band[c]	$\sim 0.037\,\mathrm{eV}$
ε_h	quantized energy level of a hole in the valence band[c]	$\sim 0.011\,\mathrm{eV}$
$k_B T$	temperature of electron-hole plasma	$25.9\,\mathrm{meV}$
N_c^{2D}	$m_e k_B T/\pi\hbar^2$, 2D effective density of states for the conduction band in a QW	$6.51{\cdot}10^{11}\,\mathrm{cm}^{-2}$
$n_{\mathrm{QW}}^{\mathrm{2D}}$	2D carrier density of electrons[d]	variable
$p_{\mathrm{QW}}^{\mathrm{2D}}$	2D carrier density of holes[d]	variable
Γ	optical confinement factor of one QW	$1.838\,\%^f$

[a] we use the value of the optical confinement layer (InGaAsP).
[b] of the QW material (InGaAs).
[c] measured from the band edge.
[d] carriers confined to the QW.
[e] from Levinshtein *et al.* [194]
[f] calculated with the mode solver of Lumerical Solutions, Inc.

a single QW. Note that, even if we could let the carrier densities tend to infinity, the gain would saturate at $g_\infty := g(n_{\mathrm{QW}}^{2\mathrm{D}}, p_{\mathrm{QW}}^{2\mathrm{D}} \to \infty) = 49.4\,\mathrm{cm}^{-1}$.

Figure 4.11 shows the modal gain for the structure of Fig. 4.9 as a function of 2D carrier density in one, two, and three QWs. The curves are computed using Eq. (4.5) and the numerical values of Table 4.1 for the physical parameters. The assumption is made that electron and hole densities in the QW are the same, $n_{\mathrm{QW}}^{2\mathrm{D}} = p_{\mathrm{QW}}^{2\mathrm{D}}$. For narrow QWs, this is not strictly true, since holes are more strongly localized to the QW than electrons, due to the difference in effective mass between the two types of carriers. The 3D carrier density is obtained by division by the QW width.
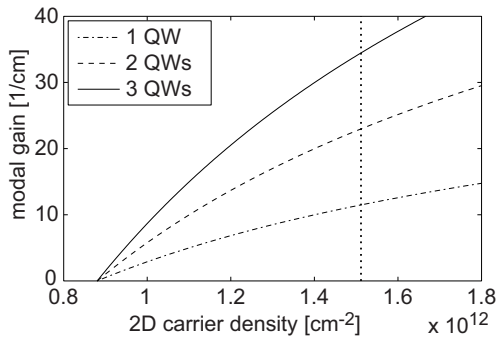
Figure 4.11. Modal gain of the SCH shown in Fig. 4.9 with one, two, and three QWs as a function of 2D carrier density. The curves are computed using Eq. (4.5) and the numerical values of Table 4.1 for the physical parameters. The dotted vertical line indicates the carrier density at which the QWs are filled up to the band edge of the barrier.

Equation 4.5 relates the optical gain to the densities of electrons and holes in the QWs. In order to obtain gain as a function of the pumped current density, the next task is to relate the carrier densities in the QWs to the applied current density. Apart from radiative recombination in the QWs, there are a number other paths that carriers can take when pumped through the structure. The following effects can be taken into account:

- Radiative recombination in the QW: In the small signal regime, the radiative current density is proportional to the spontaneous emission rate and, therefore, to the electron and hole densities. This is often represented in the simplified form $J_R \sim n^2$, where $n = n_{QW}^{2D} = p_{QW}^{2D}$ (charge neutrality).

- Auger recombination: The Auger recombination is non-radiative and often the dominant process [189]. The energy released by electron-hole recombination is transferred to another electron or hole, and hence no photons are emitted. Several types of Auger recombination processes exist [195, Chap. 2]. An electron in the conduction band can be excited to a higher state in the conduction band; or a hole can be transferred between the three hole sub-bands in the valence band. All these processes can be summarized in the simplified form $J_A \sim n^3$. Since Auger recombination is a strong effect, the correct estimation of the Auger coefficient(s) is crucial for a quantitatively meaningful estimation of the relation between current density and gain.

- Sidewall recombination: Dangling bonds at etched surfaces present defects which can introduce a continuum of states in the semiconductor bandgap. Therefore, non-radiative recombinations of electrons and holes can occur near the surface. For waveguides with lateral guiding by shallow ridges, this effect is generally neglected. However, for deeply etched trenches or PhCs, the process can become important. The current produced is proportional to the carrier density, $J_S \sim n$.

- Interface recombination: If there is roughness at the epitaxial interfaces between QWs and barriers, surface recombination can occur there [196]. This effect is considered negligible here.

- Current spreading: Lateral spreading of current occurs, when there is no lateral confinement for the carriers in the claddings. This effect is relevant for narrow active regions [197].

- Lateral diffusion leakage: Carriers confined to the QWs can diffuse laterally away from the active region. In a ridge waveguide, where the QWs are not etched through, the leakage current can be modeled by $J_D \sim \mathrm{d}n/\mathrm{d}y$, where y is the in-plane coordinate perpendicular to the propagation direction of the optical mode. In the case of PhC waveguides, the problem is more complex. On one hand, the lateral diffusion can be expected to be reduced due to the smaller volume available; on the other hand, an increased carrier concentration in the vicinity of PhC holes will increase

the surface recombination.

- Recombination in the guiding layer: Although the carriers are largely concentrated in the QW region, some of them can recombine in the guiding layer. This type of leakage is favored by high injection and is reduced for an increasing number of QWs [196]. It will not be taken into account here.

- Carrier leakage over the heterojunctions (cf. Ref. [192, Sec. 3.5.1]): Through drift and diffusion of electrons and holes, carrier leakage into the cladding layers occurs. For QWs embedded in a SCH, this effect can be neglected.

- Recombination at defects: Defects other than surface defects are considered negligible here. Their effect would also be proportional to the carrier density.

- Recombinations outside the QWs: Before the carriers are captured by the QW layers, they can recombine radiatively or non-radiatively in the InGaAsP guiding layer and the claddings. These effects are often neglected as a contribution to the total current below threshold. However, their role in the propagation of optical modes is generally considered important. Through free-carrier absorption in the conduction band of n-doped semiconductors and IVBA in p-doped semiconductors, the injected carriers are responsible for propagation losses. The more carriers are injected into the device, the higher the intrinsic losses get which have to be compensated by the gain material.

- Localization of electrons and holes in QWs: Due to the difference in effective mass between electrons and holes, the localization of the two types of carriers in a QW is different. Therefore, the simplification of $n = n_{\mathrm{QW}}^{\mathrm{2D}} = p_{\mathrm{QW}}^{\mathrm{2D}}$ does not strictly hold. Considering the holes to be entirely confined to the QW, the electron density in the continuous spectrum of the barrier, n_b^{2D}, can be used to write $p_{\mathrm{QW}}^{\mathrm{2D}} = n_{\mathrm{QW}}^{\mathrm{2D}} + n_b^{\mathrm{2D}}$. Taking into account $n_b^{\mathrm{2D}} \neq 0$ can lead to significantly increased computed threshold current densities as compared to the case of $n_b^{\mathrm{2D}} = 0$ [198].

- Carrier dynamics in MQWs: If more than one QW is incorporated into the guiding layer, then the carrier injection process becomes non-trivial. Carriers have to overcome one QW in order to reach the next one. They are captured and re-emitted [199] by the QW. The more QWs are present, the more non-uniform the resulting carrier distribution. This effect is especially important for dynamic injection. Electrons and holes might arrive at a par-

ticular QW at different times, and the gain condition might be fulfilled with a time lag between different QWs.

For our specific structure, considering all effects which govern the relation between the carrier density and the injection current is rather challenging. For a highly complex structure such as a PhC waveguide, one of the principal uncertainties is the modelling of surface recombinations, current spreading and lateral outdiffusion. For narrow structures, these leakage currents can become the dominant contributions to the total current. Dry-etched sidewalls and a complex waveguide geometry make it questionable if standard models and tabulated physical constants will lead to reliable estimates. For further discussions, we will use the following decomposition of the current density,

$$J_{\text{tot}} = J_S + J_R + J_A + J_E, \tag{4.7}$$

where J_E summarizes the contributions that have to do with lateral escape of carriers (spreading current in the claddings, lateral outdiffusion in the QWs). The other symbols are defined in the preceding list of current contributions. In deeply etched trench waveguides or in broad PhC waveguides we will consider J_E to be negligible, so that we can write

$$\begin{aligned} J_{\text{tot}} &= J_S + J_R + J_C \\ &= An + Bn^2 + Cn^3. \end{aligned} \tag{4.8}$$

B is the radiative recombination constant ($\sim 0.96 \cdot 10^{-10}\,\text{cm}^3\,\text{s}^{-1}$ for InGaAs [194, p. 81]) and C is a simplified Auger coefficient (e.g., $C = C_{\text{CHCC}} + C_{\text{CHHS}} = 1.52 \cdot 10^{-17}\,\text{cm}^4\,\text{s}^{-1}$ for InGaAs [200]). The linear term with proportionality constant A is related to surface recombinations. The value of A is unknown, and we expect that it will depend significantly on the waveguide width, especially if the width is comparable to or smaller than the top cladding thickness. For the moment, we consider the individual contributions to the total current density as unknown, but we assume that one of the contributions is dominant, such that we can write

$$J_{\text{tot}} \sim n^s, \tag{4.9}$$

where $s \in \{1, 2, 3\}$ is the exponent of the dominant term (e.g., $s = 3$, if Auger recombinations are dominant). This approach was followed, e.g.,

by Rosenzweig *et al.* [189]. Equation (4.1) now rewrites as

$$g(n) = sg_0 \cdot \ln\left(\frac{n}{n_0}\right), \tag{4.10}$$

with $n_0 \sim J_0^{1/s}$. We can fit this relation to the curves of Fig. 4.11 to obtain $sg_0 = 21.25 \, \text{cm}^{-1}$. Note that this result was obtained without having to estimate the proportionality constant, A, B, or C, of the dominant current (it cancels out in the derivation of Eq. (4.10)). We will see in Sec. 4.2.5 that this theoretical number is in good agreement with experimental values from lasers using waveguides formed of deeply etched trenches as well as by PhCs.

4.2.4. Justification for the empirical gain relation

We will now compare in more detail the empirical logarithmic relation of Eqs. (4.1) and (4.10) to the physical model of Eq. (4.5). To unravel the essential functional dependencies in Eq. (4.5) we reduce the equation to the form

$$g_1(\nu) = g_\infty \cdot \left[1 - \exp(-\nu) - \exp(-\frac{\nu}{M})\right], \tag{4.11}$$

where $\nu = n_{\text{QW}}^{2D}/N_c^{2D} = p_{\text{QW}}^{2D}/N_c^{2D}$, and g_∞ is the gain of Eq. (4.5) for $\nu \to \infty$. Similarly, Eq. (4.10) rewrites as

$$g_2(\nu) = sg_0 \cdot \ln\left(\frac{\nu}{\nu_0}\right), \tag{4.12}$$

with $\nu_0 = n_0/N_c^{2D} \sim J_0^{1/s}$. There is no apparent similarity between the two expressions of Eqs. (4.11) and (4.12). To assess their compatibility, we introduce the functions

$$F_{1,2}(\nu) \doteq \nu \cdot \frac{d}{d\nu} \, g_{1,2}(\nu). \tag{4.13}$$

This is a useful operation because, according to Eq. (4.12), $F_2(\nu)$ is a constant equal to sg_0. $F_1(\nu)$, on the other hand, is a more complex function. However, if $g_1(\nu)$ and $g_2(\nu)$ should be compatible over some range of ν, then $F_1(\nu)$ must approach a constant behavior over that same range. In Fig. 4.12, the function $F_1(\nu)$ is plotted against ν. Various values of M are used, in order to allow for a comparison between different laser materials. Our own material is InGaAs with approximately $M = 9$. Other values used in the plots include $M = 18$ (InAs),
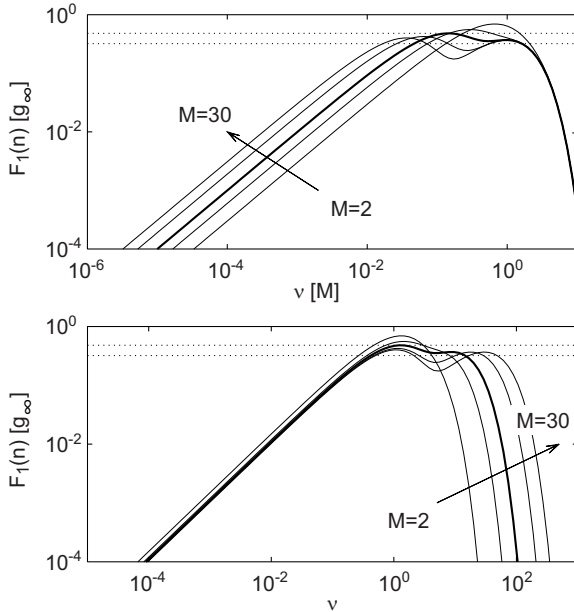
Figure 4.12. $F_1(\nu) = \nu \cdot \mathrm{d}g_2/\mathrm{d}\nu$ as a function of $\nu = n_{\mathrm{QW}}^{2\mathrm{D}}/N_c^{2\mathrm{D}} = p_{\mathrm{QW}}^{2\mathrm{D}}/N_c^{2\mathrm{D}}$ for several values of $M \in \{2, 5, 9, 18, 30\}$. The arrow indicates the direction of increasing values of M. The thick line corresponds to $M = 9$, which is approximately the value of our active material (cf. Table 4.1). In the upper panel, the ordinate is scaled in units of M, whereas in the lower panel the scaling is unitless. The "flat" region of the plots spans an approximate range from $\nu = 0.4$ (cf. lower panel) to $\nu = 2\,M$ (cf. upper panel). The two dotted horizontal lines delimit the range of $F_1(\nu) = (0.4 \pm 0.08)\,g_\infty$ for $M = 9$.

and $M = 30$ (InSb). In the upper panel, the ordinate is scaled in units of M for each curve. This pronounces the fact that all curves drop off at an upper limit of about $\nu = 2\,M$. In the lower panel, the scaling of the ordinate is unitless. Here, a lower drop-off boundary of roughly $\nu = 0.4$ can be identified. It is interesting that a constant behavior of the function $F_1(\nu)$ is more pronounced for $M = 9$ than for other values of M. This means that in materials other than InGaAs the empirical logarithmic gain model is expected to be somewhat less accurate. For $M = 9$, we have $F_1(\nu) = (0.4 \pm 0.08)\,g_\infty$ in a range of $n_{\mathrm{QW}}^{2\mathrm{D}} \in (2.7 \cdot 10^{11}, 9.5 \cdot 10^{12})\,\mathrm{cm}^{-2}$ (at room temperature). In terms

of 3D carrier density, this range is $n_{\text{QW}}^{3D} \in (3.6 \cdot 10^{17}, 1.3 \cdot 10^{19})\,\text{cm}^{-3}$ (division by the QW width). This confirms that the empirical model is reasonable over a rather large range of carrier densities.[2] In our particular QWs, the upper population limit is well within that range of validity.

It is interesting to observe that, with $F_1(\nu) = F_2(\nu)$ and $g_\infty = 49.4\,\text{cm}^{-1}$, we get

$$g_0 = \frac{19.8 \pm 4.0\,\text{cm}^{-1}}{s}. \tag{4.14}$$

This is consistent with our previous finding of $sg_0 = 21.25\,\text{cm}^{-1}$. An important implication of Eq. (4.14) is that g_0 will *increase*, if current leakage through surface recombination becomes dominant ($s \sim 1$). This might seem counter-intuitive if we think of g_0 as a measure of performance for a given device. Evidently, the second important performance measure is J_0. If any contribution to J_{tot} becomes dominant that does not help to populate the upper states in the QWs, then J_0 will get large.[3]

4.2.5. Experimental gain measurements

Two different types of waveguides were fabricated from the material shown in Fig. 4.9. They are depicted schematically in Fig. 4.13. Both waveguide types are dry-etched using ICP-RIE (cf. Sec. 3.3). Triangular-lattice PhC and trench waveguides were fabricated on the same chip. The InGaAsP core layer is completely etched through, i.e., there is a strong lateral mode confinement, which results in multi-moded waveguiding unless the waveguide is very narrow ($\lesssim 400\,\text{nm}$). Contacts of type C1 (cf. Fig. 4.1) are added after etching of the waveguides. Oscillation cavities of length $L = 2.1\,\text{mm}$ and two identical partially reflective facets were formed by cleaving the chips along a crystal plane. Spontaneous emission spectra are measured using Fourier transform infrared spectroscopy (FTIR, cf. Appendix A.8). Gain spectra are

---

[2]It should be noted that the 20%-range of $F_1(\nu) = (0.4 \pm 0.08)\,g_\infty$ is somewhat arbitrary. However, the upper drop-off of $F_1(\nu)$ is rather sharp, such that a different choice of the tolerance will lead to current density limits in the same order of magnitude. The lower drop-off is not quite as sharp, but the corresponding current densities are so small that the ensuing inaccuracies can be neglected.

[3]Note that, according to our definition of the transparency current, J_0 cannot be seen as a *material property* in the narrow sense of the word. In our notation, $g = g_0 \cdot \ln(J_{\text{tot}}/J_0)$, where J_{tot} includes recombinations occurring outside the active region. The more significant these contributions are, the higher is J_0. Therefore, we have to think of J_0 as a combined property of material and geometry.

computed using the Hakki-Paoli method (cf. Appendix A.5).
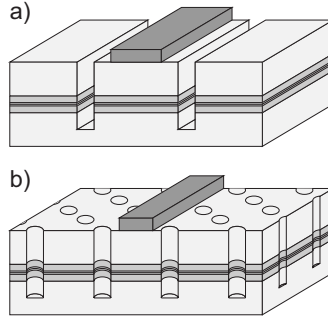
Figure 4.13. Schematical waveguide types fabricated from the material shown in Fig. 4.9. (a) Deeply etched trench waveguide; (b) PhC waveguide.

Figure 4.14 shows exemplary gain spectra measured from a $5\,\mu$m wide trench waveguide. The maximum in the modal gain curve shifts towards shorter wavelengths as the pumping current is increased. This can be attributed to band-filling, which dominates over the bandgap shrinkage effect [201]. In the left panel of Fig. 4.15, the maxima of the net modal gain is plotted over the injected current of the PhC waveguide of Fig. 4.14. The panel on the right shows a similar measurement for a trench waveguide of the same width. The logarithmic gain relation of Eq. (4.1) is fitted to the data points in order to extract the gain coefficients g_0.[4] We note that the current required to pump the PhC waveguide to transparency is substantially higher than that for the trench waveguide. This is due to a combination of higher waveguide losses and more severe carrier leakage in the PhC waveguide. In Sec. 4.3 we will make an attempt to distinguish between the two contributions.

The gain coefficient g_0 was measured for trench and PhC waveguides of various widths. Table 4.2 summarizes the results. There is no apparent dependence on waveguide type or width. An average value

---

[4]The current density J_0 cannot be extracted directly from the measurement, as long as the waveguide loss α is not accurately known. The relevant loss figure is that of the waveguide pumped to the transparency level. In lossy waveguides, the transparency current density can be substantial, and an additional loss due to free carrier absorption in the guiding layer of the SCH has to be taken into account.
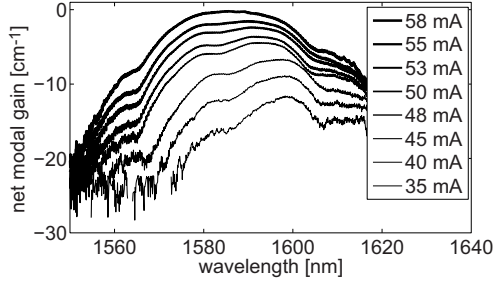
Figure 4.14. Gain spectra for various pumping currents from a $5\,\mu\text{m}$ wide trench waveguide.
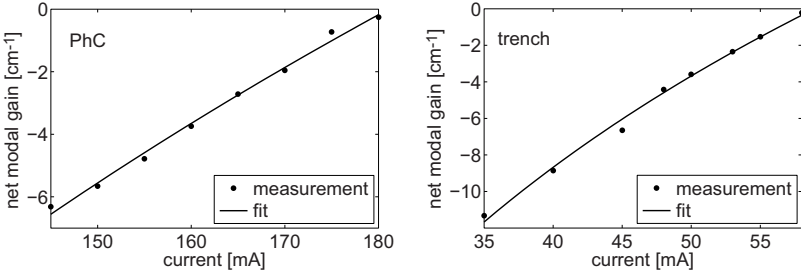
Figure 4.15. Net modal gain $(g(J)-\alpha)$ of two $5\,\mu\text{m}$ wide waveguides versus injected current density. Left: PhC waveguide; right: trench waveguide. Both devices are pumped below threshold, and the maximum net modal gain is extracted by the Hakki-Paoli method (cf. Appendix A.5).

of $g_0 = 8.4\,\text{cm}^{-1}$ is observed with a standard deviation of $1.8\,\text{cm}^{-1}$, if all measurements of the table are taken into account. We can now compare this value to the expected one of Eq. (4.14), and we get a good agreement for a value of $s = 2$. If our assumption of a single dominant contribution to the total current $J_{\text{tot}} = An + Bn^2 + Cn^3$ was correct, then we can conclude that radiative recombinations are the most important factor. However, we have to keep in mind that a combination of linear, quadratic and cubic contributions might result in a similar gain coefficient. Nevertheless, the fact that we see no clear dependence on waveguide width gives us some confidence, that surface recombination is not important for waveguide widths larger than $3\,\mu\text{m}$. Surface recombinations would enhance the linear contribution ($s = 1$). At smaller waveguide widths, we would expect this contribution to gain

Table 4.2. Gain coefficient g_0 of the logarithmic gain relation of Eq. (4.1), measured for trench and PhC waveguides of various widths.

	$3\,\mu$m width	$5\,\mu$m width	$20\,\mu$m width	$30\,\mu$m width
trench	$9.5\,\mathrm{cm}^{-1}$	$7.6\,\mathrm{cm}^{-1}$	$9.5\,\mathrm{cm}^{-1}$	$6.5\,\mathrm{cm}^{-1}$
PhC	$8.9\,\mathrm{cm}^{-1}$	$9.8\,\mathrm{cm}^{-1}$	$9.9\,\mathrm{cm}^{-1}$	$5.1\,\mathrm{cm}^{-1}$

importance and g_0 to increase.

Now that we have an estimate of g_0, we can go back to Eq. (4.4) and compute the optimum number N of QWs for a given value α of the waveguide loss

$$N = \frac{\alpha}{8.4\,\mathrm{cm}^{-1}}. \qquad (4.15)$$

State-of-the-art intensity loss values in a substrate-type W1 PhC waveguide are reported to be around $200\,\mathrm{cm}^{-1}$ [58]. Our own measurements reveal a loss figure at $\lambda = 1550\,\mathrm{nm}$ of $125\,\mathrm{cm}^{-1}$. This yields an optimum QW number of $N = 15$, which is a rather high number. At the time of fabrication of the active devices presented here, the complete fabrication process as used in Sec. 3.4 was not yet available. Typical loss figures at that time were around $300\,\mathrm{cm}^{-1}$ for W1 waveguides. For these high-loss waveguides, the optimum QW number is $N = 36$.

These results lead us to the next question to be answered: Is it a realistic goal to achieve gain (or lasing) in a single-moded (W1) substrate-type PhC waveguide? So far, we have addressed the balance between gain and loss, and we conclude that for the large propagation losses typically observed in W1 waveguides, the optimum number of QWs is rather high. But is it *too* high? The number of QWs is experimentally limited by the epitaxial capabilities to grow them uniformly (this problem is considered negligible here) and by the practical carrier/current densities that can be injected without causing thermal saturation. The current pumped through an active device increases the temperature of the active region through non-radiative recombinations. This broadens the gain spectrum and decreases the spectral gain maximum.[5] Thermal saturation occurs if this decrease in gain is so large that it cannot be compensated by a further increase of the pumping current. In order

---

[5]In addition, an elevated temperature has a negative influence on the Auger recombination coefficient [190, p. 178], [198, 202], on carrier leakage [190, p. 178], [203], and on IVBA [204, 205].

to make a well-founded theoretical feasibility statement for the realization of gain in an electrically pumped W1 waveguide, the thermal behavior would have to be studied in detail. In other words, a 3D simulation would have to be performed that combines electronic and thermal dynamics in a self-consistent manner. Suitable tools for this task are available [206, 207]. The simulations would have to be calibrated with experimental data for physical quantities such as the surface recombination velocity (as a function of waveguide width) and diffusion constants of our specific materials. A high confidence in the input parameters for the simulation is crucial, because a feasibility statement is only of value in combination with a statement about its trustworthiness. A relatively small error in the computation of the achievable gain can lead to completely different conclusions about the feasibility.

A rigorous theoretical/numerical treatment of the electro-thermal limitations in our devices is beyond the scope of the present thesis. Instead, we will proceed to analyze the feasibility of gain in a W1 PhC waveguide from a purely experimental point of view. In Sec. 4.3, we present threshold measurements of laser devices formed by deeply etched trench and PhC waveguides. The measured data will be used to extrapolate estimates for threshold levels of W1 PhC waveguides. These estimates will be benchmarked by a critical value of $10 \, \mathrm{kA/cm^2}$, that should not be exceeded.

The critical current density can be derived as follows: From the literature [208] or from a simple 1D heat conduction model [116] we see that the temperature increase ΔT of the active region is on the order of $10\text{-}20\,\mathrm{K}$ per $1\,\mathrm{kA/cm^2}$ of cw pumped current density. To define an upper bound for the current density, we can use the often-cited exponential dependence of the pumping threshold on temperature [190, p. 58], $J_{\mathrm{th}} \sim \mathrm{e}^{T/T_0}$, where T_0 is a characteristic temperature of the material system. For devices based on an InP substrate, T_0 is in a range of $50\text{-}100\,\mathrm{K}$ [190, p. 178] [209], whereas it is significantly higher for GaAs-based materials. In order not increase the pumping threshold by orders of magnitude, ΔT should not exceed a value of $\sim 150\,\mathrm{K}$. Hence, critical injection levels are reached at $\sim 10\,\mathrm{kA/cm^2}$. This value is in agreement with experimental values for cw breakdown reported in the literature (e.g., in [203]), which confirms its suitability as a benchmark. Under pulsed operation, the generation of heat is largely suppressed, and the limitations are of different nature. Since we are interested in

devices used for PICs (such as amplifiers or cw sources that can be used for signal modulation), this topic will not be addressed here. An instructive treatment can be found in Ref. [203].

4.3. Photonic crystal lasers

This section deals with PhC waveguide lasers of various widths. For narrow waveguides, both optical and electrical properties are strongly dependent on the waveguide width. Therefore, the pumping threshold of PhC lasers is a complicated function of waveguide width. To untangle the separate influences of optical loss and different channels of current leakage, the PhC lasers are compared to laser devices formed by deeply etched trench waveguides.

In terms of carrier dynamics, the main difference between the two types of devices is that carriers can escape laterally out of the PhC waveguide (carrier spreading in the cladding, lateral outdiffusion in the QWs), whereas the trench waveguide is terminated laterally by interfaces to air, and the dominant leakage mechanism is surface recombination at the dry-etched sidewalls. Using the decomposition $J_{\text{tot}} = J_S + J_R + J_A + J_E$, as in Eq. (4.7), we can set $J_E = 0$ for trench waveguides, but not for PhC waveguides. Therefore, to estimate the importance of the additional leakage channels in PhC devices, the comparison to trench waveguide lasers is instructive. The main difficulty is the fact that our PhC waveguides have significantly higher propagation losses than trench waveguides of equivalent width. This complicates a direct comparison. Nevertheless, some information can be extracted from lasing threshold measurements by using the following approach: First, an empirical model is derived to relate the sum of $J_S + J_R + J_A$ at threshold to the width of a trench waveguide laser. The threshold data of the trench waveguide lasers and experimental propagation loss values can be used to determine the empirical parameters of the model. Then, the resulting model can be used to generate an approximate prediction of the sum $J_S + J_R + J_A$ for PhC laser thresholds (using experimental propagation loss values of PhC waveguides). If the thresholds of the PhC lasers are accurately predicted in this way, it means that the additional leakage channels have a negligible impact. If the predictions are far off the measured thresholds, then we can conclude that the lateral leakage is significant. In this sense, we can view

the model derived from the trench waveguides as a best-case estimate for the pumping threshold of PhC waveguide lasers.

4.3.1. Experimental demonstration of photonic crystal lasers

Figure 4.16 shows the cw lasing thresholds of trench and PhC waveguides of various widths (contacts of type C1). Both waveguide types were fabricated on the same chip to allow for a direct comparison. The active material is that of Fig. 4.9 with 3 QWs. All devices are pumped at room temperature and cw, exclusively. The narrowest PhC laser for which lasing was achieved was the W4 waveguide, which is a bit more than $1.5\,\mu$m wide.[6] To our knowledge, no narrower electrically pumped substrate-type PhC lasers have been reported in the literature. For the trench waveguides, we achieved lasing down to a W1-equivalent width.
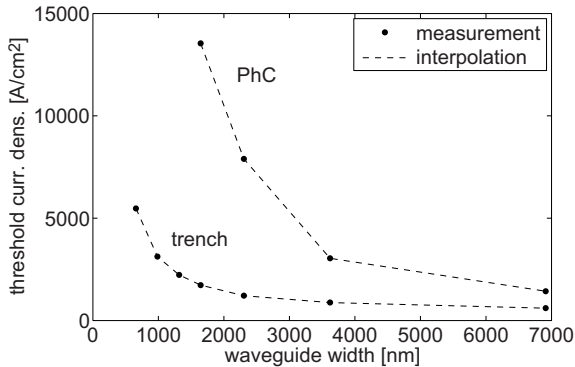
Figure 4.16. Lasing thresholds for trench and PhC waveguides of various widths.

For both types of waveguides the threshold increases dramatically with decreasing width. This is due, on one hand, to the increasing waveguide loss and, on the other hand, to more severe carrier leakage in narrow waveguides. However, it is not immediately clear which factor

---

[6]In the Wx-notation, x denotes the number of omitted rows of holes in a PhC. The width is determined as $w(x) = (x + 1) \cdot \frac{\sqrt{3}}{2}\Gamma$, where Γ is the lattice constant. Here, the width of a PhC waveguide is measured between the centers of the first row of holes. An alternative definition, which is often applied, measures the width between the innermost hole edges. In that case one hole diameter would have to be subtracted.

is dominant. In addition, for the PhC waveguides it is not clear what kind of leakage would be dominant, J_S or J_E. We will therefore introduce an empirical model for the threshold current density $J_{\text{th}}(w)$ as a function of waveguide width, taking into account the width-dependence of the propagation losses $\alpha(w)$. We will use the data from the trench waveguide lasers (where $J_E = 0$) to calibrate the model and then use the model to derive a best-case estimate of the threshold current density of PhC waveguides. Comparing these results to experimental data from PhC lasers, we will conclude that J_E is not negligible in the case of PhC waveguides.

4.3.2. Carrier leakage in trench waveguide lasers

In Sec. 4.2.5, the logarithmic gain coefficient g_0 of our active material was determined experimentally for waveguide of widths $\geq 3\,\mu\text{m}$. Carrier leakage was concluded to play a minor role in the pumping process. We now turn to the narrower waveguides of Fig. 4.16, and we model the threshold current density of a laser as the sum

$$J_{\text{th}}(w) = N\, J_0 \cdot \mathrm{e}^{\alpha(w)/(Ng_0)} + J_S(w), \tag{4.16}$$

where $\alpha(w)$ is the sum of waveguide losses and mirror losses. The first term on the righthand side is the current density required to reach threshold in a broad waveguide, where J_S can be neglected. It corresponds to the widely used model of Eq. (4.3), and it includes the contributions J_R and J_A. The second term is the width-dependent leakage current density due to surface recombinations. We can relate the two terms to each other if we use the power law of Eq. (4.9) for the first term. According to Sec. 4.2.5, we can assume it to be $\sim n^s$ with $s = 2$ (possibly $s = 3$, if Auger recombination becomes the dominant process). On the other hand, surface recombination is linear, $J_S \sim n$ [195, Sec. 2.3]. Combining the dependencies on n of the two terms, we obtain the relation $J_S \sim [N\, J_0 \cdot \mathrm{e}^{\alpha/(Ng_0)}]^{1/s}$. It remains to include the dependence on waveguide width. We use an inverse power law, because it displays the correct limiting behavior:

$$J_S(w) = D\left(\frac{d}{w}\right)^{\eta}[N\, J_0 \cdot \mathrm{e}^{\alpha(w)/(Ng_0)}]^{\frac{1}{s}}. \tag{4.17}$$
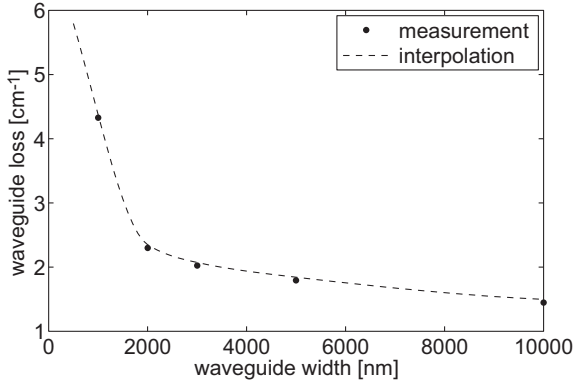
Figure 4.17. Propagation losses at $\lambda = 1550\,\mathrm{nm}$ in passive trench waveguides of various widths, reproduced from Ref. [76] with permission of Dr. Patric Strasser. The dashed line is an interpolation of the measured data.

D is a proportionality constant carrying units of $(\mathrm{A/cm^2})^{1-1/s}$, d is a length constant, and η is the exponent of the power law.[7] We will use this relation as our empirical model and determine η by fitting Eq. (4.16) to the experimental data of Fig. 4.16. The main challenge is the fact that the waveguide loss $\alpha(w)$ is a function of waveguide width. Measurements are available for passive waveguides [76], and they are reproduced in Fig. 4.17. In active devices with doped cladding layers, an absorption loss has to be added, which can exceed $10\,\mathrm{cm^{-1}}$ (e.g., in Ref. [188] a value of $15\,\mathrm{cm^{-1}}$ is specified). Furthermore, a mirror loss of about $6\,\mathrm{cm^{-1}}$ must be taken into account. However, if we think of these additional losses as independent of waveguide width, then they have no impact on the fitting procedure. We can clearly see this if we rewrite Eq. (4.16) as

$$J_{\mathrm{th}}(w) = N\,J_c \cdot \mathrm{e}^{\alpha_{\mathrm{pas}}(w)/(Ng_0)} + \left(\frac{d'}{w}\right)^{\eta} [N\,J_c \cdot \mathrm{e}^{\alpha_{\mathrm{pas}}(w)/(Ng_0)}]^{\frac{1}{s}}, \quad (4.18)$$

where $J_c = J_0 \cdot \mathrm{e}^{\alpha_c/(Ng_0)}$, $d' = d \cdot D^{1/\eta}$; and the loss figure $\alpha(w) = \alpha_{\mathrm{pas}}(w) + \alpha_c$ is the sum of the loss in a passive waveguide and a width-independent loss value, which is a combination of mirror loss and free

---

[7]At first glance, it might seem odd that the leakage current density should be dependent on the waveguide loss. Here, we are talking about the leakage *at threshold*. For increasing loss, the threshold goes up and with it the leakage current density.

carrier absorption. Using the data of Fig. 4.17 for $\alpha_{\mathrm{pas}}(w)$, we see that the term $\mathrm{e}^{\alpha_{\mathrm{pas}}(w)/(Ng_0)}$ varies by no more than $\sim 20\,\%$ between wide and narrow trench waveguides. Therefore, the width-dependence of the losses is not expected to play a dominant role in the sharp increase of J_{th} in Fig. 4.16. This is fundamentally different for PhC waveguides, where $\alpha_{\mathrm{pas}}(w)$ can go well beyond $100\,\mathrm{cm}^{-1}$ for narrow waveguides.

Figure 4.18 shows a numerical fit (solid line, left ordinate) of Eq. (4.18) to the experimental threshold values of the trench waveguides of Fig. 4.16. The width-dependence of the waveguide loss of Fig. 4.17 was used. The free parameters of the fit were J_c, η, and d'. Fixed values of $g_0 = 8.4\,\mathrm{cm}^{-1}$, $N = 3$, and $s = 2$ were used. The best fit was found for $\eta = 1.49$, and $d' = 23.6\,\mu\mathrm{m}\,(\mathrm{A/cm}^2)^{1/2\eta}$. If we assume a value of $\alpha_c = 20\,\mathrm{cm}^{-1}$, then we obtain $J_c = 69.2\,\mathrm{A/cm}^2$, which results in $J_0 = 31.3\,\mathrm{A/cm}^2$. Alternatively, for $\alpha_c = 15\,\mathrm{cm}^{-1}$, a value of $J_0 = 46.5\,\mathrm{A/cm}^2$ is obtained. Although the empirical model of Eq. (4.17) is only partially motivated by physical reasoning, we still find an excellent agreement with Ref. [197], where a total transparency current density of $63\,\mathrm{A/cm}^2$ is reported for an InGaAsP/InP laser with two QWs emitting at $\lambda = 1580\,\mathrm{nm}$ (i.e., $J_0 = 31.5\,\mathrm{A/cm}^2$).
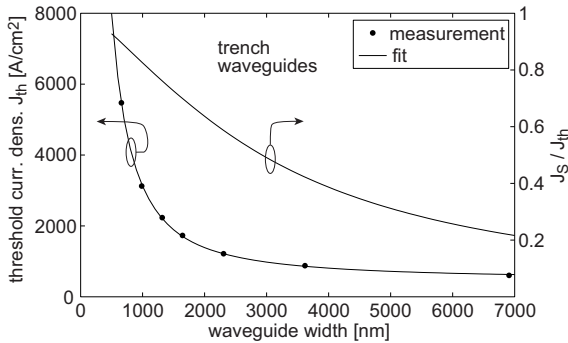
Figure 4.18. Lasing thresholds for trench waveguides as in Fig. 4.16 (bullets). The solid line plotted to the lefthand ordinate represents the empirical model of Eq. (4.16) fitted to the experimental data. The modeled ratio J_S/J_{th} is plotted to the righthand ordinate.

The empirical model reproduces our experimental data very accurately in Fig. 4.18. This is promising for a comparison between trench

and PhC waveguides. The contributions of surface recombinations to the total current density is plotted to the righthand ordinate of Fig. 4.18. For a W1-equivalent trench waveguide width, the model indicates that 90 % of the carriers are lost through surface recombinations. If the leakage mechanisms are more or less the same in both types of waveguides, then we would expect a reasonably good fit to the threshold data of the PhC waveguides, as well. If additional contributions to the total current (J_E) are significant, then we expect that the empirical model for the trench lasers underestimates the threshold current density of PhC lasers.

4.3.3. Carrier leakage in PhC waveguide lasers

We now use the empirical model obtained for trench waveguides, apply it to the PhC waveguides, and compare the results to the measured threshold current densities of Fig. 4.16. Unfortunately, the available data of $\alpha_{pas}(w)$ are limited for PhC waveguides. We have measurements for a passive W3 PhC waveguide ($\alpha_{pas} \simeq 30\,\mathrm{cm}^{-1}$); and we have measurements for W1 PhC waveguides. At the time of fabrication of these active devices, the full process used for the loss measurements presented in Sec. 3.4 was not yet available and the losses were on the order of $\alpha_{pas} \simeq 300\,\mathrm{cm}^{-1}$. Nevertheless we will use a value of $\alpha_{pas} \simeq 125\,\mathrm{cm}^{-1}$ (which corresponds to the most recent results at $\lambda = 1550\,\mathrm{nm}$) for the ensuing considerations. In Fig. 4.19 the predicted threshold current densities for these two waveguide widths are plotted together with the experimental data from Fig. 4.16 for the wider waveguides. We can clearly see from Fig. 4.19 that a lot of carriers are lost in the PhC waveguide that cannot be accounted for by surface recombinations. The threshold of the W3 PhC waveguide is estimated to be $1750\,\mathrm{A/cm}^2$, which is almost an order of magnitude lower than the threshold measured for the W4 waveguide. Even the threshold measured for a W7 waveguide is higher. In other words, the current contribution of carriers escaping from a W3 PhC waveguide (J_E) is about 10 times larger than the sum of all other contributions. In a W1 waveguide, we expect the carrier loss to be even more severe.

The predicted threshold value for the W1 PhC waveguide in Fig. 4.19 is $67\,\mathrm{kA/cm}^2$. This can be used as a lower estimation for $N = 3$. For an optimized material with $N = 15$ (cf. Sec. 4.2.5), a value of $\sim 3.6\,\mathrm{kA/cm}^2$ is obtained. This would be a realistic value to be ap-
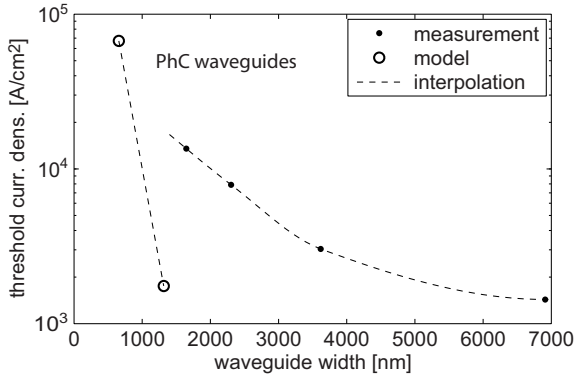
Figure 4.19. Lasing thresholds for PhC waveguides as in Fig. 4.16 (filled circles). The dashed line is an interpolation of the measured data. The open circles represent the predicted thresholds for W1 and W3 waveguides on the basis of the empirical model of Eq. (4.16).

plied experimentally; but based on the above findings, we believe that it is an underestimation by at least an order of magnitude. Furthermore, we should keep in mind that some best-case assumptions have been made, which cannot be fulfilled anymore if the number of QWs is as large as $N = 15$:

- The overlap of the optical mode with the QWs is assumed to be the same for all QWs. This assumption is no longer reasonable when the number of QWs is high, since not all of the QWs can be located close to the intensity maximum of the optical mode.
- All QWs are assumed to be of exactly the same thickness and, therefore, to have the same emission spectrum. If this is not the case (e.g., due to fluctuations in the epitaxy), the spectrum will be broadened and the gain maximum will be lowered.

In conclusion, for a W1 PhC waveguide, we expect a threshold current density well above the critical value of $10\,\text{kA/cm}^2$, even if an optimized number of QWs is used. It seems questionable if this waveguide, fabricated with state-of-the-art technology, can be brought to lasing. Cooling to cryogenic temperatures might help to increase the gain coefficient g_0. However, our research is motivated by the vision of PICs as an alternative to electronic circuits in real-world applications. In this

context, cryogenic cooling is not an option (for reasons of practicability). We cannot fully rule out the feasibility of an electrically driven W1 PhC laser under extreme conditions, but we are rather confident that a cw laser at room temperature will not be possible.

To achieve gain in a W1 PhC waveguide, measures have to be taken either to reduce the propagation losses or to increase the lateral carrier confinement to the small interaction volume in a narrow PhC waveguide. If the waveguide design is left unchanged, we have seen in Sec. 3.4 that no substantial progess is to be expected by merely improving the etching process. For a reduction in carrier leakage, the narrow channel between top contact and the active region would have to be provided with a lateral boundary. Variations of doping concentrations in the cladding layer could be used to create a local maximum in conductivity (e.g., by ion implantation or a regrowth process). However, the required spatial resolution would be a technological challenge.

In Sec. 4.4.1 we propose a new waveguide design which is beneficial in terms of both propagation loss and carrier leakage. Using wet etching, the top and bottom claddings are etched away in the PhC region, while a narrow post remains above and below the waveguide core. This design reduces the losses by pushing the background above the PhC waveguide mode. The lateral escape of carriers in the cladding region is inhibited by the semiconductor interface to air. Since the surface recombination on wet-etched sidewalls is typically lower than that of dry-etched sidewalls, an additional improvement in pumping efficiency might be expected.

4.4. Outlook

4.4.1. A new waveguide design

We have seen in Sec. 2.3 that PhC waveguides, operated above the so-called background line, are expected to exhibit severe inherent propagation losses. The standard substrate-type devices presented in Sec. 4.3 and in the literature [54, 56, 210] are, indeed, operated above the background line. To correct this, we have to either shift the operation range (frequency) or modify the properties of the background (and hence the location of the background line). Here we present a waveguide design
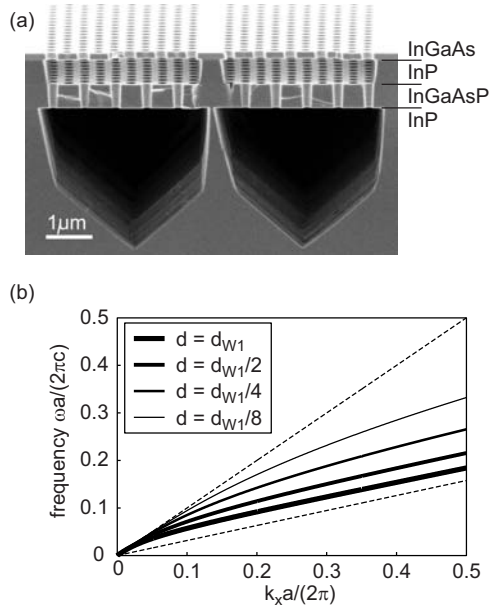
Figure 4.20. (a) Prototype W1 PhC waveguide for electrically pumped active devices; (b) Dispersion curves of the fundamental TE modes of four symmetric dielectric slab waveguides of different width d. The widths are indicated in units of $d_{W1} = 458\,\mathrm{nm}$, which corresponds to the width of a W1 waveguide with $\Gamma = 435\,\mathrm{nm}$ and $r/\Gamma = 0.34$. The waveguides are composed of InP and air and serve as an approximation of the background system of the waveguide shown in (a). The dashed lines are the light lines of air (upper line) and InP (lower line).

based on the latter approach. We first proposed this design in Ref. [72].

The proposed device geometry is depicted in Fig. 4.20 (a). The figure shows an SEM image of an InP/InGaAsP/InP layer structure with an additional InGaAs cap layer on top. The quaternary layer could host one or several quantum wells providing for optical gain (not the case here). The sample was etched in hydrochloric acid to remove the InP claddings; only a narrow post remains on both sides of the guiding layer. The background of this system can be thought of as a narrow vertical slab waveguide of InP surrounded by air. The dispersion curves of the fundamental TE modes of this idealized background are shown in

Fig. 4.20 (b) for various widths of the posts. For decreasing post width, the background line approaches the light line of air, which gives a substantial amount of theoretical design freedom for the PhC waveguide. A loss-free device is theoretically possible; and in terms of fabrication, the proof of principle is given in Fig. 4.20 (a). Furthermore, the lateral escape of carriers is restricted to the core layer. However, the narrower the posts are, the less efficient the vertical current injection will be (increased surface recombination in the claddings, increased resistance, less efficient heat dissipation). For an active device, a trade-off between optical and electrical performance will have to be made, taking into account the available fabrication capabilities. An attempt in this direction is presented in Ref. [116]. The proposed waveguide promises propagation losses below $20\,\mathrm{dB/cm}$ in a bandwidth of $\Delta\lambda = 23.3\,\mathrm{nm}$ around a center frequency of $\lambda = 1550\,\mathrm{nm}$, and the feasibility of an electrically pumped device based on the new design is concluded to be real.

So far, the wet etching process that removes the PhC pattern in the cladding layers is not controlled very well. However, we believe that there is room for improvement (e.g., by additions of citric acid to the etching chemistry [173]). It should be noted that our proposed device bears some similarity to the electrically pumped point-defect PhC lasers reported in Refs. [49, 211]. These devices were successfully fabricated, although they use electrically conducting posts that have to be controllably etched from all sides, whereas our structure requires the control of etching only along one crystal orientation. From this point of view, our geometry is not quite as challenging. However, there is a top cladding in our structure of Fig. 4.20 (a), which has to be controlled as well. It is, therefore, not immediately clear which structure is more difficult to fabricate reliably. In Sec. 3.5, we have outlined alternative approaches to design a low-loss substrate-type PhC waveguide: The Fourier component above the background line can be suppressed by shifting the PhC on one side of the waveguide by half a period along the waveguide axis [117]; or the PhC holes can be enlarged (to modify the background line) instead of removed completely by a more gentle wet etching process than the one presented here.

4.4.2. Active/passive integration

From the experimental data of Sec. 4.3 we concluded that the studied substrate-type devices cannot be considered a promising technol-

ogy, on the basis of which we can conceive an integration platform for PICs. Therefore, we take a step back and briefly consider the case of an integration platform, in which PhCs are employed only for specific functionalities which cannot be obtained otherwise. We look at the specific device example of a relatively broad trench waveguide laser, which couples into a passive W1 PhC waveguide (which might support slow light propagation in a future application). Since the membrane-type PhC technology reported in the literature has reached a rather high level of sophistication, it would be of particular interest to demonstrate an electrically pumped source that emits directly into a monolithically integrated membrane-type PhC waveguide. The integration of a laser with a PhC waveguide has been demonstrated in a purely membrane-based geometry [212], but the pumping of the active material was done optically. To our knowledge, electrically pumped devices have not been reported so far. The following results are on the level of a feasibility study and serve as an outlook on how PhC devices might be employed in PICs in the future.

The schematics of the presented devices are shown in Fig. 4.21. The upper panel represents a top view of the trench waveguide which is

output PhC waveguide   PhC mirror
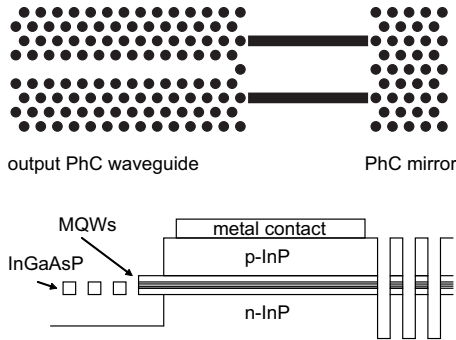
Figure 4.21. Schematics of laser devices that couple light directly into passive PhC waveguides. The device is shown in cross-section (upper panel) as well as from top (lower panel). The cavity is formed by a 2 mm long trench waveguide (not drawn to scale) of a width equivalent to that of a W3 PhC waveguide. It is terminated by a single hole on the output side and by a PhC block on the opposite side; the output is a membrane-type W1 PhC waveguide.

terminated by PhC mirrors on both sides. The length of the trench waveguide (2 mm) is not drawn to scale; the width is equivalent to that of a W3 PhC waveguide. The lower panel depicts the cross-section of the device. The output section can be a membrane-type (as shown in the figure) or a substrate-type PhC waveguide (not shown here). The output waveguides are $200\,\mu$m long and are terminated by a cleaved facet. For the membrane-type output, an additional lithography and wet-etching step is required in the fabrication process. Fig. 4.22 shows what the freed membranes ideally look like. The full fabrication process and some of the challenges involved are detailed in Appendix B.3.
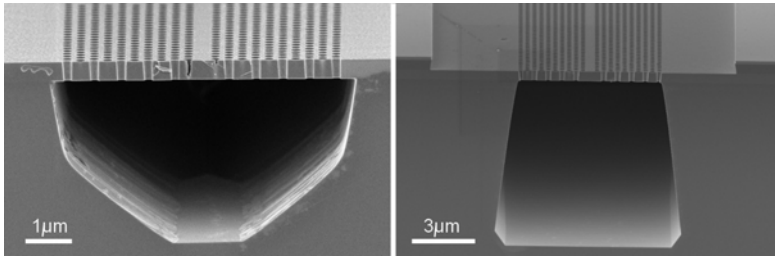
Figure 4.22. InGaAsP membrane-type PhC waveguides after HCl etching; the waveguides are oriented along two different crystal directions. Left: waveguide along [01$\bar{1}$]; right: waveguide along [011]. Due to different etching speeds of the crystallographic planes [213, 214], the results are different for the two waveguide orientations.

In Fig. 4.23, we present the laser characteristics of two devices, operatated in cw mode at room temperature. The output waveguide is substrate-type for the plot on the left hand side and membrane-type for the plot on the right (both $200\,\mu$m long). The emitted light is collimated by a microscope objective (magnification $\times 40$, numerical aperture 0.65) and measured in an InGaAs detector. The onset of lasing is clearly visible in both cases. The measured power is rather weak for both types of output waveguides. This can be due to a poor coupling of the laser mode to the output waveguide. In addition, for the membrane-type output, we observed wedge-shaped residuals below the waveguide, whose influence on the propagation characteristics we cannot estimate at this point. To improve the performance of the devices, the cavity modes have to be analyzed in detail. The design of both the cavity waveguide and the mirrors must be optimized to maximize the
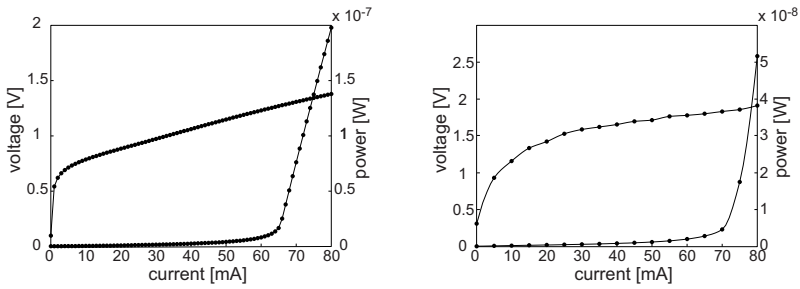
Figure 4.23. Characteristic P-I-V curves of two laser devices according to the schematics of Fig. 4.21. The devices are operated in cw mode at room temperature. Left: substrate-type output waveguide; right: membrane-type output waveguide.

coupling efficiency to the output waveguide. For the membrane-type output, the final wet-etching step needs further investigation and its reproducibility must be ensured.

5

Conclusions

To conclude this thesis, we go back to the questions that we had asked in Chap. 1:

- Is it possible from a theoretical point of view to design a low-loss W1 PhC waveguide that allows for vertical current injection?
- How much room for improvement is there in terms of etching of deep holes in InP-based structures?
- How do we implement electrical pumping of active PhC waveguides, without disturbing the PhC dispersion properties?

Up to recently, the first question would have been answered by a clear "no", based on the light line argument. According to conventional wisdom, the light line of the substrate is seen as the separatrix in the dispersion diagram of a substrate-type PhC waveguide that splits it into a region of guided modes (low loss) and non-guided modes (high loss). We could show (Sec. 2.3, Ref. [72]) that this statement is not quite correct, and that the light line has to be replaced by a different concept, that we call the "background line". The new concept becomes relevant in cases where the lateral mode confinement is much stronger

than the vertical confinement. In particular, it becomes relevant for narrow waveguides formed by deeply etched trenches or PhCs. Depending on the exact geometry of the studied waveguide, the background line can lie significantly above the substrate light line. In other words, there can be modes which are located *above the light line* but *below the background line*. These modes have low propagation losses. Hence, the low-loss regions in the dispersion diagram are larger than it would be expected according to the light line argument. Therefore, the clear "no" to our first question has to be revised. Instead, our answer would be an optimistic "yes". The main obstacle is the fact that the photonic bandgap is typically located significantly above the substrate light line. Therefore, to achieve low propagation losses, the background line has to be pushed quite far away from the light line. This imposes rather stringent design requirements. In the outlook of Chap. 4 we propose a specific design of a low-loss W1 PhC waveguide. This waveguide is analyzed in detail in Ref. [116]. Propagation losses below $20\,\mathrm{dB/cm}$ are predicted in a bandwidth of $\Delta\lambda = 23.3\,\mathrm{nm}$ around a center frequency of $\lambda = 1550\,\mathrm{nm}$, and electrically pumped gain is found to be realistic.

The second question is answered in Chap. 3. After demonstrating a robust fabrication process for a high-quality hardmask, the limitations of InP etching were assessed in a statistically systematic experiment. Using ICP-RIE etching in Cl_2-based chemistries, we can claim with some confidence that a substantial improvement of our PhC holes is hardly possible. Furthermore, the propagation losses that we measured in W1 substrate-type PhC waveguides are in very good agreement with 3D FDTD simulation results using idealized hole shapes. A significant reduction in propagation losses is, therefore, not to be expected, even if the fabrication process is further improved. Our experimental loss figures are around $335\,\mathrm{dB/cm}$ at a wavelength of $\lambda = 1490\,\mathrm{nm}$ and around $540\,\mathrm{dB/cm}$ at $\lambda = 1550\,\mathrm{nm}$. Although these are still rather high numbers, they constitute an improvement by a factor of $1.5\text{-}1.8$ with respect to literature values of comparable waveguides.

The third question is addressed in Chap. 4. A fabrication process of air-bridge contacts was demonstrated. However, it turned out that we overestimated the urgency of the question. So far, most of the unique properties of PhCs (such as slow light) have only been experimentally demonstrated in membrane-type waveguides. As long as the dispersion properties cannot be exploited in substrate-type waveguides, the issue

of disturbances from the isolating layer or the contact itself is of secondary importance.

This leads us to the ultimate question whether substrate-type PhC waveguides are promising candidates to be used as basic building blocks in a generic integration platform for PICs. We have seen that the answer stands and falls with the propagation losses of the waveguides and with the carrier injection efficiency. For state-of-the-art waveguide structures, the potential for PICs is clearly very low. In terms of propagation losses, we believe that the etching technology is not the main limiting factor. Simply improving the etching quality without modifying the waveguiding structure will not dramatically reduce the propagation losses. Our experimental results on PhC lasers suggest that electrically pumped optical gain will only be possible even with our "low-loss" waveguide. Therefore, a different waveguide structure will be needed, and the next step would be to exhaust the design flexibility for low-loss waveguides using the concept of the background line. The specific design that we propose not only promises low propagation losses, but it also seems attractive in terms of carrier injection efficiency.

A

Formal Additions and Derivations

A.1. Average energy density of a Bloch mode

For the discussion of the energy velocity in Sec. 2.2.3, the following identity was used:

$$\lim_{L \to \infty} \langle \mathcal{U} \rangle_L = \langle \langle \mathcal{U} \rangle_T \rangle_\Gamma, \tag{A.1}$$

where $\mathcal{U}$ is the energy density of a Bloch mode in a 1D-periodic medium. The brackets $\langle \cdot \rangle$ denote an average over an interval of time or space (as indicated by the index). $T = 2\pi/\omega$ is the time period of the carrier field oscillations, while ω is the angular frequency of the Bloch mode. Γ denotes the lattice constant of the periodic medium. Here, we provide the proof of the identity (A.1).

The field of a Bloch mode is composed of two periodic functions with different periods, e.g., $E \sim u(x) \cos(kx - \omega t)$ with $u(x + \Gamma) = u(x)$. It is a harmonic oscillation with a superimposed modulation $u(x)$ that is induced by the periodicity of the medium. We will further use the

symbol $\lambda = 2\pi/k$. To prove Eq. (A.1), we write the energy density as $\mathcal{U} = u^2(x) \cdot f^2(kx - \omega t)$. The periodic function $f(\varphi + 2\pi) = f(\varphi)$ contains the field oscillation and some proportionality constant. For the proof, we only need the property that f and u are periodic. The right-hand side of Eq. (A.1) is

$$
\begin{aligned}
\langle\langle \mathcal{U} \rangle_T \rangle_\Gamma &= \frac{1}{\Gamma} \int_0^\Gamma \frac{1}{T} \int_0^T \mathcal{U}(x,t)\, \mathrm{d}t \mathrm{d}x \\
&= \frac{1}{\Gamma} \int_0^\Gamma u^2(x) \left(\frac{1}{T} \int_0^T f^2(kx - \omega t)\, \mathrm{d}t \right) \mathrm{d}x \\
&= \frac{1}{\Gamma} \int_0^\Gamma u^2(x) \left(\frac{1}{\lambda} \int_0^\lambda f^2(kx' - \omega t)\, \mathrm{d}x' \right) \mathrm{d}x \\
&= \langle u^2 \rangle_\Gamma \cdot \langle f^2 \rangle_\lambda.
\end{aligned}
\tag{A.2}
$$

For the third equality, the periodicity of the function f was used. Integrating f over a full period of 2π yields the same result, no matter if time or space is used as the independent variable and regardless of the starting point of the integration. Hence, Eq. (A.1) rewrites as

$$
\lim_{L \to \infty} \langle u^2 \cdot f^2 \rangle_L = \langle u^2 \rangle_\Gamma \cdot \langle f^2 \rangle_\lambda.
\tag{A.3}
$$

To show this identity, the functions u^2 and f^2 are expanded in Fourier series,

$$
\begin{aligned}
u^2(x) &= \sum_{n=-\infty}^{\infty} A_n\, \mathrm{e}^{\mathrm{i}n \frac{2\pi}{\Gamma} x} \\
f^2(kx - \omega t) &= \sum_{m=-\infty}^{\infty} B_m\, \mathrm{e}^{\mathrm{i}m(kx - \omega t)} \\
&= \sum_{m=-\infty}^{\infty} \left(B_m\, \mathrm{e}^{-\mathrm{i}m\omega t} \right) \mathrm{e}^{\mathrm{i}m \frac{2\pi}{\lambda} x}.
\end{aligned}
\tag{A.4}
$$

The Fourier coefficients are A_n and B_m with $n, m \in \mathbb{Z}$. The average over a full period of a periodic function is simply given by the "dc" coefficient (coefficient of zeroth order). The right-hand side of Eq. (A.3), therefore, reduces to

$$
\langle u^2 \rangle_\Gamma \cdot \langle f^2 \rangle_\lambda = A_0 \cdot B_0,
\tag{A.5}
$$

independent of time t. The left-hand side of Eq. (A.3) is a bit more tricky:

$$
\begin{aligned}
\lim_{L\to\infty} \langle u^2 \cdot f^2 \rangle_L &= \lim_{L\to\infty} \frac{1}{L} \int_0^L u^2(x) f^2(kx - \omega t)\, \mathrm{d}x \\
&= \lim_{L\to\infty} \frac{1}{L} \int_0^L \sum_{n=-\infty}^{\infty} \sum_{m=-\infty}^{\infty} A_n \left(B_m\, \mathrm{e}^{-\mathrm{i}\,m\omega t} \right) \mathrm{e}^{\mathrm{i}[n\frac{2\pi}{\Gamma} + m\frac{2\pi}{\lambda}]x}\, \mathrm{d}x \\
&= \sum_{n=-\infty}^{\infty} \sum_{m=-\infty}^{\infty} A_n \left(B_m\, \mathrm{e}^{-\mathrm{i}m\omega t} \right) \lim_{L\to\infty} \frac{1}{L} \int_0^L \mathrm{e}^{\mathrm{i}[n\frac{2\pi}{\Gamma} + m\frac{2\pi}{\lambda}]x}\, \mathrm{d}x.
\end{aligned}
\tag{A.6}
$$

In the limit of $L \to \infty$, the integral is zero unless the term in the square brackets is zero. This can only happen if $n = m = 0$ or if the ratio Γ/λ is a rational number. Since the set of rational numbers $\mathbb{Q}$ is countable, while $\mathbb{R}\backslash\mathbb{Q}$ is uncountable, it is reasonable to assume that $\Gamma/\lambda \in \mathbb{R}\backslash\mathbb{Q}$. This leaves us with $n = m = 0$ as the only remaining coefficients contributing to the sums, and we get

$$
\lim_{L\to\infty} \langle u^2 \cdot f^2 \rangle_L = A_0 \cdot B_0 = \langle u^2 \rangle_\Gamma \cdot \langle f^2 \rangle_\lambda,
\tag{A.7}
$$

which completes the proof.

A.2. Design of experiments using orthogonal arrays

Orthogonal arrays are a useful tool in experimental situations where the number of parameters that define a single experiment is large and sampling the entire parameter space is too time-intensive. For instance, the performance of a given process might be dependent on five *input parameters*, A, B, C, D, and E. Input parameters can be quantities such as process temperature, pressure in a vacuum chamber, or any other condition of the equipment used. These parameters either have a predefined number of states (open/closed for a valve) or they have to be sampled by a number of *levels*. A good range and level settings often have to be determined in preliminary experiments. For instance, a series of trial-and-error runs can be performed to identify a good process temperature to lie between $100°C$ and $200°C$ for a given process. If four different level settings are defined for each of the five input parameters, that results in a total of $4^5 = 1024$ experiments to be performed for the determination of the optimum parameter configuration. This is clearly too much, if less than 10 experiments can be carried out per day. Therefore, a method is required which can provide a meaningful result without sampling the entire parameter space. This is where orthogonal arrays come into play. An orthogonal array defines a relatively small set of experiments that allows for a statistically systematic analysis of the parameter space.

The performance of a process is measured by one or several *output parameters*, typically a quality measure of the produced sample (such as sidewall verticality of an etched hole, in our case) or process yield (in industrial production). Ideally, all output parameters are optimized for the same configuration of input parameters. However, this is not always the case. If contradictory results are found for different output parameters, then trade-offs have to be made between them. It is crucial for a process engineer to be aware of such trade-offs. Using orthogonal arrays, the process trade-offs can be rendered visible in an efficient way.

In the following, the design of experiments using orthogonal arrays will be explained in detail. Reference to the specific experiments of Secs. 3.1 and 3.3 will be made. First, some number-theoretic remarks about *latin squares* (LS) are made, and then their use for optimization applications is addressed.

A.2.1. Latin squares and orthogonal arrays

Let P be the number of input parameters under test and L the number of levels each parameter can take. For the moment we assume that all parameters allow the same number of levels. Let (p, l) denote a level setting l of a parameter p ($p \in \{1, \ldots, P\}$, $l \in \{1, \ldots, L\}$). An experiment can be specified by the levels of each input parameter, $E = \{(1, l_1), \ldots, (P, l_P)\}$. The idea of an orthogonal design is to define a set of experiments such that for each pair of input parameters, p_i and p_j ($i \neq j$), and for any choice of corresponding levels l_i and l_j an equal number of experiments combining the two parameter levels occurs. In our optimization applications, this number will always be 1. In other words, in our sets of experiments, all combinations of (i, l_i) and (j, l_j), $i \neq j$, will occur exactly once. This property of evenly distributed level settings is referred to as "orthogonal", for reasons that will become clear below. For a given (p, l), an average effect on the output parameter can be computed by

$$\langle f(p, l) \rangle = \frac{1}{L} \sum_{(p,l) \in E} f(E), \tag{A.8}$$

where $f(E)$ is the output function for the studied output parameter. The orthogonality of the array of experiments guarantees that this average effect is statistically relevant, as long as the input parameters are decoupled, i.e., the impact of each input parameter on the output parameter can be treated as independent of the level settings of all other input parameters. This mutual independence of input parameters is an important prerequisite for meaningful statements deduced from experimental data obtained using orthogonal arrays. Using the values $\langle f(p, l) \rangle$, each input parameter can be evaluated separately by identifying the level l, which maximizes $\langle f(p, l) \rangle$.

The main challenge in designing an orthogonal set of experiments lies in the fact that orthogonal arrays do not exist for any arbitrary choice of P and L. To further complicate the the matter, the construction of certain *existing* orthogonal arrays can be very hard. However, it can be shown that the construction is straightforward if L is a prime power, i.e., $L = q^n$, where q is a prime number and $n \geq 1$ an integer. In this case, there exists a complete set of $L - 1$ mutually orthogonal latin squares (MOLS) [215, 216]. A latin square of order L is an L by L array ($L \in \mathbb{N}$) containing L different symbols, each occurring exactly once in each row and exactly once in each column. Two latin squares

Table A.1. Orthogonal array for $P = 5$ and $L = 4$. Each row represents an experimental run. The level settings are indicated for each input parameter p (arranged in columns).

Run no.	$p = 1$	$p = 2$	$p = 3$	$p = 4$	$p = 5$
1	1	1	1	1	1
2	1	2	2	2	2
3	1	3	3	3	3
4	1	4	4	4	4
5	2	1	2	3	4
6	2	2	1	4	3
7	2	3	4	1	2
8	2	4	3	2	1
9	3	1	3	4	2
10	3	2	4	3	1
11	3	3	1	2	4
12	3	4	2	1	3
13	4	1	4	2	3
14	4	2	3	1	4
15	4	3	2	4	1
16	4	4	1	3	2

are said to be orthogonal if each ordered pair of the L symbols occurs exactly once when one square is superimposed on the other. From a $L - 1$ MOLS, an array of L^2 rows (experiments) and $L + 1$ columns (input parameters) can be readily obtained [215, 217], which fulfills the orthogonality requirement. Here, the term "orthogonal" simply refers to the mutual orthogonality of the latin squares from which the array is constructed. For a detailed construction algorithm of MOLSs, the reader shall be referred to [215, Chap. 8].

If we restrict ourselves to those orthogonal arrays that we can easily obtain from complete sets of MOLSs, then we have the following conditions:

- The number of levels must be a prime power, i.e., $L \in \{2, 3, 4, 5, 7, 8, 9, 11, \ldots\}$.
- The number of input parameters is $P = L + 1$.

- The number of experiments to be performed is L^2 or an integer multiple of it.

A.2.2. Applications

Orthogonal arrays were used for the optimization of the cyclic RIE process in Sec. 3.1 and for the assessment of the Cl_2/O_2-based ICP-RIE process in Sec. 3.3. In both cases, five input parameters were used. According to the above discussion, an orthogonal array can be set up for $P = 5$ if the number of levels equals $L = 4$. The resulting array contains 16 experiments as shown in Table A.1. According to the terminology used in [135], this is a $L_{16}\,4^5$ array. It is easily verified that each ordered pair of level settings occurs only once. For the RIE optimization experiment in Sec. 3.1, the input parameters and the corresponding level settings are listed in Table 3.2 in sequential order. For InP etching in Sec. 3.3, a permutation of the level settings was used to avoid combinations of extreme plasma conditions. The orthogonality of the array is preserved upon permutations of either input parameters or level settings. The permutation used for the experiment is indicated in Table A.2.

Table A.2. Permutation of Table 3.6 as it was used with the orthogonal array of Table A.1 to reproduce the experimental setup of Sec. 3.3. Input parameters are arranged in sequential order (top to bottom), and the corresponding level settings used for the experiment are indicated. The permutation guarantees, e.g., that runs no. 1 and 4 do not combine extreme level settings for all input parameters.

Input parameter	Level 1	Level 2	Level 3	Level 4
Ar flux (sccm)	4	6	2	8
O_2 flux (sccm)	1	2	3	0
He flux (sccm)	5	5	15	15
Self-bias (V)	280	320	360	400
ICP power (W)	600	900	1200	1500

A.3. Derivation of etching rate dynamics in CHF$_3$-based RIE of SiN$_x$

In Sec. 3.1.4, the dynamics of SiN$_x$ etching in a pure CHF$_3$ plasma. During etching, a fluorocarbon layer is formed on the etched surface. this layer gradually builds up and slows down the SiN$_x$ etching rate. After a long time of continuous etching, a steady-state situation sets in, with constant rates of etching and deposition. The mathematical description of this process relies on empirical formulas for both rates. Some of the mathematics were skipped in the main text, and it is the purpose of this appendix to supply them in full detail.

For the etching rate r, an exponential dependence on the fluorocarbon film thickness d is assumed,

$$r(d) = r_0 \, e^{-d/\lambda}, \tag{A.9}$$

where r_0 is the etching rate on a clean SiN$_x$ surface and λ is a characteristic length parameter. This behavior was confirmed experimentally by Schaepkens *et al.* [127]. The dynamics of the fluorocarbon layer thickness is governed by a constant polymer deposition term and two different mechanisms of polymer removal during the etching process. The relation is given in Eq. (3.2) of the the main text (p. 57) and it can be brought into the form

$$\frac{d}{dt} \, d = \delta - \sigma \, (1 - e^{-d/\lambda}). \tag{A.10}$$

The constants $\sigma > \delta > 0$ are defined on p. 57 of the main text. They are introduced solely for formal simplicity of the equations. If we start the etching process on a clean surface, we have the initial condition at time $t = 0$

$$d(0) = 0. \tag{A.11}$$

In the following, we will show how the deposition dynamics $d(t)$ can be obtained from the initial value problem of Eqs. (A.10) and (A.11), and then we insert the resulting relation into Eq. (A.9) to find the etching rate as a function of time, $r(t)$. Finally, the etching depth $h(t)$ (Eq. (3.4) on p. 58 of the main text) will be derived by integration over time.

Equation (A.10) is a first-order autonomous differential equation [218]. Autonomous means that it does not explicitly depend on the

independent variable t. Differential equations of this type are *separable*, i.e., they can be rearranged into an integral form. In the case of Eq. (A.10), the resulting integral can be solved analytically, which yields

$$-\frac{1}{\sigma - \delta}\left[d + \lambda \ln\left(\frac{\sigma}{\sigma - \delta}e^{-d/\lambda} - 1\right)\right] = t + c, \tag{A.12}$$

where c is an integration constant. After applying the initial condition $d(0) = 0$ and using the relation $d = \lambda \ln(e^{d/\lambda})$, Eq. (A.12) can be rearranged to

$$-\frac{\lambda}{\sigma - \delta}\ln\left(\frac{\sigma}{\delta} - \frac{\sigma - \delta}{\delta}e^{d/\lambda}\right) = t. \tag{A.13}$$

Solving for $d(t)$ results in

$$d(t) = \lambda \ln\left(\frac{\sigma}{\sigma - \delta} - \frac{\delta}{\sigma - \delta}e^{-\frac{\sigma - \delta}{\lambda}t}\right). \tag{A.14}$$

This relation describes the temporal evolution of the fluorocarbon layer thickness, starting from a clean SiN$_x$ surface. A steady-state behavior for $t \to \infty$ is immediately apparent if $\sigma > \delta$. Insertion of $d(t)$ into Eq. (A.9) returns the etching rate

$$r(t) = r_0\left(\frac{\sigma}{\sigma - \delta} - \frac{\delta}{\sigma - \delta}e^{-\frac{\sigma - \delta}{\lambda}t}\right)^{-1}. \tag{A.15}$$

For long times, $t \to \infty$, the etching rate tends towards the steady-state rate $r_s = r_0\frac{\sigma - \delta}{\sigma} < r_0$. The etching depth $h(t)$ can be found by integration:

$$\begin{aligned} h(t) &= \int_0^t r(\tilde{t})\,d\tilde{t} \\ &= r_s \cdot t + r_0\frac{\lambda}{\sigma}\ln\left(\frac{r_0}{r_s} - \left(\frac{r_0}{r_s} - 1\right)e^{-\frac{r_s}{r_0}\cdot\frac{\sigma}{\lambda}\cdot t}\right). \end{aligned} \tag{A.16}$$

This relation corresponds to Eq. (3.4) of the main text. It was used to fit experimental data, and the results are summarized in Table 3.4 of p. 59.

A.4. Construction of sidewall deposition thickness for the SAMR method

The key step of the SAMR method (Sec. 3.2) is the angled deposition of a masking layer on the surface of a rotating sample. The tilt of the sample ensures that the bottom surface of a circular hole is not covered during mask deposition, but at the same time it means that there will be some material deposited on the sidewalls. The thickness of this sidewall layer shall be derived here. The starting point are the schematics of the geometry depicted in Fig. A.1. A similar figure is given in the main text (p. 62); the only difference is the orientation of the coordinate system.
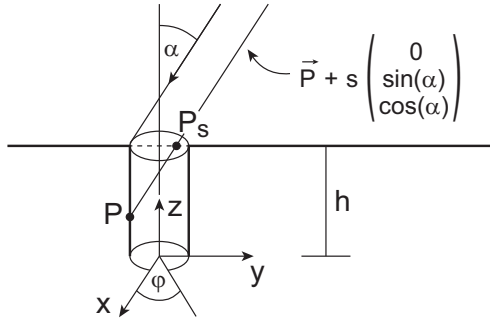
Figure A.1. Self-aligned mask renewal method. A line-of-sight (vertical arrow) deposition process is used to deposit the new mask. The sample is tilted by an angle, α, to avoid covering the bottom surface of the etched hole with masking material. To guarantee a homogeneous layer, the sample is rotated about an axis perpendicular to the sample surface. The drawing illustrates the construction of the point P_s starting from a point P on the sidewall surface, for the derivation of the final layer thickness as a function of the z-position.

The final sidewall layer thickness depends on the z-position of the considered point P. During deposition, there are phases of constant deposition rate and phases in which point P is shadowed by the rim of the hole. In the absence of shadowing, the deposition rate is $r_{\mathrm{hor}} \cdot \sin(\alpha)$, where r_{hor} is the rate on the top surface of a horizontally mounted ($\alpha = 0$) sample. To find the final layer thickness, the rate has to be integrated over time. Differently put, the duration of the deposition phases needs

to be determined and multiplied by the deposition rate. Hence, the problem reduces to the question whether or not, for a given time t, the considered point is shadowed on its trajectory $P(t)$. Using Fig. A.1, this question can be answered by parameterizing a line originating in $P(t)$ with a vector pointing in the reverse deposition direction. A point p on this line is described by

$$p(t, s) = P(t) + s \begin{pmatrix} 0 \\ \sin(\alpha) \\ \cos(\alpha) \end{pmatrix} \qquad \text{for} \quad 0 < s < \infty. \qquad (A.17)$$

If the intersection of this line with the plane of the sample surface lies outside the circumference of the hole, then point $P(t)$ is shadowed. The intersection point $P_s(t)$ is found by setting the z-component of $p(t, s)$ equal to h. To do so, the trajectory $P(t)$ has to be specified. As long as the thickness of the sidewall layer d_{side} is negligible compared to the hole radius R (i.e., if $d_{\text{side}} \ll R$), the position of the point can be written as

$$P(t) = \begin{pmatrix} R\cos(\varphi(t)) \\ R\sin(\varphi(t)) \\ z \end{pmatrix} \qquad \text{with} \quad \varphi(t) = 2\pi f \cdot t, \qquad (A.18)$$

where φ is the azimuthal angle and f is the rotation frequency of the sample holder. If d_{side} were no longer negligible, R would have to be replaced by $R - d_{\text{side}}(t)$ in Eq. (A.18). This case will not be considered here, but an analytical treatment would still be possible. Insertion of Eq. (A.18) into Eq. (A.17) and setting the z-component equal to h yields

$$
\begin{aligned}
&z + s\cos(\alpha) = h \\
\Rightarrow \quad &s = \frac{h - z}{\cos(\alpha)} \\
\Rightarrow \quad &P_s(t) = \begin{pmatrix} R\sin(\varphi(t)) \\ -R\cos(\varphi(t)) + (h - z)\tan(\alpha) \\ h \end{pmatrix}.
\end{aligned}
\qquad (A.19)
$$

Now it is easy to verify whether the intersection point $P_s(t)$ lies within

or outside of the circumference of the hole. If it is inside, then

$$
\begin{aligned}
&\sqrt{x_{P_s(t)}^2 + y_{P_s(t)}^2} < 0 \\
\Rightarrow \quad &R^2 - 2R(h-z)\cos(\varphi(t))\tan(\alpha) + (h-z)^2 \tan^2(\alpha) < R^2 \\
\Rightarrow \quad &\cos(\varphi(t)) > \frac{h-z}{2R}\tan(\alpha) \\
\Rightarrow \quad &|\varphi(t)| < \arccos\left(\frac{h-z}{2R}\tan(\alpha)\right) \quad \text{for} \quad -\pi < \varphi(t) < \pi.
\end{aligned}
\tag{A.20}
$$

In a case where $\varphi(t)$ is linear in t, the last inequality of Eq. (A.20) directly implies the relative duration of the deposition phase, $\Delta t_{(dep)}$, with respect to the duration of a full roundtrip, $T = 1/f$. It is

$$
\frac{\Delta t_{\text{dep}}}{T} = \frac{1}{\pi}\arccos\left(\frac{h-z}{2R}\tan(\alpha)\right).
\tag{A.21}
$$

The multiplication of this result with the deposition rate during the deposition phase constitutes the average deposition rate, $\langle r_{\text{side}} \rangle$. Using the expression for the deposition rate on the top surface, r_{top}, and the relation $d_{\text{side}}/d_{\text{top}} = \langle r_{\text{side}} \rangle / r_{\text{top}}$, we find for the sidewall layer thickness

$$
d_{\text{side}}(z) = \begin{cases} d_{\text{top}} \cdot \tan(\alpha) \cdot \frac{1}{\pi}\arccos(\frac{h-z}{2R}\tan(\alpha)) \\ \hspace{5cm}, z > h - \frac{2R}{\tan(\alpha)} \\ 0 \hspace{4cm}, z < h - \frac{2R}{\tan(\alpha)} \end{cases}
\tag{A.22}
$$

This relation corresponds to Eq. (3.5) on p. 62 of the main text.

A.5. Fabry-Pérot method for optical propagation loss measurements

A Fabry-Pérot interferometer is a cavity between two semi-reflecting mirrors. Light which is coupled into such a cavity (or which is generated within it) undergoes multiple roundtrips, losing some of its power at each reflection. Depending on the wavelength of the light, the interference of the outcoupled waves can interfere constructively or destructively. In a transmission experiment such a port-to-port measurement, constructive interference leads to a transmission maximum, whereas destructive interference leads to a minimum. A plot of transmitted power versus wavelength or frequency shows a pattern of interference fringes. The spacing between the fringes spacing contains information about the cavity length and the effective refractive index of the propagating mode. The fringe contrast (defined below) is related to the damping of the mode due to power outcoupling through the mirrors or, in the case of a waveguide cavity, due to waveguide losses. Here, the exact formulas for the Fabry-Pérot fringes will be derived using the transfer matrix method. The treatment is similar to that of Ref. [219, Chap. 7]. Using the mathematical description of the fringes, experimental data can be fitted, and accurate values of propagation loss can be extracted. In the case of a gain material, amplified spontaneous emission (ASE) can be used in a similar manner to measure gain coefficients. This was first proposed by Hakki and Paoli [220] and is, therefore, often referred to as the Hakki-Paoli method.

The transfer matrix method is used to describe an optical element or an optical system by a complex 2×2 matrix which maps the amplitudes of left- and right-propagating waves on the input side to those on the output side of the system. This is particularly useful if the combined effect of several concatenated elements is of interest. If the matrices for all individual elements are know, the problem reduces to a simple matrix multiplication. Let $A_1^{(-)}$ denote the left-propagating and $A_1^{(+)}$ the right-propagating wave amplitude at the input of an optical element. Similarly, $A_2^{(-)}$ and $A_2^{(+)}$ are the amplitudes at the output. The wave-transfer matrix $\mathbf{M}$ relates them through

$$\begin{pmatrix} A_2^{(+)} \\ A_2^{(+)} \end{pmatrix} = \mathbf{M} \begin{pmatrix} A_1^{(+)} \\ A_1^{(+)} \end{pmatrix}. \tag{A.23}$$

For normal incidence of a plane wave on a Fabry-Pérot etalon we get

the following transfer matrix

$$\mathbf{M} = \begin{pmatrix} M_{11} & M_{12} \\ M_{21} & M_{22} \end{pmatrix} = \begin{pmatrix} \frac{1}{t_2^*} & \frac{r_2}{t_2} \\ \frac{r_2^*}{t_2^*} & \frac{1}{t_2} \end{pmatrix} \begin{pmatrix} \mathrm{e}^{-\mathrm{i}kd} & 0 \\ 0 & \mathrm{e}^{\mathrm{i}kd} \end{pmatrix} \begin{pmatrix} \frac{1}{t_1^*} & \frac{r_1}{t_1} \\ \frac{r_1^*}{t_1^*} & \frac{1}{t_1} \end{pmatrix}, \qquad \text{(A.24)}$$

which is composed of two matrices describing reflection/transmission at the interfaces and one intermediate matrix taking account of phase shift and loss arising during propagation. The interfaces are separated by a distance d and the angular wave number is denoted by $k = \beta - \mathrm{i}\alpha/2$, where α is the attenuation constant for field intensities. The real part of the wave number, β, can be written as $\beta = k_0 n = \frac{\omega}{c}n$, where k_0 is the wave number in vacuum, n is the refractive index of the medium,[1] ω is the angular frequency, and c is the vacuum speed of light. The symbols r_1, r_2, t_1, t_2 are the reflection (r) and transmission (t) coefficients of the interfaces on the input (1) and output (2) side. The asterisk denotes a complex conjugate.

In an experimental setting, the transmitted power $P_2^{(+)} \sim |A_2^{(+)}|^2$ is usually measured. Setting $A_2^{(-)} = 0$, we can solve Eq. (A.23) for $A_2^{(+)}$:

$$A_2^{(+)} = M_{11} A_1^{(+)} - \frac{M_{12} M_{21}}{M_{22}} A_1^{(+)} = \frac{\det(\mathbf{M})}{M_{22}} A_1^{(+)}. \qquad \text{(A.25)}$$

The determinant of $\mathbf{M}$ can be determined as

$$\begin{aligned}
\det(\mathbf{M}) &= \det \begin{pmatrix} \frac{1}{t_2^*} & \frac{r_2}{t_2} \\ \frac{r_2^*}{t_2^*} & \frac{1}{t_2} \end{pmatrix} \cdot \det \begin{pmatrix} \mathrm{e}^{-\mathrm{i}kd} & 0 \\ 0 & \mathrm{e}^{\mathrm{i}kd} \end{pmatrix} \cdot \det \begin{pmatrix} \frac{1}{t_1^*} & \frac{r_1}{t_1} \\ \frac{r_1^*}{t_1^*} & \frac{1}{t_1} \end{pmatrix} \\
&= \left(\frac{1}{|t_2|^2} - \frac{R_2}{|t_2|^2} \right) \cdot 1 \cdot \left(\frac{1}{|t_1|^2} - \frac{R_1}{|t_1|^2} \right) \\
&= \frac{T_2}{|t_2|^2} \cdot \frac{T_1}{|t_1|^2} = \frac{n_{\mathrm{air}}}{n} \cdot \frac{n}{n_{\mathrm{air}}} = 1,
\end{aligned} \qquad \text{(A.26)}$$

where n and n_{air} are the refractive indices of the Fabry-Perot etalon and of air, respectively. We made use of the relations $|r|^2 = R$, $R + T = 1$, and $T = \frac{n_2}{n_1}|t|^2$ for normal incidence. As a consequence, we only have to evaluate the element M_{22} of the transfer matrix. Using the relations $r_1 r_2 = -\sqrt{R_1 R_2}$ and $|t_1|^2 |t_2|^2 = T_1 T_2 = (1 - R_1)(1 - R_2)$, we find after

---

[1]In case of a waveguide cavity, the n has to be replaced by the effective refractive index of the considered waveguide mode.

some calculation

$$\frac{1}{|M_{22}|^2} = e^{-\alpha d} \frac{(1-R_1)(1-R_2)}{(1-e^{-\alpha d}\sqrt{R_1 R_2})^2 + 4\sqrt{R_1 R_2}\, e^{-\alpha d} \sin^2(\beta d)}. \quad \text{(A.27)}$$

From Eq. (A.27) we can extract the minimum and maximum power transmission. We find the ratio

$$\begin{aligned} u = \frac{P_{\min}}{P_{\max}} &= \frac{(1-e^{-\alpha d}\sqrt{R_1 R_2})^2}{(1-e^{-\alpha d}\sqrt{R_1 R_2})^2 + 4\sqrt{R_1 R_2}\, e^{-\alpha d}} \\ &= \frac{(1-e^{-\alpha d}\sqrt{R_1 R_2})^2}{(1+e^{-\alpha d}\sqrt{R_1 R_2})^2}. \end{aligned} \quad \text{(A.28)}$$

Solving for α we get

$$\alpha = \frac{1}{d}\,\ln\left(\frac{1+\sqrt{u}}{1-\sqrt{u}}\right) + \frac{1}{2}\,\ln(R_1 R_2). \quad \text{(A.29)}$$

Equation (A.29) is convenient to get a quick estimate of the loss figure from a measured transmission spectrum. For a more sophisticated fitting routine, the expression of Eq. (A.27) can be used. The independent variable is the frequency (hidden in $\beta = \frac{\omega}{c}n$), and the fringe spacing (distance between two maxima) can easily be identified as $\Delta\omega = \frac{c\pi}{nd}$ or $\Delta\lambda = \frac{\lambda^2}{2nd}$. The length d of the cavity is generally known to a good accuracy and, using a Fourier transform, $\Delta\omega$ can be computed from the measured transmission spectrum. This allows for an accurate determination of the index of refraction n. If the cavity is terminated by two identical interfaces, then we can use $R_1 = R_2 = R$ and the reflection coefficient can be computed as $R = ((n-n_{\text{air}})/(n+n_{\text{air}}))^2$. Now, we rewrite Eq. (A.27) as

$$P_2^{(+)} = P_{\max}\left[1 + \frac{4R\,e^{-\alpha d}\sin^2(\frac{\omega}{c}nd + \varphi)}{(1-R\,e^{-\alpha d})^2}\right]^{-1} \quad \text{(A.30)}$$

The phase shift φ is introduced to correct for variations in the absolute position of the fringe maxima. Using fixed values for d, n, and R, the relation of Eq. (A.30) can be fitted to experimental data. The free fitting parameters are $P_{\max}$, α, and φ.

To generate plots of gain spectra, such as the ones shown in Fig. 4.14 of the main text, a MATLAB routine is used, performing the following steps:

1) The measured data (power versus wavelength) are read from a text file. The spectrum is recorded by a VERTEX 70 system (FTIR) from Bruker.

2) The wavelength scale is converted into a frequency scale. An even spacing of the frequency points is obtained by interpolation.

3) The spacing of the Fabry-Pérot fringes in the vicinity of the global power maximum is determined using a Fourier transform. According to Eq. (A.30), this spacing is valid for the entire spectrum (independent of frequency). We call it the *global* fringe spacing.

4) The spectrum is divided into segments containing four Fabry-Pérot fringes. From each segment, a gain/loss value will be extracted in a later step. Depending on the desired sampling resolution of the final gain spectrum, the segments can overlap or not.

5) To test the usability of each segment, the fringe spacing is computed and compared to the global fringe spacing. In cases where there is a substantial deviation, the segment is discarded. This is, e.g., the case where the power is in the noise floor of the setup.

6) For all good segments, the gain/loss value is computed by a numerical fit of Eq. (A.30) to the measured data.

A.6. Cutback method for optical propagation loss measurements

Cutback measurements are used in Sec. 3.4 for the measurements of optical propagation losses in passive PhC waveguides. Several PhC waveguides of different lengths are integrated with deeply etched trench waveguides of $5\,\mu$m width on a single chip of total length $L_{\text{tot}} = 2.1$ mm. The propagation loss of the trench access waveguides, α_T, was measured on a reference waveguide (without PhC section) using the Fabry-Pérot method (Appendix A.5). It is roughly $2\,\text{cm}^{-1}$ at a wavelength of $\lambda = 1550$ nm. Losses of the PhC waveguide are measured in a port-to-port configuration, where cw light from a tunable laser is coupled into the access waveguide through a cleaved chip facet using a lensed fiber. After propagation through the chip, the light is collimated by a microscope objective and detected by an InGaAs detector. Depending on the length L of the PhC section of the waveguide, the output power P_{out} varies. We assume constant input power P_{in} and coupling coefficients, T_{in} and T_{out}, at the input and output ports, respectively.[2] The output power can be written as

$$P_{\text{out}}(L) = P_{\text{in}}\,T_{\text{in}}\,\text{e}^{-\alpha_T(L_{\text{tot}}-L)}\,\text{e}^{-\alpha_{\text{PhC}}L}\,T_{\text{out}}, \qquad (A.31)$$

where α_{PhC} is the power loss coefficient of the PhC waveguide. Taking the logarithm on both sides of Eq. (A.31) and collecting the length-independent factors in the constant $C = \ln(P_{\text{in}}\,T_{\text{in}}\,T_{\text{out}}) - \alpha_T L_{\text{tot}}$ yields

$$\ln(P_{\text{out}}) = C - (\alpha_{\text{PhC}} - \alpha_T)\,L. \qquad (A.32)$$

Hence, a linear fit to $P_{\text{out}}(L)$ gives direct access to the figure $\alpha_{\text{PhC}} - \alpha_T$. If α_T is either negligible or determined experimentally, α_{PhC} can be easily extracted.

In order for the cutback method to deliver reliable results, multiple reflections have to be suppressed. This can either be done by using access waveguides with appreciable propagation losses, or by using low-reflection interfaces between access and PhC waveguides. In this respect, there is no point in optimizing the access waveguides for low loss. In fact, our deeply etched trench waveguides might be criticized as being "too good". Over a distance of 1 mm, they damp the

---

[2]Coupling into access waveguides was investigated and optimized in Ref. [76, Chap. 5], and the assumption of constant coupling coefficients was confirmed to be reasonable.

light intensity by less than 1 dB. However, we have shown numerically that the reflection coefficients are small at the interfaces to the PhC waveguides [170]. More than 10 dB attenuation can be expected in the reflected mode.

To define a good set of PhC waveguide lengths, the following criteria have to be taken into account:

- The shortest waveguide should be chosen such that the loss in the PhC section is not negligible compared to the loss of the access waveguide. Therefore, a good length of the shortest PhC section would be $L \simeq \alpha_T / \alpha_{\mathrm{PhC}} \cdot L_{\mathrm{tot}}$. The loss of a W1 PhC waveguide is in the order of 100 times larger than that of an access waveguide. For $L_{\mathrm{tot}} \simeq 2\,\mathrm{mm}$, this results in a lower length limit of $L \simeq 20\,\mu\mathrm{m}$.

- The longest waveguide should be chosen such that the final output power is significantly above the noise level of the detection setup. In our case, this is around -70 dBm. For an input power of 0 dBm and waveguide losses of 800 dB/cm ($\simeq 200\,\mathrm{cm}^{-1}$), the upper length limit would be of the order of 400 - 800 μm.

A.7. Linear gain of a quantum well

The aim of this section is to outline the derivation of the gain relation of Eq. (4.5) on p. 101 of the main text. The essential physical principles involved are addressed without going deeply into the technical details. Two textbooks are mainly used as a reference [192, 221].

Let ϕ denote the photon density in units of cm^{-3}. In a stimulated emission process, the increase in photon density along the propagation direction x is proportional to ϕ,

$$\frac{\mathrm{d}\phi}{\mathrm{d}x} = g\,\phi, \tag{A.33}$$

where g is the gain figure. A similar expression might be written for the optical field intensity, the photon flux, or optical power. If g is independent of P, then it is referred to as *linear* gain. To derive an expression for g from the rate equations for absorption and stimulated emission in a QW, Eq. (A.33) has to be restated in terms of the time derivative $\mathrm{d}\phi/\mathrm{d}t$ instead of the space derivative $\mathrm{d}\phi/\mathrm{d}x$. It can be shown[3] for pulses propagating in a linear medium that

$$\frac{\mathrm{d}\phi}{\mathrm{d}t} = v_{\mathrm{gr}}\frac{\mathrm{d}\phi}{\mathrm{d}x} = g\,v_{\mathrm{gr}}\,\phi, \tag{A.34}$$

where v_{gr} is the group velocity of the pulse. The change in photon density is governed by an absorption rate $W_{v\to c}$ and an emission rate $W_{c\to v}$. Here, the letters "c" and "v" stand for conduction and valence band, respectively, and the arrow indicates the direction of the electronic transition. The procedure to derive an expression for g is as follows:

First, the transition rates $W_{e\to h}$ and $W_{h\to e}$ between a conduction band state ψ_e and a particular valence band state ψ_h are computed using Fermi's golden rule. For the emission process, we have

$$W_{e\to h} = \frac{2\pi}{\hbar}\,|H'_{eh}|^2\,\delta(E_{eh} - \hbar\omega), \tag{A.35}$$

---

[3]At a fixed location, let $f(t)$ describe the power envelope of a pulse propagating at group velocity v_{gr}. Further, let's assume a medium in which the *shape* of the envelope is conserved, but the amplitude A increases as the pulse propagates. The power of this pulse can be written as $P(x,t) = A(x)f(t - x/v_{\mathrm{gr}})$. Now we consider a fixed point on the moving envelope: $t - x/v_{\mathrm{gr}} = C$, where C is some constant. We find $\frac{\mathrm{d}}{\mathrm{d}t}P = \frac{\mathrm{d}}{\mathrm{d}t}A(v_{\mathrm{gr}}(t-C))f(C) = v_{\mathrm{gr}}\frac{\mathrm{d}}{\mathrm{d}x}A(x)f(C) = v_{\mathrm{gr}}\frac{\mathrm{d}}{\mathrm{d}x}P$.

where H'_{eh} is the matrix element $\langle\psi_e|H'(\mathbf{r})|\psi_h\rangle$ of the time-independent part of the perturbation Hamiltonian. For details on this, we refer the reader to the textbooks (e.g., Ref. [87, Chap. 13]). E_{eh} is the transition energy between the two states, and $\hbar\omega$ is the energy of the photon that induced the transition. A similar expression is obtained for the absorption process $W_{h\to e}$.

Next, to find the total transition rates $W_{c\to v}$ and $W_{v\to c}$ between conduction and valence band, an integration over all possible states ψ_e and ψ_h is necessary. The integration can be performed in k-space using the density of states $\rho(k)$ as a weighting,

$$W_{c\to v} = \frac{2\pi}{\hbar} \int |H'_{eh}|^2 \, \delta(E_{eh} - \hbar\omega)\rho(k)\,\mathrm{d}k. \tag{A.36}$$

Using the relations $E_e(k)$ and $E_h(k)$ for the energy states of electrons and holes of the quantum mechanical system, the density of states $\rho(k)$ can be replaced by the *reduced* energy density of states $\rho_{\mathrm{red}}(E_{eh})$ which expresses the weighting of transitions in terms of the transition energy. In the case of a QW and assuming parabolic energy bands,

$$E_e(n, k_x, k_y) = \varepsilon_{e,n} + \frac{\hbar^2}{2m_{e,n}}k_e^2 \tag{A.37}$$

$$E_h(n, k_x, k_y) = \varepsilon_{h,n} + \frac{\hbar^2}{2m_{h,n}}k_h^2 \tag{A.38}$$

for the nth subband, where $m_{e,n}$ and $m_{h,n}$ are the effective masses of electrons and holes, respectively; and k_e^2 and k_h^2 are 2D wave vectors in the QW plane. A different convention using a single energy reference for both types of carriers might be used [221], in which case there would be a minus sign on the right hand side of Eq. (A.38). The reduced energy density of states in a QW is

$$\rho_{\mathrm{red}}(E_{eh}) = (2)\frac{m_r}{2\pi\hbar^2}\left(\frac{1}{a}\right). \tag{A.39}$$

The "2" in brackets takes into account the fact that two electrons or holes of opposite spin can occupy the same state in k-space. The thickness of the QW is denoted by a, and m_r is the reduced mass of electrons and holes. The integral of Eq. (A.36) can now be evaluated to yield

$$W_{c\to v} = \frac{2\pi}{\hbar} |H'_{eh}|^2 \, \rho_{\mathrm{red}}(E_{eh} - E_0), \tag{A.40}$$

where E_0 is the bandgap between two given subbands in the QW.

So far, we have a transition rate between all possible states of the QW. Now, the occupation probability of these states has to be taken into account. The fermionic nature of electrons implies a Fermi-Dirac distribution denoted $f_c(E)$ for electrons in the conduction band and $f_v(E)$ for holes in the valence band. In our notation,

$$f_{c,v}(E_{e,h}) = \frac{1}{1 + e^{(E_{e,h} - E_{fc,fv})/k_B T}}, \qquad (A.41)$$

where $E_{fc,fv}$ are the Fermi levels in the conduction and valence band, respectively; k_B is the Boltzmann constant and T is the temperature of the material. In an emission process $(c \rightarrow v)$, the two states, ψ_e and ψ_h, must be occupied to enable recombination. In an absorption process, on the other hand, the two states must be empty. Hence,

$$W_{c \rightarrow v} = \frac{2\pi}{\hbar} |H'_{eh}|^2 \rho_{\text{red}} f_c f_v \qquad (A.42)$$

$$W_{v \rightarrow c} = \frac{2\pi}{\hbar} |H'_{eh}|^2 \rho_{\text{red}} (1 - f_c)(1 - f_v). \qquad (A.43)$$

For the computation of the gain figure, the net emission rate is of interest,

$$W = W_{c \rightarrow v} - W_{v \rightarrow c} = \frac{2\pi}{\hbar} |H'_{eh}|^2 \rho_{\text{red}} (f_c + f_v - 1). \qquad (A.44)$$

W is a photon emission rate per unit volume. It corresponds to an increase in the photon density per unit time, $W = \mathrm{d}\phi/\mathrm{d}t$. To find g, this has to be divided by the photon density ϕ, which can be written out explicitly for a plane plane wave (not shown here). Furthermore, the matrix element H'_{eh} has to be evaluated. In bulk semiconductors, this can be done using the Kane band model [222]. In Ref. [192] it is assumed that, for a QW, the same matrix element can be used. Under these premises, and assuming $v_{\text{gr}} = c/n$, the material gain produced within a specific subband can be written as

$$g(E_{eh}) = \frac{1}{3} \frac{\pi}{a} \frac{\alpha_f}{\sqrt{\epsilon}} \frac{m_r}{m_e} \frac{E_g(E_g + \Delta_0)}{E_g + \frac{2}{3}\Delta_0} \frac{1}{E_{eh}} \times [f_c(E_e) + f_v(E_h) - 1], \ (A.45)$$

where $\alpha_f = e^2/(4\pi\varepsilon_0 c\hbar)$, e is the elementary charge, ε_0 the vacuum permittivity, and c the speed of light. Equation A.45 corresponds to

equation (9.4.7) of Ref. [192].

Finally, the Fermi levels E_{fc} and E_{fv} can be related to carrier densities of electrons n and holes p. For simplicity, we restrict the discussion to transitions between the lowest energy levels of electrons and holes in a QW. This is the transition with the highest gain and, therefore, is normally the relevant one for applications such as lasers. By definition of the Fermi level, we get for the electron density in the conduction band

$$
\begin{aligned}
n &= \int_{E_{e,0}}^{\infty} \rho(E - E_{e,0}) f_c(E) \, \mathrm{d}E \\
&= N_c \ln \left[1 + \mathrm{e}^{(E_{fc} - E_{e,0})/k_B T} \right],
\end{aligned}
\tag{A.46}
$$

where $N_c = m_e k_B T (\pi \hbar^2 a)$. A similar expression can be obtained for the hole density p. Solving for E_{fc} yields

$$
E_{fc} = E_{e,0} + k_B T \ln \left[\mathrm{e}^{n/N_c} - 1 \right].
\tag{A.47}
$$

Using this expression in Eq. (A.41), we can write the Fermi functions, $f_c(E_e, n)$ and $f_v(E_h, p)$, as a function of carrier densities. The highest gain occurs for photon energies $\hbar\omega = E_0$, i.e., for $E_e = E_{e,0}$ and $E_h = E_{h,0}$. In this case the Fermi levels as a function of carrier densities are

$$
f_c(n) = 1 - \mathrm{e}^{-n/N_c}
\tag{A.48}
$$

$$
f_v(p) = 1 - \mathrm{e}^{-p/(MN_c)},
\tag{A.49}
$$

where $M = m_h/m_e$. Inserted into Eq. (A.45), we can write the gain at $E_e h = E_0$ as

$$
\begin{aligned}
g(E_0, n, p) = &\frac{1}{3} \frac{\pi}{a} \frac{\alpha_f}{\sqrt{\epsilon}} \frac{M}{1+M} \frac{E_g(E_g + \Delta_0)}{E_g + \frac{2}{3}\Delta_0} \frac{1}{E_0} \\
&\times \left[1 - \mathrm{e}^{-n/N_c} - \mathrm{e}^{-p/(MN_c)} \right].
\end{aligned}
\tag{A.50}
$$

To arrive at Eq. (4.5), the optical confinement factor Γ has to be added and 3D densities (n, p, N_c) are replaced by 2D densities ($n_{\mathrm{QW}}^{\mathrm{2D}}$, $p_{\mathrm{QW}}^{\mathrm{2D}}$, N_c^{2D}) by a multiplication with the QW thickness a (e.g., $n_{\mathrm{QW}}^{\mathrm{2D}} = a\,n$).

A.8. Fourier transform infrared spectroscopy

There are two basic approaches to measure the frequency spectrum of a given light signal. Firstly, the light can be split up into its spectral components, and the intensity of each component can be measured separately. A grating spectrometer is a typical example. The second approach is to gain access to the frequency spectrum via a time-domain measurement and a Fourier transform. Naïvely, one could think of measuring the fully time-resolved field oscillations $E(t)$ of infrared light and then computing the Fourier transform $\tilde{E}(\omega) = \int_{-\infty}^{\infty} E(t)\, \mathrm{e}^{\mathrm{i}\omega t}\mathrm{d}t$. However, there is no detector fast enough to cope with variations on a femtosecond time scale. A more sophisticated procedure is required. In the following, we will provide the mathematical foundations of the technique that has become known as Fourier transform infrared spectrometry (FTIR). More details can be found in Ref. [223].

The key element of FTIR spectrometry is a Michelson interferometer. The studied beam is directed onto a beam splitter, ideally dividing it into two beams of equal intensities. Both beams are reflected by a mirror and recombined at the beam splitter. In one arm of the interferometer, the mirror is mounted on a delay stage which introduces a variable retardation τ to beam. Depending on this retardation, the two beams interfere differently at the output of the beam splitter. In the case of constructive interference, the full power of the incoming beam will (ideally) be detected. The measured power as a function of τ can be used to compute the spectrum of the incoming beam. To show this, we first have to make a few definitions of the quantities that we intend to use:

- $E(t)$ is the time evolution of the *real* electric field of the incoming beam.
- $\tilde{E}(\omega) = \int_{-\infty}^{\infty} E(t)\, \mathrm{e}^{\mathrm{i}\omega t}\mathrm{d}t$ is the frequency spectrum of $E(t)$, and $\tilde{E}(-\omega) = \tilde{E}^{*}(\omega)$
- $E(t) = \frac{1}{2\pi} \int_{-\infty}^{\infty} \tilde{E}(\omega)\, \mathrm{e}^{-\mathrm{i}\omega t}\mathrm{d}\omega = 2\,\Re[\varepsilon(t)]$
- $\varepsilon(t) = \frac{1}{2\pi} \int_{0}^{\infty} \tilde{E}(\omega)\, \mathrm{e}^{-\mathrm{i}\omega t}\mathrm{d}\omega$ is the *complex* electric field of the light
- $I = \langle |\varepsilon(t)|^2 \rangle_t = \frac{1}{(2\pi)^2} \int_{0}^{\infty} |\tilde{E}(\omega)|^2 \mathrm{d}\omega$ is the time-averaged intensity.

We start out with an input signal $\varepsilon(t) = \frac{1}{2\pi} \int_{0}^{\infty} \tilde{E}(\omega)\, \mathrm{e}^{-\mathrm{i}\omega t}\mathrm{d}\omega$, which is

split into two identical beams with amplitudes $\frac{1}{\sqrt{2}}\varepsilon(t)$. After recombination of the two beams, we get an output of

$$|\varepsilon_{\text{out}}(t)|^2 = \left| \frac{1}{2\pi} \int_0^\infty \tilde{E}(\omega) \frac{1}{2}(1 + e^{i\omega\tau}) e^{-i\omega t} \, d\omega \right|^2 \tag{A.51}$$

Now we perform an average over time,

$$
\begin{aligned}
I_{\text{out}} &= \langle |\varepsilon_{\text{out}}(t)|^2 \rangle_t \\
&= \frac{1}{(2\pi)^2} \int_0^\infty \left| \tilde{E}(\omega) \frac{1}{2}(1 + e^{i\omega\tau}) \right|^2 \, d\omega \\
&= \frac{1}{(2\pi)^2} \int_0^\infty |\tilde{E}(\omega)|^2 \frac{1}{2}(1 + \cos(\omega\tau)) \, d\omega \\
&= \frac{1}{2}I_{\text{in}} + \frac{1}{2}\frac{1}{(2\pi)^2} \int_0^\infty |\tilde{E}(\omega)|^2 \cos(\omega\tau) \, d\omega
\end{aligned}
\tag{A.52}
$$

After some rearrangement, we get

$$
\begin{aligned}
2\pi \cdot 4 \left[I_{\text{out}}(\tau) - \frac{1}{2} I_{\text{in}} \right] &= 2 \frac{1}{2\pi} \int_0^\infty |\tilde{E}(\omega)|^2 \cos(\omega\tau) \, d\omega \\
&= \frac{1}{2\pi} \int_{-\infty}^\infty |\tilde{E}(\omega)|^2 e^{-i\omega\tau} \, d\omega
\end{aligned}
\tag{A.53}
$$

The last expression is in the form of an inverse Fourier transform. The spectral intensities can be extracted by another Fourier transform,

$$|\tilde{E}(\omega)|^2 = \int_{-\infty}^\infty 2\pi \cdot 4 \left[I_{\text{out}}(\tau) - \frac{1}{2} I_{\text{in}} \right] e^{i\omega\tau} \, d\tau. \tag{A.54}$$

From Eq. (A.54) we see that from a data series $I_{\text{out}}(\tau)$ the spectral intensities $|\tilde{E}(\omega)|^2$ can easily be computed. For many applications, this information is sufficient. However, the full time evolution of the field $E(t)$ is only accessible if the phase of $\tilde{E}(\omega)$ is known. To measure the spectral phase, more sophisticated methods are required, such as the SPIDER (spectral phase interferometry for direct electric-field reconstruction) technique, which is used for the measurement of ultrashort laser pulses [224]. In addition to a retardation in one arm of the interferometer, a frequency shear is introduced in the other arm using sum-frequency generation in a non-linear crystal.

B

Process Details

B.1. Photonic crystal fabrication

The detailed processing steps for PhC fabrication, including the parameter settings on our specific equipment, are given here. For the hardmask fabrication, we use the term "standard process" when we use a 400 nm thick SiN_x hardmask and apply the cyclic RIE process described in Sec. 3.1 and in Ref. [73]. The thicker hardmasks described in Sec. 3.2 were used only once for optical devices (cf. Sec. 3.4), whereas the standard process was used for the active devices in Chap. 4 as well as for several passive devices presented in Refs. [59,170]. For ICP-RIE etching of InP, ternary and quaternary material, the "standard" process is the one based on Cl_2/N_2, developed by Strasser *et al.* [75,76]. This process was used for all optically characterized devices presented in the present dissertation.

Epitaxy: All layers were grown lattice-matched onto (100) oriented n-doped InP wafers in a MOVPE reactor AIX200/4 from AIXTRON. The grown layer thicknesses for the passive waveguides presented in Sec. 3.4 are: 500 nm bottom cladding InP; 640 nm guiding layer InGaAsP Q1.2, 300 nm top cladding InP. The layers are non-intentionally doped (nid)

and the wafer no. is P2312. The layer stack used for the active devices presented in Secs. 4.2.5 and 4.3 (wafer no. P1856) is shown in Fig. 4.9 of the main text. The same QWs were used for active/passive integration in Sec. 4.4.2 (wafer no. P2017), but there the growth was performed in two steps (growth, patterning, regrowth), as detailed in Appendix B.3. All wafer growths were performed by Dr. E. Gini. It is the only process step that was not carried out by the author of this dissertation.

SiN_x deposition: SiN_x layers were deposited by PECVD (Plasmalab System80Plus from Oxford Instruments). The plasma chemistry is composed of SiH_4 (800 sccm) and NH_3 (30 sccm). The deposition takes place at $300°C$ and 900 mTorr, using 20 W of rf power (13.56 MHz). The deposition rate is on the order of 20 nm/min. The Si/N ratio of the final layers was determined to be 1.35 ± 0.1, using the relation between refractive index (measured by ellipsometry) and nitrogen content found by Mäckel *et al.* [225]. The value was confirmed by an elemental analysis of the layer surface, carried out by XPS (VG ESCALAB 220IXL spectrometer, monochromatic Al $K\alpha$ source, constant analyzer energy mode, 20 eV pass energy, using Scofield's excitation cross sections [226] for a quantification of the elements).

Titanium deposition: Titanium (and all other metals) was deposited using EBPVD. Three different systems were used in the course of time, due to reorganizations in the lab (Univex500, Plassys MEB550S, Plassys MEB550SL). For the hardmask process, slightly different layer thicknesses were used on the different machines (Univex500: 35 nm, Plassys MEB550S: 40 nm, Plassys MEB550SL: 42 nm). The Ti thickness was adjusted to yield sufficient etching resistance in the CHF_3-based dry-etching process for 400 nm of SiN_x. It could not be established with certainty whether the different machines had a different calibration of the thickness or if it was the quality of the Ti layer that was slightly different.

EBL lithography: All nanostructures were written in poly(methyl methacrylate), better known as PMMA. A 6:1 solution of PMMA 950k (from Allresist GmbH) in ethyl lactate was used. The resist was spin-cast on wafers or dies to a thickness of ~ 220 nm. Exposures were carried out in EBL systems from Raith GmbH (Raith150, Raith150TWO). Both machines operate with an acceleration voltage of 30 kV. A write field (WF) of $100 \times 100\,\mu m$ was used. For stuctures exceeding these

dimensions (waveguides), several WFs were stitched together using a motorized stage (piezoelectric) and laser interferometry. Nanoscale elements were written with an aperture of $10\,\mu m$ diameter (step size 8 nm); larger structures were written with a $30\,\mu m$ aperture (step size 30.4 nm). The clearing dose (large area dose) was determined to be $130\,\mu C/cm^2$. Proximity effect corrections of the exposure dose for small features were computed with NanoPECS [69, 227]. After exposure, the samples were developed for 65 s at $22°C$ in MIBK (methyl isobutyl ketone), diluted with isopropanol (IPA), MIBK:IPA $= 1{:}3$. The development was terminated by a 60 s rinse in IPA.

RIE etching of hardmask: Dry-etching of the hardmask was performed by RIE (Plasmalab System80Plus from Oxford Instruments). The reactor is driven by a 13.56 MHz plasma source, and the applied rf power determines both the negative self-bias and the ion density in the plasma. Samples are placed on a carbon stage plate, and the system operates at $18°C$ (cooling water flowing through stage electrode). In a first step, the thin Ti film is etched through the openings in PMMA; in a second step, Ti acts as a mask for SiN_x etching. The detailed process parameters are as follows: Initially, a 30 s Ar plasma (Ar flux: 50 sccm, pressure: 40 mTorr, rf power: ~ 200 W, dc bias: 580 V) is applied to remove residuals of PMMA on the surface of the Ti layer. The plasma chemistry of the Ti etching step is composed of SF_6 (40 sccm) and N_2 (10 sccm) (pressure: 30 mTorr, rf power: ~ 100 W, dc bias: 250-255 V). The etching of SiN_x is performed in alternating cycles of a 140 s pure CHF_3 etching plasma[1] (CHF_3 flux: 60 sccm, pressure: 21 mTorr, rf power: ~ 40 W, dc bias: 260 V), and a 15 s O_2 plasma (O_2 flux: 100 sccm, pressure: 200 mTorr, rf power: ~ 30 W, dc bias: 90-110 V) for the removal of fluorocarbon depositions. Table B.1 summarizes the etching rates measured for the various materials present on a hardmask sample during the different plasma steps.

ICP-RIE etching of InP: The semiconductor materials (InP, In-GaAs, and InGaAsP) were etched by ICP-RIE (Plasmalab System100Plus from Oxford Instruments). The reactor is driven by two

---

[1]After an upgrade of the RIE machine, the relation between rf power and dc self-bias was no longer the same as before. Adjustments were made such that the dc bias was the same as before the upgrade. The rf power had to be changed by up to 20 %, depending on the plasma chemistry. The rf power listed here is the most recent one. Hence, it differs from the value reported in Sec. 3.1 and Ref. [73].

Table B.1. Etching rates of the materials (columns) present on a hardmask sample in the various plasmas (rows) involved in the etching process. For the cyclic part, CHF_3 (O_2), the rate is indicated in units of nm per cycle (cy).

plasma	PMMA	Ti	SiN_x
Ar	~ 20 nm/min	~ 0 nm/min	—
SF_6/N_2	160 nm/min	41 nm/min	220 nm/min
CHF_3 (O_2)	69 nm/cy	1.5 - 2 nm/cy	32 - 37 nm/cy

separate rf power sources (both 13.56 MHz). Samples were "glued" to a Si carrier wafer using a thermally conductive silicone paste (Dow Corning 340 Heat Sink Compound). the carrier wafer is placed on a heatable stage electrode. A thermal contact between stage and carrier wafer is established by helium (brought to the backside of the wafer through an opening in the stage). The standard etching plasma is based on Cl_2 (13 sccm) and N_2 (5 sccm). Additions of Ar (5 sccm) and He (15 sccm) are made. The plasma is operated at $200°C$ and a pressure of 2.2 mTorr. An RIE power of 160 W and an ICP power of 600 W are used, leading to a dc self-bias around 330 V. Typical etching times for a 400 nm SiN_x hardmask are around 90 s, which leads to an etching depth on the order of $3\,\mu m$. After etching, the samples are removed from the carrier wafer, and the silicone paste is wiped off with a Q-tip soaked in IPA, while the front side of the sample is protected by some resist.

Finalization: To remove the residuals of the hardmask, the samples are dipped in HF (typically diluted in water, $HF:H_2O = 1:5$). Facets of waveguides are formed by cleaving the InP substrate along a crystal plane. The breaking point is defined by a scratch made by a diamond tip.

B.2. Contact fabrication

The detailed processing steps for contact fabrication, including the parameter settings on our specific equipment, are given here. Two types of contacts are discussed. The "standard" contact is implemented in a SiN_x layer which acts as an electrical isolation on an active chip. Openings are etched into the SiN_x layer to make contact to the semiconductor. The second type of contacts is the air-bridge contact described in Sec. 4.1.2.

B.2.1. Standard contacts

Planarization: After producing PhC waveguides, the formation of contacts requires a planarization of the perforated surface. Our solution is to deposit a layer of SiN_x, which covers the holes. After the deposition of 300 - 400 nm of SiN_x, the holes are closed, but a surface topology remains (dimples at the location of each hole). To fully close larger structures, such as trenches of access waveguides, a thicker layer would be required. However, to form a $\sim$ 300 nm wide contact, the thickness of the isolation layer should not be exceedingly high. Therefore, we apply a cyclic routine, in which a SiN_x layer is deposited, etched back, deposited, etc. This procedure was described in Sec. 4.1.1 of the main text and illustrations of the planarization process are given by SEM micrographs (Figs. 4.3 and 4.4). The deposition parameters are the same as those of the hardmask (Appendix B.1). The etching is performed by RIE (Plasmalab System80Plus from Oxford Instruments). The plasma chemistry is composed of CHF_3 (55 sccm) and O_2 (5 sccm), and the pressure is 45 mTorr. The rf power is 86 W, resulting in a dc self-bias around 380 V. It is crucial that a calibration be used, since the etching rate can fluctuate in the course of time (it is on the order of 100 nm/min). For easy and accurate determination of layer thicknesses by ellipsometry, a Si calibration sample is well-suited. For the lasers presented in Sec. 4.3.1, the thickness of the final planarization layer was 200 nm.

Contact definition: The standard contacts make use of the planarization layer to provide electrical isolation of the contact pads. Contacts are defined by EBL using a 220 nm PMMA layer that is spin-cast directly onto the SiN_x surface without adhesion promoters. The exposure and development parameters are the same as those for PhC writing. A precise alignment of the contacts with respect to the waveguides is

achieved by means of alignment markers that are produced together with the PhC patterns (deeply etched crosses). Each waveguide has its own set of alignment markers in order to minimize the effect of stage drift in the EBL chamber. The alignment errors are estimated to be below 50 nm (by SEM inspection). After development, the contact openings are transferred into the SiN_x layer by an anisotropic RIE process. The same CHF_3 plasma as for the hardmask fabrication (CHF_3 flux: 60 sccm, pressure: 21 mTorr, rf power: ~ 40 W, dc bias: 260 V) is applied for 20 min, but no intermediate O_2 plasma steps are used (the PMMA layer would be removed too quickly). Finally, the PMMA residuals are removed by an O_2 ashing for 60 s directly in the RIE reactor (O_2 flux: 50 sccm, pressure: 80 mTorr, rf power: 100 W, dc bias: 365 V).

Metalization: The contacts are evaporated by EBPVD. For the active devices presented in Chap. 4, a Univex500 system was used. First, the p-type contacts on the top side of the samples are deposited. Contact pads are formed in a $\sim 1\,\mu m$ thick layer of the copolymer P(MMA/MAA) that is spin-cast on the samples in two equal steps (the two-step procedure helps to planarize any large etched features on the samples). The pads are defined by EBL (30 keV, $30\,\mu m$ aperture, $100\,\mu m$ WF, $290\,\mu C/cm^2$ dose, 30.4 nm step size) and developed in MIBK:IPA = 1:3 for 90 s (rinsing in IPA for 60 s). In the evaporator chamber, an Ar^+ sputtering is performed (in order to clean the contact surface and to improve metal adhesion [175]), before the metal layers are deposited (5 nm Pt, 15 nm Ti, 40 nm Pt, 500 nm Au). Lift-off is performed in acetone, and the contacts are annealed for 2 min at $370°C$ in a SiC containment. Then, the InP substrate is lapped down to a thickness of $\sim 150\,\mu m$. An additional $\sim 10\,\mu m$ are removed in a BCK etching solution ($CH_3COOH:HBr:K_2Cr_2O_7 = 1:1:1$, 10 min at room temperature [188]), which leaves a smooth contact surface. Finally, the n-type backside contact is evaporated (30 nm Ti, 40 nm Pt, 100 nm Au) after performing another in-situ Ar^+ sputtering.

Finalization: Laser bars are cleaved from the dies and soldered onto copper blocks using an indium paste at $180°C$. To measure the performance of the devices, a contact needle is used to access the sub-mm contact pad and connect it to a current source (Newport Modular Controller, Model 8000). The contact to the backside of the devices is established via the copper block. A LabVIEW program was written to automate the recording of P-I-V characteristics.

B.2.2. Air-bridge contacts

The fabrication of air-bridge contacts is somewhat more complicated than that of the standard contacts. Since the SiN_x layer serves as a sacrificial layer here, the electrical isolation of the contact pads has to be provided by a different material. We use Photo BCB (4000-series of CycloteneTM resins from the Dow Chemical Company). It is a photosensitive material that can also be patterned by EBL [179]. We use a dilution of one part of Cyclotene 4022-35 in 4 parts of mesitylene, and spin-cast it directly on InP surfaces. At higher concentrations of resin, an adhesion promoter (AP3000) is necessary. Layer thicknesses of 150 - 200 nm are obtained after hard-curing.

To form isolating pads for the contacts of active devices, Photo BCB is applied to the samples after the PhC fabrication. To avoid exposure of the BCB film by ambient light, the samples must be transferred to the EBL chamber in the dark. The structures are exposed at 5 keV using a $30 \, \mu m$ aperture and a dose of $130 \, \mu C/cm^2$. The development is done for 4 min in DS3000 at 35°C, followed by 2 min of DS3000 at room temperature. Then the BCB is hard-cured (1 hour at 250°C, slow temperature ramp-up) in a programmable oven from Koyo Thermal Systems Co.

After the definition of the BCB pads, the planarization of the PhC holes is carried out in the same way as for the standard contacts. Also, EBL for the contact strips on the waveguides is the same. However, at the same time, large openings are defined on the BCB pads. To form the contacts on the BCB layer, the SiN_x has to be removed. This somewhat complicates the dry-etching of the contact openings. An O_2 ashing must be avoided, because this would severely attack the BCB. Only a CHF_3 plasma is used. The PMMA residuals are removed in acetone at 50°C (at least 10 min).

The rest of the process is similar to that of the standard contacts. Only after the evaporation of the backside contact, an additional step is introduced: the SiN_x layer is removed in HF. To facilitate the penetration of HF underneath the contacts, the design of the metalization must include some openings at regular intervals. After releasing the free-standing contacts, the samples are rinsed in IPA and left to dry.

B.3. Active/passive integration

The detailed fabrication steps for active/passive integration are presented here. The process was used in Sec. 4.4.2 for laser devices which emit into passive waveguides. Two types of passive output waveguides were used, substrate-type and membrane-type (cf. Fig. 4.21 of the main text). The latter requires an additional wet-etching step, which will also be detailed here.

To integrate active and passive sections, we choose the approach of butt-joint transitions. This involves two epitaxial growths steps. First, the lower part of the waveguide including the QWs is grown. Then the QWs are removed in those area of the wafer that are to be passive. Finally, the upper part of the waveguide is grown. This procedure leads to slightly different thicknesses of the waveguide layer in active and passive sections. At the interfaces, there is a risk for spurious reflections due to imperfect mode matching (not assessed quantitatively here).

Growth of active material: The lower part of the waveguide is grown on an InP substrate: the lower InP cladding, the lower part of the In-GaAsP waveguide, and the InGaAs QWs (separated by InGaAsP barriers). The growth is terminated by a 12 nm of InGaAs (top surface for regrowth) and 10 nm of InP (sacrificial layer to be etched away before regrowth).

Definition of passive sections: After the first growth step, the QWs need to be removed for the passive sections. The wafer is covered by 100 nm of SiN_x (PECVD), and the active regions of the wafer are masked by photoresist (630 nm AZ1505). After exposure (48 mJ/cm^2) and development ($\sim$ 35 s in KOH 0.8%), the SiN_x is etched down by RIE (3 cycles CHF_3 etching with the PhC recipe, 40 s of SF_6/N_2 etching as in the PhC recipe, 3 min O_2 ashing at 50 mTorr and 100 W rf power). Then the InP sacrificial layer is etched down in HCl:H_2O = 3:1 (60 s). Now, the step (mask + sacrificial InP) is measured by a surface step profiler (Tencor Alpha-Step 500) to set a reference point for later etching depth verification. The QWs are etched by ICP-RIE (9 sccm CH_4, 50 sccm H_2, 10 sccm Ar, 135 W RIE power, no ICP power, 100°C, 30 mTorr, with intermediate O_2 ashings). The etching rate is about 7 nm/min. After dry-etching of the QWs, the SiN_x hardmask is re-

moved in HF.[2] To obtain a clean surface for regrowth, the wafer is dipped into pure sulfuric acid (60 s at room temperature), then the rest of the sacrificial InP layer is removed in HCl:H$_2$O $= 3$:1, and the wafer is rinsed in a water bath (15 min) as well as on a wet spinner (5 min at 1000 rpm with running water, 40 s at 4000 rpm dry).

Growth of upper waveguide part: The rest of the waveguide is grown on the clean InGaAsP surface: upper part of waveguide, upper InP cladding, InGaAs capping layer. The cleanliness of the wafer surface is crucial for a high-quality regrowth.

Marker fabrication: The trench and PhC waveguides that shall be integrated over the active/passive interfaces have to be aligned with the active and passive sections on the wafer. Therefore, alignment markers are needed. During photolithography for the removal of the QWs in the passive areas of the wafer, markers are included in the design. However, after regrowth of the upper part of the waveguide, the interface steps between active and passive sections are too shallow to be easily visible in an SEM. In an optical microscope, on the other hand, the markers are sharp and clear. Therefore, another lithography and lift-off process is applied to add metal on the existing markers. This is done in an image reversal process using AZ5214E resist. Finally, the metal (10 nm Cr, 100 nm Au, 10 nm Cr) is evaporated by EBPVD (Univex500), and the lift-off is performed in acetone at 50°C (until the metal), followed by a cleaning in NMP:ethylenglycol $= 1$:1.

Laser fabrication: The lasers are fabricated using the processes for PhC fabrication (Appendix B.1) and contact fabrication (Appendix B.2).

Formation of a membrane-type output: For a membrane-type output section, another lithography step is required. The active part of the sample is covered by resist (AZ1505). First, the chip is immersed into an etching solution that removes the InGaAs capping layer selectively (InGaAsP guiding layer should not be affected). Then, the membrane

---

[2]An alternative to dry-etching would be a wet-etching process. Photolithography would be done directly on the semiconductor surface. After the removal of the sacrificial InP layer in HCl:H$_2$O $= 3$:1, the QWs can be etched down to an etch stop (which has to be added below the QW during epitaxy) in H$_2$O:H$_2$SO$_4$:H$_2$O$_2$ $= 10$:1:1 (rate: 20 - 30 nm/min).

is released in HCl:H_2O = 3:1 (10 min at 0°C). For InGaAs etching, a solution of HF/CrO_3 was used, which can provide an InGaAs/InGaAsP selectivity of up to 50 [228]. The mixture is prepared from HF (40 wt. % in H_2O) and CrO_3 (10 wt. % in H_2O). They are mixed at a volume ratio of HF/CrO_3=0.2 and then diluted in H_2O at HF/CrO_3:H_2O = 1:3. The etching time to remove the InGaAs capping layer was 50 s at room temperature. The etching rates determined in preliminary experiments are 430 - 470 nm/min for InGaAs and 800 - 825 nm/min for SiN_x.

Bibliography

[1] S. E. Miller, "Integrated optics - an introduction," *Bell System Tech. J.*, vol. 48, no. 7, pp. 2059–2069, 1969. 2

[2] R. N. Hall, R. O. Carlson, T. J. Soltys, G. E. Fenner, and J. D. Kingsley, "Coherent light emission from GaAs junctions," *Phys. Rev. Lett.*, vol. 9, no. 9, pp. 366–368, 1962. 2

[3] H. Rupprecht, J. M. Woodall, and C. D. Pettit, "Efficient visible electroluminescence at $300°$K from $Ga_{1-x}Al_xAs$ p-n junctions grown by liquid-phase epitaxy," *Appl. Phys. Lett.*, vol. 11, no. 3, pp. 81–83, 1967. 2

[4] E. A. J. Marcatili, "Dielectric rectangular waveguide and directional coupler for integrated optics," *Bell System Tech. J.*, vol. 48, no. 7, pp. 2071–2102, 1969. 2

[5] E. A. J. Marcatili, "Bends in optical dielectric guides," *Bell System Tech. J.*, vol. 48, no. 7, pp. 2103–2032, 1969. 2

[6] I. Hayashi, M. B. Panish, P. W. Foy, and S. Sumski, "Junction lasers which operate continuously at room temperature," *Appl. Phys. Lett.*, vol. 17, no. 3, pp. 109–111, 1970. 2

[7] K. C. Kao and G. A. Hockham, "Dielectric-fibre surface waveguides for optical frequencies," *Proceedings IEE*, vol. 113, no. 7, pp. 1151–1158, 1966. 2

[8] T. Tamir, *Integrated Optics*, 2nd ed., Ser.: Topics in Applied Physics. Berlin: Springer, 1979. 2

[9] R. G. Hunsperger, *Integrated Optics*, 6th ed. New York: Springer, 2009. 2

[10] R. J. Mears, L. Reekie, I. M. Jauncey, and D. N. Payne, "Low-noise erbium-doped fibre amplifier operating at 1.54 mu m," *Electron. Lett.*, vol. 23, no. 19, pp. 1026–1028, 1987. 2

[11] C. G. P. Herben, D. H. P. Maat, X. J. M. Leijtens, M. R. Leys, Y. S. Oei, and M. K. Smit, "Polarization independent dilated

WDM cross-connect on InP," *IEEE Photonics Technol. Lett.*, vol. 11, no. 12, pp. 1599–1601, 1999. 3

[12] E. Parra and J. R. Lowell, "Toward applications of slow light technology," *Optics & Photonics News*, vol. 18, no. 11, pp. 40–45, 2007. 3

[13] D. F. Welch, F. A. Kish, R. Nagarajan, C. H. Joyner, R. P. Schneider, Jr., V. G. Dominic, M. L. Mitchell, S. G. Grubb, T.-K. Chiang, D. D. Perkins, and A. C. Nilsson, "The realization of large-scale photonic integrated circuits and the associated impact on fiber-optic communication systems," *J. Lightwave Technol.*, vol. 24, no. 12, pp. 4674–4683, 2006. 3

[14] M. Kato, P. Evans, S. Corzine, J. Gheorma, M. Fisher, M. Raburn, A. Dentai, R. Salvatore, I. Lyubomirsky, A. Nilsson, J. Rahn, R. Nagarajan, C. Tsai, B. Behnia, J. Stewart, D. Christini, M. Missey, A. Spannagel, D. Lambert, S. Agashe, P. Liu, D. Pavinski, M. Reffle, R. Schneider, M. Ziari, C. Joyner, F. Kish, and D. Welch, "Transmitter PIC for 10-channel x 40 Gb/s per channel polarization-multiplexed RZ-DQPSK modulation," in *Proc. OFC: 2009 Conference on Optical Fiber Communication.* Optical Society of America, 2009. 3

[15] R. Nagarajan, J. Rahn, M. Kato, J. Pleumeekers, D. Lambert, V. Lal, H.-S. Tsai, A. Nilsson, A. Dentai, M. Kuntz, R. Malendevich, J. Tang, J. Zhang, T. Butrie, M. Raburn, B. Little, W. Chen, G. Goldfarb, V. Dominic, B. Taylor, M. Reffle, F. Kish, and D. Welch, "10 channel, 45.6 Gb/s per channel, polarization-multiplexed DQPSK, InP receiver photonic integrated circuit," *J. Lightwave Technol.*, vol. 29, no. 4, pp. 386–395, 2011. 3

[16] S. C. Nicholes, M. L. Masanovic, B. Jevremovic, E. Lively, L. A. Coldren, and D. J. Blumenthal, "An 8 x 8 InP monolithic tunable optical router (MOTOR) packet forwarding chip," *J. Lightwave Technol.*, vol. 28, no. 4, pp. 641–650, 2010. 3, 4

[17] M. Notomi, A. Shinya, K. Nozaki, T. Tanabe, S. Matsuo, E. Kuramochi, T. Sato, H. Taniyama, and H. Sumikura, "Low-power nanophotonic devices based on photonic crystals towards dense photonic network on chip," *IET Circ. Devices Syst.*, vol. 5, no. 2, pp. 84–93, 2011. 3

[18] H. P. M. M. Ambrosius, X. J. M. Leijtens, T. de Vries, J. Bolk, E. Smalbrugge, and M. K. Smit, "A generic InP-based photonic integration technology," in *Proc. 23rd International Conference on Indium Phosphide and Related Materials*. VDE Verlag, 2011, pp. 367–370. 4, 5

[19] L. A. Coldren, "Recent advances in InP PICs," in *Proc. 21st International Conference on Indium Phosphide and Related Materials*, 2009, pp. 1–2. 4

[20] R. Kaiser, K. O. Velthaus, T. Brast, B. Maul, M. Gruner, H. Klein, M. Hamacher, D. Hoffmann, and M. Schell, "Monolithic flip-chip compatible twin-IQ Mach-Zehnder modulators for hybrid assembly onto high capacity optical transmitter boards," in *Proc. 23rd International Conference on Indium Phosphide and Related Materials*. VDE Verlag, 2011, pp. 419–422. 4

[21] R. Nagarajan, M. Kato, J. Pleumeekers, P. Evans, S. Corzine, S. Hurtt, A. Dentai, S. Murthy, M. Missey, R. Muthiah, R. A. Salvatore, C. Joyner, R. Schneider, Jr., M. Ziari, F. Kish, and D. Welch, "InP photonic integrated circuits," *IEEE J. Sel. Top. Quantum Electron.*, vol. 16, no. 5, pp. 1113–1125, 2010. 5

[22] L. A. Coldren, S. C. Nicholes, L. Johansson, S. Ristic, R. S. Guzzon, E. J. Norberg, and U. Krishnamachari, "High performance InP-based photonic ICs - A tutorial," *J. Lightwave Technol.*, vol. 29, no. 4, pp. 554–570, 2011. 5, 6

[23] E. J. Skogen, J. S. Barton, S. P. Denbaars, and L. A. Coldren, "A quantum-well-intermixing process for wavelength-agile photonic integrated circuits," *IEEE J. Sel. Top. Quantum Electron.*, vol. 8, no. 4, pp. 863–869, 2002. 5

[24] V. Tolstikhin, "Regrowth-free multi-guide vertical integration in inp for optical communications," in *Proc. 23rd International Conference on Indium Phosphide and Related Materials*. VDE Verlag, 2011, pp. 363–366. 5

[25] M. Paniccia, V. Krutul, R. Jones, O. Cohen, J. Bowers, A. Fang, and H. Park, "A hybrid silicon laser: Silicon photonics technology for future tera-scale computing," *White Paper, Intel Corporation*, 2006. 5

[26] N. Keil, C. Zawadzki, Z. Zhang, J. Wang, N. Mettbach, N. Grote, and M. Schell, "Polymer PLC as an optical integration bench," in *Proc. OFC: 2011 Conference on Optical Fiber Communication.* Optical Society of America, 2011. 6

[27] M. T. Hill, "Silicon nanophotonics: Nanolasers with a twist," *Nat. Photonics*, vol. 5, no. 3, pp. 130–131, 2011. 6

[28] P. Dumon, G. Roelkens, W. Bogaerts, D. Van Thourhout, J. Wouters, S. Beckx, P. Jaenen, and R. Baets, "Basic photonic wire components in silicon-on-insulator," in *Proc. 2nd IEEE International Conference on Group IV Photonics*, 2005, pp. 189–191. 6

[29] A. Mekis, J. C. Chen, I. Kurland, S. H. Fan, P. R. Villeneuve, and J. D. Joannopoulos, "High transmission through sharp bends in photonic crystal waveguides," *Phys. Rev. Lett.*, vol. 77, no. 18, pp. 3787–3790, 1996. 6

[30] S.-Y. Lin, E. Chow, V. Hietala, P. R. Villeneuve, and J. D. Joannopoulos, "Experimental demonstration of guiding and bending of electromagnetic waves in a photonic crystal," *Science*, vol. 282, no. 5387, pp. 274–276, 1998. 6

[31] S. Assefa, S. J. McNab, and Y. A. Vlasov, "Transmission of slow light through photonic crystal waveguide bends," *Opt. Lett.*, vol. 31, no. 6, pp. 745–747, 2006. 6

[32] J. W. S. Rayleigh, "On the remarkable phenomenon of crystalline reflexion described by Professor Stokes," *Philos. Mag.*, vol. 26, no. 160, pp. 256–265, 1888. 6

[33] J. C. Slater, *Microwave Electronics*, 3rd ed., Ser.: The Bell Telephone Laboratories Series.   New York: Van Nostrand, 1954. 6

[34] H. Kogelnik and C. V. Shank, "Stimulated emission in a periodic structure," *Appl. Phys. Lett.*, vol. 18, no. 4, pp. 152–154, 1971. 7

[35] C. V. Shank, J. E. Bjorkholm, and H. Kogelnik, "Tunable distributed-feedback dye laser," *Appl. Phys. Lett.*, vol. 18, no. 9, pp. 395–396, 1971. 7

[36] K. Ohtaka, "Energy band of photons and low-energy photon diffraction," *Phys. Rev. B*, vol. 19, no. 10, pp. 5057–5067, 1979. 7

[37] P. A. Hiltner and I. M. Krieger, "Diffraction of light by ordered suspensions," *J. Phys. Chem.*, vol. 73, no. 7, pp. 2386–2389, 1969. 7

[38] E. Yablonovitch, "Inhibited spontaneous emission in solid-state physics and electronics," *Phys. Rev. Lett.*, vol. 58, no. 20, pp. 2059–2062, 1987. 7

[39] S. John, "Strong localization of photons in certain disordered dielectric superlattices," *Phys. Rev. Lett.*, vol. 58, no. 23, pp. 2486–2489, 1987. 7

[40] T. F. Krauss, R. M. De La Rue, and S. Brand, "Two-dimensional photonic-bandgap structures operating at near infrared wavelengths," *Nature*, vol. 383, no. 6602, pp. 699–702, 1996. 7

[41] J. C. Knight, J. Broeng, T. A. Birks, and P. S. J. Russell, "Photonic band gap guidance in optical fibers," *Science*, vol. 282, no. 5393, pp. 1476–1478, 1998. 7, 37

[42] J. O'Brien, O. Painter, R. Lee, C. C. Cheng, A. Yariv, and A. Scherer, "Lasers incorporating 2D photonic bandgap mirrors," *Electron. Lett.*, vol. 32, no. 24, pp. 2243–2244, 1996. 7

[43] T. D. Happ, A. Markard, M. Kamp, A. Forchel, S. Anand, J. L. Gentner, and N. Bouadma, "Nanofabrication of two-dimensional photonic crystal mirrors for $1.5\,\mu$m short cavity lasers," *J. Vac. Sci. Technol. B*, vol. 19, no. 6, pp. 2775–2778, 2001. 7

[44] S. Mahnkopf, "Photonic crystal based widely tunable laser diodes and integrated optoelectronic components," Ph.D. dissertation, Bayerische Julius-Maximilians-Universität Würzburg, 2005. 7, 33

[45] O. Painter, R. K. Lee, A. Scherer, A. Yariv, J. D. O'Brien, P. D. Dapkus, and I. Kim, "Two-dimensional photonic band-gap defect mode laser," *Science*, vol. 284, no. 5421, pp. 1819–1821, 1999. 7

[46] O. J. Painter, A. Husain, A. Scherer, J. D. O'Brien, I. Kim, and P. D. Dapkus, "Room temperature photonic crystal defect lasers at near-infrared wavelengths in InGaAsP," *J. Lightwave Technol.*, vol. 17, no. 11, pp. 2082–2088, 1999. 8

[47] Y. Yamamoto, S. Machida, and G. Björk, "Microcavity semiconductor laser with enhanced spontaneous emission," *Phys. Rev. A*, vol. 44, no. 1, pp. 657–668, 1991. 8

[48] H. Altug, D. Englund, and J. Vučković, "Ultrafast photonic crystal nanocavity laser," *Nat. Phys.*, vol. 2, no. 7, pp. 484–488, 2006. 8

[49] H. G. Park, S. H. Kim, S. H. Kwon, Y. G. Ju, J. K. Yang, J. H. Baek, S. B. Kim, and Y. H. Lee, "Electrically driven single-cell photonic crystal laser," *Science*, vol. 305, no. 5689, pp. 1444–1447, 2004. 8, 123

[50] B. Ellis, M. A. Mayer, G. Shambat, T. Sarmiento, J. Harris, E. E. Haller, and J. Vučković, "Ultralow-threshold electrically pumped quantum-dot photonic-crystal nanocavity laser," *Nat. Photonics*, vol. 5, no. 5, pp. 297–300, 2011. 8, 9, 11

[51] A. Sugitatsu and S. Noda, "Room temperature operation of 2D photonic crystal slab defect-waveguide laser with optical pump," *Electron. Lett.*, vol. 39, no. 2, pp. 213–215, 2003. 8

[52] A. Sugitatsu, T. Asano, and S. Noda, "Characterization of line-defect-waveguide lasers in two-dimensional photonic-crystal slabs," *Appl. Phys. Lett.*, vol. 84, no. 26, pp. 5395–5397, 2004. 8

[53] N. Susa, "Threshold gain and gain-enhancement due to distributed-feedback in two-dimensional photonic-crystal lasers," *J. Appl. Phys.*, vol. 89, no. 2, pp. 815–823, 2001. 9

[54] M. Kamp, T. Happ, S. Mahnkopf, G. Duan, S. Anand, and A. Forchel, "Semiconductor photonic crystals for optoelectronics," *Physica E*, vol. 21, no. 2-4, pp. 802–808, 2004. 9, 121

[55] A. Talneau, L. LeGratiet, J. L. Gentner, A. Berrier, M. Mulot, S. Anand, and S. Olivier, "High external efficiency in a monomode full-photonic-crystal laser under continuous wave electrical injection," *Appl. Phys. Lett.*, vol. 85, no. 11, pp. 1913–1915, 2004. 9

[56] S. de Rossi, I. Sagnes, L. LeGratiet, A. Talneau, A. Berrier, M. Mulot, S. Anand, and J. L. Gentner, "Longitudinal mode selection in constricted photonic crystal guides and electrically injected lasers," *J. Lightwave Technol.*, vol. 23, no. 3, pp. 1363–1368, 2005. 9, 121

[57] M. Notomi, T. Tanabe, A. Shinya, E. Kuramochi, H. Taniyama, S. Mitsugi, and M. Morita, "Nonlinear and adiabatic control of high-Q photonic crystal nanocavities," *Opt. Express*, vol. 15, no. 26, pp. 17 458–17 481, 2007. 9

[58] A. Talneau, M. Mulot, S. Anand, and P. Lalanne, "Compound cavity measurement of transmission and reflection of a tapered single-line photonic-crystal waveguide," *Appl. Phys. Lett.*, vol. 82, no. 16, pp. 2577–2579, 2003. 10, 82, 112

[59] R. Kappeler, "Reducing the propagation losses of slab photonic crystal waveguides for active photonic devices," Ph.D. dissertation, Diss. ETH No. 20485, 2012. 10, 83, 85, 155

[60] P. Friedli, "Electrical characterization of contacts for active photonic crystals," Master's thesis, ETH Zurich, 2008. 11

[61] A. Berrier, M. Mulot, G. Malm, M. Östling, and S. Anand, "Carrier transport through a dry-etched InP-based two-dimensional photonic crystal," *J. Appl. Phys.*, vol. 101, no. 12, p. 123101, 2007. 11

[62] S. Matsuo, A. Shinya, T. Kakitsuka, K. Nozaki, T. Segawa, T. Sato, Y. Kawaguchi, and M. Notomi, "High-speed ultracompact buried heterostructure photonic-crystal laser with 13 fJ of energy consumed per bit transmitted," *Nat. Photonics*, vol. 4, no. 9, pp. 648–654, 2010. 11

[63] K. Takeda, T. Sato, A. Shinya, K. Nozaki, C.-H. Chen, Y. Kawaguchi, H. Taniyama, M. Notomi, and S. Matsuo, "80°C continuous wave operation of photonic-crystal nanocavity lasers," in *Proc. 23rd International Conference on Indium Phosphide and Related Materials.* VDE Verlag, 2011, pp. 260–263. 11

[64] M. Notomi, K. Yamada, A. Shinya, J. Takahashi, C. Takahashi, and I. Yokohama, "Extremely large group-velocity dispersion of line-defect waveguides in photonic crystal slabs," *Phys. Rev. Lett.*, vol. 87, no. 25, 2001. 12

[65] Y. A. Vlasov, M. O'Boyle, H. F. Hamann, and S. J. McNab, "Active control of slow light on a chip with photonic crystal waveguides," *Nature*, vol. 438, no. 7064, pp. 65–69, 2005. 12

[66] H. Gersen, T. J. Karle, R. J. P. Engelen, W. Bogaerts, J. P. Korterik, N. F. van Hulst, T. F. Krauss, and L. Kuipers, "Real-space observation of ultraslow light in photonic crystal waveguides," *Phys. Rev. Lett.*, vol. 94, p. 073903, 2005. 12

[67] S. Combrié, E. Weidner, A. DeRossi, S. Bansropun, S. Cassette, A. Talneau, and H. Benisty, "Detailed analysis by Fabry-Pérot method of slab photonic crystal line-defect waveguides and cavities in aluminium-free material system," *Opt. Express*, vol. 14, no. 16, pp. 7353–7361, 2006. 12

[68] P. Strasser, R. Flückiger, R. Wüest, F. Robin, and H. Jäckel, "InP-based compact photonic crystal directional coupler with large operation range," *Opt. Express*, vol. 15, no. 13, pp. 8472–8478, 2007. 13

[69] R. Wüest, "Nanometer-scale technology and near-field characterization of InP-based planar photonic-crystal devices," Ph.D. dissertation, Diss. ETH No. 17146, 2007. 13, 157

[70] A. Talneau, "Bidimensional photonic crystals for integrated optics," *Int. J. Mater. Prod. Technol.*, vol. 34, no. 4, pp. 399–420, 2009. 13, 33

[71] R. M. De La Rue and S. A. De La Rue, "Introduction to photonic crystals and photonic band-gaps," in *Photonic Crystals: Physics and Technology*, C. Sibilia, T. M. Benson, M. Marciniak, and T. Szoplik, Eds.   Springer Milan, 2008, pp. 7–25. 13, 33

[72] P. Kaspar, R. Kappeler, D. Erni, and H. Jäckel, "Relevance of the light line in planar photonic crystal waveguides with weak vertical confinement," *Opt. Express*, vol. 19, no. 24, pp. 24 344–24 353, 2011. 13, 31, 122, 127

[73] P. Kaspar, Y. Jeyaram, H. Jäckel, A. Foelske, R. Kötz, and S. Bellini, "Silicon nitride hardmask fabrication using a cyclic CHF_3-based reactive ion etching process for vertical profile nanostructures," *J. Vac. Sci. Technol. B*, vol. 28, no. 6, pp. 1179–1186, 2010. 14, 16, 45, 46, 155, 157

[74] P. Kaspar, S. Holzapfel, E. J. Windhab, and H. Jäckel, "Self-aligned mask renewal for anisotropically etched circular micro- and nanostructures," *J. Micromech. Microeng.*, vol. 21, no. 11, p. 115003, 2011. 14, 16, 45, 61

[75] P. Strasser, R. Wüest, F. Robin, D. Erni, and H. Jäckel, "Detailed analysis of the influence of an inductively coupled plasma reactive-ion etching process on the hole depth and shape of photonic crystals in InP/InGaAsP," *J. Vac. Sci. Technol. B*, vol. 25, no. 2, pp. 387–393, 2007. 14, 45, 52, 65, 70, 72, 73, 155

[76] P. Strasser, "The development of a fabrication process for passive photonic crystal devices in InP/InGaAsP," Ph.D. dissertation, Diss. ETH No. 18062, 2008. 14, 70, 78, 81, 117, 147, 155

[77] F. Karouta, B. Docter, P. Kaspar, E. J. Geluk, and M. K. Smit, "Three level masking for improved aspect ratio InP-based photonic crystals," in *Proc. 20th International Conference on Indium Phosphide and Related Materials.* IEEE, 2008, pp. 508–511. 14, 16, 66, 71

[78] P. Kaspar, C. Fougner, R. Kappeler, and H. Jäckel, "Limitations of Cl_2/O_2-based ICP-RIE of deep holes for planar photonic crystals in indium phosphide," *Phys. Status Solidi C*, vol. 9, no. 2, pp. 239–242, 2012. 14, 69

[79] P. Kaspar, R. Kappeler, H. Jäckel, and Hafner, "Toward low-loss photonic crystal waveguides in InP/InGaAsP heterostructures," *Opt. Lett.*, vol. 37, no. 17, pp. 3717–3719, 2012. 14, 76

[80] P. Kaspar, R. Kappeler, P. Friedli, and H. Jäckel, "Air-bridge contact fabrication for in-plane active photonic crystal devices," in *Proc. 22nd International Conference on Indium Phosphide and Related Materials (IPRM 2010)*, 2010, pp. 304–307. 15, 88, 95

[81] J. O. Grepstad, P. Kaspar, O. Solgaard, I.-R. Johansen, and A. S. Sudbø, "Photonic-crystal membranes for optical detection of single nano-particles, designed for biosensor application," *Opt. Express*, vol. 20, no. 7, pp. 7954–7965, 2012. 16

[82] J. D. Joannopoulos, S. G. Johnson, J. N. Winn, and R. D. Meade, *Photonic Crystals: Molding the Flow of Light*, 2nd ed. Princeton: Princeton University Press, 2008. 18, 21

[83] K. Sakoda, *Optical Properties of Photonic Crystals*, 2nd ed., Ser.: Springer Series in Optical Sciences. Berlin: Springer, 2005. 18, 21

[84] K. Inoue and K. Ohtaka, *Photonic Crystals: Physics, Fabrication and Applications*, Ser.: Springer Series in Optical Science. Berlin: Springer, 2004. 18

[85] J.-M. Lourtioz, H. Benisty, V. Berger, J.-M. Gérard, D. Maystre, and A. Tchelnokov, *Photonic Crystals: Towards Nanoscale Photonic Devices.* Berlin: Springer, 2005. 18

[86] K. Busch, S. Lölkes, R. B. Wehrspohn, and H. Föll, *Photonic Crystals: Advances in Design, Fabrication, and Characterization.* Weinheim: Wiley-VCH Verlag GmbH & Co. KGaA, 2004. 18

[87] R. L. Liboff, *Introductory Quantum Mechanics.* San Francisco: Holden-Day, Inc., 1980. 19, 150

[88] N. W. Ashcroft and N. D. Mermin, *Solid State Physics.* South Melbourne: Brooks/Cole, 1976. 20

[89] P. Kaspar, R. Kappeler, D. Erni, and H. Jäckel, "Electromagnetic group, energy, and phase velocity of Bloch modes," *in preparation*, 2012. 21

[90] A. Yariv and P. Yeh, "Electromagnetic propagation in periodic stratified media. II. Birefringence, phase matching, and x-ray lasers," *J. Opt. Soc. Am.*, vol. 67, no. 4, pp. 438–448, 1977. 21, 27, 30

[91] P. Yeh, "Electromagnetic propagation in birefringent layered media," *J. Opt. Soc. Am.*, vol. 69, no. 5, pp. 742–756, 1979. 21, 27, 30

[92] G. B. Whitham, "Group velocity and energy propagation for three-dimensional waves," *Commun. Pure Appl. Math.*, vol. 14, no. 3, pp. 675–691, 1961. 22

[93] L. Brillouin, *Wave Propagation and Group Velocity*, Ser.: Pure and applied physics. New York: Academic Press, 1960. 23, 26, 28

[94] J. D. Jackson, *Classical Electrodynamics*, 3rd ed. New York: John Wiley & Sons, Inc., 1999. 23, 26, 28

[95] M. J. Lighthill, "Group velocity," *Journal of the Institute of Mathematics and Its Applications*, vol. 1, no. 1, pp. 1–28, 1965. 24, 26

[96] R. L. Smith, "The velocities of light," *Am. J. Phys.*, vol. 38, no. 8, pp. 978–984, 1970. 26

[97] S. C. Bloch, "Eighth velocity of light," *Am. J. Phys.*, vol. 45, no. 6, pp. 538–549, 1977. 26

[98] J. Li, T. P. White, L. O'Faolain, A. Gomez-Iglesias, and T. F. Krauss, "Systematic design of flat band slow light in photonic crystal waveguides," *Opt. Express*, vol. 16, no. 9, pp. 6227–6232, 2008. 26

[99] A. Yariv and P. Yeh, *Optical Waves in Crystals*. New York: Wiley & Sons, 1984. 26

[100] L. D. Landau and E. M. Lifshitz, *Electrodynamics of Continuous Media*, 2nd ed., Ser.: Course of Theoretical Physics. Oxford: Pergamon Press, 1984. 26, 28

[101] M. A. Biot, "General theorems on the equivalence of group velocity and energy transport," *Physical Review*, vol. 105, no. 4, pp. 1129–1137, 1957. 26

[102] H. Kogelnik and H. P. Weber, "Rays, stored energy, and power flow in dielectric waveguides," *J. Opt. Soc. Am.*, vol. 64, no. 2, pp. 174–185, 1974. 26

[103] B. Lombardet, L. A. Dunbar, R. Ferrini, and R. Houdré, "Fourier analysis of Bloch wave propagation in photonic crystals," *J. Opt. Soc. Am. B*, vol. 22, no. 6, pp. 1179–1190, 2005. 30, 41

[104] S. Hughes, L. Ramunno, J. F. Young, and J. E. Sipe, "Extrinsic optical scattering loss in photonic crystal waveguides: Role of fabrication disorder and photon group velocity," *Phys. Rev. Lett.*, vol. 94, no. 3, p. 033903, 2005. 31

[105] L. O'Faolain, S. A. Schulz, D. M. Beggs, T. P. White, M. Spasenović, L. Kuipers, F. Morichetti, A. Melloni, S. Mazoyer, J. P. Hugonin, P. Lalanne, and T. F. Krauss, "Loss engineered slow light waveguides," *Opt. Express*, vol. 18, no. 26, pp. 27 627–27 638, 2010. 31

[106] L. C. Andreani and M. Agio, "Intrinsic diffraction losses in photonic crystal waveguides with line defects," *Appl. Phys. Lett.*, vol. 82, no. 13, pp. 2011–2013, 2003. 31

[107] L. C. Andreani and D. Gerace, "Light-matter interaction in photonic crystal slabs," *Phys. Status Solidi B*, vol. 244, no. 10, pp. 3528–3539, 2007. 33

[108] T. F. Krauss, "Planar photonic crystal waveguide devices for integrated optics," *Phys. Status Solidi A*, vol. 197, no. 3, pp. 688–702, 2003. 33

[109] R. März, *Integrated Optics: Design and Modeling.* Norwood: Artech House, 1995. 33

[110] Z. Zhu and T. G. Brown, "Full-vectorial finite-difference analysis of microstructured optical fibers," *Opt. Express*, vol. 10, no. 17, pp. 853–864, 2002. 35

[111] A.-S. Bonnet-Ben Dhia and P. Joly, *Mathematical Analysis and Numerical Approximation of Optical Waveguides*, Ser.: Frontiers in Applied Mathematics. Philadelphia: Siam, 2001, pp. 273–324. 36

[112] D. Marcuse, *Theory of Dielectric Optical Waveguides*, 2nd ed., Ser.: Quantum Electronics: Principles and Applications. Boston: Academic Press, 1991. 36, 37, 38

[113] T. A. Birks, P. J. Roberts, P. S. J. Russell, D. M. Atkin, and T. J. Shepherd, "Full 2-D photonic bandgaps in silica/air structures," *Electron. Lett.*, vol. 31, no. 22, pp. 1941–1943, 1995. 37

[114] S. G. Johnson, S. Fan, P. R. Villeneuve, J. D. Joannopoulos, and L. A. Kolodziejski, "Guided modes in photonic crystal slabs," *Phys. Rev. B*, vol. 60, no. 8, pp. 5751–5758, 1999. 38

[115] S. G. Johnson and J. D. Joannopoulos, "Block-iterative frequency-domain methods for Maxwell's equations in a planewave basis," *Opt. Express*, vol. 8, no. 3, pp. 173–190, 2001. 39

[116] R. Kappeler, P. Kaspar, P. Friedli, and H. Jäckel, "Design proposal for a low-loss in-plane active photonic crystal waveguide with vertical electrical carrier injection," *Opt. Express*, vol. 20, no. 8, pp. 9264–9275, 2012. 40, 85, 113, 123, 128

[117] W. Kuang and J. D. O'Brien, "Reducing the out-of-plane radiation loss of photonic crystal waveguides on high-index substrates," *Opt. Lett.*, vol. 29, no. 8, pp. 860–862, 2004. 41, 84, 123

[118] A. P. Mahorowala and H. H. Sawin, "Etching of polysilicon in inductively coupled Cl_2 and HBr discharges. III. Photoresist mask faceting, sidewall deposition, and microtrenching," *J. Vac. Sci. Technol. B*, vol. 20, no. 3, pp. 1077–1083, 2002. 44

[119] A. Midha, S. K. Murad, and J. M. R. Weaver, "Anisotropic pattern transfer of fine resist features to silicon nitride via an intermediate titanium layer," *Microelectron. Eng.*, vol. 35, no. 1-4, pp. 99–102, 1997. 44

[120] F. Laermer and A. Schilp, "Method for anisotropic plasma etching of substrates," US Patent 5 498 312, 12 March, 1996. 45, 60

[121] C. F. Carlström, R. van der Heijden, F. Karouta, R. W. van der Heijden, H. W. M. Salemink, and E. van der Drift, "Cl_2/O_2-inductively coupled plasma etching of deep hole-type photonic crystals in InP," *J. Vac. Sci. Technol. B*, vol. 24, no. 1, pp. L6–L9, 2006. 45, 70, 73

[122] R. Grover, J. V. Hryniewicz, O. S. King, and V. Van, "Process development of methane-hydrogen-argon-based deep dry etching of InP for high aspect-ratio structures with vertical facet-quality sidewalls," *J. Vac. Sci. Technol. B*, vol. 19, no. 5, pp. 1694–1698, 2001. 46

[123] J. A. O'Neill and J. Singh, "Role of the chamber wall in low-pressure high-density etching plasmas," *J. Appl. Phys.*, vol. 77, no. 2, pp. 497–504, 1995. 46

[124] M. Schaepkens, R. C. M. Bosch, T. E. F. M. Standaert, G. S. Oehrlein, and J. M. Cook, "Influence of reactor wall conditions on etch processes in inductively coupled fluorocarbon plasmas," *J. Vac. Sci. Technol. A*, vol. 16, no. 4, pp. 2099–2107, 1998. 46, 60

[125] D. C. Marra and E. S. Aydil, "Effect of H_2 addition on surface reactions during CF_4/H_2 plasma etching of silicon and silicon dioxide films," *J. Vac. Sci. Technol. A*, vol. 15, no. 5, pp. 2508–2517, 1997. 47, 60

[126] G. S. Oehrlein, "Reactive ion etching," in *Handbook of Plasma Processing Technology: Fundamentals, Etching, Deposition and Surface Interactions*, S. M. Rossnagel, J. J. Cuomo, and W. D. Westwood, Eds. Park Ridge: Noyes Publications, 1990, Chap. 8. 47, 60

[127] M. Schaepkens, T. E. F. M. Standaert, N. R. Rueger, P. G. M. Sebel, G. S. Oehrlein, and J. M. Cook, "Study of the SiO_2-to-Si_3N_4 etch selectivity mechanism in inductively coupled fluorocarbon plasmas and a comparison with the SiO_2-to-Si mechanism," *J. Vac. Sci. Technol. A*, vol. 17, no. 1, pp. 26–37, 1999. 47, 49, 57, 60, 138

[128] B. E. E. Kastenmeier, P. J. Matsuo, J. J. Beulens, and G. S. Oehrlein, "Chemical dry etching of silicon nitride and silicon dioxide using $CF_4/O_2/N_2$ gas mixtures," *J. Vac. Sci. Technol. A*, vol. 14, no. 5, pp. 2802–2813, 1996. 47, 60

[129] D. Briggs, *Surface Analysis of Polymers by XPS and Static SIMS*, Ser.: Cambridge Solid State Science Series. Cambridge: Cambridge University Press, 1998. 47

[130] J. W. Coburn and H. F. Winters, "Plasma etching - Discussion of mechanisms," *J. Vac. Sci. Technol.*, vol. 16, no. 2, pp. 391–403, 1979. 49, 60

[131] J. Dulak, B. J. Howard, and C. Steinbrüchel, "Etch mechanism in the reactive ion etching of silicon-nitride," *J. Vac. Sci. Technol. A*, vol. 9, no. 3, pp. 775–778, 1991. 49, 60

[132] T. C. Mele, J. Nulman, and J. P. Krusius, "Selective and anisotropic reactive ion etch of LPCVD silicon-nitride with CHF_3 based gases," *J. Vac. Sci. Technol. B*, vol. 2, no. 4, pp. 684–687, 1984. 49, 60, 90

[133] J. T. Cherian and D. G. Castner, "ESCA characterization of fluoropolymer film residue on carbon-fiber-reinforced plastic components," *Surf. Interface Anal.*, vol. 29, no. 11, pp. 729–734, 2000. 49, 50

[134] C. D. Wagner, A. V. Naumkin, A. Kraut-Vass, J. W. Allison, C. J. Powell, and J. R. Rumble. (2007, August 27) NIST x-ray photoelectron spectroscopy database, version 3.5. National

Institute of Standards and Technology. Gaithersburg. [Online]. Available: http://srdata.nist.gov/xps/ 49, 50

[135] G. Z. Yin and D. W. Jillie, "Orthogonal design for process optimization and its application in plasma-etching," *Solid State Technol.*, vol. 30, no. 5, pp. 127–132, 1987. 52, 137

[136] N. R. Rueger, J. J. Beulens, M. Schaepkens, M. F. Doemling, J. M. Mirza, T. E. F. M. Standaert, and G. S. Oehrlein, "Role of steady state fluorocarbon films in the etching of silicon dioxide using CHF$_3$ in an inductively coupled plasma reactor," *J. Vac. Sci. Technol. A*, vol. 15, no. 4, pp. 1881–1889, 1997. 60

[137] T. E. F. M. Standaert, C. Hedlund, E. A. Joseph, G. S. Oehrlein, and T. J. Dalton, "Role of fluorocarbon film formation in the etching of silicon, silicon dioxide, silicon nitride, and amorphous hydrogenated silicon carbide," *J. Vac. Sci. Technol. A*, vol. 22, no. 1, pp. 53–60, 2004. 60

[138] R. Wüest, P. Strasser, F. Robin, D. Erni, and H. Jäckel, "Fabrication of a hard mask for InP based photonic crystals: Increasing the plasma-etch selectivity of poly(methyl methacrylate) versus SiO$_2$ and SiN$_x$," *J. Vac. Sci. Technol. B*, vol. 23, no. 6, pp. 3197–3201, 2005. 60

[139] G. S. Oehrlein and Y. Kurogi, "Sidewall surface chemistry in directional etching processes," *Mater. Sci. Eng. R-Rep.*, vol. 24, no. 4, pp. 153–183, 1998. 60

[140] M. Boufnichel, P. Lefaucheux, S. Aachboun, R. Dussart, and P. Ranson, "Origin, control and elimination of undercut in silicon deep plasma etching in the cryogenic process," *Microelectron. Eng.*, vol. 77, no. 3-4, pp. 327–336, 2005. 60

[141] M. J. de Boer, J. G. E. Gardeniers, H. V. Jansen, E. Smulders, M.-J. Gilde, G. Roelofs, J. N. Sasserath, and M. Elwenspoek, "Guidelines for etching silicon MEMS structures using fluorine high-density plasmas at cryogenic temperatures," *J. Microelectromech. Syst.*, vol. 11, no. 4, pp. 385–401, 2002. 60

[142] R. A. H. Heinecke, "Control of relative etch rates of SiO$_2$ and Si in plasma etching," *Solid-State Electron.*, vol. 18, no. 12, pp. 1146–1147, 1975. 60

[143] J.-K. Lee, I.-Y. Jang, S.-H. Lee, C.-K. Kim, and S. H. Moon, "Cyclic deposition/etching process to etch a bowing-free SiO_2 contact hole," *J. Electrochem. Soc.*, vol. 156, no. 8, pp. D269–D274, 2009. 60

[144] H. W. Lehmann and R. Widmer, "Profile control by reactive sputter etching," *J. Vac. Sci. Technol.*, vol. 15, no. 2, pp. 319–326, 1978. 60

[145] M. Schaepkens, G. S. Oehrlein, and J. M. Cook, "Effect of radio frequency bias power on SiO_2 feature etching in inductively coupled fluorocarbon plasmas," *J. Vac. Sci. Technol. B*, vol. 18, no. 2, pp. 848–855, 2000. 60

[146] V. Yanev, S. Krischok, A. Opitz, H. Wurmus, J. A. Schaefer, N. Schwesinger, and S.-I.-U. Ahmed, "Influence of the RF power on the deposition rate and the chemical surface composition of fluorocarbon films prepared in dry etching gas plasma," *Surf. Sci.*, vol. 566-568, pp. 1229–1233, 2004. 60

[147] W. R. Harshbarger, R. A. Porter, T. A. Miller, and P. Norton, "Study of optical emission from an rf plasma during semiconductor etching," *Appl. Spectrosc.*, vol. 31, no. 3, pp. 201–207, 1977. 60

[148] K. Wasa, M. Kitabatake, and H. Adachi, *Thin Film Materials Technology*. New York: William Andrew Publishing/Noyes, 2004. 63

[149] R. Gottscho, C. Jurgensen, and D. Vitkavage, "Microscopic uniformity in plasma etching," *J. Vac. Sci. Technol. B*, vol. 10, no. 5, pp. 2133–2147, 1992. 66

[150] D. J. Chin, S. H. Dhong, and G. J. Long, "Structural effects on a submicron trench process," *J. Electrochem. Soc.*, vol. 132, no. 7, pp. 1705–1707, 1985. 67

[151] N. Müller-Fischer, H. Bleuler, and E. J. Windhab, "Dynamically enhanced membrane foaming," *Chem. Eng. Sci.*, vol. 62, no. 16, pp. 4409–4419, 2007. 67

[152] V. Schadler and E. J. Windhab, "Continuous membrane emulsification by using a membrane system with controlled pore distance," *Desalination*, vol. 189, no. 1-3, pp. 130–135, 2006. 67

[153] A. J. Abrahamse, A. van der Padt, R. M. Boom, and W. B. C. de Heij, "Process fundamentals of membrane emulsification: Simulation with CFD," *Aiche J.*, vol. 47, no. 6, pp. 1285–1291, 2001. 67

[154] A. J. Abrahamse, R. van Lierop, R. G. M. van der Sman, A. van der Padt, and R. M. Boom, "Analysis of droplet formation and interactions during cross-flow membrane emulsification," *J. Membr. Sci.*, vol. 204, no. 1-2, pp. 125–137, 2002. 67

[155] S. J. Peng and R. A. Williams, "Controlled production of emulsions using a crossflow membrane part I: Droplet formation from a single pore," *Chem. Eng. Res. Des.*, vol. 76, no. A8, pp. 894–901, 1998. 68

[156] C. van Rijn, M. van der Wekken, W. Nijdam, and M. Elwenspoek, "Deflection and maximum load of microfiltration membrane sieves made with silicon micromachining," *J. Microelectromech. Syst.*, vol. 6, no. 1, pp. 48–54, 1997. 68, 69

[157] G. F. Cardinale and R. W. Tustison, "Fracture strength and biaxial modulus measurement of plasma silicon nitride films," *Thin Solid Films*, vol. 207, no. 1-2, pp. 126–130, 1992. 69

[158] R. L. Edwards, G. Coles, and W. N. Sharpe, "Comparison of tensile and bulge tests for thin-film silicon nitride," *Exp. Mech.*, vol. 44, no. 1, pp. 49–54, 2004. 69

[159] J. Gaspar, P. Ruther, and O. Paul, "Mechanical characterization of thin-film composites using the load-deflection response of multilayer membranes - elastic and fracture properties," *Mater. Res. Soc. Symp. Proc.*, vol. 977, pp. FF08–08 – FF08–13, 2007. 69

[160] S. J. Pearton and F. Ren, "Science of dry etching of III-V materials," *J. Mater. Sci. Mater. Electron.*, vol. 5, no. 1, pp. 1–12, 1994. 69, 70

[161] T. Ide, J.-I. Hashimoto, K. Nozaki, E. Mizuta, and T. Baba, "InP etching by HI/Xe inductively coupled plasma for photonic-crystal device fabrication," *Jpn. J. Appl. Phys.*, vol. 45, no. 3, pp. L102–L104, 2006. 69

[162] N. Sultana, W. Zhou, T. P. LaFave, Jr., and D. L. MacFarlane, "HBr based inductively coupled plasma etching of high aspect ratio nanoscale trenches in InP: Considerations for photonic applications," *J. Vac. Sci. Technol. B*, vol. 27, no. 6, pp. 2351–2356, 2009. 69

[163] S. J. Pearton, "Reactive ion etching of III-V semiconductors," *Int. J. Mod. Phys. B*, vol. 8, no. 14, pp. 1781–1876, 1994. 69

[164] T. R. Hayes, "Dry etching of In-based semiconductors," in *Indium Phosphide and Related Materials: Processing, Technology, and Devices*, A. Katz, Ed.   Norwood: Artech House, Inc., 1992, Chap. 8. 69

[165] R. van der Heijden, M. S. P. Andriesse, C.-F. Carlström, E. van der Drift, E.-J. Geluk, R. W. van der Heijden, F. Karouta, P. Nouwens, Y. S. Oei, T. de Vries, and H. W. M. Salemink, "Deep dry etching process development for photonic crystals in InP-based planar waveguides," *Proc. SPIE*, vol. 5450, pp. 523–532, 2004. 70

[166] M. Volatier, D. Duchesne, R. Morandotti, R. Arès, and V. Aimez, "Extremely high aspect ratio GaAs and GaAs/AlGaAs nanowaveguides fabricated using chlorine ICP etching with N_2-promoted passivation," *Nanotechnology*, vol. 21, no. 13, p. 134014, 2010. 70

[167] S. Miyakuni, R. Hattori, K. Sato, H. Takano, and O. Ishihara, "Low ion energy electron cyclotron resonance etching of InP using a Cl_2/N_2 mixture," *J. Appl. Phys.*, vol. 78, no. 9, pp. 5734–5738, 1995. 70

[168] K. H. Lee, S. Guilet, G. Patriarche, I. Sagnes, and A. Talneau, "Smooth sidewall in InP-based photonic crystal membrane etched by N_2-based inductively coupled plasma," *J. Vac. Sci. Technol. B*, vol. 26, no. 4, pp. 1326–1333, 2008. 70

[169] R. Kappeler, P. Kaspar, and H. Jäckel, "Loss-relevant structural imperfections in substrate-type photonic crystal waveguides," *J. Lightwave Technol.*, vol. 29, no. 21, pp. 3156–3166, 2011. 75, 84

[170] R. Kappeler, P. Kaspar, and H. Jäckel, "Propagation loss computation of W1 photonic crystal waveguides using the cutback

technique with the 3D-FDTD method," *Phot. Nano. Fund. Appl.*, vol. 9, no. 3, pp. 235–247, 2011. 78, 81, 148, 155

[171] A. F. Oskooi, D. Roundy, M. Ibanescu, P. Bermel, J. D. Joannopoulos, and S. G. Johnson, "MEEP: A flexible free-software package for electromagnetic simulations by the FDTD method," *Comput. Phys. Commun.*, vol. 181, no. 3, pp. 687–702, 2010. 81

[172] N. Shahid, S. Naureen, M. Y. Li, M. Swillo, and S. Anand, "Novel postetch process to realize high quality photonic crystals in InP," *J. Vac. Sci. Technol. B*, vol. 29, no. 3, p. 031202, 2011. 83

[173] P. Bandaru and E. Yablonovitch, "Semiconductor surface-molecule interactions," *J. Electrochem. Soc.*, vol. 149, no. 11, pp. G599–G602, 2002. 85, 123

[174] J. S. Yu, S. H. Kim, and T. I. Kim, "PtTiPtAu and PdTiPtAu ohmic contacts to p-InGaAs," in *Proc. 1997 IEEE International Symposium on Compound Semiconductors*, 1998, pp. 175–178. 92

[175] U. Hammer, "Sub-micron InP/GaAsSb/InP double heterojunction bipolar transistors for ultra high-speed digital integrated circuits," Ph.D. dissertation, Diss. ETH No. 18502, 2009. 92, 160

[176] E. G. Woelk, H. Kräutle, and H. Beneking, "Measurement of low resistive ohmic contacts on semiconductors," *IEEE Trans. Electron Devices*, vol. 33, no. 1, pp. 19–22, 1986. 92

[177] K. Busch and S. John, "Liquid-crystal photonic-band-gap materials: The tunable electromagnetic vacuum," *Phys. Rev. Lett.*, vol. 83, no. 5, pp. 967–970, 1999. 93

[178] S. W. Leonard, J. P. Mondia, H. M. van Driel, O. Toader, S. John, K. Busch, A. Birner, U. Gösele, and V. Lehmann, "Tunable two-dimensional photonic crystals using liquid crystal infiltration," *Phys. Rev. B*, vol. 61, no. 4, pp. R2389–R2392, 2000. 93

[179] J. M. Catchmark, G. P. Lavallee, M. Rogosky, and Y. Lee, "Direct sub-100-nm patterning of an organic low-k dielectric for electrical and optical interconnects," *J. Electron. Mater.*, vol. 34, pp. L12–L15, 2005. 95, 161

[180] H. Kroemer, "A proposed class of heterojunction injection lasers," *Proc. IEEE*, vol. 51, no. 12, pp. 1782–1783, 1963. 96

[181] H. C. Casey and M. B. Panish, *Heterostructure Lasers, Part A*, Ser.: Quantum Electronics - Principles and Applications. New York: Academic Press, 1978. 96

[182] R. Dingle, W. Wiegmann, and C. H. Henry, "Quantum states of confined carriers in very thin $Al_xGa_{1-x}As$-GaAs-$Al_xGa_{1-x}As$ heterostructures," *Phys. Rev. Lett.*, vol. 33, no. 14, pp. 827–830, 1974. 96

[183] J. P. van der Ziel, R. Dingle, R. C. Miller, W. Wiegmann, and W. A. Nordland, Jr., "Laser oscillation from quantum states in very thin GaAs-$Al_{0.2}Ga_{0.8}As$ multilayer structures," *Appl. Phys. Lett.*, vol. 26, no. 8, pp. 463–465, 1975. 96

[184] R. D. Dupuis, P. D. Dapkus, N. Holonyak, Jr., E. A. Rezek, and R. Chin, "Room-temperature laser operation of quantum-well $Ga_{1-x}Al_xAs$-GaAs laser diodes grown by metalorganic chemical vapor deposition," *Appl. Phys. Lett.*, vol. 32, no. 5, pp. 295–297, 1978. 96

[185] C. H. Henry, "The origin of quantum wells and the quantum well laser," in *Quantum Well Lasers*, Ser.: Quantum Electronics - Principles and Applications, P. S. Zory, Ed. Boston: Academic Press, Inc., 1993, pp. 1–16. 96

[186] Y. Arakawa and H. Sakaki, "Multidimensional quantum well laser and temperature dependence of its threshold current," *Appl. Phys. Lett.*, vol. 40, no. 11, pp. 939–941, 1982. 97

[187] Z. Alferov, "Double heterostructure lasers: Early days and future perspectives," *IEEE J. Sel. Top. Quantum Electron.*, vol. 6, no. 6, pp. 832–840, 2000. 97

[188] H.-J. Lohe, "Monolithic integration of mode locked laser diodes with a fast absorber in InGaAsP/InP technology using MOVPE based local growth," Ph.D. dissertation, Diss. ETH No. 17057, 2007. 98, 117, 160

[189] M. Rosenzweig, M. Möhrle, H. Düser, and H. Venghaus, "Threshold-current analysis of InGaAs-InGaAsP multiquantum

well separate-confinement lasers," *IEEE J. Quantum Electron.*, vol. 27, no. 6, pp. 1804–1811, 1991. 99, 104, 107

[190] L. A. Coldren and S. W. Corzine, *Diode Lasers and Photonic Integrated Circuits*, 1st ed., Ser.: Wiley Series in Microwave and Optical Engineering.   New York: Wiley & Sons, 1995. 99, 112, 113

[191] P. W. A. Mc Ilroy, A. Kurobe, and Y. Uematsu, "Analysis and application of theoretical gain curves to the design of multi-quantum-well lasers," *IEEE J. Quantum Electron.*, vol. 21, no. 12, pp. 1958–1963, 1985. 99

[192] G. P. Agrawal and N. K. Dutta, *Semiconductor Lasers*, 2nd ed. Boston: Kluwer Academic Publishers, 1993. 100, 101, 105, 149, 151, 152

[193] T. Makino, "Analytical formulas for the optical gain of quantum wells," *IEEE J. Quantum Electron.*, vol. 32, no. 3, pp. 493–501, 1996. 101

[194] M. Levinshtein, S. Rumyantsev, and M. Shur, *Ternary and Quaternary III-V Compounds*, Ser.: Handbook series on semiconductor parameters.   World Scientific, 1999, vol. 2. 102, 106

[195] M. Fukuda, *Reliability and Degradation of Semiconductor Lasers and LEDs*.   Norwood: Artech House, Inc., 1991. 104, 116

[196] R. W. H. Engelmann, C.-L. Shieh, and C. Shu, "Multiquantum well lasers: Threshold considerations," in *Quantum Well Lasers*, Ser.: Quantum Electronics - Principles and Applications, P. S. Zory, Ed.   Boston: Academic Press, Inc., 1993, Chap. 3, pp. 131–188. 104, 105

[197] N. A. Pikhtin, S. O. Sliptchenko, Z. N. Sokolova, and I. S. Tarasov, "Analysis of threshold current density and optical gain in InGaAsP quantum well lasers," *Semiconductors*, vol. 36, no. 3, pp. 344–353, 2002. 104, 118

[198] L. V. Asryan, N. A. Gun'ko, A. S. Polkovnikov, G. G. Zegrya, R. A. Suris, P.-K. Lau, and T. Makino, "Threshold characteristics of InGaAsP/InP multiple quantum well lasers," *Semicond. Sci. Technol.*, vol. 15, no. 12, pp. 1131–1140, 2000. 105, 112

[199] N. Tessler and G. Eistenstein, "On carrier injection and gain dynamics in quantum well lasers," *IEEE J. Quantum Electron.*, vol. 29, no. 6, pp. 1586–1595, 1993. 105

[200] (2005, January 26) New semiconductor materials. characteristics and properties. Ioffe, Physico-Technical Institute. St. Petersburg. [Online]. Available: http://www.ioffe.rssi.ru/SVA/NSM/ 106

[201] A. Tomita and A. Suzuki, "Carrier-induced lasing wavelength shift for quantum well laser diodes," *IEEE J. Quantum Electron.*, vol. 23, no. 7, pp. 1155–1159, 1987. 110

[202] A. S. Polkovnikov and G. G. Zegrya, "Auger recombination in semiconductor quantum wells," *Phys. Rev. B*, vol. 58, no. 7, pp. 4039–4056, 1998. 112

[203] S. O. Slipchenko, Z. N. Sokolova, N. A. Pikhtin, K. S. Borschev, D. A. Vinokurov, and I. S. Tarasov, "Finite time of carrier energy relaxation as a cause of optical-power limitation in semiconductor lasers," *Semiconductors*, vol. 40, no. 8, pp. 990–995, 2006. 112, 113, 114

[204] G. N. Childs, S. Brand, and R. A. Abram, "Intervalence band absorption in semiconductor laser materials," *Semicond. Sci. Technol.*, vol. 1, no. 2, pp. 116–120, 1986. 112

[205] V. Mikhaelashvili, N. Tessler, R. Nagar, G. Eisenstein, A. G. Dentai, S. Chandrasakhar, and C. H. Joyner, "Temperature dependent loss and overflow effects in quantum well lasers," *IEEE Photonics Technol. Lett.*, vol. 6, no. 11, pp. 1293–1296, 1994. 112

[206] (2012) Synopsys device simulation. Synopsys. Mountain View. [Online]. Available: http://www.synopsys.com/Tools/TCAD/DeviceSimulation/ 113

[207] (2012) TCAD, 3D device simulation. Silvaco, Inc. Santa Clara. [Online]. Available: http://www.silvaco.com/products/vwf/atlas/victory/victory_br.html 113

[208] D. Z. Garbuzov and V. B. Khalfin, "Single quantum well In-GaAsP and AlGaAs lasers: A study of some peculiarities," in *Quantum Well Lasers*, Ser.: Quantum Electronics - Principles and Applications, P. S. Zory, Ed. Boston: Academic Press, Inc., 1993, Chap. 6, pp. 277–327. 113

[209] E. G. Golikova, V. A. Kureshov, A. Y. Leshko, A. V. Lyutetskiĭ, N. A. Pikhtin, Y. A. Ryaboshtan, G. A. Skrynnikov, I. S. Tarasov, and Z. I. Alferov, "Properties of wide-mesastripe InGaAsP/InP lasers," *Semiconductors*, vol. 34, no. 7, pp. 853–856, 2000. 113

[210] R. Wüest, D. Erni, P. Strasser, F. Robin, H. Jäckel, B. C. Buchler, A. F. Koenderink, V. Sandoghdar, and R. Harbers, "A "standing-wave meter" to measure dispersion and loss of photonic-crystal waveguides," *Appl. Phys. Lett.*, vol. 87, no. 26, p. 261110, 2005. 121

[211] M.-K. Seo, K.-Y. Jeong, J.-K. Yang, Y.-H. Lee, H.-G. Park, and S.-B. Kim, "Low threshold current single-cell hexapole mode photonic crystal laser," *Appl. Phys. Lett.*, vol. 90, no. 17, p. 171122, 2007. 123

[212] H. Watanabe and T. Baba, "High-efficiency photonic crystal microlaser integrated with a passive waveguide," *Optics Express*, vol. 16, no. 4, pp. 2694–2698, 2008. 124

[213] F. Fiedler, A. Schlachetzki, and G. Klein, "Material-selective etching of InP and an InGaAsP alloy," *J. Mater. Sci.*, vol. 17, no. 10, pp. 2911–2918, 1982. 125

[214] P. Eliáš, I. Kostič, J. Šoltýs, and S. Hasenöhrl, "Wet-etch bulk micromachining of (100) InP substrates," *J. Micromech. Microeng.*, vol. 14, no. 8, pp. 1205–1214, 2004. 125

[215] A. S. Hedayat, N. J. A. Sloane, and J. Stufken, *Orthogonal Arrays*, Ser.: Springer Series in Statistics. New York: Springer, 1999. 135, 136

[216] C. F. Laywine and G. L. Mullen, "Mutually orthogonal latin squares," in *Discrete Mathematics Using Latin Squares*, Ser.: Series in Discrete Mathematics and Optimization. New York: John Wiley & Sons, Inc., 1998. 135

[217] G. Taguchi, "How to construct an orthogonal array and how to apply it," in *System of Experimental Design*, D. Clausing, Ed. White Plains, New York: UNIPUB/Kraus International Publications, 1987, vol. 2, Chap. 38, pp. 1021–1028. 136

[218] D. Zwillinger, *Handbook of Differential Equations*, 3rd ed. San Diego: Academic Press, 1998. 138

[219] B. E. A. Saleh and M. C. Teich, *Fundamentals of Photonics*, 2nd ed., Ser.: Wiley Series in Pure and Applied Optics. Hoboken: Wiley & Sons, Inc., 2007. 143

[220] B. W. Hakki and T. L. Paoli, "cw degradation at 300°K of GaAs double-heterostructure junction lasers. II. Electronic gain," *J. Appl. Phys.*, vol. 44, no. 9, pp. 4113–4119, 1973. 143

[221] S. W. Corzine, R.-H. Yan, and L. A. Coldren, "Optical gain in III-V bulk and quantum well semiconductors," in *Quantum Well Lasers*, Ser.: Quantum Electronics - Principles and Applications, P. S. Zory, Ed. Boston: Academic Press, Inc., 1993, Chap. 1, pp. 17–96. 149, 150

[222] E. O. Kane, "Band structure of indium antimonide," *J. Phys. Chem. Solids*, vol. 1, no. 4, pp. 249–261, 1957. 151

[223] P. R. Griffiths and J. A. Haseth, *Fourier Transform Infrared Spectrometry*, 2nd ed., Ser.: Chemical Analysis: A Series of Monographs on Analytical Chemistry and Its Applications. Hoboken: Wiley & Sons, Inc., 2007. 153

[224] C. Iaconis and I. A. Walmsley, "Self-referencing spectral interferometry for measuring ultrashort optical pulses," *IEEE J. Quantum Electron.*, vol. 35, no. 4, pp. 501–509, 1999. 154

[225] H. Mäckel and R. Lüdemann, "Detailed study of the composition of hydrogenated SiN_x layers for high-quality silicon surface passivation," *J. Appl. Phys.*, vol. 92, no. 5, pp. 2602–2609, 2002. 156

[226] J. H. Scofield, "Hartree-Slater subshell photoionization cross-sections at 1254 and 1487 eV," *J. Electron Spectrosc. Relat. Phenom.*, vol. 8, no. 2, pp. 129–137, 1976. 156

[227] F. Robin, S. Costea, G. Stark, R. Wüest, P. Strasser, H. Jäckel, A. Rampe, M. Levermann, and G. Piaszenski, "Accurate proximity-effect correction of nanoscale structures with NanoPECS," *Raith Application Note*, pp. 1–4, 2005. 157

[228] H. Huang, X. Y. Wang, X. M. Ren, Q. Wang, and Y. Q. Huang, "Selective wet etching of InGaAs/InGaAsP in $HCl/HF/CrO_3$ solution: Application to vertical taper structures in integrated op-

toelectronic devices," *J. Vac. Sci. Technol. B*, vol. 23, no. 4, pp. 1650–1653, 2005. 164

List of Publications

- Peer-reviewed articles
- Conference and workshop contributions without peer review
- E Contribution of mainly experimental nature
- T Contribution of mainly theoretical nature

E● **P. Kaspar**, R. Kappeler, H. Jäckel, and C. Hafner, "Toward low-loss photonic crystal waveguides in InP/InGaAsP heterostructures," *Opt. Lett.*, vol. 37, no. 17, pp. 3717–3719, 2012.

E○ J. O. Grepstad, **P. Kaspar**, O. Solgaard, I.-R. Johansen, and A. S. Sudbø, "Optical imaging system designed for biosensing using a photonic crystal membrane to detect nanoparticles," in *Imaging Systems and Applications*, OSA Technical Digest (online). Optical Society of America, p. IM4C.2, 2012.

E● Y. Fedoryshyn, P. Ma, J. Faist, **P. Kaspar**, R. Kappeler, M. Beck, J. F. Holzman, and H. Jäckel, "Three operation modes for Tbit/s all-optical switching with intersubband transitions in InGaAs/AlAs/AlAsSb quantum wells," *IEEE J. Quantum Electron.*, vol. 48, no. 7, pp. 885–890, 2012.

T● R. Kappeler, **P. Kaspar**, P. Friedli, and H. Jäckel, "Design proposal for a low-loss in-plane active photonic crystal waveguide with vertical electrical carrier injection," *Opt. Express*, vol. 20, no. 8, pp. 9264–9275, 2012.

E● J. O. Grepstad, **P. Kaspar**, O. Solgaard, I.-R. Johansen, and A. S. Sudbø, "Photonic-crystal membranes for optical detection of single nano-particles, designed for biosensor application," *Opt. Express*, vol. 20, no. 7, pp. 7 954–7 965, 2012.

T● **P. Kaspar**, R. Kappeler, D. Erni, and H. Jäckel, "Relevance of the light line in planar photonic crystal waveguides with weak vertical confinement," *Opt. Express*, vol. 19, no. 24, pp. 24 344–24 353, 2011.

E● **P. Kaspar**, C. Fougner, R. Kappeler, and H. Jäckel, "Limitations of Cl_2/O_2-based ICP-RIE of deep holes for planar photonic crystals in indium phosphide," *Phys. Status Solidi C*, vol. 9, no. 2, pp. 239–242, 2012.

E● **P. Kaspar**, S. Holzapfel, and E. J. Windhab, and H. Jäckel, "Self-aligned mask renewal for anisotropically etched circular micro- and nanostructures," *J. Micromech. Microeng.*, vol. 21, no. 11, 2011.

T● R. Kappeler, **P. Kaspar**, and H. Jäckel, "Loss-relevant structural imperfections in substrate-type photonic crystal waveguides," *J. Lightwave Technol.*, vol. 29, no. 21, pp. 3156–3166, 2011.

T● R. Kappeler, **P. Kaspar**, and H. Jäckel, "Propagation loss computation of W1 photonic crystal waveguides using the cutback technique with the 3D-FDTD method," *Phot. Nano. Fund. Appl.*, vol. 9, no. 3, pp. 235–247, 2011.

E● P. Ma, **P. Kaspar**, P. Strasser, Y. Fedoryshyn, and H. Jäckel, "Compact inline resonant photonic crystal Fabry-Pérot cavities for TM-polarized light," *IEEE Photon. Technol. Lett.*, vol. 23, no. 4, pp. 224–226, 2011.

E● P. Ma, P. Strasser, **P. Kaspar**, and H. Jäckel, "Compact and integrated TM-pass photonic crystal waveguide polarizer in InGaAsP-InP," *IEEE Photon. Technol. Lett.*, vol. 22, no. 24, pp. 1808–1810, 2010.

E● **P. Kaspar**, Y. Jeyaram, H. Jäckel, A. Foelske, R. Kötz, and S. Bellini, "Silicon nitride hardmask fabrication using a cyclic CHF_3-based reactive ion etching process for vertical profile nanostructures," *J. Vac. Sci. Technol. B*, vol. 28, no. 6, pp. 1179–1186, 2010.

E○ P. Ma, **P. Kaspar**, and H. Jäckel, "Low-loss photonic crystal defect waveguides and taper designs in InP/InGaAsP for transverse magnetic polarized light," *Jpn. J. Appl. Phys.*, vol. 49, no. 6, 2010, pp. 06GG06 1–3.

E○ **P. Kaspar**, R. Kappeler, P. Friedli, and H. Jäckel, "Air-bridge contact fabrication for in-plane active photonic crystal devices," in *2010 22nd International Conference on Indium Phosphide and Related Materials (IPRM 2010)*, 2010, Conference Paper, p. 4 pp.

E● Y. Fedoryshyn, M. Beck, **P. Kaspar**, and H. Jäckel, "Characterization of Si volume- and delta-doped InGaAs grown by molecular beam epitaxy," *J. Appl. Phys.*, vol. 107, no. 9, 2010.

E● P. Ma, **P. Kaspar**, Y. Fedoryshyn, P. Strasser, and H. Jäckel, "InP-based planar photonic crystal waveguide in honeycomb lattice geometry for TM-polarized light," *Opt. Lett.*, vol. 34, no. 10, pp. 1558–1560, 2009.

E○ **P. Kaspar**, R. Kappeler, F. Karouta, F. Robin, P. Strasser, and H. Jäckel, "The impact of metallic contacts on propagation losses of an underlying photonic crystal waveguide," in *Proc. SPIE*, vol. 7031, 2008, Conference Paper, p. 70310A.

E○ V. Callegari, **P. Kaspar**, P. Strasser, U. Sennhauser, and H. Jäckel, "Fabrication of 2D-InP photonic crystals by means of hole-etching using focused ion beam and characterization of the hole shape, damage and surface roughness induced by the fabrication process," in *Workshop FIB for Photonics*, 2008, pp. 30–33.

E○ F. Karouta, B. Docter, **P. Kaspar**, E. J. Geluk, and M. K. Smit, "Three level masking for improved aspect ratio InP-based photonic crystals," in *2008 IEEE 20th International Conference on Indium Phosphide and Related Materials*, ser. Conference Proceedings - Indium Phosphide and Related Materials. IEEE, 2008, pp. 508–511.

E○ F. Karouta, B. Docter, **P. Kaspar**, E. J. Geluk, and M. K. Smit, "Very high aspect ratio of photonic crystals holes in InP," in *Symposium IEEE/LEOS Benelux Chapter*, 2007, pp. 227–230.

Work to be Published

T● **P. Kaspar**, R. Kappeler, D. Erni, and H. Jäckel, "Electromagnetic group, energy, and phase velocity of Bloch modes," *to be submitted for publication*, 2012.

Acknowledgments

For the successful completion of this dissertation, I had support from many colleagues, collaborators, family, and friends. At this point I would like to express my warmest thanks and appreciation to all of you who have contributed in one way or another to this work, be it directly through scientific discussions and advice or indirectly by giving me your encouragement and by enriching my life outside the laboratories. Thank you!

I want to thank Prof. Dr. Heinz Jäckel and ETH in general for giving me the opportunity to carry out my Ph.D. studies in a very thriving research environment with access to an almost unlimited supply of know-how and equipment. I express my gratitude to Prof. Dr. Heinz Jäckel, Prof. Dr. Gian-Luca Bona, and Dr. Anne Talneau for their critical reviews of my work and for acting as referees for my dissertation.

When I started this Ph.D. project, micro- and nanofabrication was a completely new world to me. I am indebted to all those who helped me grow in it. My first steps were accompanied by Dr. Patric Strasser, Dr. Franck Robin, Dr. Hans-Jörg Lohe, Dr. Robert Wüest, Dr. Urs Hammer, Andreas Neiger, Ping Ma, Dr. Peter Cristea and Yuriy Fedoryshyn. A lot of input came from the FIRST team. Special thanks go to Dr. Otte Homan for his constant support with cleanroom equipment of all sorts; to Dr. Emilio Gini for growing many epitaxial layers on our wafers; and to Sandro Bellini and Maria Leibinger for fruitful collaborations and for cheering up the lab. Many other users of the cleanroom lab have contributed to a constructive and friendly working atmosphere. Most notably Dr. Alfredo Bismuto, Dr. Mattias Beck, Dr. Christoph Stampfer, Dr. Yohan Barbarin, Dr. Martin Hoffmann, Sebastian Holzapfel, and of course the "Bolognesi crowd": Andreas Alt, Diego Marti, Stefano Tirelli, Rickard Lövblom, Ralf Flückiger, Dr. Haifeng Sun, Dr. Yuping Zeng, Angel Pallin, and Dr. Olivier Ostinelli. I am further grateful to Prof. Dr. Colombo Bolognesi and his group for accepting me as a temporary group member on conference trips in Japan and Berlin. We had a lot of fun!

During the final period of this project, the photonics group of our institute was reduced to only four Ph.D. students: Roman Kappeler, Yuriy Fedoryshyn, Ping Ma, and myself. I want to thank you guys for keeping up the good spirit. We had many inspiring discussions during lunch and coffee breaks. Furthermore, I want to thank my project partner Roman Kappeler for being a superb office mate and for teaching me the vocabulary for numerical simulations of electromagnetics. As the runtime of our theses was increased above a certain threshold, our research efforts converged so well that there was no further need for mesh refinement on the perfectly matched layer between our projects.

My warm thanks also go to all the collaborators from outside of our institute. I thank Dr. Fouad Karouta (formerly with TU Eindhoven, Netherlands) for hosting me for a dry-etching experiment at COBRA. I thank Dr. Annette Foelske and Dr. Rüdiger Kötz (PSI, Switzerland) for finding out what kinds of atoms I had on the surfaces of my chips. I thank Sebastian Holzapfel (IFNH at ETH Zurich) for introducing my dry-etching process to the field of food engineering and for a very smooth collaboration style. I thank Jon Olav Grepstad (SINTEF, Norway) for involving me in an exciting project about biosensing and William Whelan-Curtin (University of St. Andrews, Scotland) for bringing the two of us together. I thank Prof. Dr. Daniel Erni (University of Duisburg-Essen, Germany) for useful inputs on waveguide theory and for his very motivating and inspiring attitude.

Life at the institute would not have been the same without Ruth Zähringer and Fredy Mettler. They are the glue that holds the institute together. Furthermore, I want to thank Dr. Silvan Wehrli, Dr. Victor Callegari, Glen Stark, Dr. George von Büren, Dr. David Barras, Dr. Cornelia Kappeler, Martin Kusserow, and Christina Strohrmann for interesting philosophical, political, and nonsensical discussions over lunch. I also thank the following students for their work during a semester project or a master's thesis in our group: Diego Marti, Yogesh Jeyaram, Peter Friedli, Adrian Scherer, Baran Eren, Robert Blattmann, Christopher Fougner.

Finally, and most importantly, I want to direct my warmest appreciation to my family and friends. Special thanks go to my parents Christine and Hans Peter and my brother Dominik for always being there for me. I thank Oliver Wietlisbach for being a good friend and

Matthias Wille for a long list of things. And last but not least, I want to thank you, Anja, for the many joyful hours that we spent together.

Curriculum Vitae

Personal Data

Peter Kaspar
Born July 14, 1980, in Zofingen (AG), Switzerland
Citizen of Oberkulm (AG), Switzerland

Education

2012	Degree Doctor of Sciences ETH Zurich
2006 - 2012	PhD studies in information technology and electrical engineering at ETH Zurich, Switzerland
2005	Diploma degree in physics from ETH Zurich (equivalent MSc ETH Physics)
2005	Ability Certificate for Graduate Teachership from ETH Zurich
1999 - 2005	Studies in physics at ETH Zurich
2001 - 2002	Studies in physics at EPF Lausanne
1999	Matura Typus C from Kantonsschule Wohlen AG, Switzerland
1995 - 1999	Gymnasium at Kantonsschule Wohlen AG, Switzerland
1986 - 1995	Primary/secondary school in Sierra Leone, Brazil, and Switzerland

Professional experience

2006 - 2012	Research and teaching assistant at the Electronics Laboratory, ETH Zurich, Switzerland
2006 - 2012	Equipment ownership at FIRST lab, cleanroom laboratory at ETH Zurich
2002 - 2005	Various teaching side jobs at high school and undergraduate levels